Feasibility Study on Longitudinal Phase-Space Measurements at GSI UNILAC using Charged-Particle Detectors

Vom Fachbereich Physik
der Technischen Universität Darmstadt

zur Erlangung des Grades
eines Doktors der Naturwissenschaften
(Dr. rer. nat.)

genehmigte Dissertation von
Dipl.-Phys. Timo Milosic
aus Darmstadt

TECHNISCHE
UNIVERSITÄT
DARMSTADT

Darmstadt 2014
D17

Referent:	Prof. Dr. Joachim Enders
Korreferent:	Prof. Dr. Dr. h.c./RUS Dieter H.H. Hoffmann
Tag der Einreichung:	17. Dezember 2013
Tag der Prüfung:	14. April 2014

Zusammenfassung

Für Beschleunigeranlagen ist es unabdingbar, Messdaten von Strahlparametern während des Betriebs zu bestimmen. Diese Aufgabe übernimmt die Strahldiagnose. Sie stellt ein Schlüsselglied zur Inbetriebnahme, Einstellung und Optimierung der Anlage dar. Eine wichtige Information ist die Phasenraumverteilung der beschleunigten Teilchensorten. Im Falle der Beschleunigeranlage GSI (Helmholtzzentrum für Schwerionenforschung) sind dies Ionen von Protonen bis hin zu Uran.

Nicht immer existieren etablierte Messmethoden zur Bestimmung notwendiger Strahlinformationen, sodass neuartige Ansätze verfolgt werden müssen. Vor dieser Herausforderung steht der vorliegende Messaufbau, der zur Inbetriebnahme des Hochstrominjektors von Forck et al. konzipiert und realisiert wurde. Dieser soll einen experimentellen Zugang zur longitudinalen Phasenraumverteilung bei niedrigen Energien von 1.4 AMeV ermöglichen. Etablierte Ansätze bei deutlich höheren Energien, die sich der Messung der elektrischen Feldverteilung bedienen, sind, bei gegebenen nichtrelativistischen Geschwindkeiten von 5.5 % der Lichtgeschwindigkeit, nicht praktikabel. Die vorgestellte Messmethodik basiert auf der Messung der Flugzeit einzelner Ionen zwischen zwei Teilchendetektoren. Eine Modifikation ermöglicht, alternativ, die direkte Messung der Energie mittels eines monokristallinen Diamantdetektors.

Derzeit steht, neben anderen Strahlparametern, die Kenntnis des longitudinalen Phasenraums im Fokus der Optimierung des Injektors. Sie erlaubt eine systematische Optimierung der Strahlanpassung entlang der Beschleunigerkavitäten und somit eine verbesserte Transmission sowie niedrigere Emittanzwerte. Durch den Neubau der Beschleunigeranlage FAIR (Facility for Antiproton and Ion Research) ist die Erhöhung der Strahlqualität des bestehenden Injektors eine grundlegende Voraussetzung.

In dieser Arbeit wird der Messaufbau auf seine Eignung untersucht, den longitudinalen Phasenraum hinreichend präzise abzubilden. Dabei gilt es, die Phase und Impuls einzelner Ionen längs der Strahlachse möglichst exakt zu bestimmen. Die Phasenraumverteilung ergibt sich schließlich aus dem gemessenen Ensemble.

Der Aufbau wird im Detail vorgestellt, sowie in notwendige Konzepte wie dem Phasenraum und der Emittanz eingeführt. Nach der ausführlichen Beschreibung der Datenakquisition folgt eine Diskussion der Datenanalyse. Ein maßgeblicher Bestandteil ist die Einführung eines robusten Schätzers für die Kovarianzmatrix. Diese ist direkt mit der Emittanz verknüpft, jedoch für den klassischen Schätzer sehr sensitiv auf Ausreißer in der gemessenen Verteilung. Die übliche Herangehensweise des subjektiven Setzens von Schnitten an die Daten wird damit konsequent vermieden.

Die Messeigenschaften des Flugzeitexperiments wurden für Hoch- und Niederstrom getestet. Dabei wurde die Sensitivität des Messaufbaus auf den Phasenraum bestätigt. Weiterhin

zeigte sich, dass der Gasdruck im Stripperbereich und in besonderem Maße die Einstellung der Hochstromschlitze, die zur Abschwächung bei Hochstrom benötigt werden, einen signifikanten Einfluß auf den gemessenen Phasenraum zur Folge haben. Die Streuung von Ionen an den Schlitzen führt bei kleinen Schlitzöffnungen zu einer messbaren Energieverbreiterung, grösserer Bunchlänge und, folglich, grösseren Emittanz. Unabhängig von der Messkonfiguration wurden konsistent Abweichungen von den erwarteten Werten der Energiebreite $\Delta E/\langle E\rangle \approx 1\,\%$ und des Twiss-Parameters $\alpha \approx 4$ gemessen. Die gemessenen Energiebreiten überschritten die Theoriewerte um einen Faktor 1.5-1.6. Eine direkte Messung der Bunchstruktur ist hingegen, unter Beachtung der Schlitzkonfiguration, sinnvoll.

Niederstrommessungen mit dem monokristallinen Diamantdetektor zeigten nach der Bestrahlung von $\approx 3 \times 10^4$ Argon-Ionen einen Verlust von 5 % in der Pulshöhe und 2 % im Pulsintegral. Obwohl dieser Effekt in der Datenanalyse korrigiert wurde, zeigte sich, wie bereits in der Flugzeitmessung, eine deutlich höhere Energiebreite als erwartet. Ebenso lagen die Werte für α deutlich unter 0.5. Auftretende Schleppen in den gemessenen Verteilungen zeigten ein breites Energiespektrum und konnten quantitativ auf Wechselwirkung mit den Kollimatorblenden zurückgeführt werden.

Nach diesen experimentellen Hinweisen auf eine unzureichende Energieauflösung wurde dieser Effekt in einem Gauss'schen Modellraum untersucht. Dabei konnten die Diskrepanzen zwischen erwarteten und gemessenen Werten der Größen $\Delta E/\langle E\rangle$, α und der Emittanz durch Annahme einer Systemantwort von 1.3 % aufgelöst werden. Im Rahmen des Modellraumes konnte somit vorgeschlagen werden, bei guter Kenntnis der Messauflösung, die gemessenen Daten durch Rücktransformation an die tatsächlichen longitudinalen Parameter anzunähern.

Im Umkehrschluss war es dadurch möglich, anhand des Modells eine analytische Formel für die benötigte Energieauflösung herzuleiten. Es zeigt sich eine hohe Abhängigkeit der benötigten Energieauflösung vom Twiss-Parameter α. Demnach skaliert die benötigte Auflösung mit $1/\alpha$. Um die erwartete Emittanz zu messen, muss die Messgenauigkeit bereits eine Energieauflösung von besser als 1.7 AkeV aufweisen, um eine maximale Abweichung von 10 % zu erzielen. Dies entspricht einer Zeitauflösung von besser als 30 ps.

Dies motivierte eine Erhebung möglicher systematischer Fehlerquellen. Der dominierende Beitrag ist durch die Inhomogenität der Folien gegeben. Bereits die Abschätzung für die Tantalfolie mit $\sigma_E/E \approx 1\,\%$ führt zu einer merklichen Energieverbreiterung, von der Größe des eigentlich zu messenden Wertes. In Anbetracht der benötigten Zeitauflösung, um die Emittanz mit 10 % Genauigkeit zu messen, ist jedoch auch der Beitrag der verkippten Aluminiumfolie von 25 ps kritisch. Die quantitative Erhebung sämtlicher Fehlerquellen, bestehend aus der Zeitauflösung der einzelnen Komponenten und dissipativen Beiträgen der Folien, unterstützt die besprochene Modellbetrachtung. Demnach deckt sich der erhobene Wert für die Systemantwort des Gesamtsystems mit der in der Modellbetrachtung gewählten.

Obwohl eine direkte Messung der gesamten longitudinalen Phasenraumverteilung mit dem derzeitigen Aufbau nicht möglich ist, liefert die Bunchstruktur vertrauenswürdige Werte. Der Messaufbau wurde zu diesem Zweck in mehreren Messkampagnen erfolgreich eingesetzt und für weitere angefordert.

Summary

Accelerator facilities require access to many beam parameters during operation. The field of beam instrumentation serves this crucial role in commissioning, setup and optimisation of the facility. An important information is contained in the phase-space distribution of the accelerated particles. In case of GSI (Helmholtzzentrum für Schwerionenforschung) those are ions from protons to uranium.

If established methods to access certain beam parameters do not exist, new approaches have to emerge. This is the case for the presented measurement setup which has been designed and realised by Forck et al. to support commissioning of the GSI high-current injector. It is aiming at an experimental method to access the longitudinal phase-space distribution at low energies of 1.4 AMeV. Established methods for higher energies and based on the measurement of the electric field distribution are not feasible at non-relativistic velocities. The presented method is based on a time-of-flight (TOF) measurement between two particle detectors. A modification allows, alternatively, the direct measurement of the kinetic energy using a mono-crystalline (MC) diamond detector.

Currently, besides others, the focus of the optimisation of the injector is put on the longitudinal phase-space distribution. It allows for a systematic optimisation of the matching into the accelerator cavities and, thus, an improved transmission as well as lower emittance values. The new accelerator facility FAIR (Facility for Antiproton and Ion Research), a large-scale upgrade at GSI, requires an improved beam quality at the existing injector.

In this work the experimental setup is investigated for its feasibility to measure the longitudinal phase-space distribution. To this end, the phase and momentum of the single ions along the beam axis have to be determined with high precision. Finally, the longitudinal phase-space distribution is identified with the measured ensemble.

The setup is presented in detail, introducing necessary concepts such as the phase space and emittance and is followed by a discussion of the data acquisition and data analysis. An important part of the latter is the introduction of a robust estimator for the covariance matrix of the measured distribution which is directly connected to the RMS emittance. However, the classical estimator is very sensitive to outliers in the measured data. The usual approach of subjective selection of cut regions is thereby avoided.

The TOF setup has been tested with low and high current beams where a general sensitivity to the longitudinal phase-space distribution was confirmed. Furthermore, the gas pressure at the stripper section and the setup of the high-current slits, required for beam attenuation, have an impact on the measured distributions. Scattering of ions at the slits leads to a larger energy spread, larger bunch length and, consequently, emittance. Independent of the configuration, deviations from the expected values of the energy spread $\Delta E/\langle E\rangle \approx 1\,\%$ and the Twiss parameter $\alpha \approx 4$ have been measured. The energy spreads were larger than the

theory values by a factor of 1.5-1.6. However, a direct measurement of the bunch structure, while using sensible high-current slit settings, proved valuable.

Low-current measurements with the MC diamond detector featured a gain loss of 5 % pulse height and 2 % pulse integral after irradiation with $\approx 3 \times 10^4$ argon ions. Although this effect is corrected in the data analysis, the energy spread is significantly larger than expected, like in the TOF measurements. Similarly, the values for α were below 0.5. Prominent trails in the measured distribution showed a broad energy spectrum and could be quantitatively attributed to interaction with the collimator apertures.

As the measurements hint an insufficient energy resolution, this effect has been investigated in a Gaussian model space. The discrepancies between expected and measured values $\Delta E/\langle E \rangle$, α and emittance could be resolved by assuming a system response of 1.3 %. In the scope of this model space and knowledge of the TOF resolution an approximation to the real longitudinal phase-space parameter by back transformation of the covariance matrix was suggested.

Furthermore, the Gaussian model space allowed to deduce an analytic formula for the required energy resolution. This showed a high dependency of the resolution on the Twiss parameter α which scales with $1/\alpha$. For instance, to target a precision of the emittance within 10 % requires a TOF resolution of better than 30 ps.

This motivated a survey on the possible systematic contributions. The dominating contribution was found to be the inhomogeneity of the foils. The tantalum foil alone contributes an energy broadening of $\sigma_E/E \approx 1\,\%$ and is of the same size of the expected energy spread of beam. Including all systematic sources quantitatively supports the considerations made in the Gaussian model space.

While the experimental setup is not yet able to measure the full longitudinal phase-space distribution, it is capable of providing valuable information about the bunch structure. Several campaigns have been successfully supported with bunch-structure measurements.

Contents

List of Figures

List of Tables

Abbreviations

ADC	Analog-to-digital converter
***A*keV**	Kinetic energy given in keV per nucleon
***A*MeV**	Kinetic energy given in MeV per nucleon
***A*GeV**	Kinetic energy given in GeV per nucleon
ASIC	Application-specific integrated circuit
BIF	Beam-induced fluorescence
BNC	Bayonet Neill Concelman (coaxial RF connector type)
CCE	Charge-collection efficiency
CHORDIS	Cold or hot reflex discharge ion source
CVD	Chemical vapour deposition
DAQ	Data acquisition
DLC	Diamond-like carbon
DOF	Degree of freedom
DTL	Drift-tube linear accelerator
ECR	Electron cyclotron resonance source
ESR	Experimental storage ring
FAIR	Facility for Antiproton and Ion Research
FRS	Fragment separator
FSE	First-shot ellipse
FWHM	Full width at half maximum
GSI	GSI Helmholtzzentrum für Schwerionenforschung GmbH
IH	Interdigital H-mode
HIPPI	High intensity pulsed proton injector
HLI	High charge injector (German: **H**och**L**adungs**I**njektor)
HSI	High current injector (German: **H**och**S**trom**I**njektor)
KONUS	Combined zero-degree structure (German: **KO**mbinierte **NU**ll-Grad **S**truktur)
LEBT	Low energy beam transfer
LINAC	Linear accelerator
LSB	Least significant bit
MC	Mono crystalline
MCD	Minimum covariance determinant
MCP	Microchannel plate (also multi-channel plate)
MEVVA	Metal vapour vacuum arc ion source
MUCIS	Multi-cusp ion source
MVE	Minimum volume ellipsoid
NIM	Nuclear instrumentation module
PC	Poly crystalline
PEEK	Polyether ether ketone

PHD	Pulse-height distribution
POSIX	Portable operating system interface based on UNIX
RF	Radio frequency
RFQ	Radio frequency quadrupole
RMS	Root mean square
ROI	Region of interest
SCUBEEx	Self-consistent, unbiased elliptical exclusion method
SFSE	Scaled first-shot ellipse
SHE	Super heavy elements
SIS	Heavy ion synchrotron (German: **S**chwer**I**onen-**S**ynchrotron)
SMA	SubMiniature version A (coaxial RF connector type)
SNR	Signal-to-noise ratio
SRIM	Stopping and range of ions in matter
TDC	Time-to-digital converter
TOF	Time-of-flight
UNILAC	Universal linear accelerator
USB	Universal serial bus
VARIS	Vacuum arc ion source
VME	Versa module eurocard (bus)

Chapter 1

Introduction

The goal of beam instrumentation and diagnostics [1] is the precise measurement of all relevant beam parameters of a particle accelerator. During commissioning and operating of accelerator facilities, beam diagnostics plays a crucial role. Beam diagnostics is not only an important tool for an optimised configuration of the beam-line settings, but also serves to provide feedback in case of erroneous accelerator settings or to provide experimental data for further theoretical calculations or simulations. The ideal situation, from a beam-diagnostics perspective, would be the direct access to the six-dimensional phase-space density at an arbitrary location at all times for a large energy range. This contains the maximum information and allows to derive all parameters of interest. Of course, this situation is not realistic. In fact, beam diagnostics devices only access a certain subset of parameters, such as projections of the particle distribution, and are available only at dedicated locations of the beam line. Furthermore, depending on the type of accelerated particles and their energy and intensity, access to parameters might be a technical challenge.

The GSI accelerator facility [2] belongs to the class of pulsed, radio-frequency-driven (RF) accelerators. Research areas target a wide range of ions from protons to heavy elements like uranium. Soon after emission from the ion sources, the beam is compressed and accelerated in bunches, the regular micro structure of the beam. Through cascading and reuse of cavities in ring accelerators, RF acceleration allows for higher effective field gradients than static-gradient accelerators which comes at the price of a significantly more complicated beam dynamics. All accelerated ions start their life cycle at the Universal Linear Accelerator (UNILAC), the injector stage of the Schwerionen Synchrotron (SIS18). The injector section of the GSI supports two different primary injectors, the high-current injector (HSI) and the high-charge injector (HLI). Both, HSI and HLI, inject into the Alvarez section at a design energy of 1.4 AMeV where the bunches of ions are accelerated to an energy of up to 11.4 AMeV. If required, the beam is transferred to the SIS18 which is able to provide ion energies up to 2 AGeV.

For a proper operation of the accelerator, a delicate synchronised setup is required to reach high beam transmission and beam quality. In particular, this includes the settings of the cavity structure which relies on the knowledge of the input phase space and must accordingly be operated at a matching phase and voltage. Being a versatile facility able

to accelerate all ion species, this is a special issue at GSI. Due to the various modes of operation with different beam parameters, dedicated setups for experiments at GSI often require readjustment of many settings along the beam line, where the knowledge of the phase space is an important piece of information.

The phase space is given by the location and momentum of the particles in the transverse and longitudinal degrees of freedom. While several established methods exist to access the four-dimensional transverse degree of freedom at low-energy sections of heavy-ion facilities, there are no standard methods available to access the longitudinal phase space. In particular these are the *energy spread*, the *bunch length* and the *longitudinal emittance*, a measure of the occupied longitudinal phase-space. This is the topic of this work.

The measurement of longitudinal phase-space distributions of low energy heavy particles proves difficult, compared to the transverse case, which is typically provided by the well-established slit-grid technique [3]. At low velocities, common longitudinal measurement techniques, based on the electric field distribution, fail due to the long-ranged longitudinal field component. The experiment in this work is located after the HSI, thus, at an energy of 1.4 AMeV or a velocity of $\approx 5.5\,\%$ c. Measurement techniques relying on the electric-field distribution, like capacitive pick-ups [4], consequently produce significantly convoluted output signals, rendering the determination of the bunch structure impossible. A rarely used approach is based on a horizontal dispersive dipole section, for spatial momenta separation, followed by a RF-synchronised vertical deflecting system [5]. Eventually, the beam is sampled by a slit-grid setup, thereby mapping the longitudinal phase-space distribution to a two-dimensional transverse profile distribution. Besides the high costs, in general this device is not feasible to be inserted inside existing beam lines, due to its large dimension of several meters. At low energies, most accelerator facilities omit longitudinal phase-space diagnostics altogether where possible.

In this work, a new type of device is studied which is aimed at the determination of the longitudinal phase space of heavy-ion beams at low energy. The measuring device has been developed in 1999 to support commissioning of the new high-current injector line at GSI UNILAC. At present, the device is installed inside the charge-separation chicane of the UNILAC gas-stripper section. The first design targeted the measurement of longitudinal particle distribution only, also called *bunch structure* [6]. An iteration of the design [7] in 2000 allowed, in principle, the measurement of the particle momentum by means of time-of-flight and, hence, the full two-dimensional longitudinal phase space.

With the emerging upgrade of the accelerator for the Facility for Antiproton and Ion Research (FAIR), certain design values have to be met by the existing GSI accelerator infrastructure which will serve as injector to FAIR. To reach the FAIR design values of the UNILAC high-current injector, optimisation of the matching into the Alvarez linear accelerator is one important task. Hence, the knowledge of the six-dimensional phase space near the first Alvarez tank is desirable. This work studies the feasibility of longitudinal phase-space measurements with the mentioned device. Additionally, a single-detector direct-calorimetric approach is investigated. In particular, this comprises the achievable timing resolution and the study of systematic contributions. Parts of the original data acquisition have been rewritten for the TOF system and built from scratch for the calorimetric

measurement. The data analysis of the phase spaces aims for a consistent description of statistical moments by means of robust estimators.

The restricted beam time and the required single-user operation[1] at the accelerator facility put the emphasize of this work to the analysis of the measured data.

The Programme

Chapter 2 presents fundamentals of beam dynamics by introducing the definitions of relevant quantities like the time structure of the beam and the transverse and longitudinal phase-space. It then proceeds with the characterisation of phase space via the concepts of beam emittance and Twiss parameters, quantities that are accessible for beam diagnostics measurements. After a brief overview of common linear accelerators, fundamental aspects of longitudinal beam dynamics are introduced such as phase stability or the separatrix. The chapter concludes with a description of the existing GSI linear accelerator facility.

Principles of single-particle detection via time-of-flight (TOF) measurements and a calorimetric approach with a total absorption mono-crystalline diamond detector are described in Chapter 3. Following a detailed overview of the experiment area and detector setup, particle beam attenuation via Coulomb scattering is carefully examined. A thin foil positioned in the beam path scatters a small fraction of the primary beam into the acceptance of the experiment setup.

Chapter 4 describes data acquisition and offline analysis. For both measurements, the TOF and calorimetric approach, flexible software codes had to be developed in order to handle various types of events that previously were not observed or simply disregarded. Standard procedures for calculation of emittance and Twiss parameters often failed to yield useful, unbiased results. For this reason, the robust Minimum Covariance Determinant (MCD) estimator was tested and consistently applied to all data presented in this work.

In Chapter 5 the experimental setups, in particular the TOF setup, are subjected to various test conditions in order to assess the performance of the measurement approaches such as the sensitivity or timing resolution. The data revealed that the timing resolution is not sufficient for precise phase-space measurements and that interaction of particle with the high-current slits and collimator apertures can cause a significant background.

These findings prompted the analytical study on resolution effects which is presented in Chapter 6. There, the effect of experimental resolution on the measured quantities emittance and Twiss parameters is investigated.

Chapter 7 describes a survey on sources of uncertainties in the TOF setup. The analysis showed that the current setup cannot reproduce the full longitudinal phase-space distribution due to the insufficient energy resolution. However, the results of the survey provide information on potential improvements of the setup.

Chapter 8 gives a conclusion and outlook on the presented work.

[1] Variation of the high-current slits and pressures of the gas strippers cannot be limited to a certain virtual accelerator but affects all users requesting beams for the HSI.

Chapter 2

Fundamentals

2.1 Time Structure

The time structure of the beam is described by different characteristic parameters. Usually, linear accelerators, such as the GSI UNILAC, providing particle energies above several *MeV per nucleon* (*A*MeV), feature a macroscopic and microscopic time structure as schematically depicted in Fig. 2.1. The *macro pulse* consists of multiple *bunches* (sometimes also referred to as *micro pulses*) which are a direct result of particle acceleration using an alternating electric field (radio frequency, RF). The macro-pulse structure has a different origin. Ion sources can deliver high beam intensities only for short time intervals which are typically in the order of hundreds of microseconds up to a few milliseconds at GSI [8]. Furthermore, at high beam energies and intensities, the RF power consumption of more than 1 MW and consequently the required cooling does not allow for a cw (continuous-wave) operation at reasonable expenditure. The ability to accelerate multiple ion species in an interleaved mode, sharing up to 14 distinct accelerator configurations (*virtual accelerators*) presumes a beam concept based on macro pulses. The dashed thick red line in Fig. 2.1 depicts the effective macro pulse current I_m of a single virtual accelerator. It is usually measured using beam-current transformers and represents a smoothed, averaged current of the underlying bunch train of length τ. The *repetition rate* ν_r of the macro pulses is given by the period time separating them

$$\nu_r = T_m^{-1} \,, \tag{2.1}$$

whereas the *duty cycle* f_d is given by

$$f_d = \frac{\tau}{T_m} = \tau\,\nu_r \,. \tag{2.2}$$

Repetition rates at the GSI injector facility are based on a 50 Hz pulse to pulse time reference. They typically range from the sub-Hz regime up to 50 Hz and strongly depend on the ion source and the targeted experimental area (UNILAC or synchrotron injection). Also the requested pulse length τ and the intensity may limit the maximum repetition rate for a given source.

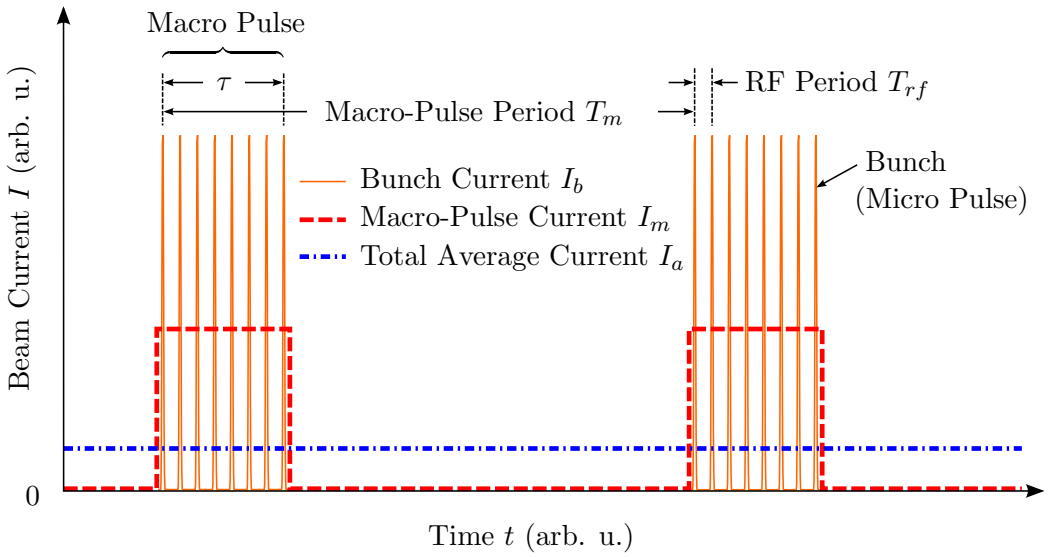

Fig. 2.1: Schematic representation of macro-pulse current I_m and bunch (micro-pulse) current I_b. The macro-pulse current I_m is typically measured using fast beam-current transformers which can resolve pulses down to several microseconds, but are incapable of resolving the time structure of the bunch current with a typical length of about a few nanoseconds (RMS).

As denoted in Fig. 2.1 by the thin orange line, the macro pulse consists of many single bunches occurring at the frequency ν_{rf} of the accelerating RF. In total a macro pulse contains about n_τ bunches with

$$n_\tau = \frac{\tau}{T_{rf}} = \tau\,\nu_{rf}\,. \tag{2.3}$$

For better visibility only a few bunches have been depicted in Fig. 2.1, whereas a typical macro pulse at the GSI UNILAC contains several thousands of bunches.

The important particle dynamics is related to the bunches which are described in a six-dimensional phase space. All bunches, within a virtual accelerator, are expected to be described by the same phase-space distribution. The goal of this work is to present and qualify a measurement setup for determination of the longitudinal subspace.

2.2 Phase Space

For many physical systems, the *phase space* is a mathematical way to define the state of a dynamic system by the parameters of the underlying model. This concept is also applied in accelerator physics. Especially particle distributions of the actual beam are represented in the appropriate phase-space parameterisation. *Phase portraits*, on the other hand, visualise the phase-space trajectories of single particles under different boundary conditions. Taking heavy ions as reference, the beam configuration is commonly considered to be sufficiently abstracted from the position and momentum along the three spatial degrees of freedom

of each ion. Thus, the ions themselves are considered as macroscopic systems, sometimes including the net charge distribution if space-charge effects are taken into account. Further degrees of freedom such as the constituents of the nucleus, the spin or the residual electronic configuration are not of relevance. The two spatial transverse degrees of freedom $\{x, y\}$ and the longitudinal degree of freedom $\{z\}$ span a six-dimensional phase space P_{6D}

$$P_{6D} = \underbrace{(x, p_x) \otimes (y, p_y)}_{\text{transverse}} \otimes \underbrace{(z, p_z)}_{\text{longitudinal}} , \tag{2.4}$$

by the so-called conjugate variables of the Hamiltonian theory.

During conception of accelerator sections, crucial distributions in phase space at several locations can be deduced by sophisticated simulations which help, in an iterative process, to meet the design goals. Nevertheless, real phase-space distributions of the beam may differ significantly from theoretical predictions making the measurement of the phase space indispensable during commissioning, optimisation and, to some extent, daily operation. Dedicated measurement systems are required for the transverse and longitudinal degrees of freedom. A universal approach does not exist. The availability of a feasible measurement method strongly depends on the type of particle, the desired subset of parameters to measure and the energy range at the location of measurement. The intensity of the beam as well as the required accuracy are relevant too. Other design criteria, for example if a non-interceptive device is targeted or the required performance of the data acquisition (DAQ), may represent strong limitations that cannot not be resolved. Finally, the total cost of design, construction and maintenance effort may affect availability of access to certain beam parameters.

Transverse Degree of Freedom. A common representation of the transverse subspace is given by the spatial displacement from the design beam axis $\{x, y\}$, usually based on a right-handed coordinate system, and the tangent of the corresponding divergence angle θ_x and θ_y. Thus, the momentum information is contained in the values $\{x', y'\}$ by the ratio of the transverse momentum components p_x and p_y with respect to the longitudinal momentum p_s of the reference particle (synchronous particle) or the local longitudinal central momentum $\langle p \rangle$, typically in units of mrad (since $p_{\{x,y\}} \ll p_z$):

$$\{x', y'\} = \frac{p_{\{x,y\}}}{p_s} = \tan\theta_{\{x,y\}} \tag{2.5}$$

This pragmatic choice of coordinate system for the transverse plane is mainly motivated by the direct measurement of position and divergence angle via the well established *slit-grid* method. It is a common method for measuring the transverse phase-space distribution at linear accelerators and transfer sections where the range in matter is short enough to fully stop the beam within the micrometer or millimeter regime and still be able to cool the absorbing geometry. A slit-grid measurement is a beam-destructive approach which cuts out a narrow area at certain position using a slit. After a free drift section the distribution is sampled with a wire grid, integrated over many bunches and directly provides the momentum distribution by the corresponding $\tan\theta$. To measure the full transverse phase space, the horizontal and vertical degree of freedom require a separate slit-grid module. Another

beam-destructive method for measuring the full four-dimensional transverse phase space immediately with a single bunch (single shot) is the *pepperpot* device [9]. Non-interceptive methods, such as *beam induced fluorescence* (BIF [10]), allow to measure transverse density profiles.

Longitudinal Degree of Freedom. As given in Eq. (2.4), the longitudinal subspace of the phase space is spanned by the spatial location z along the beam line and the corresponding momentum p_z. However, the longitudinal subspace is often parameterised relative to a reference particle, the so-called *synchronous particle* s. The synchronous particle marks the design particle of expected behaviour along the accelerating structure or sometimes, with a lower stringency, another distinguished property such as the particle that corresponds to the first central moments of the beam under consideration. Moreover, measurements of the longitudinal plane at a certain position z_0, for example when recording the arrival time distribution of ions, suggests the use of a time equivalent parameterisation instead of the spatial distribution *at a certain time* t_0. Therefore, the arrival time Δt_i of particle i relative to the synchronous particle is chosen as

$$\Delta t_i = t_i - t_s \,. \tag{2.6}$$

The same information is contained in the phase difference

$$\Delta \phi_i = \phi_i - \phi_s \,, \tag{2.7}$$

the difference between the phase of particle i with respect to the phase of the synchronous particle s and depends on the accelerating RF. Early particles, which have smaller arrival times with respect to the synchronous particle, have larger phases. Hence, the proportionality between $\Delta \phi_i$ and Δt_i is given by

$$\Delta \phi_i \propto -\Delta t_i \,. \tag{2.8}$$

The exact relation relies on the frequency ν_{rf} of the accelerating RF

$$\Delta \phi_i = -c_{sc}\, \nu_{rf}\, \Delta t_i \qquad \text{with } c_{sc} = \begin{cases} 360^\circ & (deg) \\ 2\pi & (rad) \end{cases} \,, \tag{2.9}$$

where the coefficient c_{sc} depends on the unit *deg* or *rad*, respectively.

In addition to the plain value of the longitudinal momentum p_z, other representations are common. Apart from the absolute energy, relative fractions are given with respect to the synchronous particle for the momentum (omitting the z index)

$$\frac{\Delta p_i}{p_s} = \frac{p_i - p_s}{p_s} \tag{2.10}$$

as well as for the kinetic energy

$$\frac{\Delta E_i}{E_s} = \frac{E_i - E_s}{E_s} \,. \tag{2.11}$$

As mentioned before, the theoretical synchronous particle quantities p_s and E_s are often replaced by the mean values of the corresponding distribution, $\langle p \rangle$ and $\langle E \rangle$, for practical purposes as in this work. The unit of the relative fractions $\Delta E/\langle E \rangle$ and $\Delta p/\langle p \rangle$ used in this work is 'mrad' as used by the GSI injector division. It refers to the transversal case and is identical to ‰. Values given in 'mrad' always need to be accompanied by the information if they refer to the relative energy deviation or relative momentum deviation.

Exemplary phase-space distributions and their typical representation are depicted in Fig. 2.2. The semi-theoretical distributions show the *expected* transverse and longitudinal phase-space distributions for high-current argon and uranium beams at the location of the measurement setup presented in this work.

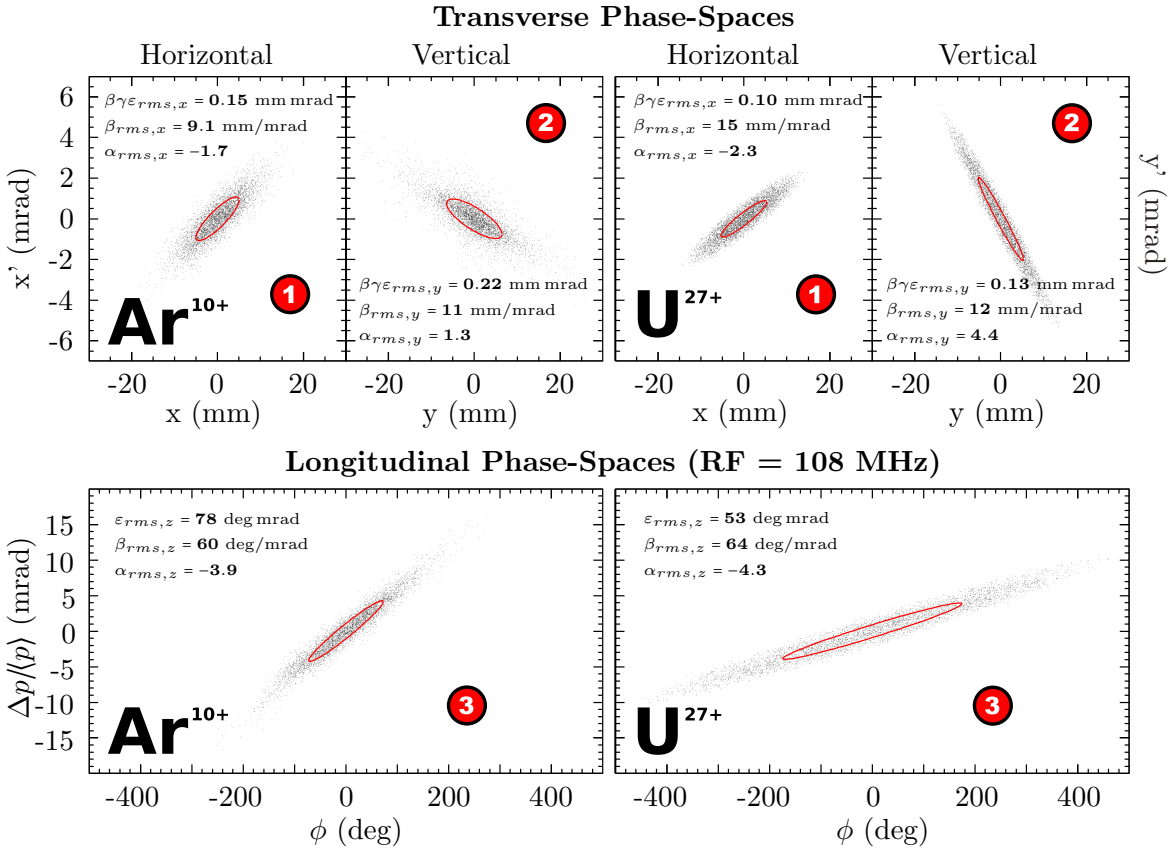

Fig. 2.2: 6-dimensional phase-space start distributions for $^{40}Ar^{10+}$ and $^{238}U^{27+}$ used for high current tracking simulation along the UNILAC post-stripper (L. Groening [11]). The distributions represent the *expected* situation at the location of the TOF setup. Both distributions refer to beam currents of 7.1 mA. For $^{40}Ar^{10+}$ a current of 7.1 mA is equivalent to the FAIR design current of 15 mA of $^{238}U^{28+}$. A detailed explanation of the procedure which yields the start distributions is given in [12], page 24 and 25. **Upper pannel**: Transverse phase-space distributions of Ar^{10+} and U^{27+}. **Lower left**: Longitudinal Ar^{10+} phase-space distribution. **Lower right**: Longitudinal U^{27+} phase-space distribution.

For both ion species, ❶ and ❷ depict the transverse horizontal and vertical phase-space distributions at the setup location, whereas ❸ shows the longitudinal degree of freedom.

Both longitudinal phase-space distribution represent divergent beams. The orientation of the longitudinal is flipped along the momentum axis if the arrival time is used instead of the phase.

2.3 Emittance

The bunch of ions, being a many-body system, can be described by the ensemble of states which represents the individual particles. While such a representation is advantageous for beam simulations of ensembles of single-particle trajectories, for example, it is not always optimal for characterisation of the beam in terms of beam diagnostics. Instead, a reduction of the phase-space distribution, as an ensemble of single particles, into few characteristic parameters is often desirable. As an analogous example, one could think of a classic ideal gas that is macroscopically characterised by its pressure, volume and temperature. Characterisation as a microscopic model, by means of the single gas particles, would be ill-suited for the majority of practical cases.

Concerning the particle distribution inside a particle accelerator, an important information is contained within the volume of the phase space which the particle distribution covers. Only a certain region of the phase space is accelerated in such a way that particles are not lost or beam quality degrades. Typically, it is possible to simulate which region of the phase space complies with stable acceleration at a certain position along the beam line. This fraction of the six-dimensional phase-space volume is called the *acceptance* of the accelerator which depends on the operating values and the location along the beam line. For example, the longitudinal acceptance at an accelerating RF section is given by the corresponding area inside the *separatrix* (see Sec. 2.6.3).

As the acceptance represents a volume (or an area) of the phase space, it is reasonable to characterise the phase-space distribution by its extension. This quantity is called *emittance* and is a measure of the beam quality. A general aim is to reduce overall emittances by optimisations of the accelerator chain to improve beam quality. The emittance ε_h of a non-realistic *homogeneous* longitudinal density distribution is given trivially by the integral of the covered phase-space area A

$$\varepsilon_h = \int_A \mathrm{d}\phi \, \mathrm{d}p \,, \tag{2.12}$$

where A is the smallest possible area that contains all particles. Realistic phase-space densities, in contrast, are of different structure depending on the history of the bunch. This includes the initial particle emission from the ion source, further complex beam dynamics and various dissipative effects. Nevertheless, assuming a Gaussian phase-space density distribution as a model space is commonly considered to be a good approximation of the bunch. The general bivariate Gaussian distribution $\{x, y\}_G$[1] is uniquely parameterised by

[1] x and y label the degrees of freedom within one of the transverse or the longitudinal subspaces. Typical naming conventions in case of the horizontal transverse, the vertical transverse and longitudinal phase-spaces are $\{x, x'\}$, $\{y, y'\}$ and$\{\phi, p\}$.

the location of its centre and the determinant $|C|$ of the variance-covariance matrix

$$C = \begin{pmatrix} \sigma_{xx} & \sigma_{xy} \\ \sigma_{xy} & \sigma_{yy} \end{pmatrix} = \begin{pmatrix} \sigma_x^2 & \sigma_{xy} \\ \sigma_{xy} & \sigma_y^2 \end{pmatrix} . \tag{2.13}$$

In this nomenclature σ_{xx} and σ_{yy} are the variances of x and y, whereas σ_{xy} denotes the covariance between x and y. Using the exemplary set of coordinates $\vec{v} = (\phi, p)$, denoting phase and momentum equivalents in the subscript, the centred Gaussian density distribution G_ρ is parameterised by

$$G_\rho(\phi, p;\, C) = \frac{1}{2\pi\sqrt{|C|}}\, \mathrm{e}^{-\frac{1}{2}\vec{v}\,C^{-1}\,\vec{v}^{\mathrm{T}}} = \frac{1}{2\pi\sqrt{\sigma_\phi^2\,\sigma_p^2 - \sigma_{\phi p}^2}}\, \mathrm{e}^{-\frac{\sigma_p^2\,\phi^2 - 2\,\sigma_\phi\,\sigma_p\,\sigma_{\phi p}\,\phi\,p + \sigma_\phi^2\,p^2}{2\left(\sigma_\phi^2\,\sigma_p^2 - \sigma_{\phi p}^2\right)}} . \tag{2.14}$$

By definition, while fading out quickly with increasing distance from the centre, this model density distribution covers the infinite phase space without boundary. This, of course, represents an obvious deficiency of the model space as realistic bunch distributions are always confined in phase space. On the other hand, realistic bunch distributions also contain populated phase-space cells far from the core region. Therefore, using an approach such as Eq. (2.12) to evaluate the phase-space extension on a Gaussian-like distribution is inappropriate. The effectively covered phase-space area would be overestimated by a large amount since a small fraction of particles has a major impact on the calculated emittance. Thus, a more reasonable and general definition of the emittance, suitable for realistic, long-ranged distributions, is the characterisation by means of the standard deviation and covariance, as implicitly provided by the covariance matrix Eq. (2.13). With the parameterisation of Eq. (2.14) this elliptical phase-space area is of size

$$A_{rms} = \pi\sqrt{\sigma_\phi^2\sigma_p^2 - \sigma_{\phi p}^2} \tag{2.15}$$

and contains about 39 % of all particles provided the underlying particle distribution is indeed of Gaussian type. It should be noted that for arbitrary particle distributions this is not generally true and might differ significantly. As proposed by Lapostolle [13] and according to Eq. (2.15) the RMS emittance is defined by the square root of the determinant of the covariance matrix

$$\varepsilon_{rms} = \sqrt{\sigma_\phi^2\sigma_p^2 - \sigma_{\phi p}^2}\,, \tag{2.16}$$

usually omitting the π. This phase-space area contains about 15 % of all particles in case of a Gaussian density distribution.[2] Figure 2.3 depicts the ellipse corresponding to the RMS-contour level of Eq. (2.14)

$$\sigma_p^2\,\phi^2 - 2\sigma_{\phi p}\,\phi\,p + \sigma_\phi^2\,p^2 = \varepsilon_{rms}^2\,. \tag{2.17}$$

[2] See Chapter 3, page 91, "Charged Particle Beams" by Stanley Humphries Jr. [14] for an introduction to the concept of emittance plus the explanation of units which are normally used in a confusing way.

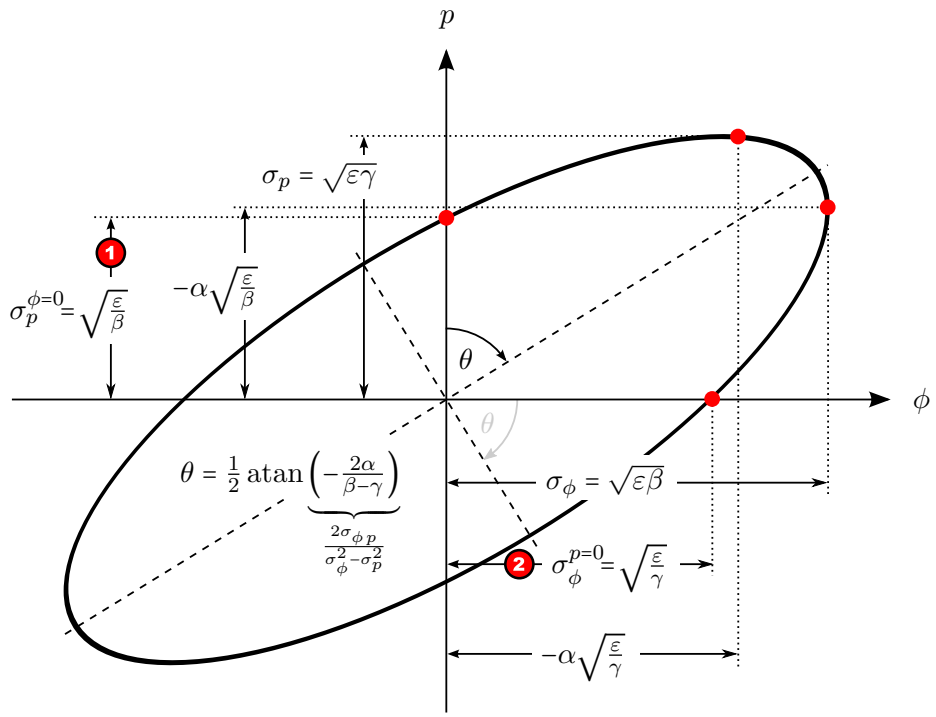

Fig. 2.3: RMS contour of elliptic phase-space density. The corresponding characteristic points are given by the standard deviations σ_ϕ, σ_p and covariance $\sigma_{\phi p}$ or, alternatively, by the emittance ε_{rms} and "Twiss parameters" α, β, γ (Sec. 2.4). Assuming a Gaussian particle density, about 39 % of all particles are covered by the area of the RMS ellipse. In this work, 1 will be called "vertical waist" $\sigma_p^{\phi=0}$, wheres 2 is the "horziontal waist" $\sigma_\phi^{p=0}$.

This parametrisation directly follows from the contour line satisfying

$$\frac{G_\rho(\phi, p)}{G_\rho(0,0)} \stackrel{!}{=} \frac{1}{\sqrt{\mathrm{e}}}\,, \tag{2.18}$$

i. e. when the value of G_ρ has dropped to a fraction of $1/\sqrt{\mathrm{e}}$. The quantity θ, the orientation of the ellipse, specifies the angle between the larger semi axis and the vertical coordinate axis. All distributions in Fig. 2.2 feature the corresponding emittance contour-line by red ellipse.

Assuming no mismatch along the beam line and treating the particle distribution as a free ensemble, the emittance shrinks with increasing normalised particle velocity β_s. This *adiabatic damping* affects the transverse as well as the longitudinal emittance in the same way. More precisely, scaling of the emittance by $\beta_s\gamma_s$

$$\varepsilon_{rms}^n = \beta_s\gamma_s\varepsilon_{rms} \tag{2.19}$$

allows comparison of the emittance at different sections of the beam line at different β_s. The quantity ε_{rms}^n is called *normalised emittance* (RMS).

According to *Liouville's Theorem*, the particle density in the vicinity of a particle trajectory is conserved when the particle dynamics can be described by conservative forces within the Hamilton Formalism. Then, for conservative forces only, the normalised emittance is a constant of motion. The real situation is different. Dissipative contributions are numerous and contribute to an increasing emittance or, in other words, heating of the beam. These are, for example, intra-beam scattering, space-charge forces, electronic stopping and straggling at gas or foil targets. Another effect, the so-called *filamentation*, which is not of dissipative origin, leads to a pseudo-increase of the emittance although Liouville's Theorem still holds. This is possible at acceleration sections when acceleration is carried out at the non-linear regime of the sinusoidal RF, i. e. the phase stabilising force (see Sec. 2.6.2) is not perfectly linear. Then, instead of a rigid rotation of the phase space in case of perfect focusing, particles rotate with a different velocity (in phase space) depending on the distance from the centre of the phase space and consequently impose a spiral-like structure on the phase space which eventually smoothes out over a large area. While the actual area covered by the phase space has not increased, this effect does indeed degrade the quality of the beam and is treated like a real growth of emittance. Non-linear contributions at quadrupole focusing sections show the same phenomenon for the transverse subspace, which usually results in an s-shaped phase-space distribution in the x and y plane.

The emittance can be related to the entropy of the bunch distribution [15]. According to the second law of thermodynamics, the entropy of an isolated system cannot decrease with time. Equally, the normalised emittance along the beam line, parameterised by the spatial parameter s, cannot get smaller within an isolated system

$$\varepsilon^n_{rms}(s) \leq \varepsilon^n_{rms}(s + \Delta s)\,. \tag{2.20}$$

The isolated system considers no particle loss and the cooling effect of beam acceleration is excluded by means of the normalised emittance. While the definition of a strictly isolated system is problematic in case of an accelerator, Eq. (2.20) still holds true. This means, in particular, that the quality of the beam is limited by the initial emittance provided by the ion source. Thus, exact determination of beam emittance ε_{rms} is crucial for accelerator optimisations.

2.4 Twiss Parameters

An alternative parameterisation of the Gaussian particle distribution is given by the *Twiss parameters* α, β and γ (see Fig. 2.3), the elements of the two-dimensional variance-covariance matrix C from Eq. (2.13) normalised by the RMS emittance $\varepsilon_{(rms)}$:

$$(-)\alpha = \frac{\sigma_{x\,y}}{\varepsilon} \qquad \textit{"correlation"} \tag{2.21}$$

$$\beta = \frac{\sigma_x^2}{\varepsilon} \qquad \gamma = \frac{\sigma_y^2}{\varepsilon} \tag{2.22}$$

The sign of α is a matter of definition and varies among different authors. In this work $\alpha = -\sigma_{xy}/\varepsilon$ is used consistently. A useful invariant, also called "Courant-Snyder invariant" [14], can be deduced from Eq. (2.16) and the definitions of the Twiss parameters Eqs. (2.21,2.22)

$$\beta\gamma - \alpha^2 = 1\,. \tag{2.23}$$

The density distribution Eq. (2.14) expressed by the Twiss parameters and RMS emittance writes

$$G_\rho(\phi, p;\, C) \to G(\phi, p;\, \alpha, \beta, \gamma\,\varepsilon) = \frac{1}{2\pi\,\varepsilon}\,\mathrm{e}^{-\frac{1}{2\varepsilon}\left(\gamma\,\phi^2 + 2\,\alpha\,\phi\,p + \beta\,p^2\right)}\,. \tag{2.24}$$

Originally, the Twiss parameters have been introduced to describe the stable transverse motion inside periodic lattices of synchrotons by means of the so-called *machine ellipse*s and, ideally, conserved emittance. The actual shapes of the ellipses depend on the location s along the beam line parameterised by $\alpha(s)$, $\beta(s)$, $\gamma(s)$ and mark the boundary of stable transverse motion. Particle distributions that are not well matched against the machine ellipse suffer filamentation or particle loss.

While a similar concept can be extended to the longitudinal phase-space plane in case of synchrotrons, by means of longitudinal machine ellipses, this is obviously not possible at linear accelerators. Machine ellipses are only meaningful in periodic lattices. Nevertheless, Twiss parameters are widely used in the LINAC community, typically in order to reuse existing software originally tailored for transverse phase-space analysis.

If uncertainties of the standard deviations and the covariance are accessible, they can be directly mapped to the uncertainties of the RMS emittance and Twiss parameters via

$$\frac{\Delta\varepsilon}{\varepsilon} \approx \beta\gamma\sqrt{\left(\frac{\Delta\sigma_x}{\sigma_x}\right)^2 + \left(\frac{\Delta\sigma_y}{\sigma_y}\right)^2 + \left(\frac{\alpha^2}{1+\alpha^2}\right)^2\left(\frac{\Delta\sigma_{xy}}{\sigma_{xy}}\right)^2}\,, \tag{2.25}$$

$$\frac{\Delta\alpha}{\alpha} \approx \beta\gamma\sqrt{\left(\frac{\Delta\sigma_x}{\sigma_x}\right)^2 + \left(\frac{\Delta\sigma_y}{\sigma_y}\right)^2 + \left(\frac{\Delta\sigma_{xy}}{\sigma_{xy}}\right)^2}\,, \tag{2.26}$$

$$\frac{\Delta\beta}{\beta} \approx \sqrt{(1-\alpha^2)^2\left(\frac{\Delta\sigma_x}{\sigma_x}\right)^2 + (1+\alpha^2)^2\left(\frac{\Delta\sigma_y}{\sigma_y}\right)^2 + \alpha^4\left(\frac{\Delta\sigma_{xy}}{\sigma_{xy}}\right)^2}\,, \tag{2.27}$$

$$\frac{\Delta\gamma}{\gamma} \approx \sqrt{(1+\alpha^2)^2\left(\frac{\Delta\sigma_x}{\sigma_x}\right)^2 + (1-\alpha^2)^2\left(\frac{\Delta\sigma_y}{\sigma_y}\right)^2 + \alpha^4\left(\frac{\Delta\sigma_{xy}}{\sigma_{xy}}\right)^2}\,. \tag{2.28}$$

2.5 Linear Accelerators

Acceleration of charged particles using static electric fields is limited by a specific breakdown voltage, usually several hundreds of kilovolts, depending on dielectric strength, surface properties and geometry of the acceleration structure. At the top end there are *Van-de-Graaff*-type accelerators which can even provide an effective voltage of above 10 MV.

This limitation can be overcome by a regular setup of shielding drift tubes with a time-varying electric field applied between the gaps. This RF power is commonly fed into a

cavity in an appropriate way, usually inductively or via waveguides, whereas the geometry determines the preferred resonant mode. Since the net energy transfer to a charged particle in a harmonically oscillating electric field is zero, shielding of the particles has to be accomplished during the decelerating half cycle of the local RF voltage using appropriate drift-tube geometries. Between the drift tubes (gaps), the beam particles are consequently exposed to an accelerating voltage and, thus, a synchronised and coherent net energy transfer is provided. Depending on the particle velocity, the drift tubes therefore have to be designed in such a way that their axial lengths scale linearly with increasing average normalised particle velocity $\langle\beta\rangle = \langle v\rangle / c$.

2.5.1 Wideröe Structures

In 1928 Rolf Wideröe suggested the first practicable concept of such a *drift-tube linear accelerator* structure (DTL [16]). As depicted in the upper half of Fig. 2.4, a schematic Wideröe structure, the drift tubes of increasing length are directly fed by the ac power with successive electrodes being of opposite electric potential. Coherent acceleration of particles

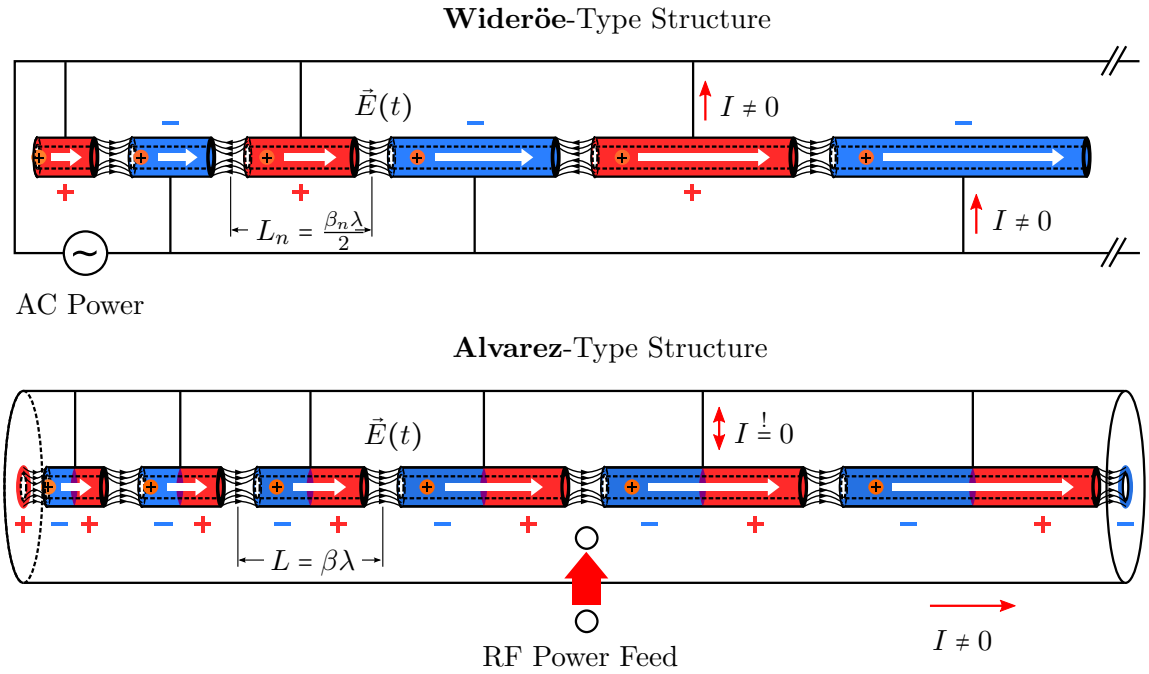

Fig. 2.4: Schematic linear accelerator structures of Wideröe (top) and Alvarez (bottom) type. The improved Alvarez cavity in comparison to the Wideröe includes transverse focusing cells inside the drift tubes to accommodate for the net defocusing effect (transverse) at the gap.

requires the time-dependent longitudinal electric field

$$E_z(t,z) = E_0 \cos\left(\phi_{\omega,k_z}(t,z)\right) \qquad (\text{with } \phi_{\omega,k_z}(t,z) = \omega_{rf} \cdot t - k_z \cdot z) \tag{2.29}$$

to have the same phase velocity $v_{ph} = \omega_{rf}/k_z$ as the current centre velocity βc of the particle at the drift section under consideration. Contiguous gaps between Wideröe drift tubes have a phase advance $\Delta\phi_{\omega,k_z,n}$ of 180° which means successive gaps contain oppositely oriented, longitudinal electric field components at all times. With n labeling the n-th drift section under consideration, the corresponding length of the drift tube is therefore implicitly given by

$$\Delta\phi_{\omega,k_z,n+1}\Big|_t = \phi_{\omega,k_z}(t,z) - \phi_{\omega,k_z}(t,z+L_n) = k_z\,L_n \stackrel{!}{=} \pi\,. \tag{2.30}$$

As mentioned above, the phase velocity v_{ph} of the electric field has to be about the same as the mean longitudinal velocity βc of the particle distributions (the *bunches*) traversing the drift tube. It follows from Eq. (2.30) with $v_{ph} = \omega_{rf}/k_z \stackrel{!}{=} \beta c$ that the length L_n of the Wideröe drift tubes scales with increasing β_n as

$$L_n = \frac{\pi}{k_{z,n}} = \frac{\pi}{\omega_{rf}}\,\beta_n c = \frac{\beta_n \lambda}{2}\,. \tag{2.31}$$

Drift tube LINACs generally come with the inherent issue that the dynamic electric field between the tubes is not perfectly homogeneous as shown in Fig. 2.4. At gap entrances, the field lines have transverse focusing properties whereas at gap exit a transverse defocusing characteristic is present. As a consequence, the overall net defocusing effect causes an additional transverse beam spread which limits the performance of the accelerating structure. The Wideröe LINAC marks an archaic approach by today's standards. At GSI the first UNILAC design featured a Wideröe structure which served as the full prestripper section after the so-called LEBT (Low Energy Beam Transfer). As of 1999 it was replaced by a modern two-stage design, consisting of an RFQ and two H-mode KONUS IH structures (see Sec. 2.5.3), to allow for higher beam intensities [17].

2.5.2 Alvarez Structures

With the iteration of the DTL concept by W. L. Alvarez [18], the *Alvarez structure*, drift tubes are housed in a circular cavity. Instead of a direct AC feed of the drift tube electrodes, a cavity is driven in resonance by the TM_{010} mode which provides the matching electric fields for particle acceleration. Contrary to the empty cavity resonating on a E-mode (or TM-mode) which features no transverse electric field component by definition, the boundary conditions of the support and drift-tube geometry impose a non-vanishing transverse electric field component nearby the gap region which, together with the RF, has an overall transverse defocusing effect. This is counteracted by the inclusion of adequate quadrupole layouts inside the drift tube geometry. Active transverse focusing together with the cavity approach confining the RF power, a much higher efficiency is accomplished compared to the Wideröe structure. According to the TM-mode characteristics, charges flow along the cavity wall and the electrode geometry only (there is no current along the stems). Concerning the length of the drift tubes, the phase advance between successive gaps is 2π and, thus, the

length L_n of the n-th drift tube is given by

$$L_n = \frac{2\pi}{k_{z,n}} = \beta_n \lambda \,. \tag{2.32}$$

The lower half of Fig. 2.4 depicts a schematic Alvarez structure with the typical circular cavity profile and drift tubes of increasing length. An *Alvarez period* consists of a drift tube including the aforementioned transverse focusing elements along with appropriate cooling and an acceleration gap between them. Acceleration is carried out using the TM_{010} mode of the empty cavity. By insertion of the drift tube cell structure a dominant longitudinal electric field component along the beam axis is conserved due to symmetry considerations and is even increased locally.

Alvarez structures are still used while more sophisticated accelerating structures with a higher effective field gradient exist. On the other hand maintenance effort is low and the design is well understood due to its simplicity. A 4-stage Alvarez structure and several single gap resonators serve as final accelerating structure of the UNILAC complex.

2.5.3 H-mode Structures

More efficient, modern heavy ion linear accelerating structures than the Alvarez approach are the so-called *H-mode LINAC Structures*, also referred to as *H-type LINAC Structures* [19]. Contrary to the Wideröe (if driven by a cavity) or the Alvarez structure, the H-mode (TE-mode) has no longitudinal electric field component in the empty cavity by definition. Only due to sophisticated boundary conditions by the geometry of the stems and drift tubes (or crossbars, respectively), longitudinal acceleration is accomplished with the advantage of a significantly enhanced effective field gradient compared to Alvarez-type DTLs. Although all H-Type cavities are based on H_{n10}-modes, one can differentiate between two major cavity designs: The 'Interdigital H-Type Structure' (IH) using the H_{110}-mode and the 'Crossbar H-Type Structure' (CH) used in the high β range resonating on the H_{210}-mode. As there are no relevant longitudinal wall currents present, since the electric field mode is fully transverse at least in the empty cavity, power losses are significantly lower compared to the Alvarez design.

KONUS Beam Acceleration. H-mode structures have been suggested already in the 70s to improve the power efficiency per unit length. Further improvements on the effective gradient can be accomplished by the concept of 'Combined Zero-Degree Structure' ('**KO**mbinierte **NU**ll-Grad **S**truktur', KONUS [20]). A *KONUS period* consists of a 0° synchronous particle structure at which the beam is injected above synchronous particle energy, a separate transverse focusing section by a quadrupole triplet or a solenoid and a longitudinal focusing section at typically $\phi_s = -35°$, usually referred to as *rebunching section*. Instead of transverse focusing elements being housed in each drift tube, the separate focusing section allows a compact LINAC design with an enhanced number of accelerating gaps per unit length compared to the Alvarez design. At the same time, the apertures of the drift tubes can be significantly reduced which further improves the shunt impedance and, thus, the power efficiency of the LINAC structure. Also the plain acceleration section

at crest voltage alone provides about 15 % improvement in efficiency (regarding the same amplitude) of the synchronous particle gradient per acceleration gap compared to Alvarez structures.

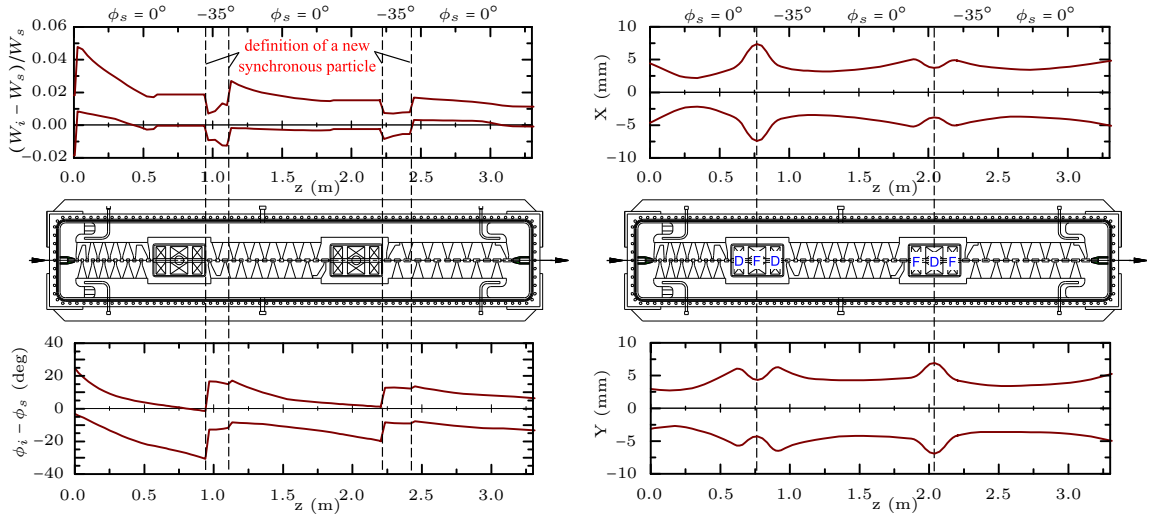

(Calculations and graphics *Rudolf Tiede*, IAP, Frankfurt)

Fig. 2.5: KONUS-driven H-Type (IH) structure cell at GSI High Charge Injector (HLI). **Left**: Longitudinal beam envelopes of the relative energy deviation (top) and deviation from synchronous particle (bottom), along the accelerating structure. The discontinuities originate from a redefinition of the synchronous particle. **Right**: Transverse beam envelopes of the horizontal and vertical degree of freedom along the accelerating structure.

From a beam dynamics point of view, KONUS is a delicate challenge. *H*-mode cavity design using KONUS is an intuitive approach based on experience with no straightforward design recipe available. This effectively ends up in a trial and error approach using simulated dynamic field distributions and particle tracking codes at hand. Most efficient acceleration at 0° phase comes at the cost of unstable, i. e. longitudinal defocusing particle trajectories with respect to the synchronous particle. While the longitudinal broadening of the bunch length is counteracted by the separate rebuncher section, the influence of the strong non-linearity of voltage around 0° cannot be fully compensated and may have an influence on the longitudinal phase-space distribution by filamentation. Although filamentation is not a process that causes an increase of the emittance, since it cannot be classified as a dissipative effect which leads to an increase of the covered phase-space area, it does indeed increase the boundaries of a phase-space distribution and, thus, introduces higher requirements on the acceptance.

A KONUS-driven cavity has been installed at GSI at the UNILAC as part of the *high current injector* in 1999 and partial replacement for the Wideröe LINAC. A KONUS cavity has been also the predestined choice of design for the *high charge injector* (HLI) due to its high effective gradient. As an exemplary tracking simulation of KONUS, Fig. 2.5 shows the new GSI HLI structure. Apart from the aforementioned KONUS period, the complicated beam dynamics compared to the Alvarez design can be seen by the required redefinition

of the synchronous particle during acceleration. This manifests itself by discontinuities of the tracked particle observables in the left graphics, showing the relative energy deviation and the relative phase. Design, commissioning and operating of KONUS structures can be challenging, but is considered worthwhile if highest requirements of effective gradient and beam intensity have to be met. To that end, reliable beam diagnostics of transverse and in particular longitudinal degree of freedom is mandatory which is the goal of the measurement setup studied in this work.

2.6 Longitudinal Beam Dynamics

To get a glimpse on the importance of longitudinal beam diagnostics targeted in this work, it is helpful to outline basic theoretical concepts of drift-tube LINACs used at the GSI injector line. Wideröe and Alvarez structures (see Sec. 2.5.2) follow a common acceleration scheme. Along the beam axis, at the gap between the shielding drift tubes, a quasi-harmonic oscillating potential provided by the TM_{010} mode accelerates the transiting charged particles. Similarly, H-mode LINACs in turn use TE_{n10} modes (H_{n10} modes) to accelerate the beam as described in Sec. 2.5.3 and the following explanation can be applied likewise. Due to the specific geometries and significant beam effects such as inter-particle space-charges, the design and optimization of modern linear accelerator structures require the use of sophisticated *tracking codes*, e. g. LORASR [21], DYNAMION [22] or PARMILA [23]. Nevertheless, it is possible to analytically model major properties of linear accelerators qualitatively. In the following, the energy gain and the longitudinal equation of motion will be described under simplified boundary conditions.

2.6.1 Energy Gain during Gap Transition

Acceleration of charged particles takes place at the gaps between the drift tubes. While the space inside the drift tube is assumed to be field-free, the electric field still reaches inside to a small extent. The relevant longitudinal electric field component amplitude $E_z(r,z)$ is depicted in Fig. 2.6 for the axial case $r = 0$. To account for the electric field reaching inside the tube volume, the effective gap length g_{eff} is taken into consideration. Since the exact electric field distribution depends on the specific accelerator geometry, an exemplary on-axis amplitude distribution is shown. Several numerical frameworks exist to calculate static and dynamic electro-magnetic field properties from the actual geometry of the accelerator cavity. Usually it is legitimate to consider $E_z(r,z)$ to be symmetric with respect to the centre of the gap. In the following the energy is denoted by W to avoid confusion with the electric field E. Using the time-dependent longitudinal electric field E_z as given by Eq. (2.29), the energy gain ΔW_i of a particle i transiting the gap can be written as

$$\Delta W_i = q \cdot \int_{-g_{eff}/2}^{+g_{eff}/2} \mathrm{d}z \; E_z(0,z) \cos\left(\omega_{rf} \cdot t + \phi_i\right) = q \cdot \int_{-g_{eff}/2}^{+g_{eff}/2} \mathrm{d}z \; E_z(0,z) \cos\left(\frac{\omega_{rf}}{\beta_i c} z + \phi_i\right), \qquad (2.33)$$

where g_{eff} denotes the effective gap length and accounts for the incomplete shielding of the

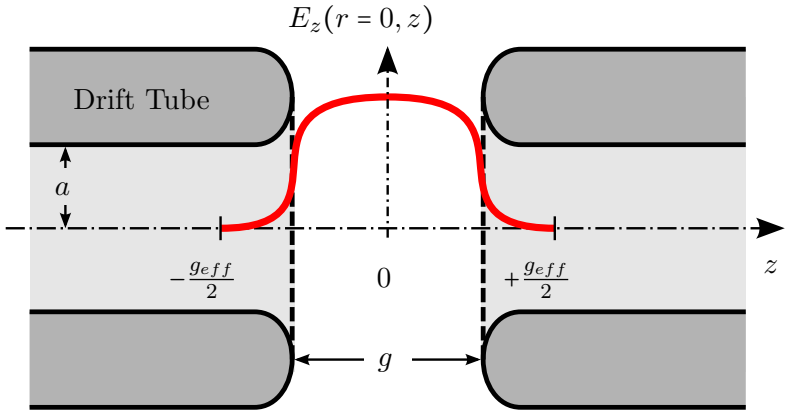

Fig. 2.6: Schematic longitudinal electric field amplitude at an acceleration gap. The electric field is not perfectly shielded inside the drift tubes which is taken into account by the effective bounds $\pm g_{eff}/2$.

field inside the drift tubes. The maximum potential difference U_0 exposed to a theoretical particle with an infinite velocity is therefore given by

$$U_0 = \int_{-g_{eff}/2}^{+g_{eff}/2} \mathrm{d}z \; E_z(0, z)\,, \tag{2.34}$$

whereas an actual particle i would see an effective potential difference $U_{eff,i}$ of

$$U_{eff,i} = \int_{-g_{eff}/2}^{+g_{eff}/2} \mathrm{d}z \; E_z(0, z) \cos\left(\frac{\omega_{rf}}{\beta_i c}\, z + \phi_i\right), \tag{2.35}$$

by assuming a constant velocity approximately at the gap under consideration for simplicity. Furthermore, with the assumed mirror symmetry of $E_z(r, z)$ with respect to $z = 0$ and the symmetric integral limits, Eq. (2.35) is identical to

$$U_{eff,i} = \cos\phi_i \cdot \int_{-g_{eff}/2}^{+g_{eff}/2} \mathrm{d}z \; E_z(0, z) \cos\left(\frac{\omega_{rf}}{\beta_i c}\, z\right), \tag{2.36}$$

the effective accelerating voltage.

A common approach to account for the effective gradient and, thus, the effective energy gain of the particle is to introduce the so-called *transit time factor*

$$T = \frac{\left|U_{eff,s}\right|}{U_0} = \frac{\left|\int_{-g_{eff}/2}^{+g_{eff}/2} \mathrm{d}z\; E_z(0,z)\cos\left(\frac{\omega_{rf}}{\langle\beta\rangle c}\, z\right)\right|}{\int_{-g_{eff}/2}^{+g_{eff}/2} \mathrm{d}z\; E_z(0,z)} \cos\phi_s \leq 1\,. \tag{2.37}$$

Characteristically, the actual value of T scales inversely with the ratio of the effective gap length g_{eff} versus the RF wavelength. Time transit factors range from 0.8 to 0.9, with shorter gaps usually reaching higher values depending on the actual gap geometry. The energy gain Eq. (2.33) for the synchronous particle at gap transition can be rewritten as

$$\Delta W_s = q\,U_0\,T\,cos\,\phi_s\,. \tag{2.38}$$

Introducing the effective mean electric field amplitude

$$E_{z,0} = \frac{U_0}{g_{eff}} = \frac{1}{g_{eff}} \int_{-g_{eff}/2}^{+g_{eff}/2} \mathrm{d}z\; E_z(0,z)\,, \tag{2.39}$$

the energy gain for any particle i, but especially the synchronous particle s can finally be expressed as

$$\Delta W_s = q\,E_{z,0}\,g_{eff}\,T\,\cos\,\phi_s = q\,U_{eff,s}\,\cos\,\phi_s \tag{2.40}$$

by means of the effective voltage U_{eff} and the synchronous phase ϕ_s.

2.6.2 Longitudinal Phase Stability

Real particle distributions inside a linear accelerator have a finite second moment attached to all degrees of freedom. In other words this means a finite phase-space volume or, in the terminology commonly referred to in accelerator physics, emittance as introduced in Sec. 2.3. The initial particle distribution provided by the ion source usually already comes with a pronounced emittance. According to Sec. 2.6.1, the energy gain depends on the relative phase ϕ_i of the particle with respect to the RF voltage. Based on the fact that the longitudinal (as well as the transverse) particle distribution is neither a sharp distribution in phase nor momentum, the principle of acceleration must be chosen in such a way that it provides stable particle motion. This means stable in the sense of *phase stability* and therefore the quest to keep the particles as localised as possible during acceleration. In the following, phase stability is discussed taking the relative phase ϕ_i with respect to the RF as the free parameter.

Figure 2.7 shows schematically the RF voltage applied between the drift tubes. With the phase origin usually located at crest voltage, the stable acceleration region at $\left[-\frac{\pi}{2}, 0\right] + n \cdot 2\pi$ (blue section), where n numbers a unique period, is commonly referred to as a *bucket* with

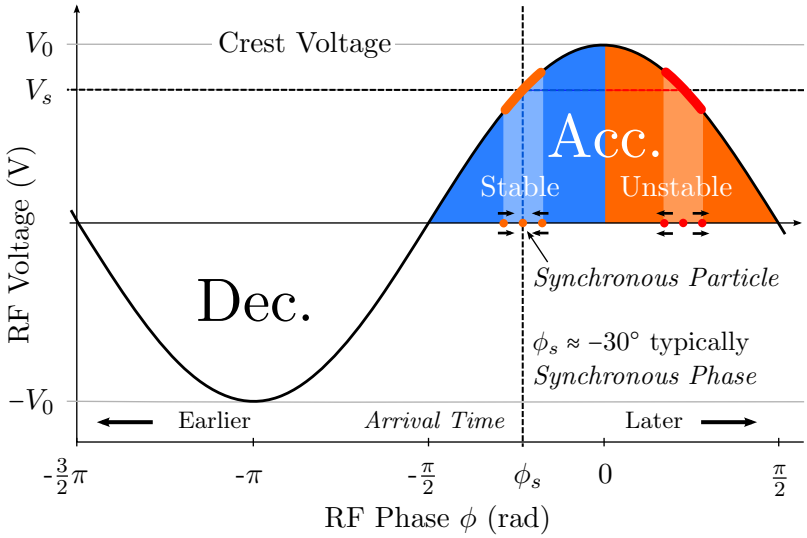

Fig. 2.7: Schematic representation of the RF voltage between drift tubes for negatively-charged particle. In this picture particles to the left of the synchronous particle are advanced, whereas particles to right are retarded. For a stable longitudinal motion at linear accelerators only the region (marked as *stable*) is useful for acceleration.

the corresponding confined, stable phase-space distribution referred to as a *bunch* or *micro pulse*. A more precise definition of a *bucket* will be given in Sec. 2.6.3, when a simplified longitudinal equation of motion is explicitly solved. The operation value of the *synchronous phase* ϕ_s, which is the reference phase of the design particle (*synchronous particle*) with respect to the RF, is typically set at around −30°. For typical Gaussian-like particle distributions, most particles with a surplus of energy compared to the *synchronous particle* i_s arrive at an earlier time/phase and as such undergo less acceleration. Together with the fact that particles of a lower energy than i_s get accelerated by a larger effective voltage, this illustrates the longitudinal focusing effect with respect to the synchronous particle. On the other hand, the phase range $[0, \frac{\pi}{2}] + n \cdot 2\pi$, while also accelerating, has an intrinsic, longitudinally defocusing tendency as depicted in Fig. 2.7 and is labeled as *unstable* region. It should be noted that the design decisions for the location of the synchronous phase mainly depend on the bunch length. Shorter bunch lengths allow for a more efficient synchronous phase nearer to the crest voltage without losing many particles to the unstable region and, thus, a more effective acceleration. Nevertheless, following the sinusoidal schematic from Fig. 2.7 it is obvious that approaching 0° phase comes with increasing nonlinear force and therefore increasing size of the phase space.

Unfortunately, longitudinal and transverse focusing at the same time is impossible using drift tube acceleration. At sections that have a net *longitudinal focusing* effect they contribute to a net *transverse defocusing* effect. From a qualitative point of view this is evident by the topology of the electric field inside the accelerating gap as depicted schematically

in Fig. 2.4. At gap entrance the transverse field components possess focusing properties, and they are defocusing the second half of the gap. Since the field amplitude is ramped while the bunch is transiting the acceleration gap, the defocusing effect at the second half is dominating, assuming a constant normalised particle velocity β for simplification. A more elaborate discussion of the topic was published first by E.M. McMillan in 1950 [24]. Usually the inherent effect of transverse defocusing needs to be compensated by separate focusing elements, i. e. magnetic quadrupole or solenoidal lenses.

2.6.3 Longitudinal Equation of Motion

For a better understanding of the characteristics of common DTL beam dynamics, this section provides the derivation of a simplified equation of motion of the longitudinal degree of freedom. Furthermore, it highlights the advantage if access to the longitudinal degree of freedom is available by beam diagnostics which allows monitoring and optimisation of the beam line. For instance, the knowledge of a longitudinal phase-space distribution can either serve as feedback to see if a LINAC is well adjusted or to pin down the starting condition for the setup of the following structures to provide optimal matching conditions.

This section will outline the derivation of the equation of longitudinal particle dynamics under simplified boundary conditions roughly following T. P. Wangler [25]. The discrete acceleration structure is approximated as a continuous differential equation under the assumption of a space-charge free, paraxially approximated system. Furthermore, the rate of acceleration is assumed to be sufficiently small to consider the terms $\frac{\mathrm{d}}{\mathrm{d}z}\beta$ and $\frac{\mathrm{d}}{\mathrm{d}z}\gamma$ negligible with respect to other terms. By switching over to a continuous description, the accelerating fields will be replaced by effective mean fields.

In the following, the separation between two contiguous gap centres is labeled by L_n for the n-th acceleration cell, at which the normalised velocity β_n and the energy W_n are treated as constant. Additionally, within the *thin gap approximation* the energy is instantaneously transferred to the particle at the gap centre by the effective voltage $U_{eff,n}$ after the $(n-1)$-th drift section. Thus, the kinetic energy gain $\Delta W_{n,i}$ between the $(n-1)$-th and n-th drift section for an *arbitrary particle* i is given by

$$\Delta W_{n,i} = W_{n,i} - W_{n-1,i} = q\,U_{eff,n}\,\cos\phi_{n,i} \tag{2.41}$$

using Eq. (2.40).[3] Taking the *synchronous particle* s as reference, the difference in energy gain therefore writes as

$$\Delta(W_i - W_s)_n = \Delta W_{n,i} - \Delta W_{n,s} = q\,U_{eff,n}\,(\cos\phi_{n,i} - \cos\phi_{n,s})\ . \tag{2.42}$$

By design, the phase advance $\Delta\phi_{n,s}$ for the synchronous particle is

$$\Delta\phi_{n,s} = N\cdot 2\pi \qquad N = \begin{cases} \frac{1}{2}, & \text{Wideröe, IH} \\ 1, & \text{Alvarez} \end{cases}\ . \tag{2.43}$$

[3] As in Sec. 2.6.1, the energy is denoted by W to avoid confusion with the electric field E.

On the other hand, the fraction of phase advance between an arbitrary and synchronous particle at the $(n-1)$-th cell equals the fraction of their transit times

$$\frac{\Delta\phi_{n,i}}{\Delta\phi_{n,s}} = \frac{\Delta\phi_{n,i}}{N\,2\pi} \overset{!}{=} \frac{T_{n-1,i}}{T_{n-1,s}} = \frac{\beta_{n-1,s}\,\lambda}{\beta_{n-1,i}\,\lambda} = \frac{1}{N}\frac{L_{n-1}}{\beta_{n-1,i}\,\lambda}\,, \tag{2.44}$$

recalling the length L_n of the n-th cell is $N \cdot \beta_{n,s}\,\lambda$. Consequently, an arbitrary particle has its phase changed by

$$\Delta\phi_{n,i} = 2\pi\,\frac{L_{n-1}}{\beta_{n-1,i}\,\lambda} \tag{2.45}$$

between gap $n-1$ and gap n. This allows to calculate the difference in phase advance between an arbitrary and the synchronous particle accumulated after transit of the $(n-1)$-th cell with

$$\begin{aligned}\Delta(\phi_i - \phi_s)_n &\overset{!}{=} \Delta\phi_{n,i} - \Delta\phi_{n,s} = 2\pi\,\frac{L_{n-1}}{\lambda}\left(\frac{1}{\beta_{n-1,i}} - \frac{1}{\beta_{n-1,s}}\right)\\ &= 2\pi\,\frac{L_{n-1}}{\lambda}\left(\frac{1}{\beta_{n-1,s} + \underbrace{\beta_{n-1,i} - \beta_{n-1,s}}_{=:\Delta\beta}} - \frac{1}{\beta_{n-1,s}}\right) = 2\pi\,\frac{L_{n-1}}{\lambda}\left(\frac{1}{\beta_{n-1,s}+\Delta\beta} - \frac{1}{\beta_{n-1,s}}\right),\end{aligned} \tag{2.46}$$

which can be further simplified by exploiting that $\frac{\Delta\beta}{\beta_{n-1,s}} \ll 1$ and, thus,

$$\Delta(\phi_i - \phi_s)_n \approx -2\pi\frac{\Delta\beta}{\beta_{n-1,s}^2} = -2\pi\frac{\beta_{n-1,i} - \beta_{n-1,s}}{\beta_{n-1,s}^2}\,. \tag{2.47}$$

The work ΔW required to change the normalised velocity by the amount of $\Delta\beta$ taking into account the linear term only

$$\Delta W = \Delta\,(E - E_0) = \Delta E \approx \frac{\mathrm{d}E}{\mathrm{d}\beta}\Delta\beta = \left(\frac{\mathrm{d}}{\mathrm{d}\beta}m_0\gamma c^2\right)\Delta\beta = E_0\,\frac{\mathrm{d}\gamma}{\mathrm{d}\beta}\,\Delta\beta = E_0\,\gamma^3\,\beta\,\Delta\beta \tag{2.48}$$

and Eq. (2.47) provides the relationship between the change in phase deviation and energy deviation with respect to the synchronous particle at the n-th cell

$$\Delta(\phi_i - \phi_s)_n = -2\pi\frac{W_{n-1,i} - W_{n-1,s}}{m_0\,c^2\,\gamma_{n-1,s}^3\,\beta_{n-1,s}^2}\,. \tag{2.49}$$

As mentioned before, the discrete model based on the real cell structure is replaced by a continuous model treating the electric fields as general mean field along the beam axis with $E_{z,0} = \frac{V_0}{L_{n-1}}$. By formally going from $\frac{\Delta}{L_{n-1}}$ to $\frac{\mathrm{d}}{\mathrm{d}z}$ and dropping the discrete index n, the relative energy deviation Eq. (2.42) writes as

$$\frac{\Delta\,(W_i - W_s)}{L_{n-1}} \quad\longrightarrow\quad \frac{\mathrm{d}}{\mathrm{d}z}\,(W_i - W_s) = q\,E_{z,0}\,T\,(\cos\phi_i - \cos\phi_s)\,. \tag{2.50}$$

In the same way the relative phase deviation $\Delta(\phi_i - \phi_s)_n$ transforms into a continuous representation

$$\frac{\mathrm{d}}{\mathrm{d}z}(\phi_i - \phi_s) = \frac{\Delta(\phi_i - \phi_s)}{L_{n-1}} = \frac{\Delta(\phi_i - \phi_s)}{\beta_{n-1}\lambda} \tag{2.51}$$

and is connected to the change in relative energy deviation by Eq. (2.49)

$$\frac{\mathrm{d}}{\mathrm{d}z}(\phi_i - \phi_s) = -2\pi \frac{W_i - W_s}{m_0\, c^2\, \gamma_s^3\, \beta_s^3\, \lambda}\,. \tag{2.52}$$

Derivation by $\frac{\mathrm{d}}{\mathrm{d}z}$ and inserting Eq. (2.50)

$$\frac{\mathrm{d}}{\mathrm{d}z}\left\{\gamma_s^3\, \beta_s^3 \frac{\mathrm{d}}{\mathrm{d}z}(\phi_i - \phi_s)\right\} = -\frac{2\pi\, q\, E_{z,0}\, T}{m_0\, c^2\, \lambda}(\cos\phi_i - \cos\phi_s) \tag{2.53}$$

provides a second order differential equation from two coupled first order differential equations. Furthermore, the rates of change $\frac{\mathrm{d}\beta_s}{\mathrm{d}z}$ and $\frac{\mathrm{d}\gamma_s}{\mathrm{d}z}$ at the acceleration gap are usually small compared to their value. Neglecting those terms, the final problem reads as

$$\frac{\mathrm{d}^2}{\mathrm{d}z^2}(\phi_i - \phi_s) = -\frac{2\pi\, q\, E_{z,0}\, T}{m_0\, c^2\, \gamma_s^3\, \beta_s^3\, \lambda}(\cos\phi_i - \cos\phi_s)\,. \tag{2.54}$$

Fortunately, given by the approximations used, this differential equation can be solved analytically. Multiplication with $\frac{\mathrm{d}}{\mathrm{d}z}(\phi_i - \phi_s)$, which is identical to $\frac{\mathrm{d}\phi_i}{\mathrm{d}z}$, and applying the inverse product rule on the left side

$$\mathrm{d}\left\{\frac{1}{2}\left(\frac{\mathrm{d}}{\mathrm{d}z}(\phi_i - \phi_s)\right)^2\right\} = -\frac{2\pi\, q\, E_{z,0}\, T}{m_0\, c^2\, \gamma_s^3\, \beta_s^3\, \lambda}(\cos\phi_i - \cos\phi_s)\ \mathrm{d}\phi_i \tag{2.55}$$

simplifies the problem significantly as Eq. (2.52) can replace $\left(\frac{\mathrm{d}}{\mathrm{d}z}(\phi_i - \phi_s)\right)^2$. This in turn provides a trivial way to integrate both sides. In doing so, the boundary condition is contained within the constant of integration C

$$\frac{\pi\ (W_i - W_s)^2}{m_0\, c^2\, \gamma_s^3\, \beta_s^3\, \lambda} = -q\, E_{z,0}\, T\ (\sin\phi_i - \phi_i\ \cos\phi_s + C) \tag{2.56}$$

and finally rearranged the kinetic energy deviation $W_i - W_s$ is given by

$$W_i - W_s = \pm\sqrt{\frac{1}{\pi} m_0\, c^2\, \gamma_s^3\, \beta_s^3\, \lambda\, q\, E_{z,0}\, T\ (\phi_i\ \cos\phi_s - \sin\phi_i - C)}\,. \tag{2.57}$$

For different start conditions, imposed by C, Eq. (2.57) provides the corresponding phase-space trajectories. The *separatrix* is a special trajectory which marks the boundary of stable particle motion with the corresponding integration constant C_s

$$C_s = -(\phi_s \cos\phi_s - \sin\phi_s)\,. \tag{2.58}$$

It is now possible to refine the definition of a *bucket* (Section 2.6.2) as the phase-space area

enclosed by the separatrix bound. At the same time this represents the acceptance of the LINAC section as stated in Sec. 2.3.

Figure 2.8 shows the phase portrait for a synchronous phase $\phi_s = -30°$ on the left, which is typically used in Alvarez structures or rebunching sections at KONUS structures. The right

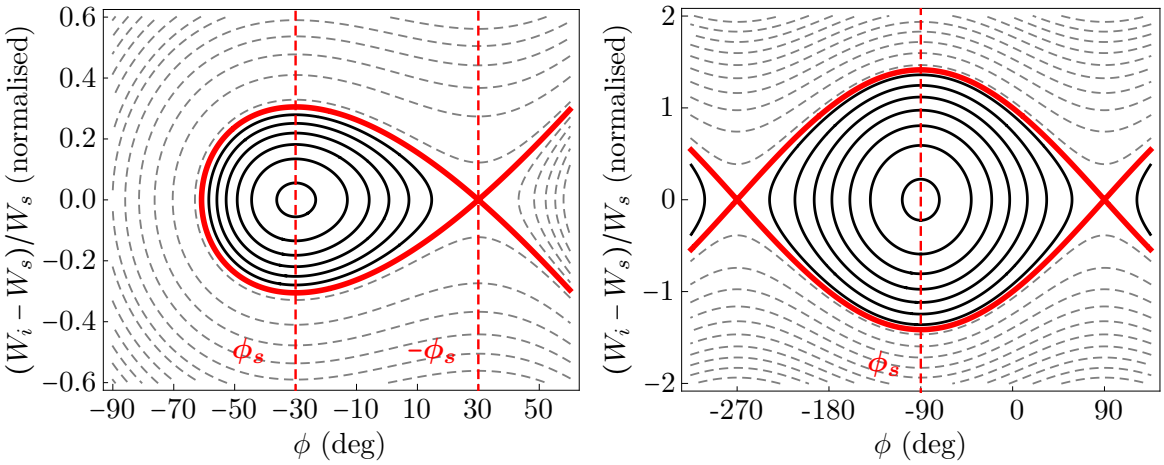

Fig. 2.8: Left: Longitudinal phase portrait for acceleration with a synchronous particle at $\phi_s = -30°$. The *separatrix* (red, thick curve) marks the boundary for the stable and confined phase-space area. **Right**: Longitudinal phase portrait for a synchronous phase of $\phi_s = -90°$. The phase-space area covered by the separatrix is maximal, but the beam undergoes no net acceleration with the accelerator acting as a buncher at optimum linearity. This phase portrait is well known from the classical harmonic oscillator.

of Fig. 2.8 depicts the phase portrait with a synchronous phase of $\phi_s = -90°$, which means operation in pure bunching mode and no net acceleration. The energy axis is displayed in the commonly used representation of the relative energy deviation

$$\frac{W_i - W_s}{W_s} = \pm\sqrt{\underbrace{\frac{\gamma_s^3\,\beta_s^3\,\lambda\,q\,E_{z,0}\,T}{\pi\,m_0\,c^2\,(\gamma_s - 1)^2}}_{=:\xi}\,(\phi_i\,\cos\phi_s - \sin\phi_i - C)}\,. \tag{2.59}$$

The factor ξ is set to 1 as a normalisation since specific accelerator and particle parameters do not lead to a qualitatively different result. Both portraits show the separatrix as a thick line with the stable orbits enclosed as continuous lines while unstable trajectories are marked by dashed lines. Around the synchronous phase ϕ_s, for small amplitudes $\Delta\phi$, the orbits are of elliptic shape. Furthermore, the enclosed areas differ significantly. Thus, the acceptance during acceleration at $\phi_s \approx -30°$ is much smaller compared to pure bunching at $\phi_s = 0°$. It should be noted that in reality, due to the acceleration and, thus, a shrinking phase space, the stable orbits are not closed in the $\phi_s = -30°$ case.

Most efficient acceleration would be carried out by setting the synchronous phase ϕ_s at crest voltage. As described in Sec. 2.5.3, this is done at certain sections of KONUS dynamics based H-mode accelerating structures. The corresponding phase portrait is depicted at Fig. 2.9. Obviously the (formal) separatrix at ❶ has shrunken to a point and does not

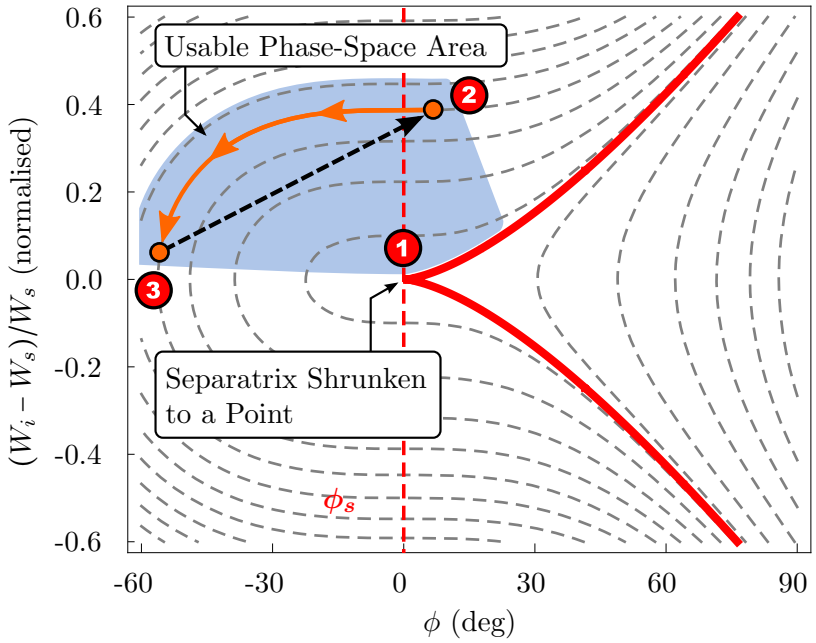

Fig. 2.9: Acceleration with a synchronous phase of $\phi_s = 0°$, i. e. at crest voltage. With the size of the phase space covered by the separatrix shrunken to a point at $(0, 0)$, no per se stable motion is possible. While the KONUS principle relies on the most efficient acceleration at $\phi_s = 0°$ it also includes rebunching sections at $\phi_s \approx -30°$ to counteract the resulting longitudinal debunching. For the marked points in the diagramme, see text.

enclose any area of the phase space. Hence, this configuration does not provide stable orbits. By definition of the axes, the phase-space cell of the synchronous particle is located at the centre at ❶. In case of KONUS beam dynamics, the reference particle and synchronous particle are not the same. At ❷ the reference particle is injected with an energy above synchronous particle energy located close to the synchronous phase $\phi_s = 0°$. This means at crest voltage particles in the vicinity of the reference particle experience neither longitudinal nor transverse focusing. When the bunch further advances through the 0°-structure, the reference particle follows the denoted phase-space trajectory and finally approaches near synchronous particle energy ❸, which is the reason for injection of the beam at greater than synchronous particle energy. During this process all particles in the environment of the reference particle are accelerated and experience longitudinal focusing due to the increasingly negative phase of the reference particle. Once the reference particle approaches quadrant II, defocusing of the bunch sets in as a particle arriving early would again see a higher accelerating field. This is avoided by resetting the KONUS section (❸→❷), thus, confining the motion mainly to quadrant II. Usually, the KONUS section is followed by a dedicated transverse focusing section, consisting of a quadrupole triplet and a rebunching section, with a synchronous phase of about $\phi_s \approx -30°$, which, as an ensemble, is called a *KONUS period*.

2.7 GSI Overview

Founded in 1969 to serve as a research institution for heavy ion studies, GSI underwent several upgrades. Initially, the setup consisted of a linear accelerator only, based on a Wideröe structure (Sec. 2.5.1) and an Alvarez structure (Sec. 2.5.2) as final stage. In 1990 the first major upgrade was accomplished, when the existing facility has been extended by a synchrotron (SIS18) and a storage ring (ESR). As of today, the GSI accelerator facility comprises the *linear accelerator* UNILAC, the *heavy ion synchrotron* SIS18 and the *experimental storage ring* ESR. The UNILAC consists of two different upstream injectors, the *high current injector* (HSI) and the *high charge injector* (HLI) feeding the Alvarez poststripper section. Those can provide all ion species from hydrogen to uranium. Before the beam is injected into the synchrotron at an energy of usually 11.4 AMeV, the ions are stripped at the transfer channel (TK) and a higher charge state is selected, e. g. $U^{28+} \rightarrow U^{73+}$. The synchrotron SIS18 (bending power $B \cdot \rho$ = 18 Tm) accelerates the ions to energies between 50 to 2000 AMeV. Finally, beams are either delivered to the high energy target area or the ESR (10 Tm) for storage and electron cooling using fast or slow extraction. For production of radioactive nuclei, a fragmentation target with a magnetic *fragment separator* (FRS) provides isotope selection for injection into the ESR or transport to the target area where experimental setups are located.

2.8 The UNILAC Facility

The GSI **UNI**versal **L**inear **AC**celerator (UNILAC) features two different prestripper injectors feeding the final Alvarez stage (see Fig. 2.10), also referred to as poststripper section. The HLI (High Charge Injector), which is equipped with an ECR ion source, is mainly used in *super heavy element synthesis* (SHE) at the SHIP/SHIPTRAP [26, 27] and TASCA experiments [28]. It injects behind the first stripper section and is not accessible by the experimental setup presented in this work.

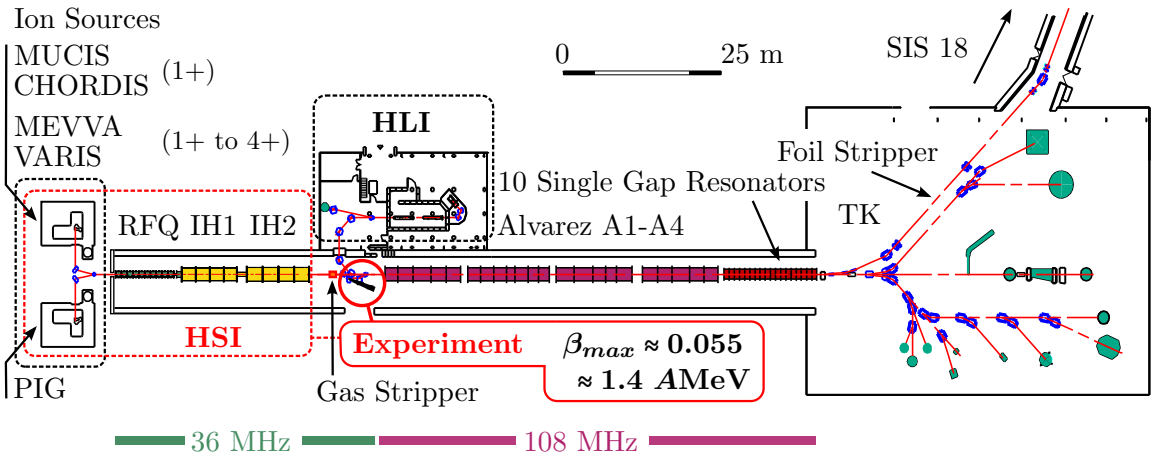

Fig. 2.10: UNILAC site overview from ion source to experiments (bottom right) and the transfer line (TK) injecting into the SIS18.

In the following, the HSI chain is introduced which plays a major role concerning the emittance of beam. Apart from its fixed design parameters, accessible parameters such as tank amplitude and phase settings influence the phase-space distribution. Also, as the total emittance of a beam is limited by the performance of the ion sources, a short overview over the available sources is given. Finally, the Alvarez section behind the experimental setup is introduced.

HSI - High Current Injector. Originally featuring a Wideröe structure, a major upgrade of the HSI has been performed in 1999 [29]. Prior to the upgrade, Penning sources fed the HSI to provide high initial charge states required by the relatively low effective gradient of the Wideröe structure (34 MV max.). As a consequence, mass numbers higher than 150 could not fill the SIS18 to its space-charge limit since the ion sources were not able to provide sufficient current for those charge states. Therefore, the Wideröe structure was removed in favour of a H-mode RFQ (further upgrade in 2004 and redesigned electrodes in 2009) and two IH cavities with a maximum effective gradient of about 91 MV. Additionally, a short 11-cell RFQ buncher, the so-called *Super Lens*, has been installed after the main RFQ for an improved matching into the first IH structure. All structures of the HSI, i. e. the RFQ, Super Lens and the IH structures, operate at a frequency of 36.136 MHz. The upgrade allows the acceleration of ions with a mass (number) to charge ratio up to $A/q = 65$. For instance, the typical charge state of uranium at the HSI after the upgrade could be lowered from U^{10+} to U^{4+}, fed by a high current ion source of MEVVA-type (see below) for SIS18 injection. At the same time, the lower charge state reduces the non-conservative space-charge effect which benefits the maximum beam intensity of the HSI.

Different ion species can be accelerated interleaved at the same time with individual accelerator settings, in particular different energies and even different charge states of the same ion species. Macro pulse operation works on a 50 Hz time base, i. e. at maximum 50 macro pulses per second can be delivered to the post-stripper section. The UNILAC facility can run up to 14 *virtual accelerators* which represent distinct accelerator settings on a pulse-to-pulse base.

Two ion source terminals are available at the HSI. Each terminal can only run one ion source at a time and, thus, the HSI can request pulses from two different ion sources interleaved. High-current ion beams are available from the *northern terminal* (see Fig. 2.10), from where short pulses of high intensity usually can be extracted only at a low duty cycle of a few Hz or even less.

The following ion sources are available:

- MUCIS - **MU**lti **C**usp **I**on **S**ource
- MEVVA - **ME**tal **V**apour **V**acuum **A**rc ion source
- CHORDIS - **C**old or **HO**t **R**eflex **D**ischarge **I**on **S**ource
- VARIS - **V**acuum **AR**c **I**on **S**ource

The *southern terminal* houses a Penning ion source (PIG - **P**enning **I**on **G**auge) applicable for almost all elements at a high duty cycle with broad charge-state spectra. On the other hand only low to medium currents are available from a Penning ion source. A recent and

complete summary of all ion sources in use at GSI and their performances can be found in [8].

The LEBT (*low energy beam transfer*) delivers ions from the ion source terminals with a sharp energy of about 2.2 *A*keV ($\Delta E/E \leq 1 \times 10^{-4}$). Subsequently the ions are bunched and accelerated inside the RFQ structure up to an end energy of 120 *A*keV. The *Super Lens*, a short RFQ working in bunching mode ($\phi_s = -90°$), prepares the bunches for an improved matching into the first IH structure. Inside the two IH structures the bunches are accelerated up to an energy of about 1.4 *A*MeV, which corresponds to a normalised velocity of $\beta \approx 0.055$.

From there the bunches reach the first stripping section. The gas stripper which has been installed in 1999 [30] and received an upgrade in 2006 [31] is a gas target, realised as a stationary, supersonic, differential nitrogen gas jet. The pressure at the nozzle can be adjusted from several bar down to 50 mbar, with typical values around 4 bar. Interaction of the beam with the gas target results in a broad charge state distribution depending on ion species and stripper pressure. A typical charge spectrum for uranium is shown in Fig. 2.11 at a nozzle pressure of about 2 bar. The stripping efficiency is about 12 % which

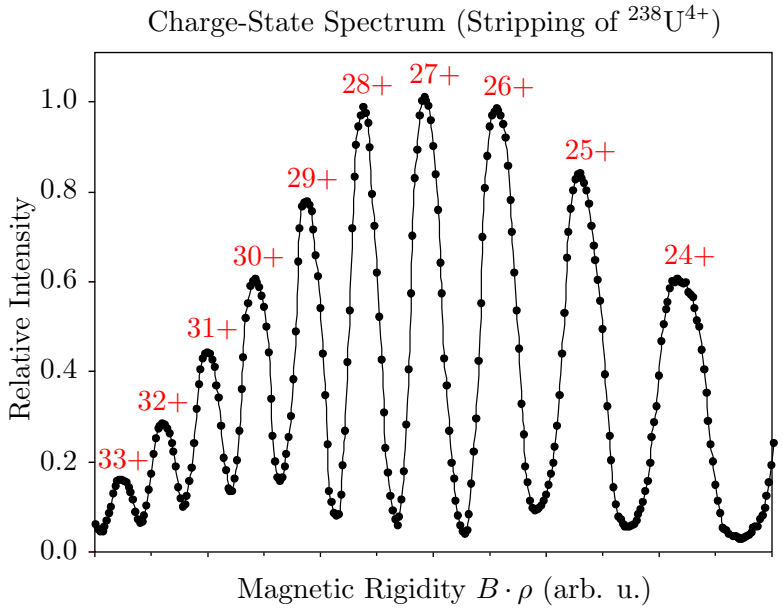

Fig. 2.11: Typical charge-state distribution of ^{238}U after stripping at an incoming energy of 1.4 *A*MeV and charge of 4+ [30]. The intensity has been normalised to the U^{27+} amplitude.

is the fraction of particles with a certain charge state after stripping (here 27+). Charge separation and selection is accomplished by a chicane acting as dispersive section with fast kicker dipoles and two horizontal actively cooled high-current slits. A technical drawing of the cooled slits can be found in the Appendix, Fig. A.2.

Alvarez A1-A4. The final acceleration section of the UNILAC, the poststripper, is provided by the four Alvarez structures with design energies of 3.6, 5.9, 8.6 and 11.4 *A*MeV and 10 single gap resonators for energies up to 17.7 *A*MeV ($^{20}Ne^{7+}$) and beam powers of more than 1 MW. Injection into the SIS18 is usually performed at 11.4 *A*MeV at a higher charge state stripped at the transfer channel (TK). An overview over the current HSI design goal parameters at uranium are given in Tab. 2.1. Furthermore, required values for SIS18 acting

Tab. 2.1: Specified design parameters of the UNILAC HSI (design ion is $^{238}U^{73+}$) to deliver 4×10^{10} of $^{238}U^{73+}$ ions within 100 µs to the SIS18 as reported in [32].

	HSI entrance	**HSI** exit	**Alvarez** entrance	**SIS18**	**FAIR**
Ion species	$^{238}U^{4+}$	$^{238}U^{4+}$	$^{238}U^{28+}$	$^{238}U^{73+}$	$^{238}U^{28+}$
El. current (mA)	16.5	15	12.5	4.6	15
Part./100 µs pulse	2.6×10^{12}	2.3×10^{12}	2.8×10^{11}	4.2×10^{10}	3.3×10^{11}
Energy (*A*MeV)	2.2×10^{-3}	1.4	1.4	11.4	11.4
ΔE/E RMS	n/a	4×10^{-3}	1×10^{-2}	2×10^{-3}	2×10^{-3}
$\varepsilon_{n,x}$ (mm·mrad)	0.3	0.5	0.75	0.8	0.8
$\varepsilon_{n,y}$ (mm·mrad)	0.3	0.5	0.75	2.5	2.5

as a booster ring for the future fast-ramped super-conducting synchrotron SIS100 of the FAIR project are listed. Improvement to the existing UNILAC facility by optimisations is a major task towards the future FAIR project. Additionally, there are plans to replace the stripper section and the Alvarez structures. At the time of writing the required UNILAC beam parameters are re-evaluated.

Chapter 3

Experimental Setup

3.1 Principle of Measurement

Compared to available standard methods of measurement for the transverse degree of freedom, straightforward approaches for the longitudinal phase space of heavy ions do not exist. The short range in matter, about 10 µm for heavy ions with an energy of 1.4 AMeV, must be considered carefully in case of interceptive measurements. Also, the low velocity at the location of measurement after the prestripper sections limits the possibility to access the longitudinal particle distribution by means of the electric field distribution, such as provided by capacitive pick-ups [4].

This is obvious from Fig. 3.1 which depicts the free longitudinal and transverse electric fields of a singly-charged particle at different velocities, neglecting the boundary condition of the pick-up geometry. The field components for three exemplary normalised velocities β are shown: 1.4 AMeV at location of measurement (stripper section), 11.4 AMeV at the transfer channel and a β of 0.9 corresponding to a kinetic energy of about 1.2 AGeV. Pronounced advanced and retarded tails are evident at lower velocities. Thus, the measured longitudinal particle distribution would be smeared out by the convolution of the electric field contribution and the long-range tails at the given velocity $\beta \approx 0.055$. A typical pick-up signal and the corresponding recorded bunch structure with the device investigated in this work is depicted in [7]. It shows a measured bunch length of 0.7 ns (FWHM) which is represented by a pick-up signal with an extension of about 10 ns.

At the first stripper section, where the measurement setup is located, particle distributions have a typical arrival time distribution of 0.5 to 2 ns (RMS). Hence, a determination of the bunch length or even detailed structures of the bunch is not possible by means of its electric field distribution. Other methods such as direct spectrometers [33] by a dispersive section and vertical deflectors are large, expensive and must be considered already during the design phase of an accelerator section. Moreover, this approach, as well as the method presented in this work, requires a prepared collimated beam in front of the dispersive section. This is usually provided by transverse and horizontal slit configurations after the first dipole.

A different approach to access the longitudinal phase space is investigated in this work. The bunch ensemble is transferred into a *single-particle measurement* by which the momen-

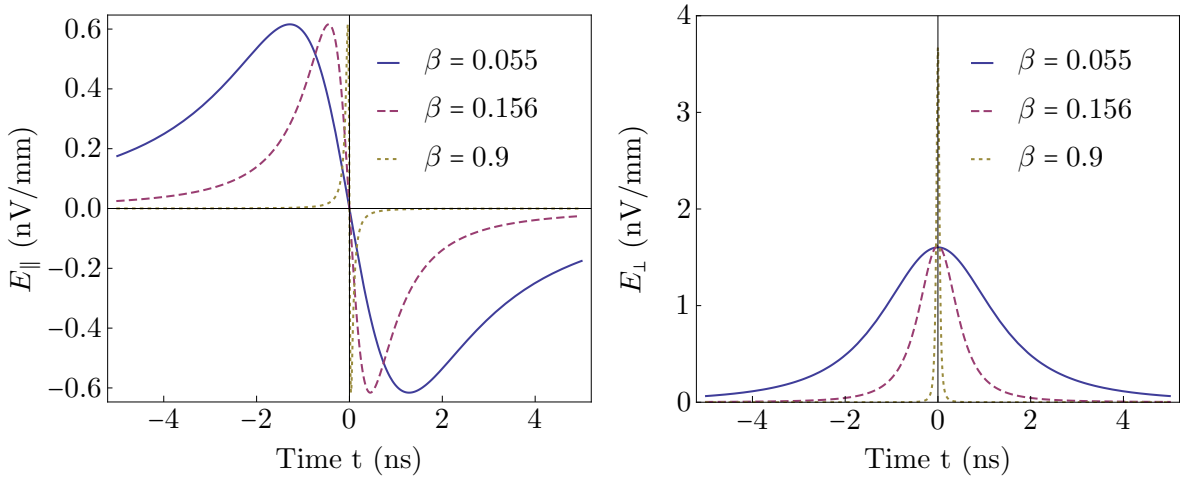

Fig. 3.1: Free longitudinal and transverse electric fields of a singly-charged particle, depicted for different values of β. The measurement setup is located at a $\beta \approx 0.055$ ($E_{kin} \approx$ 1.4 AMeV), whereas the maximum velocity behind the Alvarez structure is $\beta \approx 0.156$ ($E_{kin} \approx$ 11.4 AMeV). Post-SIS velocities can reach $\beta \approx 0.9$ ($E_{kin} \approx 1.2$ AGeV).

tum/energy information is extracted via time-of-flight (TOF). Additionally, the *relative* phase information is recorded by the arrival time with respect to a fixed RF master oscillator reference. This allows, in principle, to reconstruct the longitudinal phase space by histogramming the recorded single-particle events. As an alternative approach, a direct calorimetric measurement based on a mono-crystalline diamond detector of high purity was investigated.

3.1.1 Time-of-Flight Measurement

The design of the time-of-flight (TOF) measurement setup by Forck et al. [6,7] is based on three essential components:

- **Particle-number attenuation** via *Coulomb scattering* into a small solid angle ω.
- **Timing signal** at *MCP module* (indirect measurement via secondary electrons).
- **Timing signal** at a *poly-crystalline diamond* detector after a drift of about 800 mm.

The essential components will be covered in the following sections.

A schematic representation of the TOF setup is depicted in Fig. 3.2. Incoming bunches, entering the device at the bottom left, have been already pre-attenuated to several microamperes and undergo Coulomb scattering at a thin tantalum foil of (210 ± 10) µg/cm^2 thickness (about 126 nm) mounted behind an aperture with diameter (2.0 ± 0.1) mm. Subsequently, under a small solid angle ω of $(7.7 \pm 3.0) \times 10^{-6}$ sr and at an angle θ of $(2.50 \pm 0.05)°$ in the laboratory frame, ions are stochastically selected and registered by the MCP and poly-crystalline diamond detectors, thereby generating two timing signals. Choosing appropriate collimator dimensions, i. e. a small scattering probability into ω, most of the bunches (micro pulses) scatter no or only a single ion into the sensitive area following Poisson statistics. A negligible fraction of bunches scatter two or more ions into ω as will be discussed in

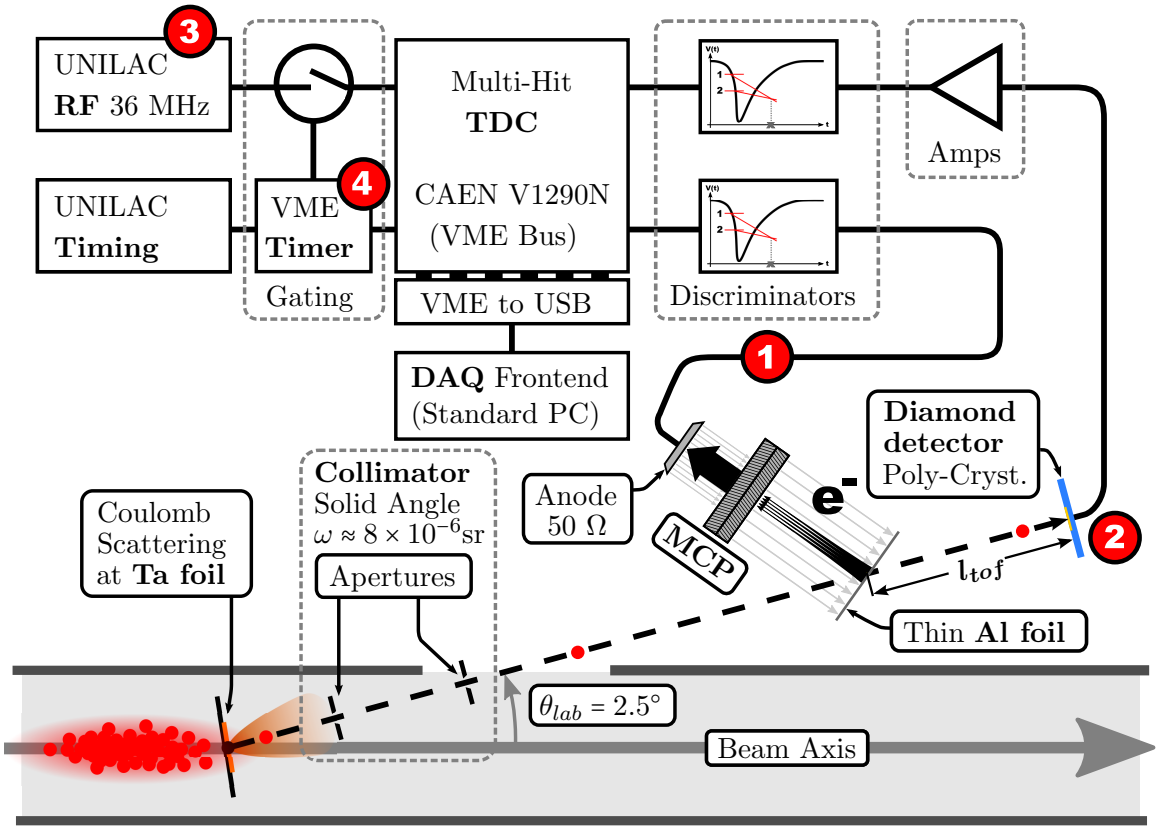

Fig. 3.2: Schematic TOF measurement setup. A simplified bunch distribution is depicted at the lower left of the figure. It enters the attenuation section consisting of the tantalum foil and the collimator as described in the text. The longitudinal phase space is reconstructed from *three timing signals* by histogramming. The timing at the PC-diamond detector t_{dia} (2) with respect to a fixed reference of the RF master oscillator t_{rf} (3) is a measure of the relative phase of the incident particle, whereas the momentum/energy information is contained within the TOF between the timing at the MCP module t_{mcp} (1) and the PC-diamond detector t_{dia} (2) separated by the distance l_{tof}. Furthermore, the macro-pulse start timing t_{macro} (4) is recorded.

Sec. 3.4.5. This is a strict requirement since the measurement relies on detector events which can be unambiguously related to a single ion.

As for the first timing signal t_{mcp} (1), it is important that the interaction of the ion with the aluminium foil is negligible compared to the width of the kinetic energy distribution of the beam. Otherwise the measured distribution is falsified. The idea is to provide the time reference by means of an indirect measurement of secondary electrons registered with a microchannel plate (MCP). Liberated secondary electrons from a thin (10 ± 1) µg/cm^2 ($\approx$ 40 nm) aluminium foil are accelerated towards the MCP front by an electric field of about 1 kV/cm. A significant gain of the net electron yield is provided by the cascading characteristic of the MCP at an applied voltage of about 2 kV. The amplified stream of electrons is collected at a conical anode (50 Ω geometry) at the backside of the MCP. From

the acquired pulse the logic timing is generated by a so-called double-threshold discriminator (see Sec. 4.1.1) and eventually registered in a fast time-to-digital converter (TDC, see Sec. 4.1.3 for a detailed description). When the TDC registers the timing pulse (NIM) it internally dumps the timing information from a global clock and, thus, provides a fixed relationship between different input channels.

After the drift l_{tof}($\approx$ 800 mm) a poly-crystalline diamond detector (thickness 185 µm) fully stops the ion. The detector signal is processed by a two-stage amplifier while the logic timing is again generated by a double-threshold discriminator. Finally, the timing signal is registered by the TDC providing the second timing signal t_{dia} (2). Furthermore, only every tenth timing from the accelerating RF is recorded to reduce overhead of the regular data significantly. This data represents a fixed timing which allows to reconstruct the RF timing reference t_{rf} (3) for each single bunch (micro pulse). Together with the arrival time of a particle at the diamond detector t_{dia} (2) the longitudinal arrival time distribution is evaluated as a measure of the longitudinal bunch structure. To account for the macro-pulse start reference, a dedicated timing signal is provided by a custom-made VME UNILAC timing module [34]. The reference timing of the macro-pulse start t_{macro} (4) allows to compare events between different macro pulses. For example, it is possible to introduce time cuts and compare the phase-space distribution between the first and second half of the macro-pulse ensemble.

The longitudinal phase space is consequently reconstructed as a 2-dimensional histogram by means of the single particle (i) event timing $(t_{dia}-t_{rf})_i$, representing the phase information, versus $(t_{dia}-t_{mcp})_i$ which is a measure of the momentum information. Chapter 4 covers the process in detail.

3.1.2 Direct Calorimetric Measurement

An alternative measurement to the time-of-flight approach has been investigated using a diamond detector with calorimetric properties. Poly-crystalline diamond semiconductor materials, as used in the TOF setup, cannot be used for direct energy measurements. Due to their large fluctuations of pulse heights for fully stopped, monochromatic particles, they are typically considered as timing detectors or within tracker geometries only. On the other hand, new diamond detector materials of high purity and improved electrode treatment, so-called mono-crystalline or single-crystalline diamonds, are able to provide a significantly more stable and enhanced linear signal response with respect to the deposited energy. Hence, this type of detector allows extraction of the energy information by calibration of the mere pulse height or integral liberated charge. These materials are still subject to research and undergo steady improvement [35].

The mono-crystalline diamond detector mounted on a pneumatic feed-through is housed in the same diagnostics chamber as the TOF setup introduced earlier. As the calorimetric measurement also requires unambiguous single-particle events, the mechanism of particle-number attenuation from the TOF approach is reused. Generated diamond pulses are amplified, digitally sampled and recorded. At the same time, the RF reference acquired from the master oscillator is sampled and recorded to provide a *relative* phase reference. Hence, after measurement, the phase space is reconstructed by post-processing the dataset

consisting of an ensemble of digitised traces which are pairwise related. The procedure is presented in detail and discussed in Chapter 4.

3.2 Experimental Site

3.2.1 UNILAC Stripper Section

The experimental setup is located inside the UNILAC stripper section. Figure 3.3 shows the stripper section at the UNILAC which connects the HSI (left) and the Alvarez A1 structure (right). The measurement setup can access the beam from the UNILAC High Current Injector (HSI, see Sec. 2.8) and is located inside the dipole chicane upstream from the gas stripper. Due to the length of the diagnostics chamber, a straight-through installation in front or behind the chicane is not possible. Hence, no alternative location to the installation inside the dispersive section is available. Also, the restricted space at the given accelerator site imposes a limit on the practicable separation of the TOF detectors.

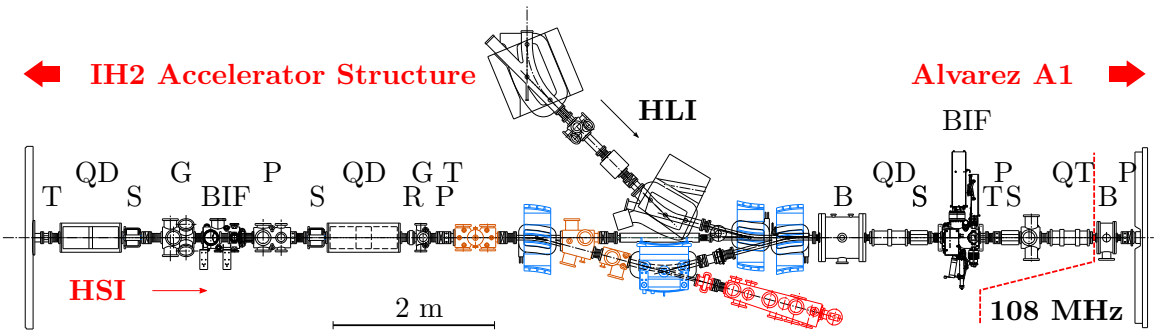

Fig. 3.3: Stripper section (as of **end of 2010**) between IH structures and Alvarez DTL tanks where the setup for longitudinal measurements is located. Apart from the charge separator section the available modules are denoted as follows: Current Transformer (**T**), Quadrupole Doublet (**QD**), Quadrupole Triplet (**QT**), Steerer Hor./Ver. (**S**), Profile Grid (**G**), Beam-Induced Fluorescence Monitor (**BIF**), Resonance Probe (**R**), Phase Probe (**P**), Buncher (**B**).

A beam from the HSI enters the stripper section (see Fig. 3.3) and can be adjusted by two quadrupole doublets and two steerers until it reaches the gas stripper. Depending on energy, pressure of gas jet nozzle and ion species, a characteristic charge state spectrum results. An exemplary charge state distribution is shown in Fig. 2.11 for ^{238}U. Subsequently, a dispersive dipole chicane, which is depicted in Fig. 3.4, spatially separates the charge states on the horizontal plane. Two high-current slits (US3DS4/5, [36]) allow to select the desired charge state. During usual delivery, the beam is deflected back towards the LINAC beam axis by a −30° dipole kicker magnet (US3MK2). Finally, dipole kicker magnet US4MK3 guides the beam back on the axis of the tank structures. Until the beam is eventually injected into the Alvarez A1 structure, the beam undergoes further preparation. Apart from transverse focusing quadrupole doublet/triplets and two steerers, longitudinal focusing is accomplished by two dedicated bunchers. A buncher, as explained in Sec. 2.6.3, provides no

net acceleration at a synchronous phase $\phi = -90°$ with a maximum possible acceptance and allows to minimise the phase extension by effectively rotating the longitudinal phase-space ellipse. One buncher is located immediately behind the dipole chicane and is driven by the 36.136 MHz of the prestripper section. Another buncher is placed next to the entrance of the Alvarez structure, as can be seen from Fig. 3.3, and operates at about 108.4 MHz. This is three times the prestripper frequency in accordance with the Alvarez base frequency.

The matching procedure from the prestripper section into the Alvarez structure represents a delicate challenge. As described in Sec. 2.3, the six-dimensional acceptance of the accelerator section under consideration determines the phase-space volume which is transported properly. Hence, to obtain high transmissions and, thus, high efficiencies the six-dimensional phase space of an incoming beam must have a large overlap with the accelerator acceptance. The task for the injector division is to find a good configuration of the transverse focusing and the bunchers for an improved injection. In particular, for a good choice of the bunching RF phase and RF voltage, the knowledge of the longitudinal phase space is advantageous.

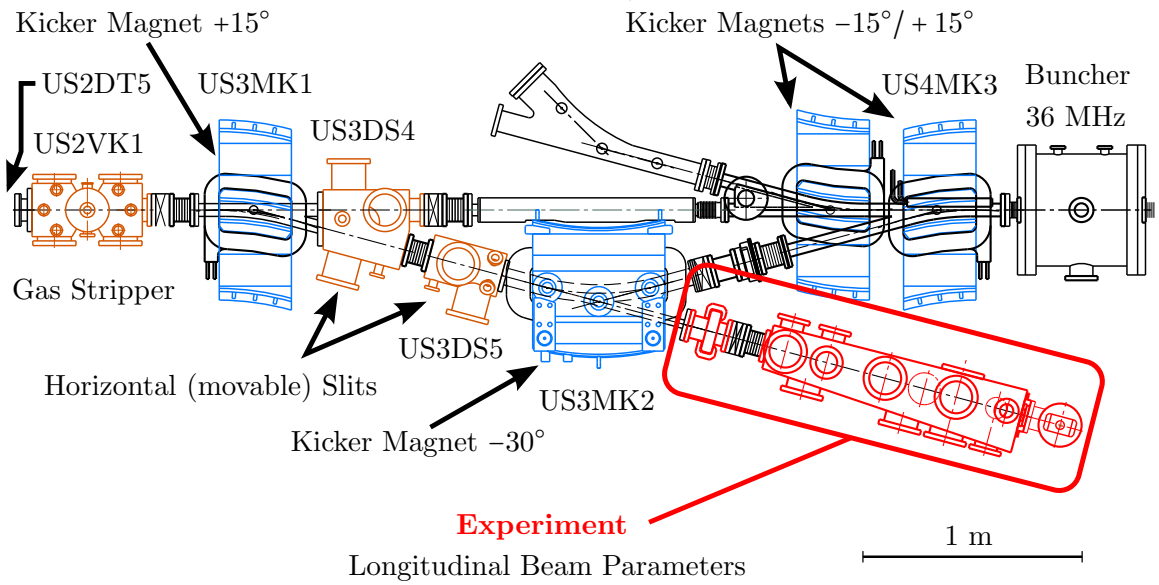

Fig. 3.4: Detailed drawing of the dipole chicane at the stripper section between HSI and Alvarez structure. The measurement setup is located behind the high-current slits US3DS4/5 and kicker magnet US3MK2 on the common beam axis. During measurement the 30° kicker magnet US3MK2 is not in operation.

The measurement setup is located behind the high-current slits inside the chicane as depicted in Fig. 3.4. During a measurement, the dipole magnet US3MK2 is not in operation. In high current mode it is of major interest to keep the space charge unmodified as long as possible. Otherwise, the measured phase-space distribution would not reflect well the situation of normal operation. Therefore, two possibilities are available to attenuate a beam of several milliamperes to only several microamperes:

- Selection of a charge state far from the equilibrium charge state.
- Use of a very narrow slit setup through which only a small fraction of the beam passes.

The method of choice concerning beam attenuation strongly depends on the beam parameters. It is sometimes easy to select a different charge state of lower intensity than the one at ordinary operation. This is accomplished by changing the dipole field US3MK1 and geometrical shadowing of the rest of the beam via the high-current slits. However, the charge state of ordinary beam operation is favourable for consistency.

3.2.2 Diagnostics Chamber

The diagnostics chamber houses the dedicated modules required for the experiment, i. e. the collimator which is responsible for particle-number attenuation and detectors of various kind. Designed by Forck et al. [6, 7], the chamber in TOF configuration has been already extensively in use during commissioning of the revised UNILAC pre-stripper section (see Sec. 2.8). Figure 3.5 shows a recent photograph of the measurement setup. All crucial modules are labeled and explained accordingly in the following sections of this chapter. The corresponding technical drawing (top view) of the diagnostics chamber in Fig. 3.6 preserves the numbering scheme given in Fig. 3.5.

A pre-attenuated beam enters on the left where the macro-pulse current (see Sec. 2.1) can be recorded with the current transformer US3DT6 [37], labeled with ❶. Knowing the incoming beam current is important to prevent the primary foil from melting. Pneumatic feedthroughs carry the tantalum foil and apertures, labeled with ❷ and ❸, which constitutes the collimator configuration responsible for particle number attenuation. The MCP module

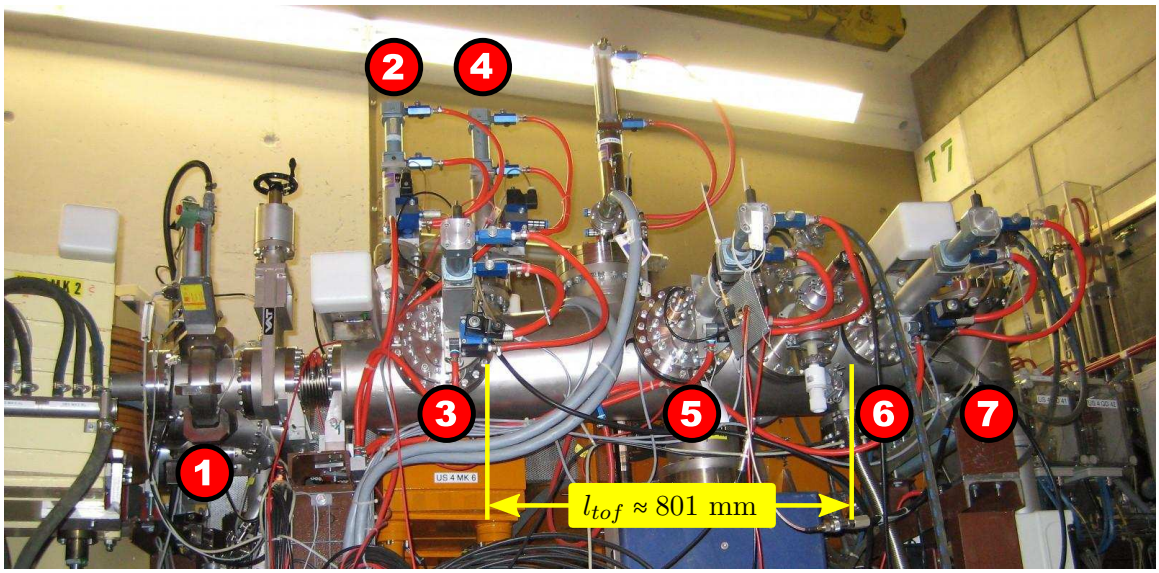

⟵ IH1/2, Gas Stripper Alvarez A1 ⟶

Fig. 3.5: Photograph of the experimental setup including: Current transformer (beam current) ❶, first collimator aperture including the tantalum foil ❷, second collimator aperture ❸, MCP module including the aluminium foil ❹, mono-crystalline diamond detector ❺, poly-crystalline diamond detector used in TOF measurement delivers second timing signal ❻, Faraday Cup beam-current measurement ❼.

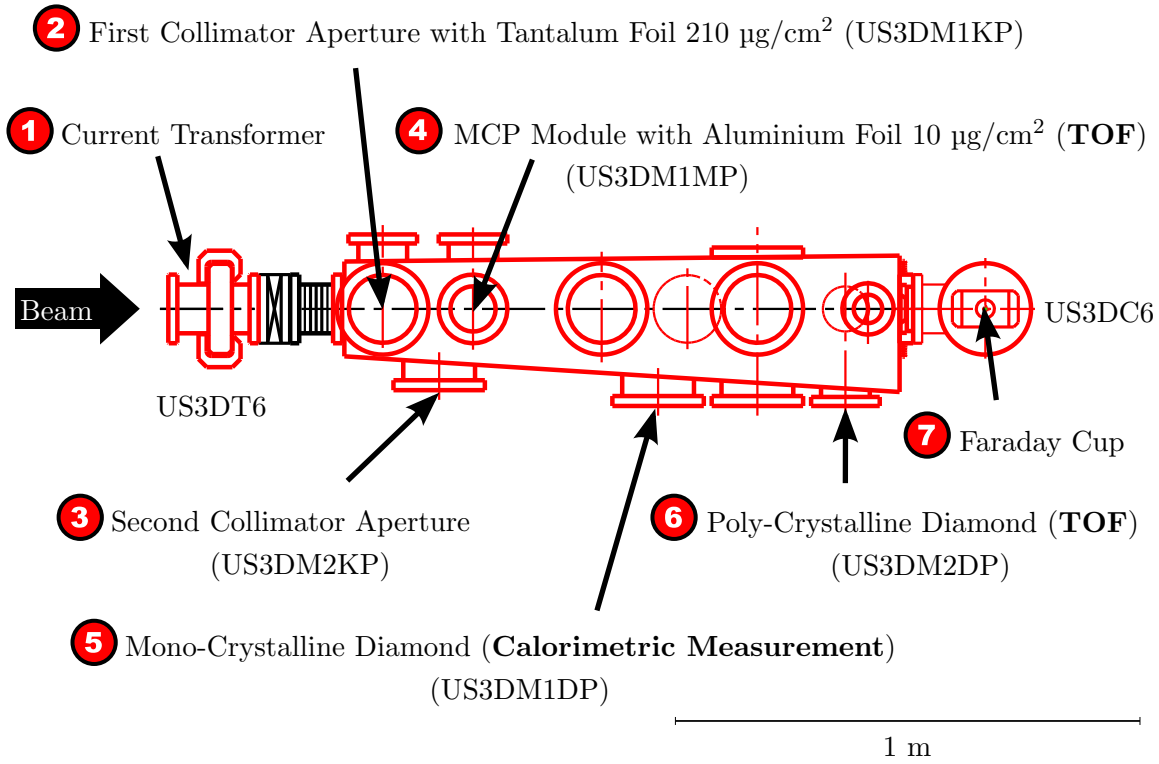

Fig. 3.6: Schematic drawing of the measurement setup in detail (top view). The numbering scheme of the components matches the one present in Fig. 3.5.

4 follows closely behind the exit of the collimator configuration as depicted in Fig. 3.6 (for a detailed technical view see Appendix, Fig. B.1). After the drift l_{tof} of ≈ 800 mm with respect to the MCP aluminium foil, the poly-crystalline diamond detector 7 is installed. In between the aforementioned TOF detectors, a mono-crystalline diamond detector 5 has been installed. All detectors are mounted on a pneumatic feed-through. Depending on the measurement method, i. e. TOF or the mono-crystalline diamond, either the MCP together with the poly-crystalline diamond detector or the mono-crystalline diamond detector are exposed to the scattered beam particles. Finally, a Faraday cup 7 can be used as a complementary measurement for adjustment of the beam current (macro-pulse current) before collimator and detectors are exposed to the beam. Table. 3.1 lists characteristic distances comprising the apertures, the MCP foil and the diamond detectors.

3.3 Particle Detectors

3.3.1 Microchannel-Plate Module

The first timing of the time-of-flight (TOF) measurement is generated using a microchannel plate (MCP), sometimes also referred to as multi-channel plate. Since the TOF requires two timing references at a well defined separation, it is obvious that the beam-device interaction at the evaluation of the first time reference must be sufficiently low, in order to preserve

Tab. 3.1: Distances between selected components of the measurement setup shown in Fig. 3.6.

Components as specified in Fig. 3.6	Separation (mm)
② ↔ ③	150.0 ± 0.5
② ↔ ④	224.0 ± 0.5
③ ↔ ⑤	479.0 ± 0.5
③ ↔ ⑥	874.0 ± 0.5

the phase-space information of the original beam. Otherwise the TOF is falsified as the measured phase space would have been significantly altered.

Manufacturing and Properties. An MCP consists of a parallel assembly of very thin tubes (typically about 10 µm diameter), usually made of lead glass, at a certain angle with respect to the front normal (typically about 10°). The fabrication process is derived from fiber glass production. Lead glass fibres with an etchable core are drawn-out and assembled in a hexagonal configuration. Those packets of fibres are drawn-out again and put together in an iterative procedure until the targeted channel size and the diameter of the MCP are met. Slices are cut from the final packet, taking care of the bias angle. The core is removed in an etching process which reveals the single channels. Subsequently, the channel surface is treated with a semiconductor material, while evaporated metallic layers on both sides of the MCP serve as electric contact. As a result of the high-ohmic coating of the channel walls, the electric resistance between the electrodes on front and back side typically ranges from 10-100 MΩ. The electrode layer reaches into the channels in such a way that the special diffused junction allows fast charge recovery after ignition to minimise the dead time per channel, while the high-ohmic surface is maintained.

Working Principle. The single channels of MCPs can be compared to photo multipliers but with a cylindric continuous-dynode geometry. In contrast to separate dynodes, connected by a voltage divider circuit, the high-ohmic surface represents a continuous resistor chain which allows to sustain the high field gradient at a very small leakage current as described by Wiza [38]. In principle, MCPs are sensitive to all kinds of ionising primary irradiation, such as electrons, heavy ions and electro-magnetic radiation.

Figure 3.7 schematically depicts the working principle, taking electrons as primary particles. The liberated secondary electrons are accelerated by the electric field inside the MCP channels and follow parabolic lines, while the voltage applied per MCP is typically about 1 kV. The electrons again collide with the channel wall and knock out further electrons, starting a cascade of generated electrons. This eventually ends in an intense electron shower emitted at the back of the MCP. If the MCP output is extracted with an anode, the pulse-height distribution (PHD) typically follows a negative exponential at lower gains, while it

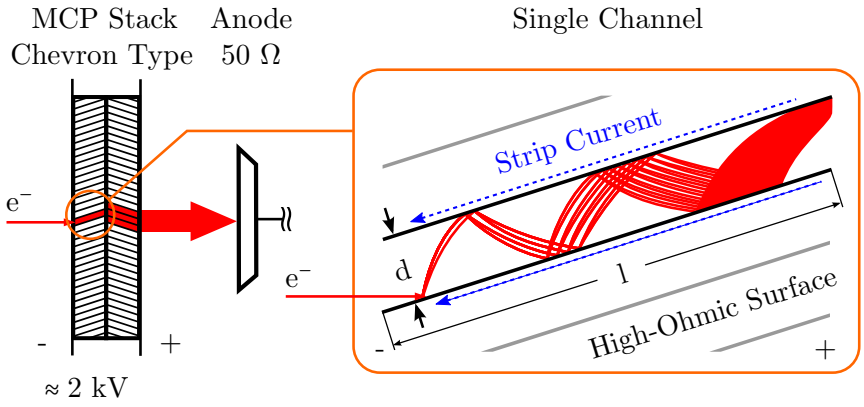

Fig. 3.7: Electrons of sufficient kinetic energy will knock out several secondary electrons when they enter the thin channels of the MCP. The voltage applied to the MCP accelerates the liberated electrons which in turn knock out secondary electrons as well. Finally an electron shower is generated with a minimum gain of 10^6.

approaches a Gaussian distribution for high gains near saturation [39]. Saturation occurs at very high space-charge densities near the channel exit when liberated electrons cannot gain any kinetic energy. Also, at high gains the probability of ionising residual gas atoms is enhanced. The positively charged gas atoms in the vicinity of the channel are accelerated in the reverse direction. When the ion eventually hits the channel wall unwanted retarded pulses occur. This effect is called *ion-feedback* and can lead to significant damage to the MCP at insufficient vacuum pressures. Therefore, MCPs must not be operated above a certain vacuum level, typically 10^{-4} Pa. It is worth noting that the performance characteristics of an MCP only depend on the fraction l/d, i.e. the effective *channel length* l and the *channel diameter* d in good approximation [38]. The longer the channels and the smaller their diameter the more collisions on the channel occur for a given MCP. On the other hand, the number of collisions decreases with increasing voltage applied and the number of liberated electrons per hit increases. When it comes to the response time which limits the time resolution, short channels with small diameters are favourable as they decrease the path length and allow for MCP configurations with rise times below 500 ps. At the same time, the time jitter is damped and a faster recovery time results from the increased channel density [39].

Application Area. MCPs are used for different purposes, originally targeted as image intensifier for night vision devices. In beam diagnostics, several devices feature an MCP of large diameter working as a preamplifier of spatial intensity distributions, where the primary particles are usually either photons or electrons [40]. While MCPs are sufficiently sensitive to photons within the ultraviolet and soft X-ray domain, visible light usually requires an additional photocathode as a first stage. The two-dimensional spatial density profile of generated electrons are mapped to the optical region by phosphor screens of various kinds. A combination of optical filters and cameras finally provide the raw data information. In the special geometry used in this work only the time resolution is of importance.

MCP Specifics (Hamamatsu F4655-13). The MCP used in the TOF setup is a commercially available compound module by Hamamatsu Photonics K.K. and has been specifically designed for TOF measurements with high timing requirements in the sub-nanosecond regime. Figure 3.8 shows the technical drawings and a photo of the module. The MCP

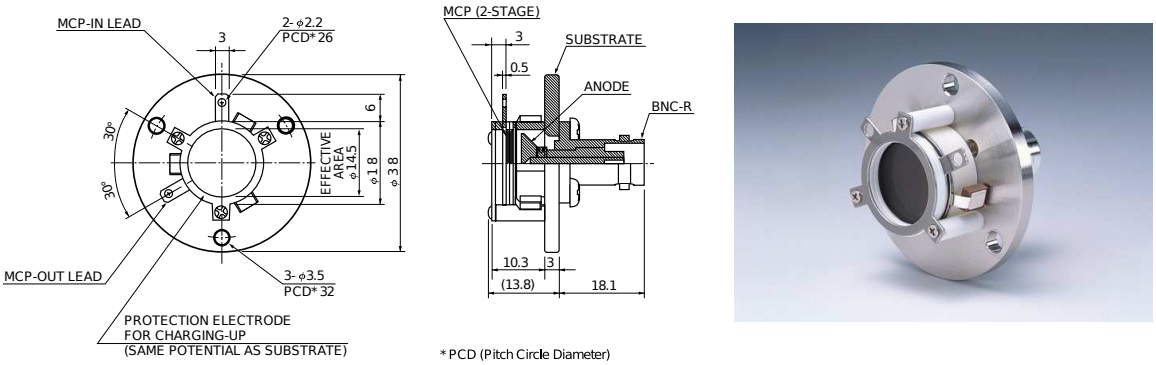

Fig. 3.8: MCP module (Hamamatsu F4655-13) used in the TOF setup. Technical drawings and the picture were taken from the corresponding specification sheet [41]. Courtesy of Hamamatsu Photonics Deutschland GmbH.

features an effective circular area of 1.65 cm^2, a thickness l of 0.41 mm, a small channel diameter d of 4 µm ($l/d \approx 100$) and an electrical resistivity of about 50 MΩ each. Per MCP a maximum voltage of 1 kV must not be exceeded. Two identical MCPs are stacked in a so-called chevron configuration, i. e. the orientation of the channels of both MCP are aligned against each other to form a "\/-shape" as denoted in Fig. 3.7. Together with the channel bias angle of 12°, the chevron configuration damps the occurrence of ion feedback while delivering an enhanced gain at the same time. In case of the module at hand the gain ranges between 10^6 to 10^7. On the other hand, the unavoidable gap between the MCPs in the chevron configuration gives rise to a broad pulse-height distribution. This is a direct cause of the lateral spread of the electron stream between the two MCP stages and activates several channels at the second MCP stage. Apart from the number of activated channels and their input intensity, this process results in a fluctuating final intensity as not all of those channels are driven into saturation. The MCP configuration at hand is specified with a PHD of 120 % (FWHM with respect to the distribution maximum), see Ref. [42]. As only the timing information is of interest, a conical anode is installed behind the MCP chevron configuration. The anode signal is extracted from a BNC connector (50 Ω geometry) and is immediately adapted to SMA connections and cabling of high bandwidth. The specification of the MCP promises rise times of less than 300 ps at fall times of less than 600 ps and pulse-length of 455 ps (FWHM) [41].

Construction and Electric Layout. As mentioned earlier, the generation of the first time reference, during the TOF measurement, is an indirect measurement. Liberated secondary electrons from a thin aluminium foil are accelerated in an homogeneous electric field and amplified by a fast MCP (Hamamatsu F4655-13). The electric field between aluminium foil and MCP which accelerates the electrons towards the MCP front is supported by three metallic guide rings and an appropriate voltage divider circuit to guarantee a homogeneous

field distribution. All components, the foil, guide rings, voltage divider circuit and MCP, are mounted inside a PEEK construction on a pneumatic feed-through. A corresponding simulation of the field distribution [43] is given in the Appendix, Fig. C.1. The simulation illustrates a good homogeneity inside the guide ring section and only minor non-axial deviations near the foil area. Particles cross the foil at an angle of 46.5° with respect to the foil normal. A copper housing which is connected to ground prevents accumulation of charges and, consequently, discharges that may destroy the MCP. The electric schematics of the MCP setup is depicted in Fig. 3.9. In this typical configuration the aluminum foil is biased by -2 kV with respect to the MCP front. The anode signal is collected with a bias tee connected to ground without further amplification. Pulses are converted to logic timing pulses and registered in the TDC electronics.

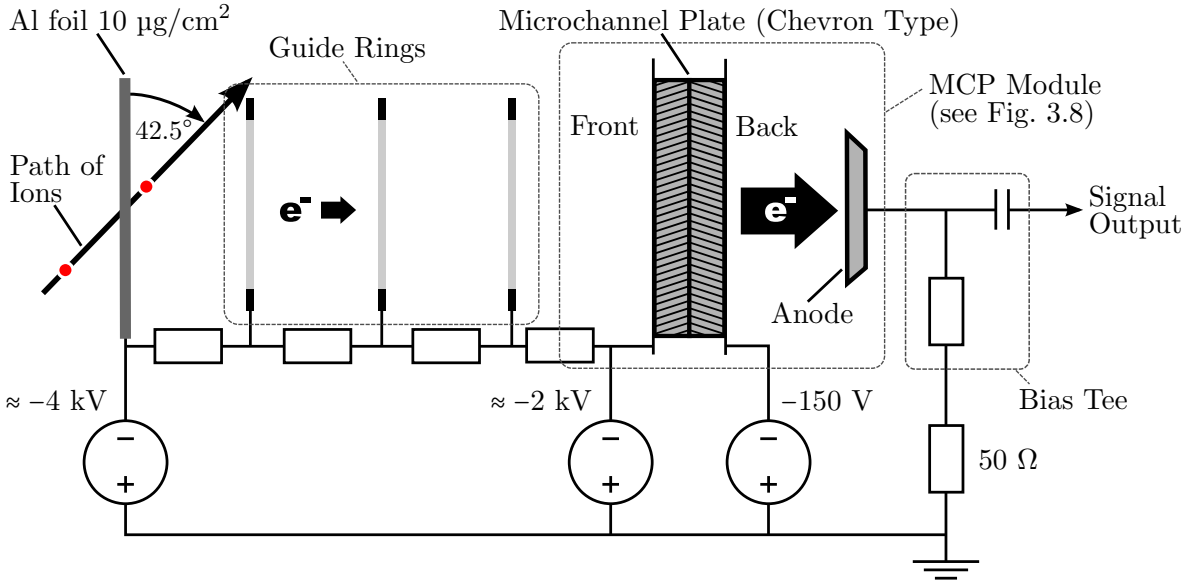

Fig. 3.9: Electric layout of the MCP compound module.

3.3.2 Poly-Crystalline Diamond Detector

After particles have passed the aluminium foil of the MCP module, the second timing in the TOF setup is generated in a so-called poly-crystalline (PC) diamond detector. The diamond semiconducting material has a band gap of 5.47 eV, which allows the detector to be used at room temperature without cooling. It is sensitive to ionising radiation providing enough energy to produce energy-hole pairs (average energy of 13.1 eV). As a drawback, this relatively high energy results in small signal amplitudes compared to other semiconductor materials. Despite the broad pulse-height distribution for monochromatic particles, the high mobility of free charges provides fast, short pulses with a uniform rise time. While this does not allow for a direct calorimetric measurement of the deposited energy, it provides excellent timing properties with rise times below 300 ps and a pulse width of about 1 ns which allows for count rates of more than 10^8 ions per second [44]. According to E. Berdermann et al. [44] the reason for the poor pulse-height resolution lies in the granular texture of PC-diamonds.

The charge-collection efficiency (CCE, see [45]), defined as the quotient of the measured to generated charge

$$CCE = \frac{Q_{meas}}{Q_{gen}}, \tag{3.1}$$

is significantly enhanced inside the region of big grains. Hence, major fluctuations of the total collected charge result from the inhomogeneity of the poly-crystalline structure. On average the CCE for PC-diamond material is less than 60 %. Typically, PC-diamond detectors are used as trackers for high energy particles where the deposited energy ΔE is much smaller than the average particle energy $\langle E \rangle$. In this work particle distributions are studied with a maximum energy of 1.4 AMeV. Hence, due to the short range in matter of about 10 µm, the total energy is deposited in the diamond material close to the surface. Significant degradation of the pulse-height distribution and leakage current has not been observed for 5×10^{10} ions/cm^2 traversing uranium ions with a high energy of 1 AGeV [46] as reported in [44] (both Berdermann et al.). The same authors report on test runs with carbon ions of 5.9 AMeV which are fully stopped within a thin layer around a depth of 57 µm [44]. At high fluences, the pulse-height resolution even improved by a factor of 5 between irradiation with 10^8 ions/cm^2 and 10^{10} ions/cm^2 (*priming*). Disadvantageous irradiation effects are not expected in the current work due to the minimal amount of implanted particles. The diamond detectors are only exposed to the attenuated single-particle beam. A measurement typically comprises about 10^4 events.

The semiconducting diamond material is synthesised in a process called *chemical vapour deposition* (CVD) which is suited for the fabrication of thin films. Especially the challenge to

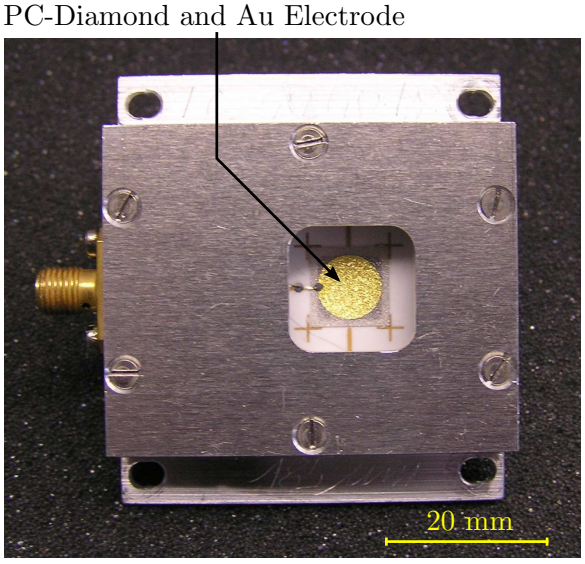

Fig. 3.10: Poly-crystalline diamond detector module used in the TOF measurement. Particles are fully stopped inside the diamond material of 185 µm thickness.

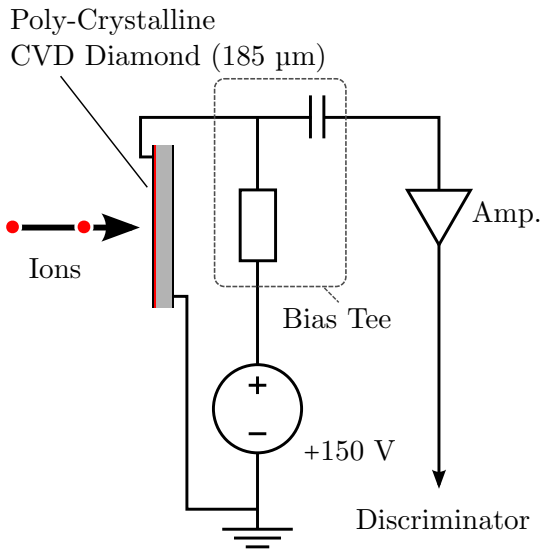

Fig. 3.11: Electrical interface to the poly-crystalline diamond detector. Extracted signals are amplified and converted to logic timing.

synthesise improved single-crystalline structures of high-purity is still ongoing research. The detector used in the TOF configuration has been assembled by the GSI detector laboratory and features a thickness of 185 µm. An identical detector module is depicted in Fig. 3.10. The golden, circular electrode has a diameter of 8 mm and marks the sensitive diamond area. Figure 3.11 shows the schematic electrical interface. The detector voltage is applied using a bias tee which allows extraction of the signals at the same time. Subsequently, a 50 Ω low noise two-stage amplifier chain is attached with a Mini-Circuits ZFL-1000LN (100 kHz - 1 GHz, 20 dB typ.) and a Mini-Circuits ZFL-1000VH2 (10 MHz - 1 GHz, 28 dB typ.) as final stage.

3.3.3 Mono-Crystalline Diamond Detector

Apart from the time-of-flight measurement, based on an MCP module and a poly-crystalline CVD diamond detector, a direct calorimetric detector, as a variation of the measurement setup, has been implemented. With the advancement of the CVD process over the last decade, which allows production of synthetic mono-crystalline diamond materials of high purity, calorimetric measurements using diamond detectors became possible. Mono-crystalline CVD diamonds (sometimes also referred to as *single-crystal* diamonds) feature an enhanced carrier mobility (J. Isberg et al. [47]) and, thus, very fast response times shorter than the typical rise times of PC-diamond detectors. Of course, this may be limited by the DAQ electronics and the time constant given by the capacitance of the detector and the impedance of the readout chain of 50 Ω. At typical detector capacitances of 3-5 pF, a time constant of 150-250 ps marks the lower limit of the measured rise time. Because the conversion factor for electron-holes is high compared to other semiconductor detector materials, and thus results in relatively small signal amplitudes, readout noise is very low. This is a direct result of the extremely low leakage current at room temperature. New electrode techniques come with steady damping of the leakage current at high electric fields. The so-called diamond-like carbon (DLC) fabrication process of the electrical contact, gives rise to leakage currents of less than 0.5 pA at electric field strengths of 2 V/µm [48]. Furthermore, compared to PC-diamond detectors, the mono-crystalline diamond structure is able to provide a charge collection efficiency up to 100 % for low electric fields. This significantly improves the pulse-height resolution and allows for direct calorimetric measurements to some extent. For the detector model in use, an energy resolution of about 1 % for α particles (5.5 MeV) is claimed by the manufacturer [48]. Ongoing efforts target improvements of the CVD process to produce mono-crystalline diamond materials of higher purity which further reduces polarisation due to charge trapping.

The mono-crystalline diamond has been installed behind the collimator setup on a pneumatic feed-trough. A photo of the module by *Diamond Detector LTD* is depicted in Fig. 3.12 together with the corresponding plain data of the specification sheet. The electrical interface is similar to the one used at the PC-diamond, see Fig. 3.11. At a thickness of 100 µm a positive bias of 100 V is used throughout the experiments. According to Pomorski et al. [49] a negative bias leads to electron trapping. The polarisation of the detector results in a reduced resistivity and, hence, may lead to breakdowns, rendering the detector unusable. Additionally, the lower drift velocity of electrons, compared to electron holes (at positive bias), produces pulse shapes of inferior quality. Together with the advantage of a positive

Diamond Detector LTD 09-003

- Thickness 100 µm
- Active diamond area 4.5×4.5 mm^2
- Circular electrode of 4.4 mm diameter
- Electrode configuration:
  3 nm DLC, 16 nm Pt, 200 nm Au
- Energy resolution about 1 % for α particles
- Leakage current < 0.1 nA

Fig. 3.12: Mono-crystalline diamond detector used for the direct calorimetric measurement and the specification as provided by the manufacturer *Diamond Detectors LTD*.

bias voltage, an electric field of 1 V/µm has been used to avoid spontaneous breakdowns for electric fields above 1.4 V/µm observed by Pomorski et al. [49]. While the heavy ion radiation hardness of mono-crystalline diamonds is considered to be very good [50], this is not a strict requirement in the setup at hand. The detector is only exposed to the beam in conjunction with the collimator setup and, thus, is only irradiated by a very small number of ions. A single measurement typically comprises in the order of 10^4 events only. In a typical measurement, with a macro-pulse length of 200 µs at 1 Hz macro-pulse repetition rate, about 10 ions are impinging on the diamond electrode per macro pulse. However, the current DAQ used in the MC diamond detector setup is only capable of registering one event per macro pulse. Hence, the total number of ions hitting the diamond detector is in the order of 10^5 at a rate of about 10 Hz.

3.4 Single-Particle Detection via Coulomb Scattering

This section covers the particle-number attenuation mechanism which allows single-particle detection and is partly based on ideas by P. Forck and P. Strehl [51].

Reconstructing the full longitudinal phase space by histogramming single-particle events requires unambiguous detection signals as a prerequisite. Avoiding overlapping events so that the detector can separate them is not sufficient in this case. Strictly speaking, an unambiguous event means only one particle event occurs per bunch (micro pulse) at most. The probability of having a certain number of particles inside a bunch (micro pulse) follows a Poissonian distribution as will be shown in Sec. 3.4.5. Therefore, it is not possible to perfectly rule out multiple particles being scattered into the collimator acceptance during a single bunch. Still, a significant suppression of multi particles is possible as described in Sec. 3.4.5. As typical bunch lengths range between 1-3 ns (RMS) and detector pulses have characteristic widths larger than 1 ns, a large fraction of the multiple-particle events would

end in disadvantageous pile-up configurations. Pile-up signals lead to distorted pulse-shapes and, thus, to an increased time jitter.

The pre-attenuated beam of several µA contains about $n_\tau \approx 10^9$ ions per macro pulse, depending on charge state q and macro pulse length τ

$$n_\tau = \frac{I}{q\,\mathrm{e}}\tau, \tag{3.2}$$

with typical parameters $I = 25$ µA, $\tau = 200$ µs and $q \approx (10-30)$. Taking theses value for an exemplary Ar^{10+} beam, a total number n_τ of 3.1×10^9 ions are contained in a macro pulse. Hence, within a bunch, $n_b \approx 4.3\times10^5$ ions are delivered on average.

An additional mechanism is therefore required to have a suitable environment for single-particle detection within the drift space between the MCP and the diamond detector. At the device entrance a collimator setup (see Fig. 3.2 and Fig. B.1) houses a thin tantalum foil of $\kappa = (210\pm10)$ µg/cm^2, tilted by an angle of $(1.25\pm0.05)^\circ$ with respect to the incoming beam axis. It is accompanied by two apertures with diameters of (0.5 ± 0.1) mm and a distance of (160 ± 0.5) mm. The already attenuated beam traverses the Ta foil and undergoes Coulomb scattering. Scattered particles are selected at an angle of $\theta = (2.50\pm0.05)^\circ$ with a resulting solid angle of $\omega = (7.7\pm3.0)\times10^{-6}$ sr, given by the geometry of the collimator setup.[1] Thus, only a small fraction of the particles of the incoming beam scatters into the TOF section. The goal of the following sections is to calculate an estimation of the attenuation achieved using the classical Rutherford scattering cross-section in non-relativistic limit ($\beta \approx 5.5\,\%$). Additionally, a complementary SRIM simulation has been performed and both results are compared for consistency.

3.4.1 Probability for Scattering into Solid Angle $\{\theta, \omega\}$

In general, at a given process p with the related cross-section σ_p, the reaction rate $j_p \cdot A$ is given by

$$j_p\,A = j\,n\,A\,d_f\,\sigma_p, \tag{3.3}$$

where j denotes the incoming particle flux, n denotes the target atomic density, while A is the geometric area affected by the incoming beam [52] and d_f the thickness of the target. Consequently, the probability for a particle to undergo process p is given by

$$P_{\sigma_p} = n\,d_f\,\sigma_p = \kappa\left(\frac{N_A}{A_t}\frac{\text{mole}}{\text{gram}}\right)\sigma_p \qquad \text{with} \quad A_t\text{: mass number of the target.} \tag{3.4}$$

To determine the relevant cross-section σ for particles passing the collimator, the differential Rutherford scattering cross-section is a good starting point

$$\frac{\mathrm{d}\sigma_{lab}}{\mathrm{d}\omega}(\theta) = \left(\frac{e^2}{4\pi\epsilon_0}\right)^2\left(\frac{Z_pZ_t}{4\,m_pv^2}\right)^2\frac{1}{\sin^4(\theta/2)} \qquad \text{with} \quad \frac{e^2}{4\pi\epsilon_0} = \alpha\hbar c \approx \frac{197}{137}\,\text{MeV fm}\,. \tag{3.5}$$

[1] Lower case letters ω and θ refer to the laboratory frame, while upper case letters Ω and Θ refer to the centre-of-mass frame.

Transformation into the centre of mass frame allows straight forward incorporation of the finite mass of the scatterer by introduction of the reduced mass $A_{red} \cdot m_u$

$$\frac{\mathrm{d}\sigma_{cms}}{\mathrm{d}\Omega}(\Theta) = (\alpha\hbar c)^2 \left(\frac{Z_p Z_t}{A_{red}\, m_u c^2}\right)^2 \frac{1}{\beta^4 \sin^4(\Theta/2)} \qquad \text{with} \quad A_{red} = \frac{A_p\, A_t}{A_p + A_t}\,. \tag{3.6}$$

The finite cross-section σ for particles scattered into the solid angle ω and scattering angle θ in the laboratory frame is received by back transformation $\{\Theta, \mathrm{d}\Omega\}_{cms} \leftrightarrow \{\theta, \mathrm{d}\omega\}_{lab}$ from the centre of mass frame [53] using

$$\frac{\mathrm{d}\Omega}{\mathrm{d}\omega} = \frac{\sin^3\Theta}{\sin^3\theta}\left(1 + \frac{A_p}{A_t}\cos\Theta\right)^{-1} \quad \text{and} \quad \tan\theta = \frac{\sin\Theta}{\frac{A_p}{A_t} + \cos\Theta}\,. \tag{3.7}$$

Figure 3.13 shows the transformation of the scattering angle from centre-of-mass to laboratory frame for different projectiles, assuming a tantalum target. It should be noted that

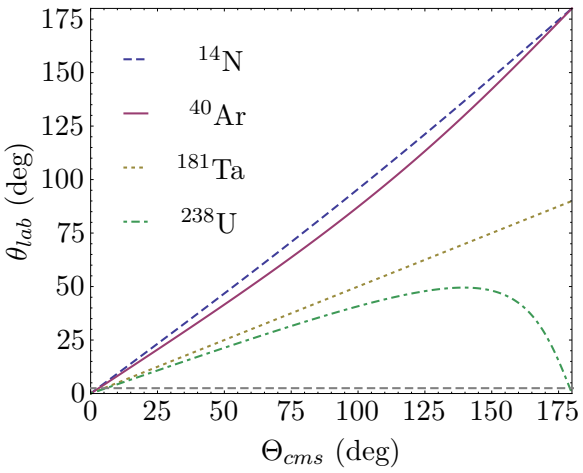

Fig. 3.13: Transformations of projectile scattering angle from centre-of-mass to laboratory frame for different projectile masses and a Ta target.

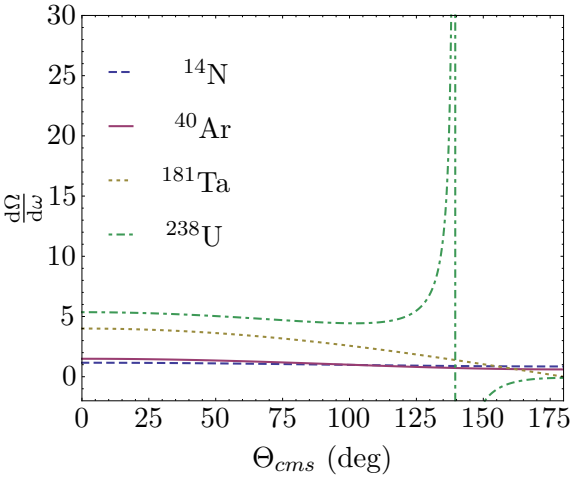

Fig. 3.14: Transformation of differential solid angles $\frac{\mathrm{d}\Omega}{\mathrm{d}\omega}(\Theta)$. Uranium has a noticeable pole at $\cos\Theta = -\frac{A_t}{A_p}$ due to $A_p > A_t$.

for projectiles with $A_p > A_t$, as is the case for an uranium ion impinging on the tantalum foil, small laboratory angles occur in pairs for one center of mass angle. These angles are connected to peripheral collisions with minor impact on the projectile, but also head-on collisions with a major energy transfer to the target. The latter is of minor relevance since the diamond detector electronics together with the discriminator settings adjusted for the 1.4 AMeV particles will not register those low-energy events. The transformation of the differential solid angles between centre-of-mass Ω and laboratory system ω is plotted in Fig. 3.14. This allows to calculate the cross-section in the laboratory system σ_{lab}, since

$$\sigma_{lab}(\theta, \omega) = \frac{\mathrm{d}\sigma_{cms}}{\mathrm{d}\Omega}\,\frac{\mathrm{d}\Omega}{\mathrm{d}\omega}\,\omega\,. \tag{3.8}$$

Together with Eq. (3.4) the probability for a particle to be scattered into $\{\theta, \omega\}$ is finally calculated to be

$$P_{sc}(\theta,\omega) = \kappa \left(\frac{N_A}{A_t}\frac{\text{mole}}{\text{gram}}\right) \sigma_{lab}(\theta,\omega) = \kappa \left(\frac{N_A}{A_t}\frac{\text{mole}}{\text{gram}}\right) \frac{\mathrm{d}\sigma_{cms}}{\mathrm{d}\Omega}\frac{\mathrm{d}\Omega}{\mathrm{d}\omega}\omega\,. \tag{3.9}$$

As Fig. 3.15 shows, the probability magnitude is about $1.6\times10^{-5}\pm5\times10^{-6}$ and differs only by a factor of less than two between nitrogen with $P_{sc}(\theta = 2.5°, \omega = 7.7\times10^{-6}) \approx 2.1\times10^{-5}$ and uranium with $P_{sc}(\theta = 2.5°, \omega = 7.7\times10^{-6}) \approx 1.2\times10^{-5}$.

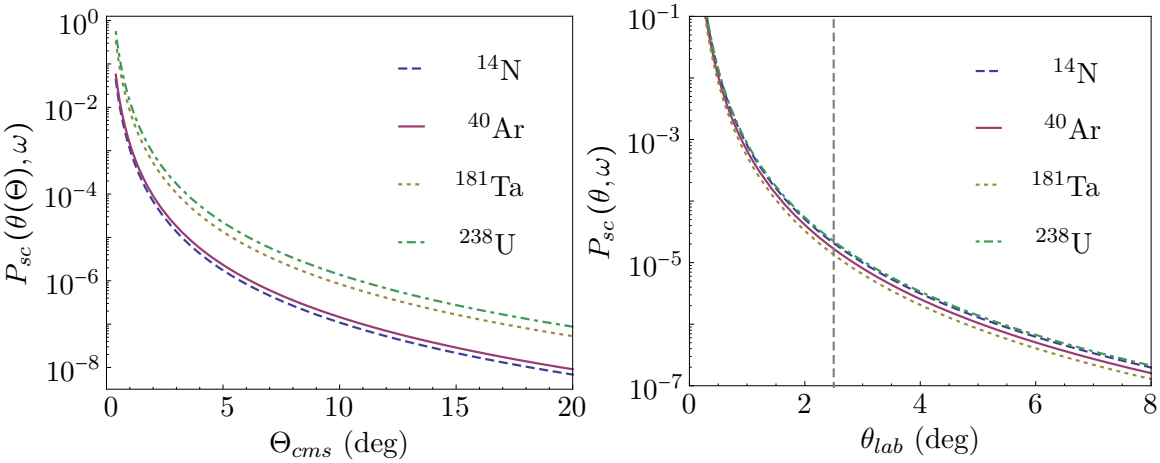

Fig. 3.15: Dependence of the fraction of particles scattered into a solid angle $\omega \approx 7.7\times10^{-6}$ sr, given in centre of mass (left) and laboratory frame (right), on angle $\{\Theta_{cms}, \theta_{lab}\}$. The dashed vertical line marks the angle $\theta = 2.5°$ between the beam axis and the collimator setup housing the tantalum foil.

3.4.2 Recoil Energy

In the picture of classical Rutherford scattering, momentum is only transferred from the projectile to the target nucleus at rest. After elastic collision, i. e. the kinetic energy of the projectile and target nucleus are the only degrees of freedom, the energy of the projectile in the centre-of-mass frame is given by

$$E(\Theta; A_p, A_t) = E_0 \left\{1 - 4\sin^2(\Theta/2)\frac{A_{red}}{A_p + A_t}\right\} \tag{3.10}$$

according to energy and momentum conservation. For the laboratory frame, Fig. 3.16 shows the transferred energy to the target, whereas the vertical, dashed line marks the angle of the collimator axis with respect to the incoming beam. The energy transfer to the target nucleus is below 0.3 % for all projectiles up to uranium. While a mean shift of energy is not a major issue for the determination of the phase-space distribution, the energy spread due to the finite solid angle has to be small. Both contributions will be discussed in Chapter 7.

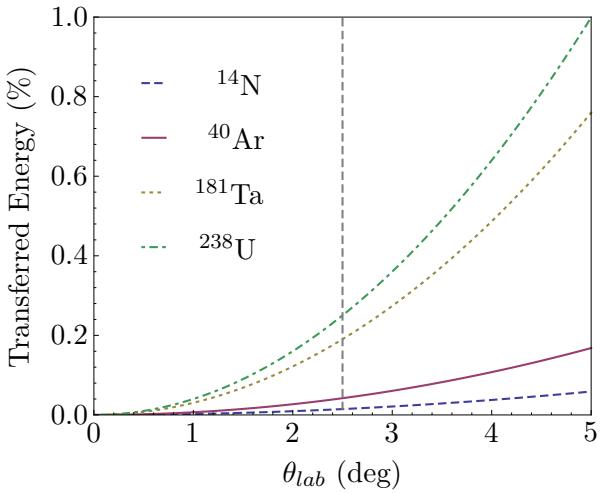

Fig. 3.16: Energy transferred to the target nucleus by the projectile given as fraction of the initial energy.

3.4.3 Complementary SRIM Calculation

Apart from the analytical estimation of the attenuation factor $P_{sc}(\theta,\omega)$ (Eq. (3.9)), a SRIM simulation has been carried out for consistency. SRIM is a commonly used semi-empirical approach to simulate the kinematics of ions in matter [54]. In contrast to the considerations in Sec. 3.4 the effect of the electronic configuration of the target is taken into account. A large pool of experimental data of stopping powers for projectile-target combinations and energies is used by the authors to continuously improve the semi-empirical Monte-Carlo simulation in addition to new theoretical understandings. SRIM only takes geometries of parallel, layered target materials with customisable thickness into account and further allows to specify the incident angle of the monochromatic, unidirectional projectiles. Since the output data contains the directional cosine information, it is possible to take the collimator acceptance $\{\theta,\omega\}$ into account.

Simulation runs have been performed with typical projectiles $\left(^{14}\mathrm{N},^{40}\mathrm{Ar},^{181}\mathrm{Ta},^{238}\mathrm{U}\right)$ at a monochromatic kinetic particle energy of 1.4 AMeV. The unidirectional stream of particles with no lateral extension enters the tantalum foil of 210 µg/cm^2 under an angle of 1.25°. Subsequently, only particles are considered which have been scattered into the collimator acceptance. Emission point angles θ from the foil to the collimator are sampled from 0° to 3.7° at a constant solid angle $\omega = 7.7 \times 10^{-6}$. Obviously, due to the low probability for a particle to pass the collimator, a large number of about 10^7 initial particles is required. In Fig. 3.17 the fraction of particles scattered into solid angle ω is plotted for different angles of the collimator setup (corresponding to Fig. 3.15). The dashed vertical line marks the actual experimental configuration of 2.5°. For comparison, the values at $\theta_{lab} = 2.5°$ are listed in Tab. 3.2 together with the those calculated in Sec. 3.4.1 showing agreement within 10 %. Additionally, the momentum transfer to the target nucleus is shown in Fig. 3.18, by means of the transferred energy. To account for the momentum transfer, the collisional straggling contribution at 0° has been subtracted as a constant offset from the data. Hence, it can be compared to the values calculated from Eq. (3.10) and Fig. 3.16. The corresponding values

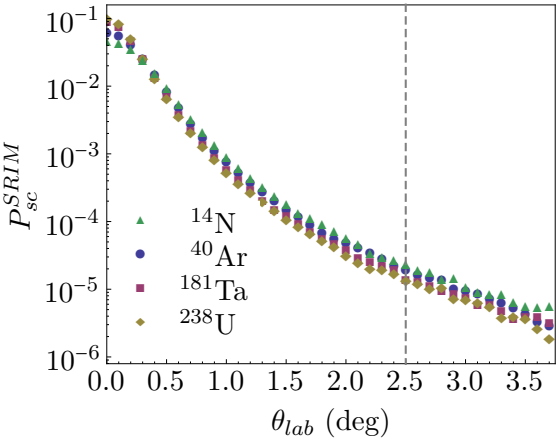

Fig. 3.17: Particle attenuation for N, Ar, Ta, and U projectiles using SRIM under consideration of $\theta = \{0°, 3.7°; \Delta\theta = 0.1°\}$ and solid angle $\omega = 7.7 \times 10^{-6}$.

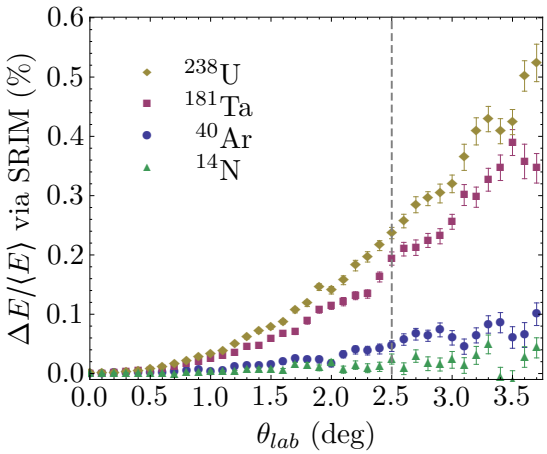

Fig. 3.18: Energy transfer for peripheral collisions using SRIM. Contributions from electronic stopping have been subtracted to be comparable to Fig. 3.16.

are listed in Tab. 3.2 and also show a very good agreement within the statistical error of the SRIM data.

Tab. 3.2: Comparison of attenuation numbers derived from classical Coulomb scattering and via the SRIM Monte-Carlo suite. The transferred energy computed by SRIM is corrected by the straggling offset at 0° for comparison.

Proj. → Ta Foil (210 µg/cm²)	**^{14}N**	**^{40}Ar**	**^{181}Ta**	**^{238}U**
Attenuation factor via classical Coulomb scattering	2.07×10^{-5}	1.67×10^{-5}	1.34×10^{-5}	1.24×10^{-5}
Attenuation factor via SRIM	2.23×10^{-5}	1.75×10^{-5}	1.46×10^{-5}	1.34×10^{-5}
Statistical uncertainty	$< 0.01 \times 10^{-5}$			
Energy transfer (%) via classical Coulomb scattering	0.015	0.042	0.19	0.25
Energy transfer (%) via SRIM	0.024	0.046	0.19	0.24
Statistical uncertainty (%)	0.009	0.009	0.01	0.01

Results of the SRIM Monte-Carlo simulation support the analytical calculations using the classical Rutherford cross-section, which includes the probability for ions to scatter into solid angle ω and the momentum transfer to the target nucleus. In general, the attenuation factor for this setup is in the order of 10^{-5}.

3.4.4 Estimate of Total Attenuation Factor

Equation (3.9) gives an estimate $P_{sc}(\theta,\omega)$ of the fraction of particles being effectively detected based on the incoming flux j. What has not been accounted for so far is the effect of the first aperture on the particle attenuation. Figure 3.19 (left) shows a typical transverse density distribution (in approximation of a Gaussian distribution) of an argon beam with the dimension of the aperture as a relatively small, black disk compared to the beam extension. On the right of Fig. 3.19 the projections onto the transverse axes are plotted.

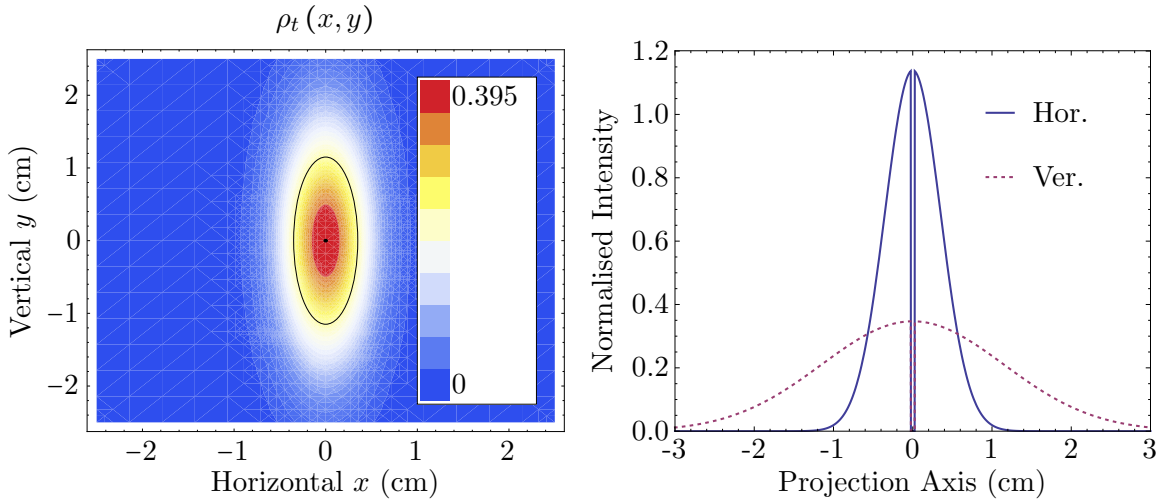

Fig. 3.19: Typical transverse particle density distribution $\rho_t(x,y)$ in Gaussian model space (normalised) during measurements (left) with $\sigma_x \approx 3.5$ mm and $\sigma_y \approx 11.5$ mm. The black dot in the centre shows the dimension of the first aperture of $r_a = 0.25$ mm with respect to the transverse beam extension. Within the black ellipse with semi-axes $\{\sigma_x,\sigma_y\} \approx 39\,\%$ of all particles are located. A projection onto both axes with a simplified shadowed cut of the aperture is shown on the right figure.

Since the beam widths in horizontal and vertical σ_x and σ_y fulfill the condition $\sigma_x \gg r_a$ and $\sigma_y \gg r_a$, the *maximum* fraction that transits the aperture $P_{ap}(r_a\,;\sigma_x,\sigma_y)$ can be calculated approximately by

$$P_{ap}(r_a\,;\sigma_x,\sigma_y) \approx \frac{1}{2\pi\sigma_x\sigma_y}\underbrace{\mathrm{e}^{-\frac{1}{2}\left\{\left(\frac{x=0}{\sigma_x}\right)^2+\left(\frac{y=0}{\sigma_y}\right)^2\right\}}}_{=1}\cdot\pi\, r_a^2 = \frac{r_a^2}{2\sigma_x\sigma_y} \approx 7.7\times10^{-4}. \tag{3.11}$$

Together with $P_{sc}(\theta,\omega)$ the estimated effective attenuation factor

$$P_{eff}(\theta,\omega,r_a\,;\sigma_x,\sigma_y) = P_{sc}(\theta,\omega)\cdot P_{ap}(r_a\,;\sigma_x,\sigma_y) \tag{3.12}$$

is of the order of 10^{-8}. Consequently, the estimated *mean* rate of particles $\lambda_b\,(\mathrm{bunch}^{-1})$ entering the experiment setup is given by

$$\lambda_b = P_{eff}(\theta,\omega,r_a\,;\sigma_x,\sigma_y)\cdot n_\tau\cdot\frac{\tau}{T_{rf}}, \tag{3.13}$$

with τ being the macro pulse length, n_τ the number of ions per macro pulse and T_{rf} the period length of the UNILAC prestripper RF of about 36.136 MHz as given in Tab. 3.3.

Tab. 3.3: Mean event rate per bunch λ_b registered at typical parameters; number of particles inside macro pulse n_τ, mean scattering angle θ, solid angle ω, radius of the first aperture r_a, transversal horizontal and vertical spreads σ_x and σ_y, macro-pulse length τ and RF period length T_{rf}.

λ_b (per bunch)	n_τ	θ (°)	ω (sr)	r_a (mm)	σ_x (mm)	σ_y (mm)	τ (µs)	T_{rf} (ns)
1.4×10^{-3}	10^9	2.5	7.7×10^{-6}	0.25	3.5	11.5	200	27.7

3.4.5 Poisson Process

The particle attenuation is described by a Poissonian process, which is characterised by its mean value λ_b only.[2] Here, the Poisson distribution

$$P_{\lambda_b}(k) = \frac{\lambda_b^k}{k!} \mathrm{e}^{-\lambda_b} \tag{3.14}$$

delivers the probability for measuring k particles of a certain bunch at a mean rate of λ_b measured particles per bunch. The probability distribution is plotted in Fig. 3.20 with the mean event rate per bunch of $\lambda_b \approx 1.4 \times 10^{-3}$ (see Tab. 3.3). Since λ_b is very small on the

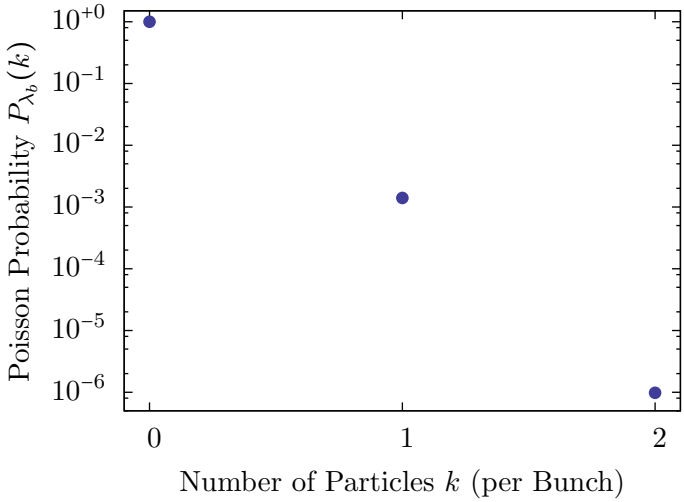

Fig. 3.20: Poisson probability for k events to occur inside a single bunch at an expectation value of $\lambda_b = 1.4 \times 10^{-3}$.

bunch time scale, the most probable situation is that no event occurs at a certain bunch.

[2] Subscript "b" highlights the reference period of occurrence which is a bunch (micro pulse) here.

While the probability for no event to occur during bunch delivery $P_{\lambda_b}(0)$ is about 1 (0.9986), it is significantly suppressed for a single event to occur $P_{\lambda_b}(1)$, which is 1.398×10^{-3} ($\approx \lambda_b$, since $\lambda_b \ll 1$). Measuring exactly two events is suppressed by more than three orders of magnitude as $P_{\lambda_b}(1) \approx 1 \times 10^{-6}$.

Moreover, the interval distribution of adjacent events

$$I(t; \lambda_b) = \lambda_b \, \mathrm{e}^{-\lambda_b t} \tag{3.15}$$

as described in [55], is shown in Fig. 3.21. The distribution is normalised,

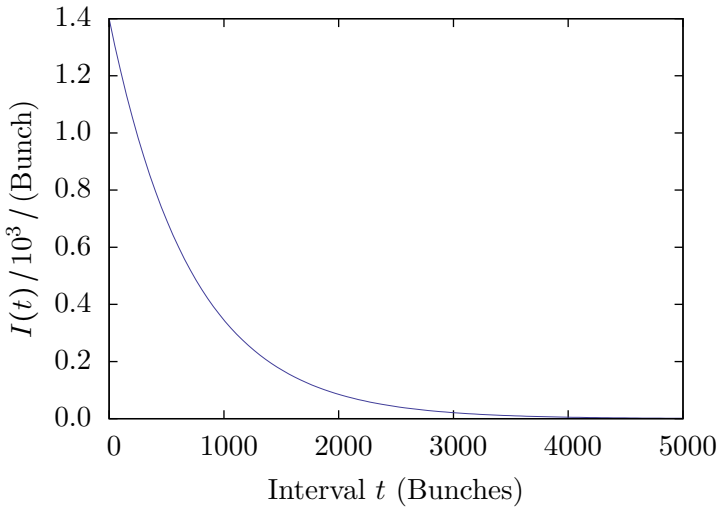

Fig. 3.21: Distribution of intervals between adjacent events. The most probable situation is that the next event occurs in the same bunch.

$$\int_0^\infty \mathrm{d}t \, I(t; \lambda_b) = 1 \,, \tag{3.16}$$

and the fraction of multiple events per bunch $P^{me}_{\lambda_b}$ can therefore be estimated by

$$P^{me}_{\lambda_b} = \int_0^1 \mathrm{d}t \, I(t; \lambda_b) = \sum_{k=2}^{\infty} P_{\lambda_b}(k) \,. \tag{3.17}$$

Since the rate of scattered particles is very small on the bunch time scale, Eq. (3.17) is approximately given by

$$P^{me}_{\lambda_b} = \sum_{k=2}^{\infty} P_{\lambda_b}(k) = 1 - \sum_{k=0}^{1} P_{\lambda_b}(k) \approx 1 - P_{\lambda_b}(0) \tag{3.18}$$

using the fact that $P_{\lambda_b}(0)/P_{\lambda_b}(1) = \lambda_b \ll 1$. Further simplification gives

$$P^{me}_{\lambda_b} \approx 1 - \frac{\lambda_b^0}{0!} e^{-\lambda_d} \overset{\lambda_b \ll 1}{\approx} 1 - (1 - \lambda_b) = \lambda_b. \tag{3.19}$$

Taking into account that at a given attenuation ratio it is not possible to completely avoid multiple hits, with a probability $P^{me}_{\lambda_b} < 2 \times 10^{-3}$ for multiple particles entering the TOF section within a certain bunch, they can be safely neglected in the present configuration. Hence, multiple hits do not significantly contaminate the data for the presented TOF setup.

Chapter 4

Data Acquisition and Data Analysis

The following chapter describes the signal handling downstream of the detectors of the TOF setup and the direct calorimetric approach. After the data acquisition has been introduced, the full post-processing chain of the raw data is described. This includes the reconstruction of the phase space and further treatment of the data.

4.1 Time-of-Flight Setup

4.1.1 Double-Threshold Discriminator

Before detector signals can be reasonably registered at the TDC module, the pulse signals must carefully be processed by discriminators. As outlined in Sec. 3.1.1, signals from the MCP detector and poly-crystalline diamond detector represent an event at two ends of a drift section of known separation. This TOF relies on the precise timing information when the particle has crossed the reference points. Therefore, pulses of nanosecond duration have to be transferred into a logic timing signal. On the technical side, the generation of the logic timing is done by so-called discriminators. Discriminators are available with different working principles. For signals of identical shape, a so-called leading-edge discriminator is sufficient. It generates the timing signal from a tunable threshold value which determines the logical timing once the detector signal crosses the threshold value. As long as the rise time is smaller than the required time resolution, a leading-edge discriminator is generally well suited for the task. Otherwise, for high timing requirements, as it is required in this work, the leading-edge discriminator is obviously an insufficient approach if pulse shapes from a detector exhibit a broad pulse-height distribution. The introduced undesired systematic time jitter of leading-edge discriminators is called *time walk* or simply *walk*. Constant-fraction discriminators [56] provide time walk correction for signals with a broad pulse-height distribution of pulse shapes that only differ by a scaling factor. If the pulse shapes vary beyond a scaling factor, a discrimination approach that solely relies on the rising edge is favourable. A method which implements the sensitivity on the slope of the rising edge only is the *double-threshold discriminator* which has been proposed by Frolov et

al. [57] and has been considered for certain TOF modules [58] of the CERN ALICE experiment. The working principle takes into account two tunable thresholds at the rising edge

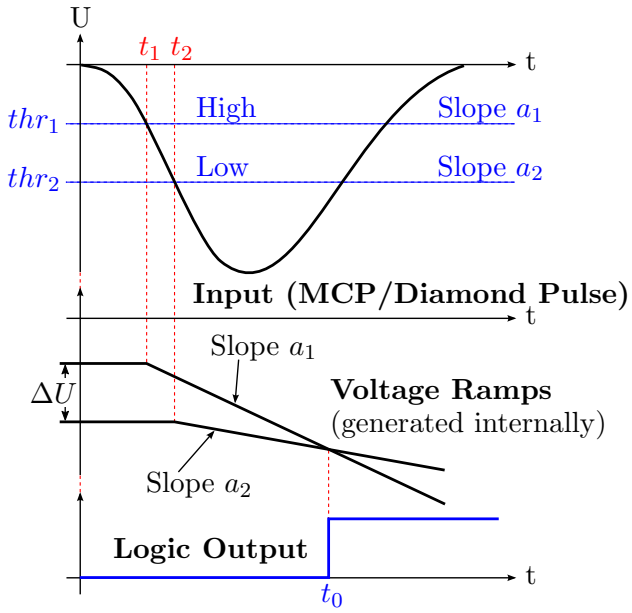

Fig. 4.1: Working principle of the *double-threshold discriminator* used for timing generation of the MCP and diamond pulses.

as schematically depicted in Fig. 4.1. It assumes linear characteristics of the pulse-shape ensemble between the two thresholds. When the signal reaches a threshold $thr_{\{1,2\}}$ a linear voltage ramp is started. The slope $a_{\{1,2\}}$ of the ramps are generated internally to comply with

$$\frac{thr_1}{thr_2} = \frac{a_1}{a_2} \,. \tag{4.1}$$

A low-walk timing pulse is triggered at the intersection of both ramps at

$$t_0 = \frac{\Delta U}{a_1 - a_2} \,. \tag{4.2}$$

According to Frolov et al. [57] a walk of only 10 ps could be obtained at a pulse-height distribution ranging from 0.2 to 1.5 V. The discriminator used in the work is based on an ASIC designed by the GSI experiment electronics department.

4.1.2 NIM Electronics Setup

The information to reconstruct the phase-space distribution (see Sec. 4.1.5) recorded using the TOF setup is based on three input timings.

- UNILAC RF timing reference (from master oscillator)
- MCP timing

- Diamond timing (Poly-crystalline diamond)

The MCP and diamond timings are used to determine the TOF, whereas the UNILAC RF serves as a relative arrival time measure for the bunch structure. A NIM setup prepares all timing signals fed into the TDC module as depicted in Fig. 4.2. In the following, the numbering scheme of the signal sources and NIM modules refers to the depicted schematics.

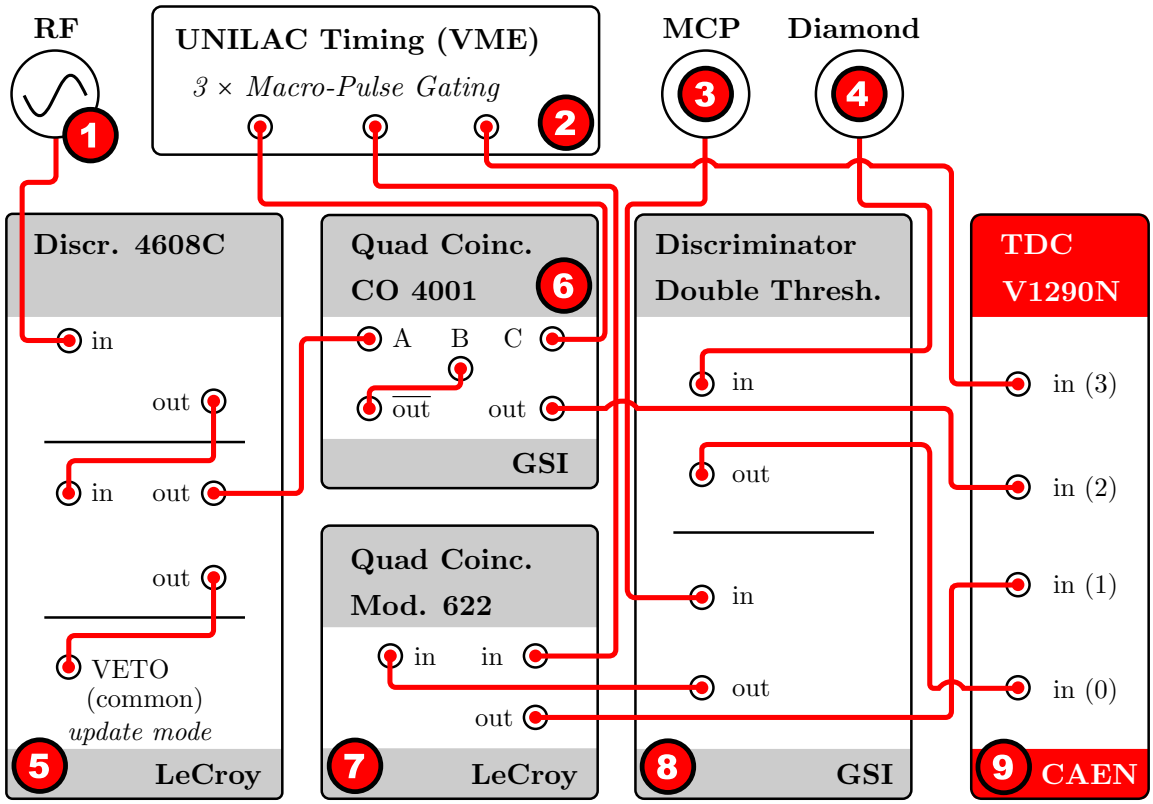

Fig. 4.2: Schematic signal-processing network for the TOF measurement. Labels 1 to 4 reference the signal sources consisting of: the UNILAC RF signal 1 provided by the master oscillator (36.136 MHz), the macro-pulse/cycle gate 2 generated by the custom-made GSI timing board (D. Liakin [34]), the anode at the back of the MCP 3 and the poly-crystalline diamond detector 4. NIM modules 5 and 6 are used as prescaler (1:10) of the generated logical RF reference to lower the overhead of the incoming data rate and block RF output outside the macro pulse gate. Similarly, module 7 limits the logical MCP output to the macro pulse only to avoid distinct dark pulses. Detector pulses are processed by the *double threshold discriminators* 8. Eventually, processed signal sources 1 to 4 are registered by a fast TDC 9.

RF Reference. 1 The RF reference from the UNILAC master oscillator is assigned to a slope-sensitive zero-crossing timing discriminator module 5. As the RF reference would contribute to an excessive amount of data, at a regular time period of $T_{rf} \approx 27.7$ ns, overhead reduction is considered and RF timings are restricted to macro-pulse delivery

by a safe margin (see Sec. 4.1.4). The amount of data is further significantly reduced by prescaling at a ratio of 1:10. Leading-edge discriminator 5 generates the RF timing pulse and provides the aforementioned prescaling by suppressing the output for nine following periods. This is accomplished using one logical output with an adjusted pulse width of about $9 \times T_{rf}$ to act as veto trigger. Finally, module 6 provides gating of the RF timing with respect to the macro-pulse delivery, while a timing module 2 generates the appropriate macro-pulse/cycle gate.

Macro-Pulse/Frame Gate.[1] 2 A UNILAC-event-timing module generates a gate pulse according to a cycle defined between two events. To enclose the actual macro pulse by a safe margin, UNILAC-timing events 4 and 8 have been chosen. This includes a RF preparation-time of at least 50 µs advancing and 40 µs after real macro-pulse delivery. For a detailed documentation of the UNILAC-timing interface and event structure, see [59].

MCP Timing. 3 Detector pulses from the MCP are processed by the double-threshold discriminator 8. To omit distinct dark counts, the detector timings are only registered during macro-pulse delivery. The corresponding gating is provided by module 7 before the timing is fed to the TDC.

Diamond Timing. 4 Since the diamond detector, contrary to the MCP, features no dark counts, the detector pulse is only processed by the double-threshold discriminator 8 and fed to the TDC.

4.1.3 Time-to-Digital Converter

After the timing signals of the TOF setup have been generated and processed by the NIM chain, as described in Sec. 4.1.2, a low time-jitter TDC registers the timing data. The TDC, a CAEN V1290N VME module [60], features a nominal resolution of better than 35 ps (RMS). Per input channel a double-hit resolution of 5 ns allows to record events that are at least 5 ns separated. Once a NIM pulse is registered, the internal global clock state is dumped to the appropriate channel output buffer.

The timing data structure, as schematically depicted in Fig. 4.3, is represented by a 4-byte vector alignment. It consists of a header field denoting the input channel and the 21-bit clock dump. With a channel width corresponding to about 24.4 ps, this data field overflows every 51.2 µs. The raw clock information is stored and the overflow-corrected values are put into relation to the preceding macro-pulse-start timing. Moreover, as the macro-pulse number is recorded, timing values are globally connected throughout the measurement.

A Struck SIS 3150 VME controller [61] acts as VME bus master to the TDC and timing module and is interfaced by a commercial PC via USB 2.0. During the measurement, a

[1] Depending on the context, this time interval is referred to as *macro-pulse gate*, *cycle* or *frame*. The term "macro pulse" is used whenever the fact of the macro pulse being enclosed during the gate is highlighted (although the gate time is not sharply clipped to the macro pulse). Furthermore, the term "cycle" is connected to the corresponding UNILAC events. The term "frame" is used in conjunction with recorded timing signals and consists of all data registered within a cycle.

TDC Event - 32-bit Data Structure

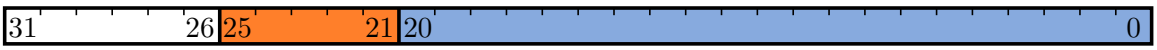

Fig. 4.3: TDC timing represented as a 4-byte vector. The lower 21-bits contain the actual dump from the internal global clock of the TDC. Given the LSB equivalent of about 24.4 ps, overflowing occurs every 51.2 µs

set of timing data, according to Fig. 4.3, is accumulated in a single file of linear data. The actual phase-space distribution is reconstructed via offline post processing developed in this work along with the data analysis. Apart from the aforementioned timing signals, the macro-pulse start timing is directly recorded via the macro-pulse gate from module 2. While it is not strictly necessary for the plain phase-space distribution, it allows to relate bunches with respect to the macro-pulse start. This becomes necessary when time cuts of the phase space are compared, e. g. the phase-space distribution of the first and second half of the macro pulses.

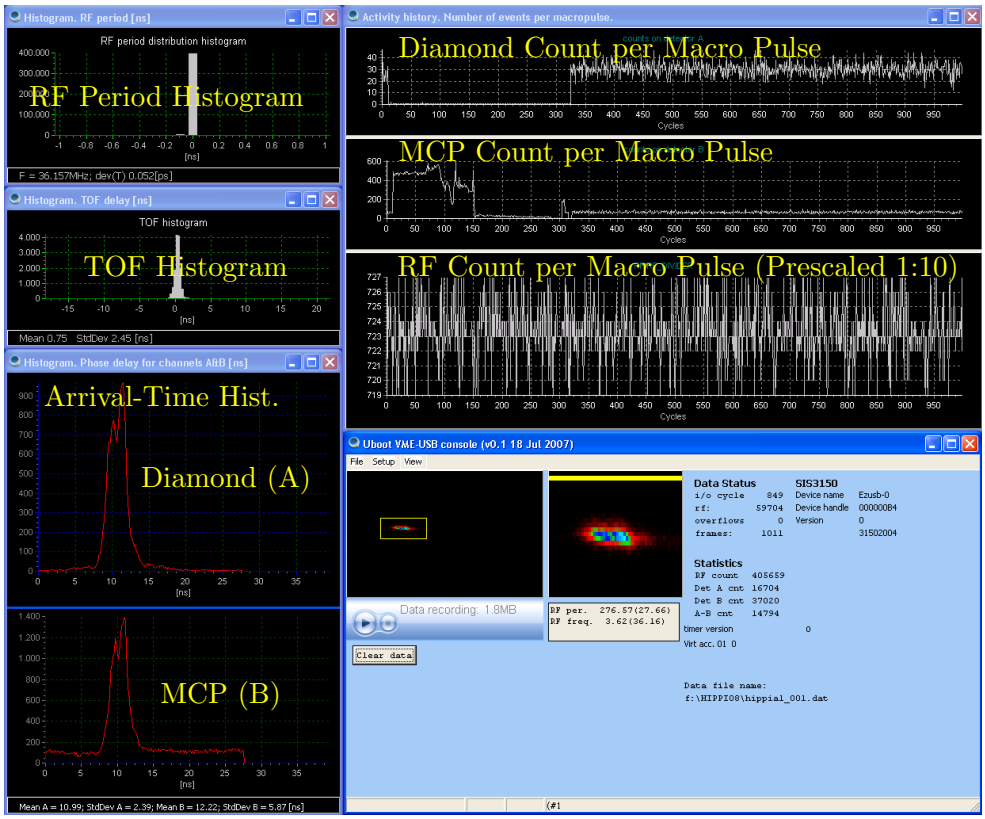

Fig. 4.4: GUI frontend by Dmitry Liakin (2006). The DAQ frontend runs on a regular PC and communicates with a USB 2.0 to VME interface (Struck SIS3150). Apart from providing an online display of all incoming timings and statistics, the high-voltage supplies can be controlled from within the program.

Figure 4.4 shows the main view of the data acquisition GUI frontend. While recording the raw data, statistics of the timing signals are provided online, in particular, the preliminary phase-space distribution (bottom right window). Histograms of the raw detector timings are shown on the bottom left. A noteworthy comparison of the poly-crystalline diamond **(A)** and MCP **(B)** histograms shows a flat background of dark counts of the MCP detector which is not present at the diamond detector.

4.1.4 Post-Processing of Raw Data

The TDC channel buffers are continuously dumped from a linear data stream. A TDC event is represented by the 4-byte data structure as depicted in Fig. 4.3. The four recorded events are characterised as follows:

- **Diamond detector** (Poly-crystalline)
  - Timing signals from the poly-crystalline diamond detector provided by a double-threshold discriminator
  - Features no dark counts
- **MCP detector**
  - Timing signals from the micro-channel plate, provided by a double-threshold discriminator
  - Dark counts occur
- **UNILAC RF**
  - Slope-sensitive zero-crossing of the UNILAC RF master oscillator signal
  - Downscaled/prescaled RF-timing data (1:10) to reduce overhead
- **Frame start**
  - Start timing provided by the macro-pulse gate reference

Post-processing of the raw data aims for the extraction of the actual plain particle events forming the phase-space distribution. This comprises the determination of the correlated MCP and diamond events, the corresponding RF reference, the bunch (micro pulse) at which the particle event occurs and the macro pulse number.

Calibration of the TDC is performed using the RF signal of 36.136 MHz provided by the UNILAC master oscillator. With the knowledge of the RF period time, a TDC channel is determined to (24.414 ± 0.002) ps by linear regression of the recorded RF timing.[2] TDC-clock dumps are represented by 21 bits. This means that an overflow occurs about every 51.2 µs per input channel and must be considered consistently. Overflow correction of the RF data is straightforward as the prescaled RF frequency is higher by about a factor of 200. Diamond and MCP timings, in contrast, are overflow corrected in accordance with the regular RF timing. Multiple particle events per bunch, which are unavoidable (see Sec. 3.4.5), will be detected and discarded as long as they are separated by more than 5 ns, given the double-hit resolution limit of the TDC.

[2] In this work 'channels' always refers to channels of the TDC in context with the TOF DAQ.

The RF timing signal is downscaled/prescaled (1:10) by the NIM setup, as described in Sec. 4.1.2, to prevent excessive data overhead. Hence, with an RF period time of ≈ 27.7 ns, an RF timing signal is registered every 277 ns. Restoration of the skipped RF events is accomplished by linear regression. At the same time, the effective RF timing precision is slightly enhanced. To characterise the stability of the linear regression, a measurement from the HIPPI [62] campaign in December 2008, with a large number of events, is taken as reference. The measured data comprises 2428 macro pulses with a gate length of 200 µs which corresponds to ≈ 720 supporting points. Each macro pulse is connected to a separate fit of the raw RF timing data. The corresponding distribution, shown in Fig. 4.5, features a mean slope of 1334.8981 channels per ten RF periods with a standard deviation of ≈ $3.5{\times}10^{-4}$ channels per ten RF periods. This results in an RMS width, with respect to the mean value,

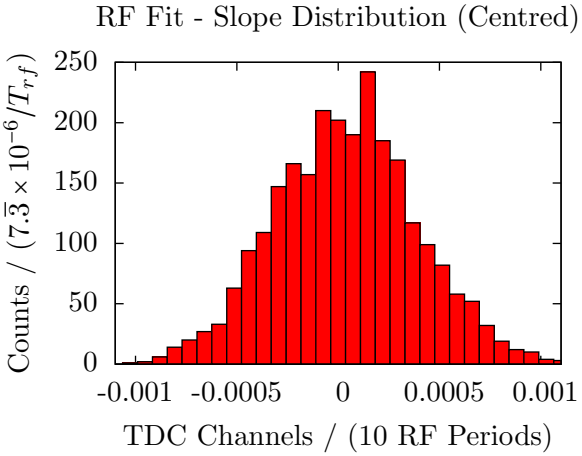

Fig. 4.5: Centred slope distribution from RF fit for RF reconstruction. Fits from all 2428 macro pulses were used, each incorporating RF timings from beam delivery start onwards.

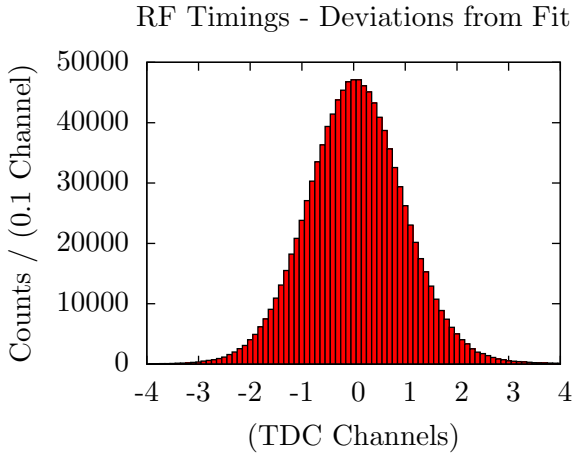

Fig. 4.6: Deviation of prescaled RF timings from the corresponding linear RF fit. Includes RF timings from all 2428 macro pulses. RF timings from beam delivery start onwards are taken into account.

of $\sigma/\mu \approx 3.1 \times 10^{-8}$ and highlights a very narrow distribution supported by the low integral non-linearity of the TDC of less than 2.5 LSB (corresponding to 61 ps) [60] and the large amount of supporting points. Typically, the fit comprises several hundreds of supporting points, depending on the macro-pulse length. Recorded RF timings preceding the actual beam delivery are skipped, as will be explained in the following paragraph.

The expected stable regularity of the RF is not sustained over the full frame. Based on the same dataset as the previous slope distribution, Fig. 4.7 shows the deviation of registered RF data with respect to the corresponding linear regression, represented by the grey data points, along a random frame. Most data points scatter around the fit reference about less than ±1 TDC channels which is in accordance with the TDC specification [60], claiming an input jitter of less than 35 ps (RMS). The red line marks the deviation averaged over all 2428 acquired frames. At the beginning of the macro-pulse gate, prescaled RF timings up to about period 230, the grey-shaded area, feature a clear deviation from a uniform behaviour along the frame. In terms of the global UNILAC event timing [59] this interval is defined

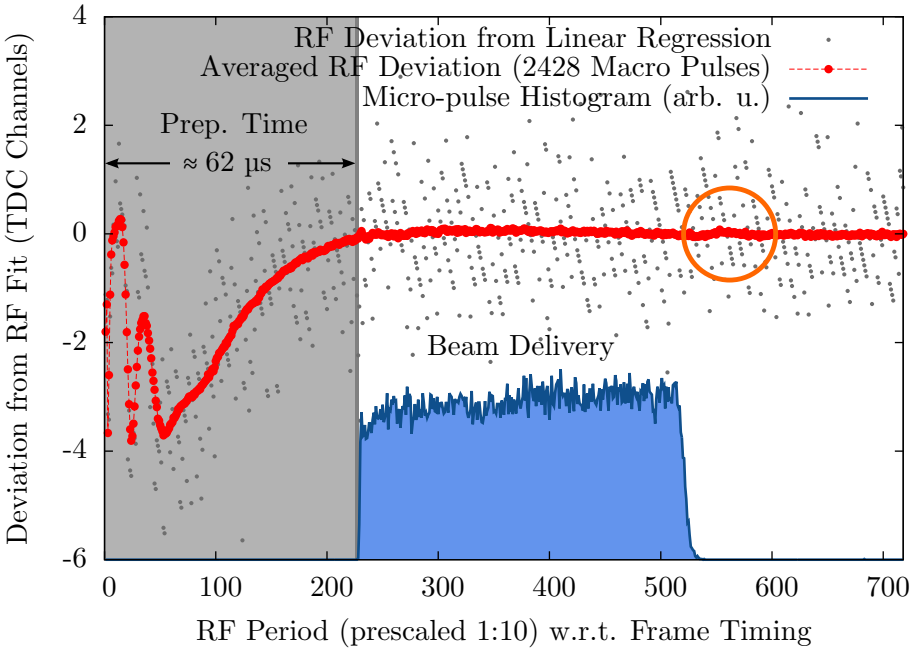

Fig. 4.7: Typical deviation of measured, prescaled RF timings from the linear regression. An avarage over all 2428 acquired cycles is shown by the red data points. The grey-shaded area marks the region which is affected by transient oscillation between UNILAC-timing event 4 and 6 [59]. For completeness, the corresponding macro-pulse-current equivalent, by means of the micro-pulse histogram, is given by the blue line. The data is taken from a measurement during the HIPPI [62] campaign 2008 which features a large number of $\approx 6 \times 10^4$ events.

between event 4 and 6. Although the UNILAC master oscillator is expected to provide a constant stable RF, the fluctuations in measured RF period length most likely origin from pick-up effects of transient oscillations during high-power RF switching. Regardless of the small impact of the fluctuations, with a relative deviation of less than 0.4 ‰ per RF period at maximum, it is taken care of by excluding the "preparation time interval" when performing the linear regression. The blue line in Fig. 4.7 shows the micro-pulse occupancy, taking all recorded frames into account. This provides information of the macro-pulse current represented at the given RF time base. It is clearly visible that the initial distortions, during "preparation time", virtually do not affect the interval of actual beam delivery. Furthermore, an additional bump is present denoted by the orange circle. Since it is correlated with the final edge of the macro-pulse current, the bump can also be attributed to power switching processes. Taking only RF events into account starting with beam delivery after the preparation time, the jitter distribution with respect to the linear RF fit is shown in Fig. 4.6. The histogram comprises prescaled RF data from all 2428 macro pulses with a total of $\approx 10^6$ events and results in an almost perfect Gaussian distribution. A standard deviation of only 0.968 channels, which corresponds to ≈ 23.6 ps, highlights a very good performance of the RF DAQ chain described earlier in this chapter. The present

characteristics were reproducible in all measurements with only minor variations.

Detector Timings. With the reconstructed RF events it is straightforward to properly align the registered MCP and diamond detector timings. Subsequently, coincidences are determined using an appropriate time window. Ambiguous events are taken care of where possible, but detection is limited by the double-hit resolution of the TDC. Multiple-ion events per bunch give rise to ambiguous coincidences within the time window. In contrast to the diamond detector, the MCP features a mean dark-pulse rate, typically in the magnitude of $1\text{–}10\,\mathrm{s}^{-1}\,\mathrm{cm}^{-2}$. Hence, in rare cases, those may also add to ambiguous event configurations which cannot be resolved and must be discarded.[3] Unfortunately, it turned out that time windows cannot be limited to a single bunch interval. In fact, large-range low-energy tails may require time windows of three to four RF periods, which will be discussed in Chapter 5. Obviously, with larger time windows ambiguous event configurations become more likely. Concerning the MCP geometry, flat distribution of dark pulses can be assumed at a mean rate of $\approx 10\,\mathrm{s}^{-1}$. This gives rise to a probability of 10^{-7} to register a *random* dark event within four RF periods which can safely be neglected. Multiple-ion events, in turn, have a bigger impact. The interval-length distribution of consecutive ions scattered into the acceptance of the collimator setup is given by Eq. 3.15. Consequently, the mean fraction $\langle p_n \rangle$ of ambiguous configurations within the first n RF periods after an ion is registered, is estimated by

$$\langle p_n \rangle = \int_0^n \mathrm{d}t\, I(t;\lambda_b) = \lambda_b \int_0^n \mathrm{d}t\, e^{-\lambda_b t} \overset{\lambda_b \ll \frac{1}{n}}{\approx} n\,\lambda_b\,. \tag{4.3}$$

Incoming mean rates λ_b typically range between 10^{-4} and 10^{-3} ions per bunch depending on the ion species. This means, for a time window spanning four bunches and using Eq. (4.3), the fraction of ambiguous event configurations is less or equal than 4 ‰. These ambiguities are detected and discarded as long the separation of the events is larger than the double-hit resolution of the TDC. With a double-hit resolution of 5 ns of the TDC (per input channel), only those events cause potential spurious coincident events which arrive within a single bunch. This estimate is supported by typical bunch lengths of 1 to 3 ns (RMS) and entails a fraction of potentially flawed events between 0.1 and 1 ‰ which cannot be identified.

4.1.5 Reconstruction of the Phase Space

As outlined in the previous section, the TOF setup presented in this work registers timing data from the MCP and diamond detector. In the following, for *particle i*, $t_{mcp,i}$ refers to the MCP timing, $t_{dia,i}$ refers to the diamond-detector timing and $t_{rf,i}$ refers to the preceding RF zero-crossing reference. Transformation from the registered timing information into phase-space coordinates is straightforward, but a few remarks are indicated.

[3] MCP pulses, which originate from dark emission of the MCP channels, possess a different characteristic shape. Compared to the biased secondary electrons emitted from the aluminium foil, those pulses have significantly lower amplitudes. Nevertheless, it is not possible to exploit this as a decision criteria. Pulse heights are not directly accessible in the TOF setup as threshold settings need to be low to reach higher timing resolutions.

The measurement does not provide absolute access to phase and energy and focuses on the particle distribution. Instead, the typical approach is to use a linear approximation to reconstruct the momentum/energy information. This allows for a translational invariant description with respect to the relative cable delays. Systematic contributions originating from the related approximations are discussed in Chapter 7. Measurement of the absolute phase and energy of the bunch centre can be performed by the phase-probe TOF sections available at different locations along the UNILAC.

Phase Information. The phase information is directly contained in the arrival time of the incoming ion at the diamond detector. As explained in Chapter 2 and Eq. (2.6), the arrival time $\Delta t_{phase,i}$ is often evaluated with respect to the synchronous particle. This is the common approach in theoretical models of beam transport and within tracking codes. Since access to the synchronous particle is not available, the preceding RF timing is considered a fixed reference as explained earlier in this chapter

$$\Delta t_{phase,i} = t_{dia,i} - t_{rf,i}\,. \tag{4.4}$$

An additional, relative cable delay is not taken into account since evaluation of the phase-space data, in terms of *Twiss parameters* and *emittance*, only covers central moments. It should be noted that, of course, the inter-particle phase relation is not affected by this method. Hence, the difference in phase between two random particles is accessed precisely within the timing resolution, which is important for the distribution characteristics.

On the other hand, the RF reference limits a non-ambiguous determination of the phase to the RF period time. As it turned out, slow particle contributions occur which may span over several RF periods. This will be covered in Sec. 5.3. To some extent it is possible to reconstruct the overflow in phase by the energy-phase correlation, i.e. the assumption that slow particles arrive later. This is a legitimate approach as bunches drift several meters after the last accelerating IH2 structure and, thus, are expected to show a significant phase-energy correlation. Commonly, the arrival time is provided in nanoseconds. For transformation to the RF phase equivalent rad and degree, see Chapter 2, Eq. (2.9).

Momentum/Energy Information. The expected mean energy $\langle E\rangle \approx 1.4$ AMeV is derived from the design value of the normalised velocity $\langle\beta\rangle \approx 5.5\,\%$. Hence, the kinematics can be restricted to the classical energy-momentum relation, with mass number A and atomic mass $\approx A \cdot m_u$

$$E\left(\overset{def.}{=} E_{kin}/A\right) \approx \frac{m_u}{2} c^2 \beta^2\,. \tag{4.5}$$

In terms of detector separation l_{tof} and time of flight $t_{tof,i}$ of *particle i*, between MCP foil and poly-crystalline diamond detector, the kinetic energy trivially writes

$$E_i = E\left(t_{tof,i}\right) = \frac{m_u}{2}\left(\frac{l_{tof}}{t_{tof,i}}\right)^2\,. \tag{4.6}$$

By separating out the mean energy $\langle E \rangle$,

$$E_i = \langle E \rangle + \Delta E_i = E\left(t_{\langle E \rangle}\right) + \Delta E_i \left(t_{tof,i} - t_{\langle E \rangle}\right) , \tag{4.7}$$

and considering the linear correction term of the Taylor series of the expansion about $t_{\langle E \rangle}$,[4]

$$\Delta E_i \overset{\frac{\Delta t_i}{t_{\langle E \rangle}} \ll 1}{\approx} \frac{\mathrm{d}}{\mathrm{d}t} E(t) \bigg|_{t_{\langle E \rangle}} \Delta t_i = -2 \langle E \rangle \frac{\Delta t_i}{t_{\langle E \rangle}} \quad \text{with} \quad \Delta t_i \coloneqq t_{tof,i} - t_{\langle E \rangle} , \tag{4.8}$$

the relative energy deviation is approximately given by

$$\frac{\Delta E_i}{\langle E \rangle} \approx -2 \frac{\Delta t_i}{t_{\langle E \rangle}} \approx -2 \frac{\Delta t_i}{t_{\langle p \rangle}} = -2 \frac{c \langle \beta \rangle}{l_{tof}} \Delta t_i . \tag{4.9}$$

Several assumptions have been made. Trivially, the linearisation is only valid in the vicinity of the expansion point $t_{\langle E \rangle}$. Furthermore, the last approximation in Eq. (4.9) relies on the assumption that $t_{\langle p \rangle}$ is sufficiently close to $t_{\langle E \rangle}$. This will be discussed in detail in Sec. 7.7. The relative momentum deviation in linear approximation can be written accordingly as

$$\frac{\Delta p_i}{\langle p \rangle} \approx -\frac{\Delta t_i}{t_{\langle p \rangle}} = -\frac{c \langle \beta \rangle}{l_{tof}} \Delta t_i . \tag{4.10}$$

The mean velocity of bunches registered at the device is provided manually and a deviation from the real situation affects the expansion point of the Taylor series. The mentioned systematic contributions are not of major negative impact and are discussed in detail in Sec. 7.7.1.

Histogramming. Recorded ion events, which have been transformed into appropriate phase-space coordinates, are accumulated in 2-dimensional histograms. A measurement, with a duration of typically several tens of minutes, relies on stable phase-space conditions. Measurements usually require exclusive access to the whole pre-stripper section of the UNILAC due to global settings. This in turn ensures stable beam delivery, from an operating point of view, with constant accelerator settings throughout the whole pre-stripper facility. Stability of beam delivery also varies between different types of ion sources and their operating time with respect to the expected life time.

Access to the macro-pulse start timing, using the TOF setup, allows to select certain classes of events and compare the corresponding phase-space distributions. For instance, phase spaces consisting of macro-pulses of the beginning of a measurement can be compared to later ones. This can reveal issues of the ion source and accelerator settings. Also, phase-space distributions of a certain bunch range within the macro pulses can be compared to others. Concerning statistics, this, of course, requires the total event count to be sufficiently large.

[4] The symbols $t_{\langle E \rangle}$ and $t_{\langle p \rangle}$ refer to the TOF of particles of mean energy $\langle E \rangle$ and mean momentum $\langle p \rangle$.

4.2 Mono-Crystalline Diamond Setup

The experimental setup based on a mono-crystalline diamond detector relies on a single detector only. Instead of a TOF measurement, a semi-conducting detector with calorimetric properties (see Sec. 3.3.3) is used. The particle attenuation mechanism is identical to the TOF approach described in Sec. 3.1.1 and Sec. 3.4. Particles of an attenuated beam, that scatter into the solid-angle acceptance of the collimator setup, will be detected at the mono-crystalline diamond. To recapitulate the experimental site, see Fig. 3.6 for an overview of the diagnostics chamber. Voltage pulse signals from the detector provide a measure of the deposited energy if the functional dependency on the total accumulated charge from with the projectiles' kinetic energy is known. In principle an injective functional behaviour is obligatory, to provide a distinct mapping of a certain pulse information to the kinetic energy. Ideally, a linear dependency is sustained over a large range.

Schematics. Schematics of the electric interface to the detector and the DAQ are depicted in Fig. 4.8. The detector pulses are extracted at the bias tee and amplified by a one- or two-stage Mini-Circuits ZX60-33LN-S+ (50 MHz - 3 GHz, 17.5 dB typ.) amplifier. A positive bias of 100 V, which corresponds to a field strength of 1 V/µm, has been applied to the diamond detector. As explained in Sec. 3.3.3, the detection of electron holes is considered favourable.

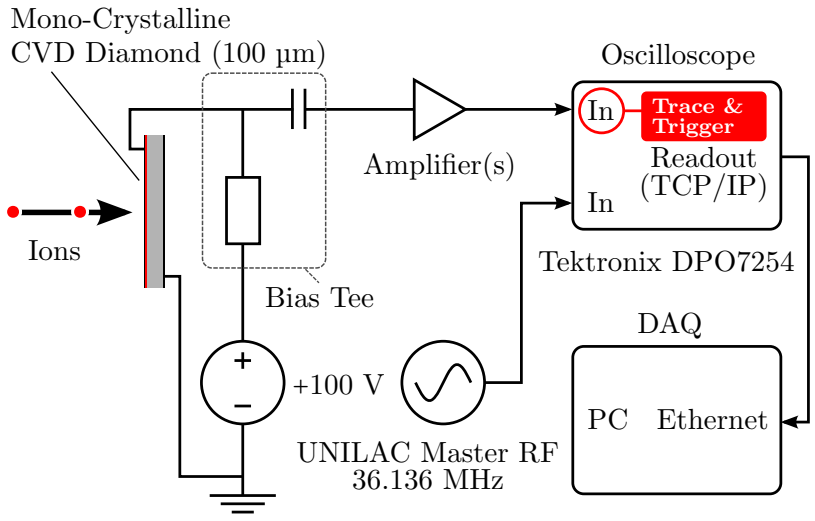

Fig. 4.8: Schematic data acquisition chain for the calorimetric measurement using a single crystalline diamond (Fig. 3.12). The diamond is fed by bias tee at a supply voltage. After amplification of the signal a fast oscilloscope is used as ADC module. The detector signal as well as the UNILAC RF from the master oscillator are streamed to a PC setup via Ethernet.

4.2.1 Data Acquisition

The data acquisition for the calorimetric measurement using the MC-diamond detector is performed with a fast oscilloscope. Post-processing tools to reconstruct the phase space and data analysis software have been purpose-built developed. For the setup at hand, preamplified pulse shaping is unfavourable with typical integration times of several µs. Hence, an approach where detector signals are amplified and sampled directly at a high sample rate has been chosen. At the same time, the UNILAC master oscillator signal is recorded as a fixed arrival-time reference. This allows to extract the relative phase information between events, as done in the TOF setup.

The oscilloscope used is a Tektronix DPO 7254 [63] which features an 8-bit ADC and a real sample rate of 20 GS/s in two-channel mode.[5] The ADC data is transfered in floating point mode. However, the actual scaling of the raw data is irrelevant due to the required energy calibration. As the amplified diamond readout and the RF reference needs to be recorded simultaneously, a sample period of 50 ps is available. During measurement, the data is streamed to a PC via Ethernet and recorded with a custom program.[6] Data traces of the diamond pulse and RF are recorded simultaneously, using the internal trigger of the oscilloscope on the diamond pulse. The threshold is set manually with a safe margin above noise level. Currently, data acquisition is limited to one acquisition per macro pulse. A higher efficiency is targeted with a later version of the program. The actual phase space is reconstructed offline.

4.2.2 Post-Processing of Raw Data

Typical examples of acquired data for a single event are shown in Fig. 4.9, recorded with an Ar^{14+} beam and a kinetic energy $E \approx 1.4$ AMeV. The diamond-pulse trace is given by the red line with linear interpolation and contains 2000 samples at 20 GS/s, i.e. the recording window corresponds to 100 ns at a sample period of 50 ps. The low noise figure of the amplifiers give rise to a comfortable signal-to-noise ratio (SNR) of ≈ 23 dB.[7] An impedance mismatch at the amplifier input seems to have caused reflections at a characteristic cable length of 1 m and could not be sorted out at the time of measurements. Nevertheless, the reflection is separated well enough from the primary pulse without overlapping signal contributions. The lower parts of each plot in Fig. 4.9 show the harmonic RF data samples from the UNILAC master oscillator. Simultaneous acquisition of the diamond trace and the UNILAC RF reference allows to extract energy and RF reference. Reconstruction of the phase space requires to post-process the raw data stream from the oscilloscope. The corresponding software has been developed in this work. In the following, the necessary steps are outlined.

[5] A real sample rate of 40 GS/s can only be achieved in single-channel acquisition mode.

[6] The source of the command-line tool is available on request and should run on any POSIX compliant system without further modification.

[7] Pulse-to-noise amplitude ratio for a typical pulse at phase-space centre at ≈ 1.4 AMeV.

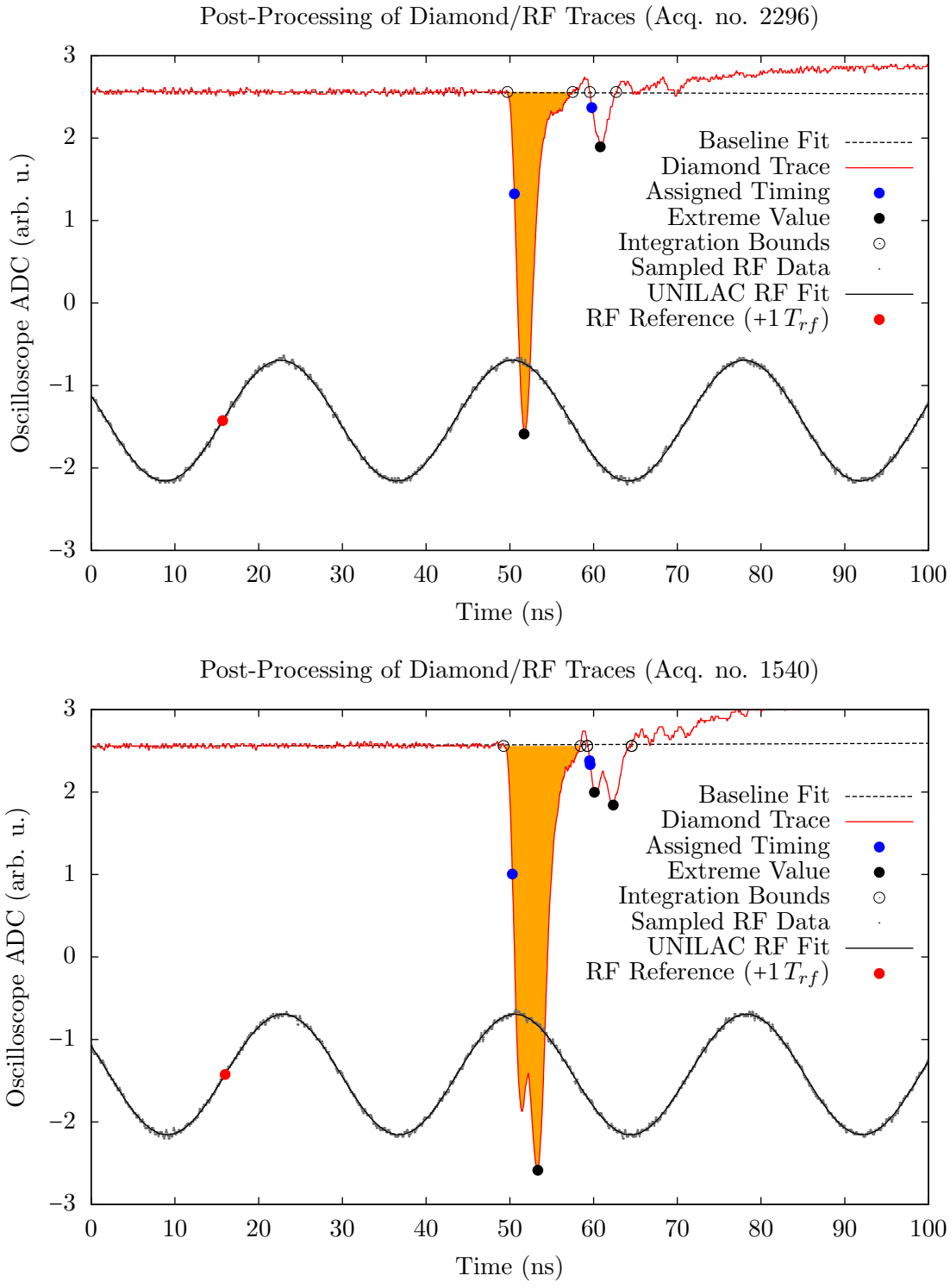

Fig. 4.9: Exemplary recordings of Ar^{14+} particle hits at the mono-crystalline diamond detector (20 GS/s, 2000 samples per trace). The red trace represents the sampled diamond pulse data. At the lower part of each plot the simultaneously sampled UNILAC RF is shown along with the corresponding fit of a sine. While the top plot shows a single particle hit from the centre of phase space, the bottom plot shows one of the rare case of two events occurring within a single bunch. Determined timing values are given in the legend.

RF Reference. Similar to the TOF setup, the arrival time at the diamond detector, with respect to a defined RF zero-crossing, is a measure of the ion phase. To obtain the RF reference timing, the RF is sampled along with the diamond trace. This allows to perform a fit of the sampled RF data to a general sine parameterisation. Once the fit parameters have been determined the zero-crossing at positive slope can be extracted straightforward. The corresponding, well-aligned, fit and assigned timings are plotted in Fig. 4.9 (see legend). By leveraging the fit to the regular RF, an accuracy of better than 10 ps is achieved.

Baseline Restoration. Determination of pulse heights and pulse integrals depend on a well defined baseline. In particular, pick-up of unwanted signals may result in a varying baseline. As it is not always possible to screen those contributions, it is advisable to perform a baseline restoration on each pulse acquisition. A linear fit using the first 45 % of samples of the diamond trace is used to determine the baseline reference. The restored baseline is given by the dashed line in Fig. 4.9. An overview of the fit parameter *offset* and *slope* is presented as a scatter plot in Fig. 4.10.

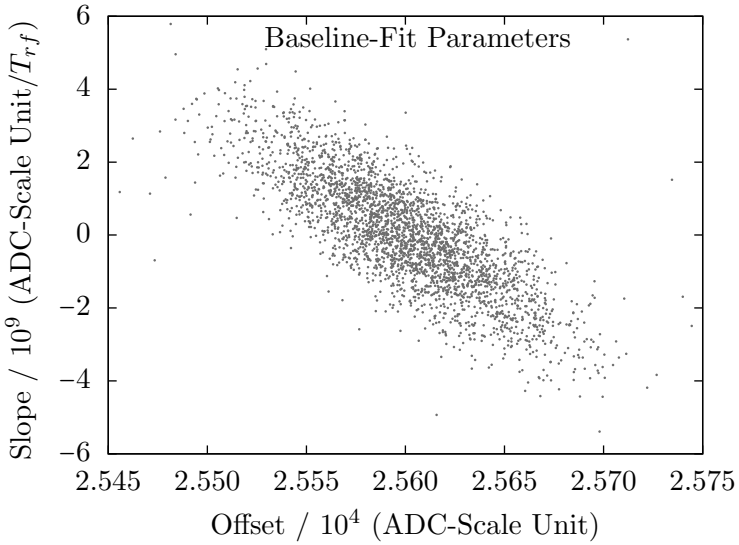

Fig. 4.10: Scatter plot of the Ar^{14+} baseline-fit parameters.

Pulse Properties. With restored baselines, crucial properties of the pulse event can be determined. This includes the peak-value index (sample index), which provides the pulse height with respect to the baseline. Furthermore, integration bounds are determined by storing the indices of the signal when it crosses the baseline. Subsequently, integration is performed with respect to the restored baseline within these limits. Finally, the pulse timing is extracted at a fixed fraction of the pulse height on the rising slope. A 30 % level has been used throughout all presented data. The determined values, as well as the pulse-integral area, are provided for all data traces. For completeness, the custom program drops all reflected pulses and checks for overlapping pulses. Overlapping pulses are marked *tainted*. This provides the option to automatically exclude double-hit events. Nonetheless,

double-hit events turned out to be a good way to judge the linearity of the pulse-integral response.

Pulse-Height/Pulse-Integral Trend. The pulse height of the Ar^{14+} measurement vs. the acquisition index is plotted on the left side in Fig. 4.11. The gap between $\approx -0.5 \times 10^4$ and 0 originates from the trigger threshold, manually set at the oscilloscope. A clear trend towards smaller pulse-heights is apparent. This means that irradiation, at least in this

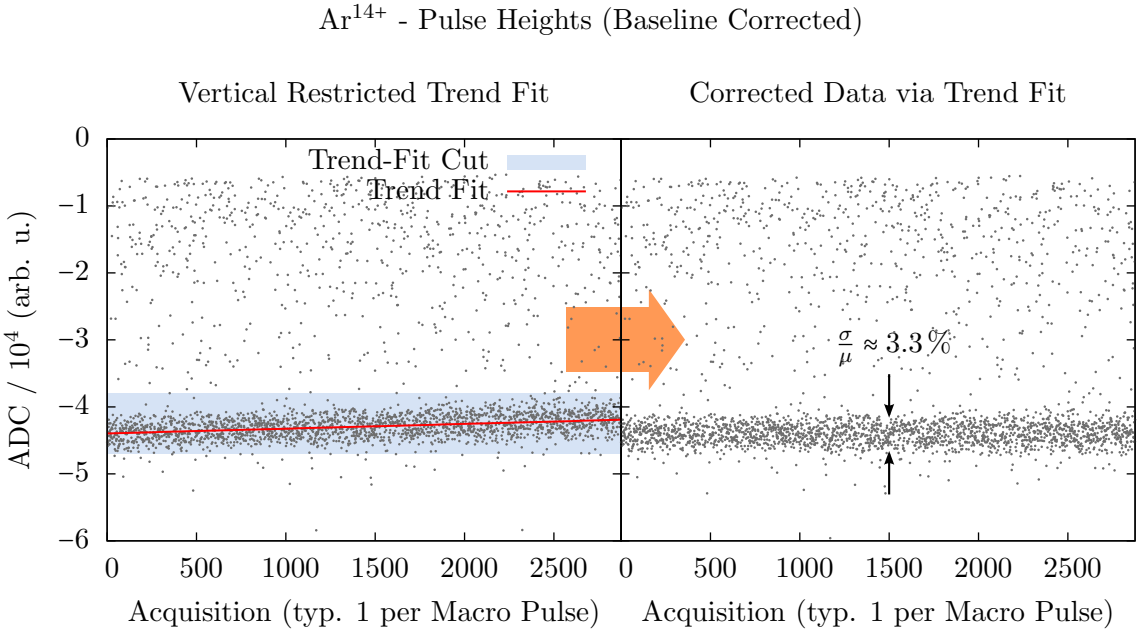

Fig. 4.11: Left: Baseline-corrected pulse-height vs. progressional acquisition number of an Ar^{14+} beam. Additionally, the linear trend fit of the phase-space core region is given by the read line together with the light-blue region which denotes the particles included in the linear fit. **Right:** Data corrected by rescaling with respect to the corresponding trend fit.

experimental configuration, has an effect on the response of the detector. A linear fit to the core region is used to rescale the measured data. The fit region is marked by the light-blue band, whereas the fit is given by the red line, parameterised by the slope s_h and offset o_h. Assuming a sufficiently linear systematic, correction of the pulse-height data is performed according to the linear fit parameters[8]

$$t_h(n) = s_h \cdot n + o_h, \tag{4.11}$$

with n being the continuous acquisition number. Hence, the rescaling factor $c_h(c)$ of pulse-height n is trivially given by

$$c_h(n) = \frac{o_h}{t_h(n)}\,. \tag{4.12}$$

[8] Index "h" references the pulse **height**.

The rescaled data is plotted on the right side of Fig. 4.11. A gain loss of ≈ 4.9 % of the last event (acq. 2876) emphasize the impact of the irradiation on the pulse height. The total amount of ions reaching the diamond detector during the measurement was about 10^5 only. Above the densely populated band at $\approx -4.4 \times 10^4$, which marks the core region of the phase space and is connected with the expected mean energy ≈ 1.4 AMeV, many events of smaller pulse height are apparent. These events will be discussed in Chapter 5. The core region, using the baseline and trend corrected pulse-height information, features a relative width of $\sigma/\mu \approx 3.3\,\%$ as denoted in Fig. 4.11. The fraction of the standard deviation σ with respect to the mean value μ provides a qualitative measure of the energy resolution.

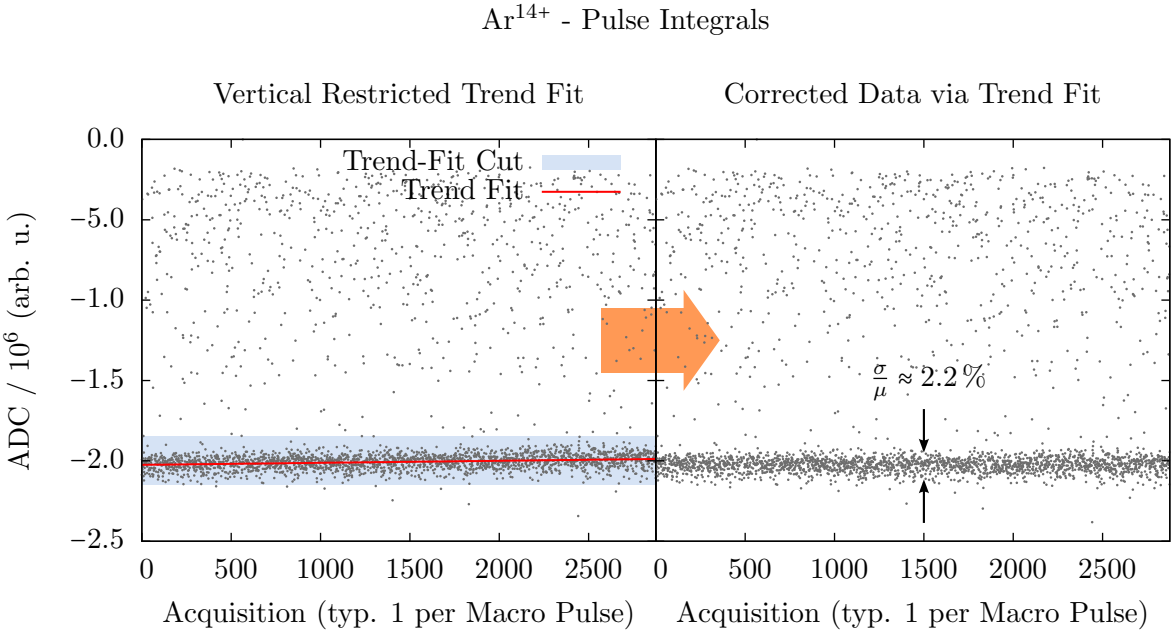

Fig. 4.12: Left: Pulse integral vs. progressional acquisition number of an Ar^{14+} beam including the linear trend fit. **Right:** Data corrected by rescaling with respect to the corresponding trend fit.

In contrast, the left side of Fig. 4.12 shows the pulse-integral data plotted versus the acquisition number. Similar to the pulse-height values, the trend of the pulse-integral values is determined by a linear fit within a narrow band around the core region. Rescaling of the data is provided by the same scheme according to Eq. (4.12). It is evident that the pulse-integral response is also affected by the irradiation of the diamond material in this experimental configuration, but at a lower impact. The effect is significantly smaller compared to the pulse-height behaviour at irradiation, with a gain loss of only 1.8 % at the last recorded event. On the right side of Fig. 4.12, the corrected data is shown. Comparison of the pulse-height data clearly shows a smaller relative width of the core band for the integral approach with ≈ 2.2 %. This suggests a higher energy resolution for the pulse-integral measurement. While it is clear that integrating over the sampled pulse reduces the effect of the quantised, effective ADC resolution and additional noise, it may also hint the presence of different pulse shapes. As will be shown in Chapter 5, MC diamond pulses can be grouped

into different classes. Only the baseline and gain-loss corrected pulse-integral information are used in the following.

Phase-Space Equivalent Representation. Using the trend-corrected integral values of the pulses, it is possible to plot the longitudinal phase space. The left side of Fig. 4.13 shows the trend-corrected integral values with respect to the sequential acquisition number, also including the rare double hits. On the right side, events are reordered with respect to the arrival time. The double-hit events give rise to integral values of about twice as big as those from the phase-space centre. This supports a linear calibration scale for this experimental configuration. It should be noted that this is not necessarily a general characteristic. The double-hit event marked by the arrow is associated with the traces in the lower plot of Fig. 4.9.

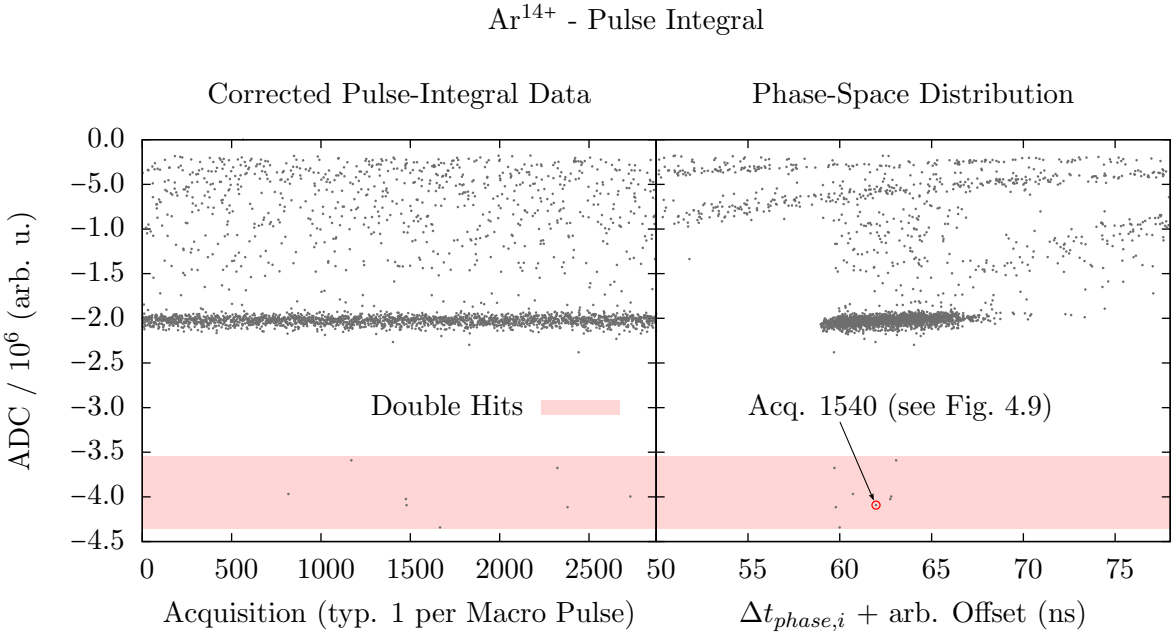

Fig. 4.13: Left: Trend-corrected pulse integral vs. progressional acquisition number. Double particle hits occur inside the light-red band. **Right:** Events ordered with respect to the arrival time as a phase-space equivalent representation.

4.3 Data Analysis

The preceding sections dealt with the electronic DAQ setups and offline reconstruction of the recorded longitudinal phase-space events. This section presents the data analysis in detail. The data analysis has been developed using the ROOT C++ framework [64].

Characterisation of the measured phase-space is typically provided by the determination of the covariance matrix, from which, as described in Sec. 2.3, the RMS emittance is derived.

Thereby the most important statistical parameters, such as location, spread and covariance are extracted.

Classical location estimates and in particular variances are very sensitive to outlying events. This means that even a small fraction of outlying events can have a huge negative impact on the estimates. More advanced estimators exist which show a reduced sensitivity on outlying events. As will become apparent, the measured data contains outliers from different contributions. A consistent approach for determination of the variance-covariance matrix in the presence of outliers will be presented which does not rely on manual cuts.

4.3.1 Robustness of Estimators

Determination of covariance matrices can be challenging for different reasons:

- Low event count
- Contaminated data
- Systematic contributions
- Low robustness of estimators

Incomplete sampling of distributions is inherently connected to statistical uncertainties of derived values by means of so-called estimators. This is also true in case of an idealistic system where the underlying distribution can be sampled without background or systematically disturbing contributions. For example, the estimator of the univariate mean

$$\langle x \rangle = \frac{1}{n} \sum_{i=1}^{n} x_i \tag{4.13}$$

has a well-known statistical uncertainty (1-sigma) of

$$\Delta\langle x \rangle = \frac{\sigma_x}{\sqrt{n}}\,, \tag{4.14}$$

depending on sample standard deviation σ_x and sample size n. The estimator for the standard deviation

$$\sigma_x = \frac{1}{n-1} \sum_{i=1}^{n} (x_i - \langle x \rangle)^2\,, \tag{4.15}$$

in contrast, is connected with a statistical uncertainty (1-sigma) of

$$\Delta\sigma_x \approx \frac{\sigma_x}{\sqrt{2(n-1)}} \tag{4.16}$$

in good approximation ([65], p. 133). Hence, in this idealistic case, confidence intervals can be contracted by increasing the number of recorded events.

Practically, it may not be always possible to record a large number of events as is the case with the experimental setup at hand (typically about 10^4 events). While this already imposes an uncertainty of the estimated statistical moments, the situation is more difficult

considering the influence of disturbing effects, such as outliers, as listed above. Recordings can be contaminated with data that does not reflect real phase-space events. For example, in very rare cases ($\ll 1\,\%$), uncorrelated events are considered coincident, using the TOF setup, resulting from detector efficiencies or missed trigger thresholds. Most of these artificial events can be discarded. Trivially, unphysical events which would be faster than light are easy to filter, while for other coincidences it is difficult to impossible to differentiate between sane data and artefacts. Still, the majority of the unwanted overlaying distributions are of physical systematic origin which will be covered in Chapter 7. The differentiation between contamination and general systematic effects is made to highlight the different characteristics of superimposed distributions and systematic contributions from which all events are affected. An example for the latter are the foils mounted in the setup. All recorded ions are passing the tantalum and aluminum foil. Hence, dissipative contributions are unavoidable and give rise to an energy spread which affects all particles. In contrast, systematic contributions which lead to contamination affect only a fraction of the recorded events. For example scattering at the high-current slits or collimator apertures can be classified as contaminating effects as only a fraction of the bunch is affected. Nevertheless, while contamination is of systematic origin, not all systematic effects are considered contamination.

Classical estimators, as mentioned above, are extremely sensitive to even individual outlying, "bad", events. A quantitative measure of the sensitivity is usually determined by the *(empirical) influence function* (E)IF, whereas the *breakdown point* defines the fraction of bad observations which are sufficient to result in estimations which can potentially rise beyond all limits. For the definitions of the (E)IF and breakdown point, see [66]. In particular, the classical estimators for the mean and standard deviation, Eq. (4.13) and Eq. (4.15), provide a breakdown point of 0, which means a single outlying event potentially can significantly distort the estimation of the respective statistical moment. It is therefore evident that the recorded data must be processed before applying a classical estimator can provide meaningful results. A common approach is trimming data points, either manually or by defining cuts, usually judged by "experience". When data points can be unambiguously identified as *outliers*, manual trimming is straightforward. Obviously, this is only consistently possible if contaminations are disjoint sets from the phase-space region of interest. Otherwise, manually defined cuts, and consequently estimated values in case of non-robust estimators, can vary significantly between different persons evaluating the raw data.

A defined set of rules is crucial when analysing the recorded data. Objectivity is of major concern when it comes to a consistent approach of data evaluation. This is a precondition to warrant reproducibility, in particular, given low event counts, contamination and systematic effects as stated above.

Well-established methods for consistent evaluation of phase-space scatter data are rare. Common scenarios deal with systematic background models assuming a flat bias and noise figure, typically originating from current amplifiers present in various types of (transverse) phase-space diagnostics. Such data sets are often treated by successively subtracting a constant amount from all bins, setting resulting negative values to zero, while monitoring, for example, the emittance value. A good approximation to the "real" values is considered when corresponding gradients change significantly, interpreted as a feedback on when the actual signal is affected by the flat subtraction. This defines the %-intensity level with

respect to the total, accumulated amount of content which has been subtracted. In contrast, an advanced and widely accepted approach for such scenarios is called SCUBEEx [67]. This method accounts for the fact that noise contributions average out when integrating regions with no signal by variation of exclusion ellipses which eventually define a consistent core region. Since neither the TOF setup nor the setup using a mono-crystalline diamond detector features a bias/noise floor in that sense, the previously mentioned methods, in especially SCUBEEx, to analyse the recorded data are ill-suited for the experimental setup at hand.

An exemplary histogram of $^{40}Ar^{10+}$ events is shown in Fig. 4.14. The data, recorded using the TOF setup, contains an exceptionally high amount of $\approx 6 \times 10^4$ events and allows to highlight the main characteristics. It is apparent that the data features no flat noise floor.

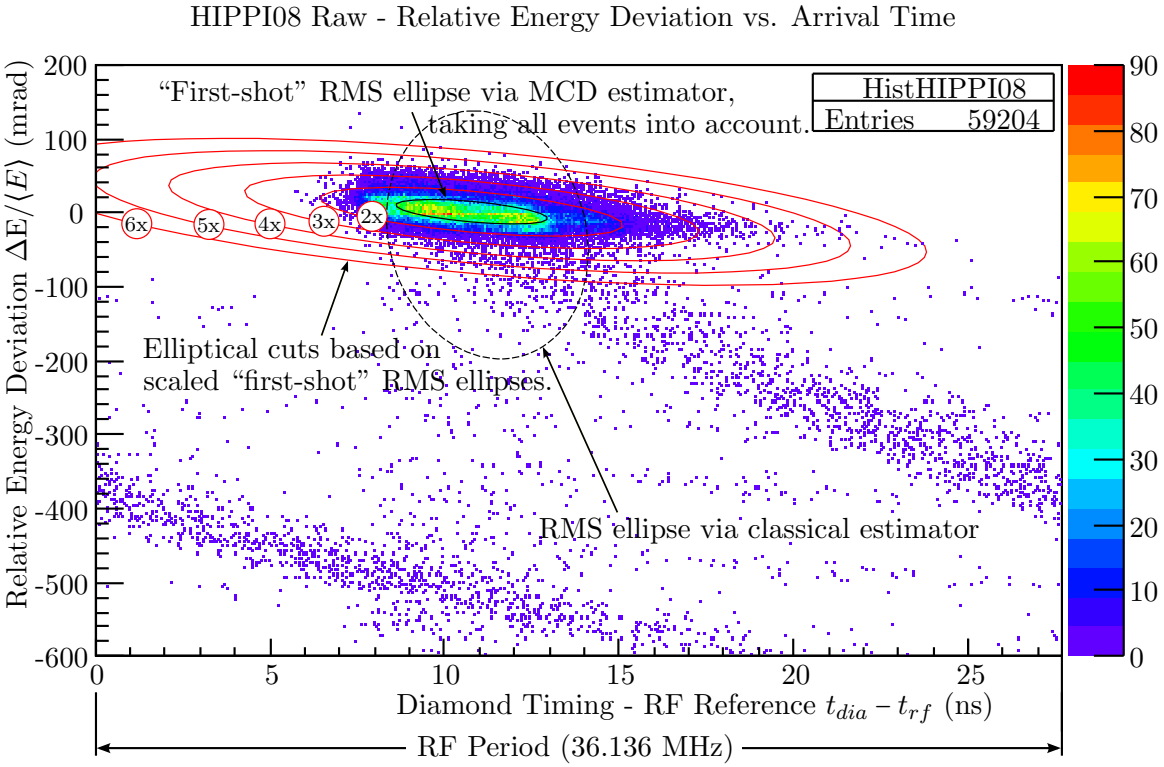

Fig. 4.14: Exemplary $^{40}Ar^{10+}$ phase-space data recorded during the HIPPI [62] campaign 2008. The phase-space region of interest is located where the red ellipses are plotted.

Instead, prominent contamination in terms of trails need to be taken care of. They are of systematic origin and will be discussed in the next chapter. The actual phase-space region of interest, i.e. the longitudinal phase-space when the ions enter the setup, is located where the elliptical shapes are plotted. While the residual events are, effectively, real phase-space events, they are introduced by the measurement process. Hence, they must be excluded from entering in the covariance matrix in a consistent way to keep contamination of the covariance matrix, by spurious events, as low as possible. Methods that are aimed at providing robust estimates in the presence of outliers are called *robust estimators.* Such a

robust estimator, the Minimum Covariance Determinant (MCD) estimator, will be used in this work and is introduced in the next sections.

4.3.2 Minimum Covariance Determinant Estimator

As mentioned above, using the classical covariance and location estimators would require a biased preparation of the raw data by means of manually set cuts to exclude spurious data. Evaluation of measured data, such as shown in Fig. 4.14, can only be consistently accomplished if an estimator with a high breakdown point is used. An alternative quantitative approach used in this work is the so-called *Minimum Covariance Determinant* (MCD) robust estimator for multivariate data, which was first proposed in 1985 by Rousseeuw [68]. MCD is a variant of the *Minimum Volume Ellipsoid* (MVE) concept proposed in the same report. Both concepts are based on the idea to only take into account a fractional subsample size[9] α_{mcd} of the original data containing n points, with $1/2 \leq \alpha_{mcd} < 1$. By minimizing either the smallest ellipsoid covering all data points (MVE) or the variance-covariance matrix determinant (MCD) over all possible subsamples for a given fraction α_{mcd}, a robust estimate of the location and scatter is provided. To ensure consistency in case of multivariate normality, the covariance matrix is multiplied by a correction factor depending on α_{mcd}. For bivariate cases, in particular the longitudinal subspace, the determinant of the variance-covariance matrix C writes

$$|C| = \begin{vmatrix} \sigma_{xx} & \sigma_{xy} \\ \sigma_{xy} & \sigma_{yy} \end{vmatrix} = \begin{vmatrix} \sigma_x^2 & \sigma_{xy} \\ \sigma_{xy} & \sigma_y^2 \end{vmatrix} = \sigma_x^2\sigma_y^2 - \sigma_{xy}^2 \stackrel{!}{=} \varepsilon_{rms}^2 \,, \tag{4.17}$$

and thus equals the square of the RMS emittance ε_{rms}. Since the square function is a strictly monotonic function, the MCD algorithm effectively minimizes the estimated RMS emittance. Hence, in case of a bivariate distribution this can be interpreted as minimising the ellipsoidal area.

Roderich Keller et al. [69] used a method similar to MVE, to successfully analyse transverse phase-space data of small size. Calculation of the MVE and MCD, even for bivariate data, is combinatorially expensive which practically limits the reasonable size of the data. According to Rousseeuw [68], MCD is favourable over MVE, due to its higher statistical efficiency and higher accuracy. In case of MCD, a more efficient algorithmic approach exists, proposed by Rousseeuw et al. [70] in 1999, often referred to as FAST-MCD. It allows to calculate MCD multivariate location and variance-covariance matrices even for large data sets.

The data analysis in this thesis is based on the ROOT C++ framework [64] that includes an implementation of the FAST-MCD algorithm [71]. Unfortunately, benchmarks based on known bivariate Gaussian distributions revealed a significant mismatch between the variance-covariance matrix compared to the known parameterisation, which is not expected. While the values of variance-covariance matrix are flat for different values of α_{mcd}, which is favourable, they differed from the expected values by about $\approx 10\,\%$. This behaviour is unexpected and not in agreement with the MCD method. Consequently, this lead to the

[9] If the subsample size equals the size of the original data, i.e. $\alpha_{mcd} = 1$, the MCD approach delivers the values of the classical estimators. Depending on the implementation this is not always true due to partitioning of sizes of initial data above a certain threshold (typically 600 points).

decision to not use the *TRobustEstimator* implementation. Instead, this work uses the R (*The R Project for Statistical Computing*) [72] implementation of FAST-MCD which directly interfaces the FORTRAN routine [73, 74] by the original authors P. J. Rousseeuw et al.[10] Additionally, the most recent correction factors for multivariate normality [76] are included in the R calling routines. Contrary to the ROOT implementation, the variance-covariance matrices of sampled bivariate Gaussian densities are reproduced as expected.

MCD on Actual Data. In the following, the values of the MCD estimator are compared to those of the classical estimator using the phase-space data shown in Fig. 4.14. Elliptical cuts are systematically generated to monitor the impact of event exclusion on the MCD and classical estimator. A "first-shot" ellipse is acquired from the MCD estimator with $\alpha_{mcd} = 0.75$. Typically, this already provides a good estimate of the covariance matrix and its location of the phase-space region of interest where most events agglomerate. Table 4.1 lists the scatter values computed via the classical estimator and those of the "first-shot" variance-covariance matrix ($\alpha_{mcd} = 0.75$). Apart from the phase location $\langle x \rangle$ all other values in Tab. 4.1 differ significantly between the classical and robust estimator. While the classical estimator for the bunch length σ_x is larger by about 30 %, the measure for the energy spread σ_y is larger by more than a factor of five in case of the classical estimator. The magnitude of the covariance σ_{xy} is larger using the classical estimator due to the long-ranged trails. For the same reason, the location of the energy centre and the RMS emittance differ significantly between the classical and robust estimator. The classical estimator of the RMS emittance is larger by more than a factor of seven. This clearly shows that even with a pronounced fraction of contamination the MCD estimator provides a reliable, robust estimate of location, size and orientation, as can be seen from Fig. 4.14. The "first-shot" ellipse is well-aligned in the core phase-space region, although only one parameter, α_{mcd}, has been specified.

Tab. 4.1: Comparison of MCD ($\alpha_{mcd} = 0.75$) and classical estimator without event exclusion on the HIPPI [62] 2008 data, as seen in Fig. 4.14. The MCD values of location and scatter are referred to as "first-shot" RMS ellipse. For a better readability $x = t_{dia}$ and $y = \Delta E/\langle E \rangle$ has been substituted.

Estimator "first-shot"	σ_x (ns)	σ_y (mrad)	σ_{xy}	$\langle x \rangle$ (ns)	$\langle y \rangle$ (mrad)	ε_{rms} (mrad·ns)
MCD	2.08	17.08	-17.84	10.80	0.48	30.72
Classical	2.71	91.39	-66.01	11.09	-19.48	238.70

Estimators using Different Cuts. Study of the influence of different cuts on the estimators has been performed in a consistent way. The cuts used to compare estimator values belong to a certain class of cuts. It is sensible to use elliptical cuts which are generated from scaled entities of the "first-shot" covariance matrix with a common centre location. The core

[10] The R framework is interfaced by C++ using RInside [75] by D. Eddelbuettel et al.

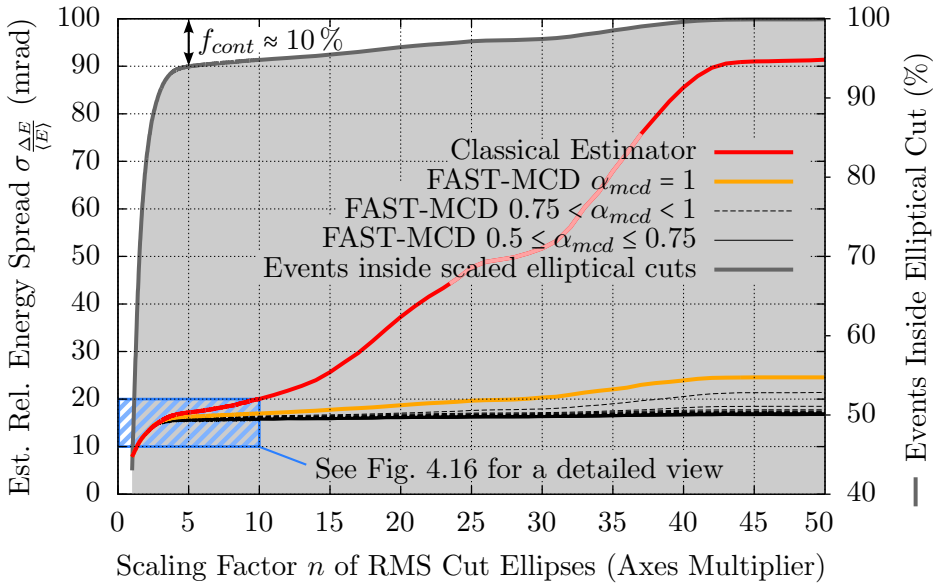

Fig. 4.15: The plot shows the classical estimator (red line) and robust MCD estimators (black dashed and solid lines) for the standard deviation of the relative energy deviation acting on real data (HIPPI [62], 2008). The horizontal axis denotes the scaling factor of the "first-shot" covariance matrix used to define automated cuts.

phase space of interest is automatically located well by the MCD algorithm. Furthermore, scaling of the covariance matrix makes it easy to define a reasonable region of interest (ROI). Linear scaling of both semi axes by a factor of n equals scaling of the covariance matrix by n. At the same time the emittance scales by a factor n^2. The first six ellipses, the black "first-shot" ellipse and the red ellipses with scaling factors 2 to 6 (see labels), are plotted in Fig. 4.14.[11] Classical and robust MCD[12] estimator values $\sigma_{\Delta E/\langle E \rangle}$ corresponding to cut ellipses of different size are plotted in Fig. 4.15 with respect to the scaling factor n. Additionally, the fraction of total events inside the cuts is represented by the grey line. The fraction grows fast until it reaches a quasi plateau of lower gradient at a cut-scaling factor of ≈ 5. For this cut ellipse, the area is 25 times the size of the "first-shot" ellipse and includes $\approx 90\,\%$ of all events. In other words, as denoted in Fig. 4.15, $f_{cont} \approx 10\,\%$ of all recorded events contribute to the contamination located in the long-ranged trails in this measurement. This assumption agrees with the elliptical cuts plotted in Fig. 4.14, i.e. at a scaling factor of 4-5, the cut region encloses the phase-space distribution of interest. Further scaling to larger cut regions mostly accumulate events from contamination by means of the prominent trails. As expected, the classical estimator (red line) has a strong dependency on the cut size with no obvious cut scaling that allows for a meaningful evaluation.[13] In contrast, the robust MCD estimator data shows a significantly lower dynamics above cut

[11] Given scaling factors in this section refer to the linear axis scaling.

[12] MCD estimators are evaluated for α_{mcd} in the range $0.5 \leq \alpha_{mcd} \leq 1$ at a step size of 0.025.

[13] The intermediate plateau of lower gradient at cut scalings between 25-30 is an artefact which is due to the wrapped phase information with respect to the RF period as seen by the trails in Fig. 4.14.

scalings ≈ 5. Only estimations which exclude less than the fraction of contamination, i.e. $\alpha_{mcd} \gtrsim 0.9$ in this measurement, are prone to deviate from the otherwise stable band at larger cut scalings.

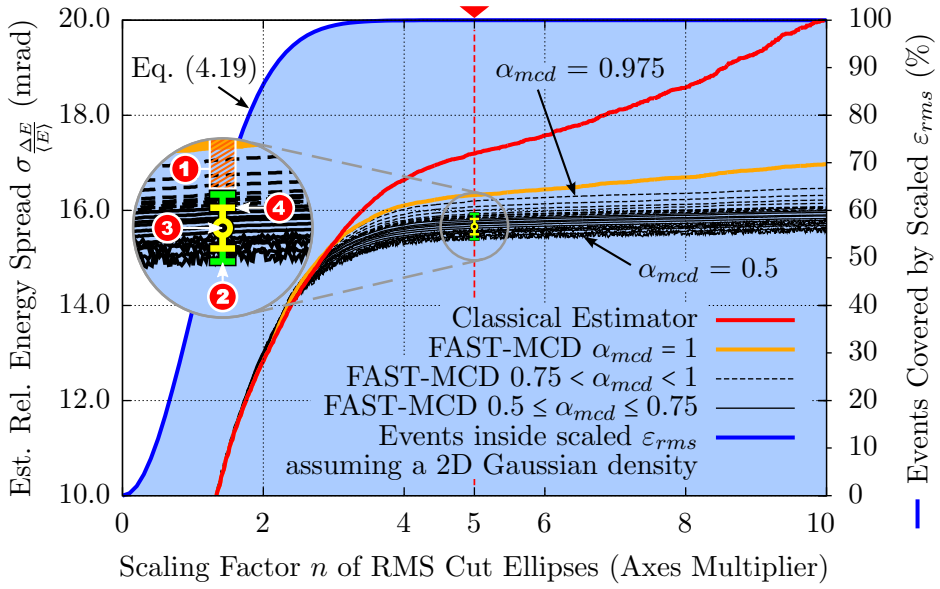

Fig. 4.16: This plot refers to the same data of the estimators as Fig. 4.15 at a different viewport. The blue line represents the *theoretical* fraction of particles inside the scaled elliptical cuts, by taking a 2-dimensional Gaussian distribution as reference which is parameterised by the "first-shot" covariance matrix. Values provided by the robust estimators are drawn dashed for sub-sample fractions $0.75 < \alpha_{mcd} < 1$ and solid from $0.5 \leq \alpha_{mcd} \leq 0.75$. Evaluation is carried out at a cut scaling of 5. A magnified view of the evaluation region is provided on the left and is explained in the text.

A magnified plot, as marked by the blue rectangle in Fig. 4.15, is shown in Fig. 4.16. Compared to the classical estimator, a band of MCD estimators using different α_{mcd} displays a very low gradient for cut scalings of $n \gtrsim 4$. Additionally, the blue line represents the fraction of events inside the scaled "first-shot" ellipse, assuming a bivariate Gaussian density distribution. The corresponding functional relation between the fraction f of events inside the scaled "first-shot" ellipse only depends on the determinant of the variance-covariance matrix and, thus, the RMS emittance ε_{rms}. By means of the scaled emittance $\varepsilon(f)$ this relation is given in [1] (p. 68)

$$\varepsilon(f) = -2 \ln(1 - f)\, \varepsilon_{rms}\,. \tag{4.18}$$

If the scaling is parameterised by $\varepsilon(f) = n^2_{(f)}\varepsilon_{rms}$, Eq. (4.18) yields the fraction f in terms of the scaling multiplier n

$$f = 1 - \mathrm{e}^{-\frac{n^2}{2}}\,, \tag{4.19}$$

which is represented by the blue line in Fig. 4.16. Effectively all events (> 99.9 %) are enclosed at a cut scaling by a factor of $n = 4$ under the assumption of a bivariate distributed phase-space region of interest. Although this assumption is only a rough model to realistic phase-space distributions, it agrees with the cut scaling $n \gtrsim 4$ where the band of MCD estimator reaches a low-gradient quasi plateau. This suggests, with a small margin, evaluation and comparison of the estimators at a cut-scaling factor $n = 5$ as a consistent rule.

Evaluation and Error Bounds. The FAST-MCD estimator routine has been evaluated for subsample fractions $0.5 \leq \alpha_{mcd} < 1$ at a step size of 0.025. For non-Gaussian distribution this leads to an unavoidable spread of the calculated values which is clearly visible by the resulting band. In this example, values increase with increasing α_{mcd}. A magnified view of the point of evaluation at $n = 5$ is shown on the left of Fig. 4.16. The hatched interval (1) defines the range of α_{mcd} which is excluded from the final evaluation. According to Rousseeuw et al. [70], choosing $\alpha_{mcd} = 0.75$ is a good compromise between breakdown value and statistical efficiency if contamination f_{cont} is lower than 25 %. However, even when contamination is lower than 10 %, as it is the case at the discussed cut scaling $n = 5$, α_{mcd} should not exceed 0.9. For subsample sizes close to 1, the break down value drops significantly, which effectively means the estimator loses robustness. As a general rule, setting $\alpha_{mcd}^{max} \leq 1 - f_{cont}$ is reasonable. The green bounds (2) mark the range of included α_{mcd} values of subsample sizes. In good approximation, the corresponding estimator values v are uniformly distributed for constant step sizes of α_{mcd}.[14] This allows to determine the centre of the evaluated range (3) by taking the arithmetic mean of the bounds (2)

$$\langle v \rangle_{uni} = \frac{v_{min} + v_{max}}{2} \,. \tag{4.20}$$

The spread is interpreted as the statistical uncertainty and consequently the standard deviation (4) is extracted via the standard deviation of uniform distributions

$$\sigma_v^{uni} = \frac{v_{max} - v_{min}}{\sqrt{12}} = \frac{v_{max} - \langle v \rangle_{uni}}{\sqrt{3}} \,. \tag{4.21}$$

This approach allows to extract a target value $v \pm \sigma_v$ based on a defined set of rules and statistical uncertainty σ_v. Exemplary values for the phase-space data in Fig. 4.14 are listed in Tab. 4.2. The table lists the classical and MCD estimator values at a cut scaling of $n = 5$, including both, the variance-covariance matrix elements, location estimates and the derived RMS emittance. As it is possible to define a measure for the statistical uncertainties in case of the MCD method, as described above, those are also listed together with the corresponding relative uncertainty where meaningful. Estimator values evaluated according to Eq. (4.20) deviate by less than 1 % compared to the approach of taking all estimators into account within the bounds (2) and evaluating the arithmetic mean. Standard deviations, according to Eq. (4.21), deviate by less than 10 %. All MCD estimator values provided in this work incorporate the full set of estimators within the evaluation bounds. Nevertheless, Eq. (4.20) and Eq. (4.21) are typically very good approximations which could be used likewise.

[14] The estimator v is a placeholder for any location and scatter parameter accessible by the MCD routine.

Tab. 4.2: MCD estimator values for the data shown in Figs. 4.14 - 4.16. For a better readability x refers to the arrival time t_{dia} (ns) and y refers to the relative energy deviation $\frac{\Delta E}{\langle E \rangle}$ (mrad).

SFSE $n = 5$	**Classical**	**MCD**		
Cut Scaling	**Estimator**	**Estimator**	**Std. Dev.**	**Uncertainty**
σ_x (ns)	1.88	2.00	0.04	2 %
σ_y (mrad)	17.19	15.67	0.14	1 %
σ_{xy}	−14.16	−16.57	0.70	4 %
ε_{rms} (mrad·ns)	29.04	26.60	0.13	0.5 %
$\langle x \rangle$ (ns)	10.88	10.80	$\ll 10^{-2}$	-
$\langle y \rangle$ (mrad)	1.13	0.21	0.20	-

At the given cut scaling, comparison of both estimators features no distinct outlier. While all values are close, the energy spread σ_y is smaller in case of the MCD, as can be also seen from Fig. 4.16. This shows a typical and appreciated behaviour since the influence of the contamination, in particular the trails, is damped using the MCD over the classical approach. At the same time, the covariance σ_{xy} is higher for the same reason. The standard deviations of the scatter estimators are in the order of only few %. The more the region of interest deviates from a bivariate normal distribution, the larger the relative width of the bands and, thus, the uncertainty will be. In case of ideal bivariate Gaussian distributions and disjoint contamination, the relative spread between estimators using different α_{mcd} effectively completely contracts.

Calculation of Robust Estimator Values. It is now possible to define a procedure for the determination of estimator values. This procedure will be consistently applied to measured data presented in this work.

- The MCD algorithm is used to determine the first-shot ellipse (FSE) at $\alpha_{mcd} = 0.75$.[15]
- The FSE is scaled by $n = 5$ and serves as geometric cut parameterisation, denoted as *scaled first-shot ellipse* (SFSE).
- The MCD algorithm is applied again on the data contained in the SFSE.
- This is done by sampling robust estimator covariance matrices and centre locations with α_{mcd}-values from 0.75 to 0.9 at a step size of 0.05.
- As described in the previous paragraph, the average values and uncertainties of the covariance-matrix data and centre locations are calculated from the set of covariance matrices for the α_{mcd} range. This is also done for the RMS emittance and Twiss parameters, being derived parameters from the covariance matrix.

[15] In case of very high contamination, larger than 25 %, manual discarding of most outlying events may be required until the contamination is reduced below this threshold. Alternatively, the value of α_{mcd} can be lowered down to $\alpha_{mcd} = 0.5$ for the first-shot ellipse.

Final Remarks. When comparing the classical and MCD estimator applied to contaminated data, the advantage of robust estimators, such as the MCD estimator, is evident. Table 4.1 highlights the expected deviation from the classical and robust estimator. The RMS emittance is larger in case of the classical estimator by more than a factor of seven. On the other hand, location, size and orientation of the robust estimate does not significantly change under various cut conditions, as long as the core phase-space distribution is included entirely. This provides an improved procedure compared to the usage of the classical estimator which require trimming, i. e. manual, biased exclusion of events. While Fig. 4.16 may suggest to apply the classical estimator under a defined cut scaling, for example $n = 5$, and discard the MCP approach, this is not possible. The "first-shot" ellipse already strictly relies on the robust MCD routine.

4.4 Additional Information Provided by the TOF Setup

As outlined in Sec. 4.1.2, the TOF setup DAQ also records the macro-pulse start timing provided by the VME-timing module. The overflow-corrected timing is known precisely relative to the macro-pulse start timing which allows to access further information beyond the plain longitudinal phase-space.

4.4.1 High-Resolution Macro-Pulse Structure

The high-resolution macro-pulse structure information provides further information about the state of the ion source and the real macro-pulse duration. This is achieved by histogramming the bunch number at which an event occurs, with respect to the start of the macro-pulse timing and can be considered to provide similar information than a high-resolution beam-current transformer. Two exemplary macro pulses are shown in Fig. 4.17.

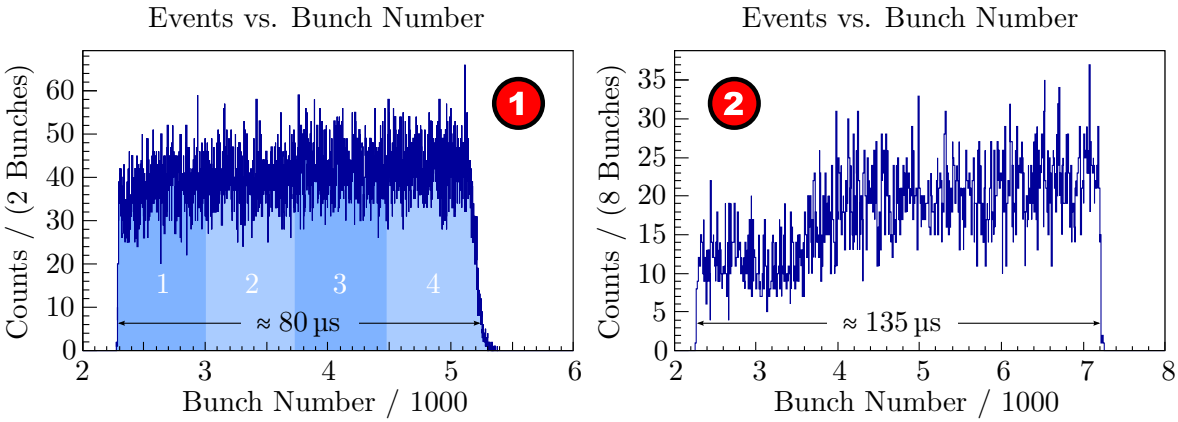

Fig. 4.17: Exemplary macro-pulse structures extracted from different TOF recordings.

Both macro pulses belong to different argon measurements. Despite from the shorter macro-pulse duration, recording (1) shows a more regular macro-pulse shape compared to recording (2). This information may hint a performance degradation of the ion source through aging or, less likely, unoptimised settings of the UNILAC RF.

4.4.2 Time-Sliced Phase Spaces

The data analysis of the TOF setup allows to select events inside a custom micro-pulse range. For example, the macro pulse ❶ in Fig. 4.17 features four sections, labeled 1 to 4. Each micro-pulse range cut represents a subset of the total phase-space distribution. The phase spaces can be evaluated separately and compared to each other. This requires a sufficiently large number of total events, depending on the range of the cuts.

The macro pulse ❶ corresponds to the argon data recorded during the HIPPI campaign in December 2008 as shown in Fig. 4.14. In a later section (see Sec. 5.2.4) these time slices will be analysed as the data set contains a relatively high amount of events ($\approx 6 \times 10^4$ events).

4.4.3 Event-Separation Statistics

The event statistics discussed in Sec. 3.4.5 can be verified by histogramming the separating time intervals between adjacent events recorded within the macro pulses. A typical histogram is shown in Fig. 4.18 together with a fit of to the expect distribution Eq. (3.15). The fit is in agreement with the data. At low time separations a "hole" is apparent, which

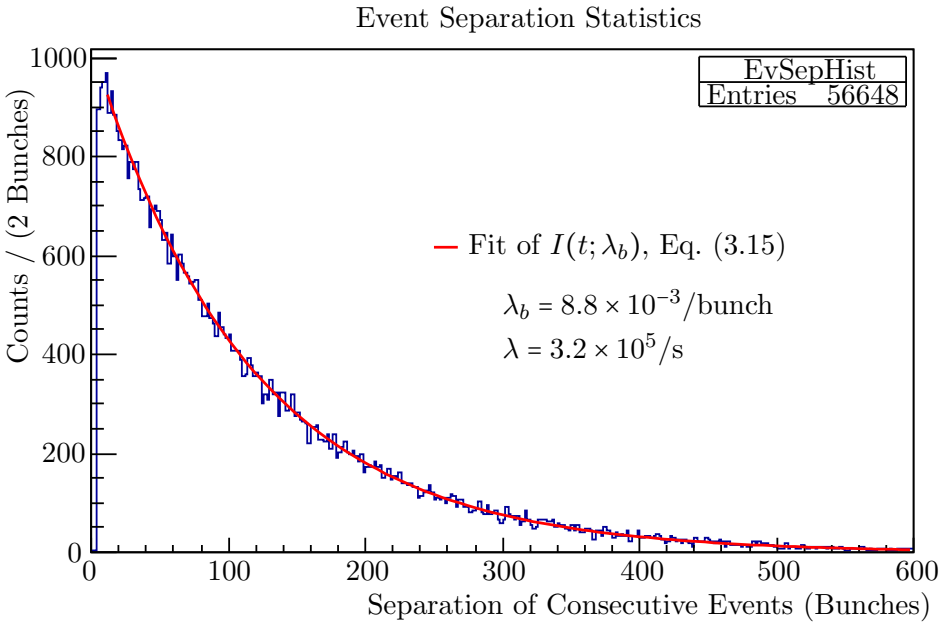

Fig. 4.18: Exemplary event separation histogram for the HIPPI 2008 data. The red line is a fit to Eq. (3.15).

is excluded from the fit range. This missing information is a result of the time window used to determine coincidence events at the MCP and diamond detector. Any multiple events occurring within the time span of the coincidence window are considered ambiguous and are discarded.

Chapter 5

System Tests and Measurements

The experimental setup described in this work cannot perform measurements simultaneously with other experiments which request beam from the high-current injector. Settings of the gas pressure and high-current slits at the stripper section, to attenuate the primary high-current beam, do not allow for selective adjustment of individual virtual accelerator targets. Hence, the global nature of the attenuation settings turn the experimental setup into an exclusive measurement. In the following, the measurement procedure and in particular the attenuation settings, will be outlined. The chapter continues with a discussion of selected data sets recorded using the TOF setup and closes with the first recorded data using the mono-crystalline-diamond detector setup.

5.1 Measurement Procedure

Typically a measurement comprises three parts.

- Find appropriate attenuation settings of the beam.
- Set parameters of measurement setup (TOF or MC diamond).
- Run data acquisition.

The TOF setup relies upon well-defined threshold settings for the MCP discriminator and to a lesser extent the threshold settings of the PC diamond discriminator. Furthermore, the supply voltages of the PC diamond detector and the MCP module are set via the DAQ frontend (see Sec. 4.1.3). In contrast, the MC diamond setup relies upon the supply voltage of the detector and appropriate vertical and horizontal range settings of the oscilloscope.

After the beam is attenuated and parameters are set, the modules are exposed to the beam via pneumatic feed-throughs and the data acquisition is started. Depending on the beam configuration, the targeted event count and measurement method, measurement times typically range between 15 minutes to several hours per phase-space recording.

Because of their importance, the attenuation procedures are covered, as well as the determination of the MCP discriminator values.

5.1.1 Attenuation Settings

As discussed in Section 3.4, reconstruction of the longitudinal phase-space distribution requires unambiguous single-particle coincidences in case of the TOF measurement. With the beam containing about up to 10^9 particles per bunch, a mechanism to attenuate the particle flux entering the device is strictly necessary. Otherwise, without a sufficiently diluted particle rate on the bunch time scale, most of the timing signals of the two detectors cannot be unambiguously connected to a certain event.

Furthermore, the heating power of the beam scales with the nuclear charge of the ion beam, the particles per unit time, the macro-pulse length and the thickness of the foils. Since fabrication processes do not allow for significantly thinner foil targets than those installed in the experimental setup, beam attenuation is strictly necessary to prevent the tantalum foil from melting. A common beam of several milliamperes at typical macro-pulse lengths would immediately destroy the thin foil.

Low-Current Beams. When measuring low beam currents, much smaller than 1 mA, space-charge effects during acceleration and transport of the ion beam, leading to emittance blow-up, are negligible. In this case it is feasible to attenuate the beam in front of the RFQ entrance (see Fig. 2.10) by using a transverse defocusing configuration at the quadrupole magnets. The imposed extended transverse beam spread leads to a reduced transmission due to the limiting transverse acceptance of the RFQ structure. This is a typical setting to provide a test environment for the measurement setup.

Intermediate- to High-Current Beams. At high-intensity beam currents of several milliamperes, space-charge effects play a major role. Non-linear space-charge forces result in an increasing emittance after a drift. Attenuation must therefore accomplished as close to the entrance of the measurement setup as possible. Otherwise, the reduced space charge would falsify the measured phase-space distribution.

Several methods are used in combination to achieve a well-adjusted incoming beam. The gas stripper (see Sec. 2.8 and Fig. 2.11), for generation of higher charge states, and the following chicane, for charge-state separation preceding the Alvarez structures, are leveraged to reduce the number of particles impinging on the tantalum foil down to several tens of microamperes. For a detailed technical drawing of the stripper/chicane section, see Fig. 3.4.

Depending on the ion species and beam intensity, individual settings are necessary for a well-adapted entrance current. Viable parameters, in case of high-intensity measurements, are the pressure of the gas jet (US2VK1), selection of a certain charge state via dipole adjustment (US3MK1) and slit settings (US3DS4/5). The pressure of the gas stripper affects the charge distribution after stripping, whereas the slits are used to geometrically shadow large parts of the beam close to the device entrance. Section 5.2.2 and 5.2.3 investigate the effect of the attenuation on the measured phase-space distribution.

5.1.2 MCP - Voltage and Discrimination Threshold

A crucial component of the achievable time resolution is the correct setting of discrimination thresholds which assigns timings to detector pulses. MCP signal shapes inherently feature a broad pulse-height distribution (see Sec. 3.3.1). Additionally, distorted rising edges have been experienced and will be discussed in 7.4.1. In order to decide on reasonable settings for MCP front voltage and discriminator thresholds, a measurement varying both parameters has been performed.

A stable low-current $^{40}Ar^{10+}$ beam served as test distribution. Under variation of discriminator thresholds and applied voltages to the MCP front side, the spread in TOF has been evaluated. Extraction of the covariance and mean values has been performed using the robust MCD estimator, according to Sec. 4.3.2. The evaluated data is shown in Fig. 5.1. Error bars reflect the statistical uncertainty of the robust estimator. A general trend to-

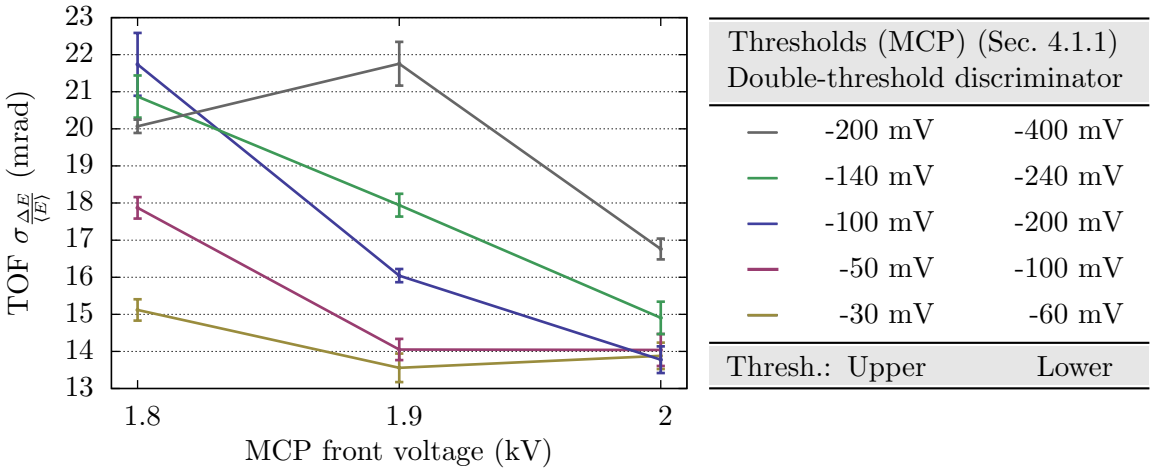

Fig. 5.1: MCP discrimination performance at different MCP front voltages and discriminator thresholds. The measurement is based on a low-current $^{40}Ar^{10+}$ beam.

wards measuring smaller TOF spreads at higher MCP front voltages is evident. The lowest three threshold configurations agree within the statistical uncertainty. Larger thresholds result in significantly larger measured energy spreads. Hence, it is reasonable to apply a MCP front voltage of 2 kV and keep thresholds at -100 mV/-200 mV (upper/lower threshold) or below. These settings define a stable operating region.

The poly-crystalline diamond detector, in contrast, features a significantly smaller pulse-height distribution, where a low threshold level above noise floor is reasonable.

5.2 Time-of-Flight Measurements

The following sections cover different TOF measurements aimed at testing several aspects of the presented measurement approach. This comprises the measurement of a longitudinal phase-space distribution which has been intentionally distorted by detuning of the IH RF-settings, in order to test the general sensitivity on the longitudinal phase-space, as well as

the influence of different pressures of the gas stripper on the measured data. Furthermore, the effect of the high-current slits, used for attenuation of the beam, is investigated. The TOF measurements conclude with a high-current argon measurement which was recorded as part of the HIPPI campaign supporting the GSI injector division.

5.2.1 Sensitivity on Different Phase-Space Distributions

This section investigates the sensitivity of the TOF setup on different phase-space distributions. A straightforward way to prepare significantly different phase-space distributions is detuning of the synchronous phase ϕ_s at the IH cavities. The test beam was a low-current $^{40}Ar^{10+}$ beam. Appropriate attenuation has been performed at the RFQ entrance using a defocusing setting of the quadrupole doublet, Before entering the stripping section a beam current of 10 µA was measured by current transformer US2DT5. After stripping this resulted in an entrance current of 20 µA. Furthermore, the gas pressure of the stripper was set to 2.8 bar, high-current slits have been open at ±15 mm (DS4) and ±5 mm (DS5).

Optimal phase settings for the IH cavities are calculated as a function of the ion mass to charge state ratio A/q. In case of Ar, reference phases are set to 189° at IH1 and 199° at IH2. Detuning of the last IH stage was performed in steps of 5° from 199° to 219°. As described in Sec. 2.5.3 and Sec. 2.6, KONUS beam dynamics is sensitive to the adjustment of the synchronous phase ϕ_s. By detuning the synchronous phase, significantly different phase-spaces are to be expected, in particular an increase of the emittance.

Figure 5.2 shows the two-dimensional distributions and the corresponding projected bunch structures. To be visually comparable, the ranges of the axes are kept for all phase-space distributions. The phase spaces are spanned by the relative energy deviation $\Delta E/\langle E\rangle$, with β = 5.5 %, versus the time arrival of the ion at the diamond detector t_{dia} with respect to the UNILAC RF t_{rf}. The orange symbol ● marks the MCD centre location of the phase space at reference phase 199° for comparison. Other phase-space MCD centre locations are denoted by the white symbol ○. The arrival time has been consistently shifted so that the reference phase-space is centred at zero. Hence, the phase-space distributions indicate the relative arrival time with respect to the reference phase space at 199°.

Ellipses plotted on top of the phase space represent the scaled first-shot ellipse (SFSE) cut region ❶ and the robust covariance ellipse ❷. This nomenclature will be kept in the following sections.

- Red-dashed ellipses ❶ represent the SFSE of the robust MCD estimator. The scaling factor has been chosen to be 5, as discussed in Sec. 4.3.2. This ellipse also defines the systematic cut region for events included in bunch-structure histograms and energy projections.
- The red solid ellipse ❷ is the covariance ellipse calculated from the robust estimator and is considered the relevant estimation of the location and covariance matrix.

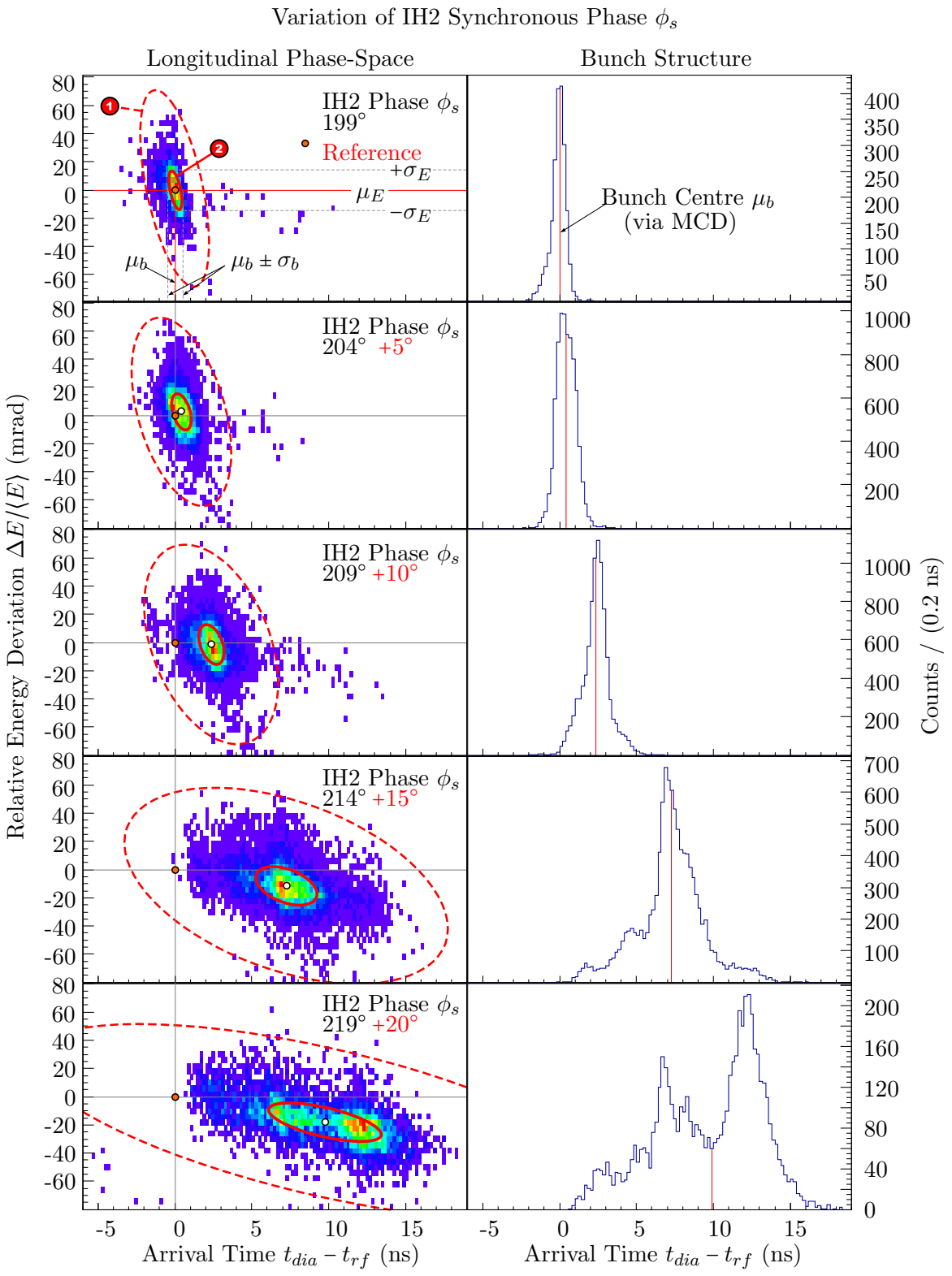

Fig. 5.2: Longitudinal argon TOF phase-space distribution after detuning the synchronous phase ϕ_s of the IH2 cavities with entrance current of 20 µA. IH2 Reference setting for argon is $\phi_s = 199°$. The meaning of the ellipses is given in the text.

Table 5.1 lists the calculated estimator data. It comprises the centres (μ_b, μ_E) of the covariance ellipses (2), the bunch lengths σ_b, the relative energy spread σ_E and the covariance *cov*. To recapitulate, the values σ_b and σ_E are the RMS values in either degree of freedom and the square root values of the diagonal elements of the covariance matrix. Furthermore, Tab. 5.1 features the RMS emittance value ε_{rms} and the Twiss parameter α, which is not to be mixed up with α_{mcd}. The last row denotes the *maximum* statistical uncertainty Δ_{mcd} of the MCD approach for the given column, as described in Sec. 4.3.2.

Tab. 5.1: Estimator values (MCD) of phase-space data shown in Fig. 5.2.

ϕ_s (deg)	μ_b (ns)	μ_E (mrad)	σ_b (ns)	σ_E (mrad)	cov (mrad·ns)	ε_{rms} (mrad·ns)	α "Twiss"
199	0.0	0.0	0.4	13.7	-3.4	4.8	0.69
204	0.4	2.8	0.6	12.9	-3.5	7.4	0.47
209	2.4	-1.3	0.8	14.1	-4.6	10.5	0.43
214	7.3	-11.5	2.0	13.7	-11.6	24.6	0.47
219	9.8	-17.9	3.7	13.7	-31.9	38.6	0.82
Δ_{mcd}	< 0.2	< 0.4	< 0.1	< 0.6	< 1.6	< 0.6	< 0.05

When moving away from the synchronous phase towards larger phases, the populated phase space increases. This can be clearly seen from the distributions in Fig. 5.2 and matches the steadily increasing emittance values in Tab. 5.1. Also, for larger deviations from the synchronous phase, the mean energy drops. In case of ϕ_s = 219° the mean energy drops about 2 % as listed in Tab. 5.1 with $\Delta E/\langle E\rangle$=-17.9 mrad. At the same time, the bunch arrives later. The drift of the bunch after leaving the IH section to the diamond detector is about 10 m (see Fig. 3.3). Without further accelerating or bunching structures, this results in a correlation between the bunch centre μ_b and the mean energy μ_E, which is reflected by the measurement. The emittance scales linearly with the bunch length σ_b, whereas the energy spread σ_E stays about constant. This is noteworthy, as one could expect a larger energy spread to be responsible for a larger bunch length after a drift. For all settings, the correlation α is well below one.

Most noticeable is the deformation of the bunch structure. Initially, at ϕ_s = 199°, the bunch has an almost Gaussian, but slightly asymmetric, longitudinal density distribution. By deviating from the reference synchronous phase a multi-peak structure with different energies forms for ϕ_s = 214°, 219°. To this point, sensitivity on the centre phase and centre energy is evident. While the bunch structure can be resolved, the small variation of the energy spread σ_E does not hint a fine energy resolution beyond the centre energy. This is supported by the consistently Gaussian-like energy profiles for all recorded data. As an example, the energy projections for the reference distribution (ϕ_s = 199°) and a significant variation of the phase ϕ_s by +20° is shown in Fig. 5.3. Even for heavily distorted longitudinal phase-space distributions, as expected in case of a ϕ_s = 219°, the energy distribution is close

to a Gaussian and reveals no further structure. Moreover, apart from the shift of mean energy μ_E, the measured energy spread σ_E is almost identical. Also Forck et al. measured Gaussian TOF profiles as can be seen from Figure 5 in [7]. Therefore, graphical plots of the energy distribution will be omitted as they don't carry further information beyond centre energy and RMS energy spread.

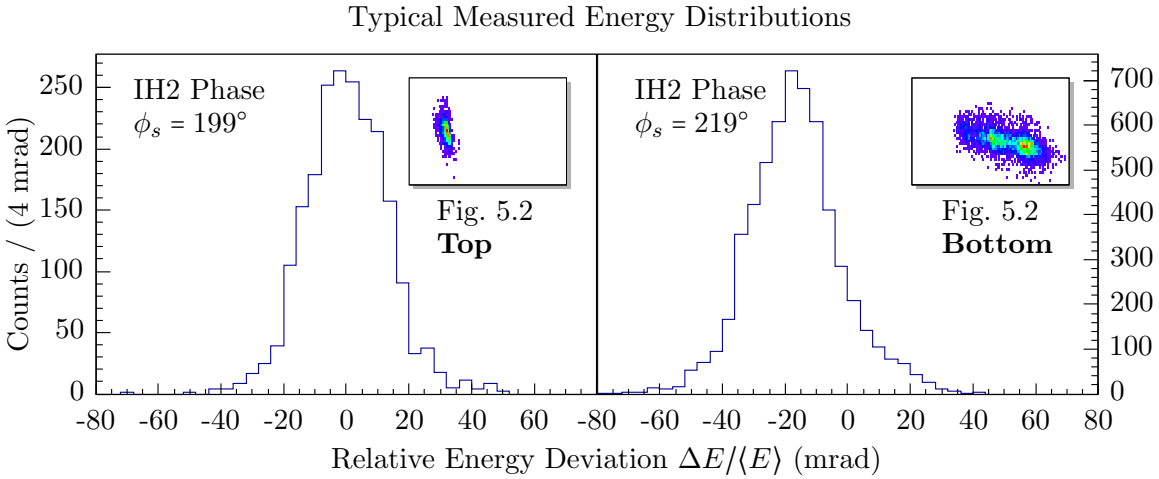

Fig. 5.3: The histograms represent typical measured longitudinal energy projection and correspond to the measurements shown in Fig. 5.2 for the IH2 phase settings of 199° and 219°. The histograms includes all events inside the SFSE, the red-dashed ellipses. While the longitudinal phase-spaces significantly differ, the energy distribution does not, despite the mean energy shift.

5.2.2 Variation of Stripper Pressure

In this section, the influence of the stripper pressure on the measurement is studied. For a proper attenuation process of the beam, changing the pressure of the gas stripper can be necessary in order to alter the charge spectrum. An exemplary charge spectrum is plotted in Fig. 2.11. To investigate the effect of different pressures on the measured longitudinal phase-space distributions an Ar beam of 4.3 mA served as test beam. The beam current is measured with the high-current transformer US2DT5 (see Fig. 3.4) preceding the gas stripper US2VK1.

The pressure of the gas stripper, see Sec. 3.2.1, has been varied from 2000 mbar to 1000 mbar in steps of 200 mbar and an additional measurement at 500 mbar to fill the gap to lower pressures. To account for varying count rates at the different pressures, the macro-pulse duration has been adjusted from 50 µs to 300 µs at a constant macro-pulse repetition rate of 1 Hz. The change of macro-pulse length and repetition rate is considered to have no significant influence on the bunch phase-space distribution. Other parameters are kept constant among the different measurements. The high-current slits have been set at a typical UNILAC operation configuration with ±15 mm (DS4) and ±6 mm (DS5).

At high currents it is difficult to attenuate the beam without using a very small slit opening to shadow a large fraction of the particles. If the charge-state spectrum features a suppressed

charge state with an appropriate beam current, this one can be used to attenuate the beam. Additionally, the current should be sufficiently high to produce a practicable count rate. It depends on the ion species, beam energy and beam current if such a suitable suppressed charge-state exists and, thus, does not require narrowing of the high-current slits. The given beam configuration, with a charge-state equilibrium at $^{40}Ar^{10+}$, provided a good candidate of a suppressed charge state with $^{40}Ar^{14+}$ which is used in this measurement.

The full set of recorded longitudinal phase-space distributions are depicted in the left column of Fig. 5.4 where the gas pressure varies from 2000 mbar to lower pressures from top to bottom. Horizontal axes represent the arrival time of the ions at the PC-diamond detector with respect to the UNILAC RF. The vertical phase-space axis represents the energy by means of the relative energy deviation at a reference energy corresponding to $\beta \approx 5.5\,\%$. Recorded timings have been consistently shifted, so that the reference phase space at 2000 mbar is centred at (0,0).

The right column of Fig. 5.4 features the corresponding longitudinal bunch-structure by means of the arrival-time histogram. It comprises only events inside the red-dashed SFSE. The reference phase space at 2000 mbar, centred at $(0, 0)$, features an asymmetric bunch structure with an RMS width of about 2 ns. As the gas pressure is lowered to 1760 mbar, a two-peak bunch structure evolves. This structure remains for lower pressures until, at 970 mbar, the high-energy peak merges with the peak at a later arrival time. Finally, at 470 mbar only one peak exists along with a pronounced low-energetic tail of late arrival times. A low-energetic tail emerges at a pressure of ≈ 1170 mbar and gets more prominent towards lower pressures. This is evident from the phase-space distributions. At 470 mbar a distinct trail is visible and reaches down to very low kinetic energies.

Estimator values and derived values of the measured longitudinal phase-spaces are listed in Tab. 5.2. As the gas pressure is lowered, the mean energy rises and the bunch arrives earlier. Also, the energy spread σ_E through straggling at the gas jet gets smaller and, consequently, the bunch length σ_b decreases which in turn results in a smaller emittance. This behaviour is expected and is reflected by the extracted estimator data as listed in Tab. 5.2. However, at around 1170 mbar and below this trend is reversed. The estimator values are significantly affected by the trailing particles being more pronounced towards lower pressures in this configuration.

It is reasonable to compare the values in Tab. 5.2 with the longitudinal Ar phase-space distribution from Fig. 2.2, the expected longitudinal distribution for 7.1 mA $^{40}Ar^{10+}$ at the location of the TOF device. While the beam current is lower in the present experiment, 4.3 mA compared to 7.1 mA, the energy spread σ_E is expected to be smaller than the one given in Fig. 2.2 with $\sigma_E \approx 0.93\,\%$ due to the reduced space-charge and the comparable bunch length. The measured energy spreads are consistently larger than 1.3 %. Also, all Twiss-α values are well below one. This is important to note as the expected value for α by the GSI injector division [77, 78] should be ≈ 4.

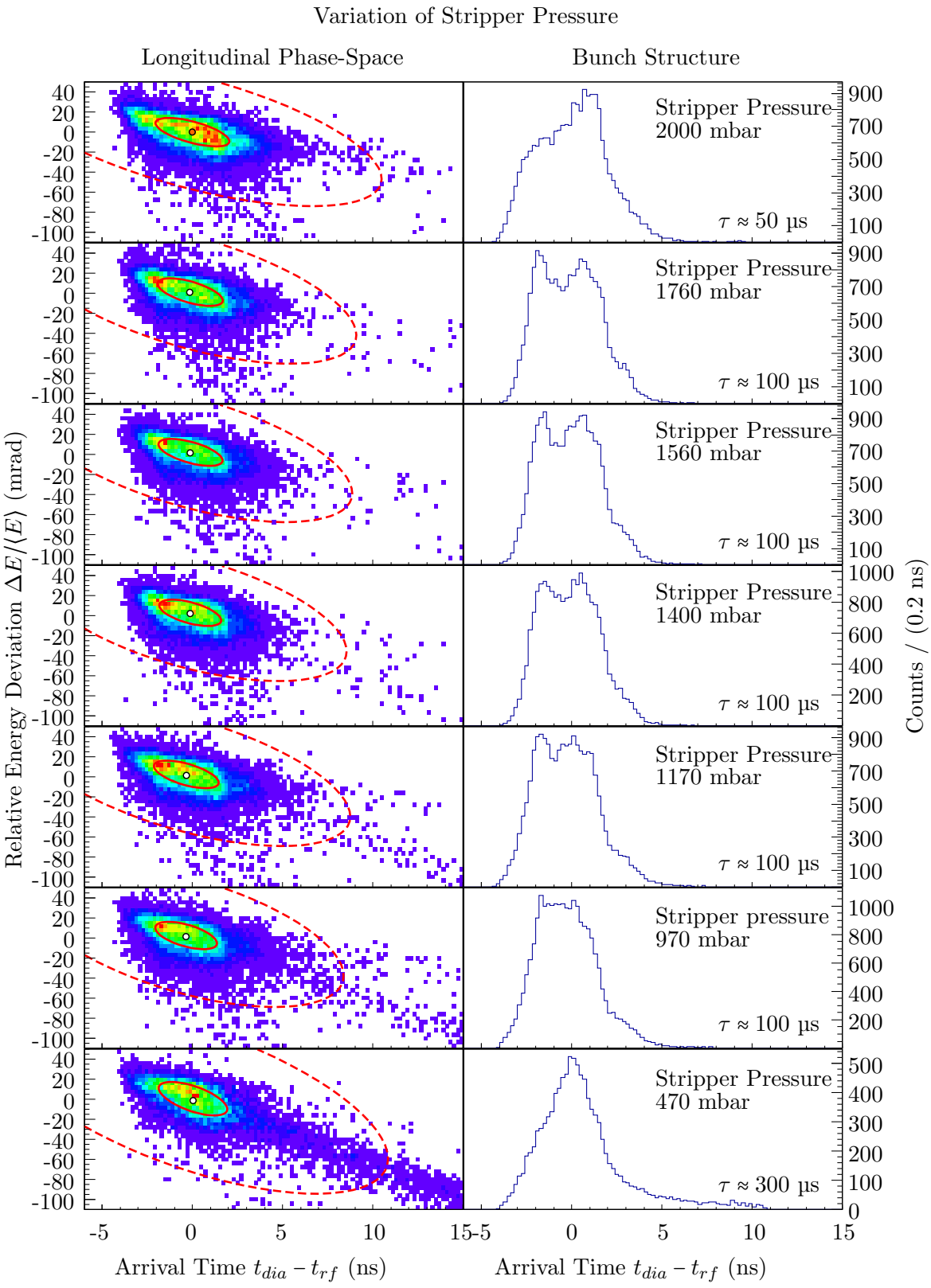

Fig. 5.4: Longitudinal phase-space distributions at varying pressures at the gas-stripper nozzle, recorded with the TOF setup. The high-current slits were set to typical UNILAC operation values at ±15 mm (DS4) and ±6 mm (DS5). For the meanings of the ellipses see Sec. 5.2.1.

Tab. 5.2: Estimator values (MCD) of phase-space data shown in Fig. 5.4.

Pressure (mbar)	μ_b (ns)	μ_E (mrad)	σ_b (ns)	σ_E (mrad)	**cov** (mrad·ns)	ε_{rms} (mrad·ns)	α "Twiss"
2000	0.0	0.0	2.04	14.2	-18.78	22.22	0.85
1760	-0.15	1.6	1.81	13.8	-15.31	19.69	0.78
1560	-0.12	2.5	1.78	13.5	-14.38	19.13	0.75
1400	-0.14	3.2	1.72	13.1	-12.91	18.50	0.70
1170	-0.34	2.7	1.80	13.7	-14.81	19.73	0.75
970	-0.36	3.0	1.71	13.7	-13.31	19.20	0.69
470	0.03	0.9	1.90	16.8	-19.98	24.83	0.80
Δ_{mcd}	< 0.02	< 0.4	< 0.04	< 0.2	< 0.65	< 0.26	< 0.03

Several statements can be made about the prominent trail. The presence of the trails is unexpected but the events inside the trail are real phase-space events. Furthermore, the longitudinal phase-space covered by the trails cannot originate from the preceding accelerator cavity. This can be ruled out by the presence of the dipole magnet in front of the measurement setup. If the trails originate from the interaction of the beam with components along the accelerator, this should result in a characteristic relationship between the kinetic energy and the measured arrival time. Exploiting this fact for the prominent trail at 470 mbar and do the calculation for the point (15 ns, 0.975 mrad) reveals a location of interaction about 2.5 m upstream the PC-diamond detector. The high-current slit DS5 resides at this location as can be seen from Fig. 3.4. This is consistent with the supposition that the origin of the trail cannot be located before the dipole magnet US3MK1 as the large energy spread would not match the acceptance of the measurement setup after traversing the dipole section. Hence, the trails are not a direct result of the stripper pressure. Instead, it is to assume that the horizontal radii of the bunch trajectories at the dipole section, resulting from the pressure-dependent energy losses inside the gas jet, may give rise to an enhanced interaction of bunch ions with the high-current slits. However, the underlying effect is not understood and requires further investigations. This motivates dedicated measurements to study the effect of the high-current slits on the longitudinal phase-space distribution of the next section.

5.2.3 Variation of High-Current Slits

The previous section hinted an unexpected influence of the high-current slits on the longitudinal phase-space distribution. Limiting the transverse geometric trajectories of particles is one way to attenuate the beam. By symmetric openings, with respect to the horizontal beam axis, parts of the beam are scraped off the beam distribution. At the given beam energies of about 1.4 AMeV ions have a typical range in matter of several micrometers

only. Due to the short range in matter, the assumption has been that ions either pass the slit opening unaffected or are absorbed at the slit geometry. A dedicated measurement has been performed with different high-current slit settings. For comparison with the measurements in Sec. 5.2.2, an identical high-current injector setup has been targeted. The high charge-state $^{40}Ar^{14+}$ served as primary beam attenuation at stripper pressure of 2000 mbar. Of both charge-separating high-current slits US3DS4 and US3DS5, see Sec. 3.2.1, the slit DS5 closer to the measurement has been varied, whereas DS4 is fixed at an open setting ±15 mm.

In the following, longitudinal phase-space measurements with different symmetric slit settings of US3DS5 have been performed using the TOF setup. The slit openings have been ±5 mm to ±1 mm in steps of 1 mm and a slit opening of ±0.5 mm, which is the smallest possible slit setting. To account for the high dynamics in count rate at different slit settings, the macro-pulse length has been adjusted between 50 µs to 250 µs and the macro-pulse repetition rate between 1 Hz and 2 Hz. This procedure is not considered to have an influence on the six-dimensional phase space of the bunches. Longitudinal phase-space distributions and corresponding bunch structures are given in Fig. 5.5. The bunch structures are based on all events contained in the corresponding SFSE. Axes scalings are kept from the previous section. Horizontal axes represent the arrival time of the ions at the diamond detector with respect to the UNILAC RF. The vertical phase-space axis represents the energy by means of the relative energy deviation and a reference energy corresponding to $\beta = 5.5\,\%$. Recorded timings are consistently shifted, so that the reference phase space at 2000 mbar is centred at (0,0).

Comparing the reference phase space to the one in Sec. 5.2.2 shows a good agreement. The corresponding bunch structure also agrees in the characteristic shape. Minor deviations are expected after a readjustment of the accelerator settings. Also estimator values in Tab. 5.3 agree to large extent. The larger bunch length σ_b correlates with a slightly higher energy spread σ_E.

Comparison of the first four measurements with slit openings from ±5 mm to ±2 mm reveals no significant deviations of the longitudinal phase-space distribution and the bunch structure. The estimator numbers hint a small increase in energy spread towards a smaller slit opening but this does not noticeably affect the bunch length due to the short drift of about 1.6 m between slits and measurement setup. A slit setting of ±1 mm shows a clear distortion of the bunch structure. While the edge of the faster ions matches with the reference distribution, a second peak evolves at the end of the bunch as some ions arrive later compared to the previous slit settings. This is reflected by the estimator data with a larger bunch length σ_b of about 10 % accompanied by an increased energy spread σ_E. The phase space of the narrowest possible slit setting at ±0.5 mm is shown in the bottom row of Fig. 5.5. This phase space noticeably depletes near the center which results in two pronounced peaks of the bunch structure. Again, the edge of early-arriving ions is sustained for the most part. The second peak forms around the original edge of the reference bunch structure and the bunch length is significantly enlarged by about 21 % over the reference bunch structure.

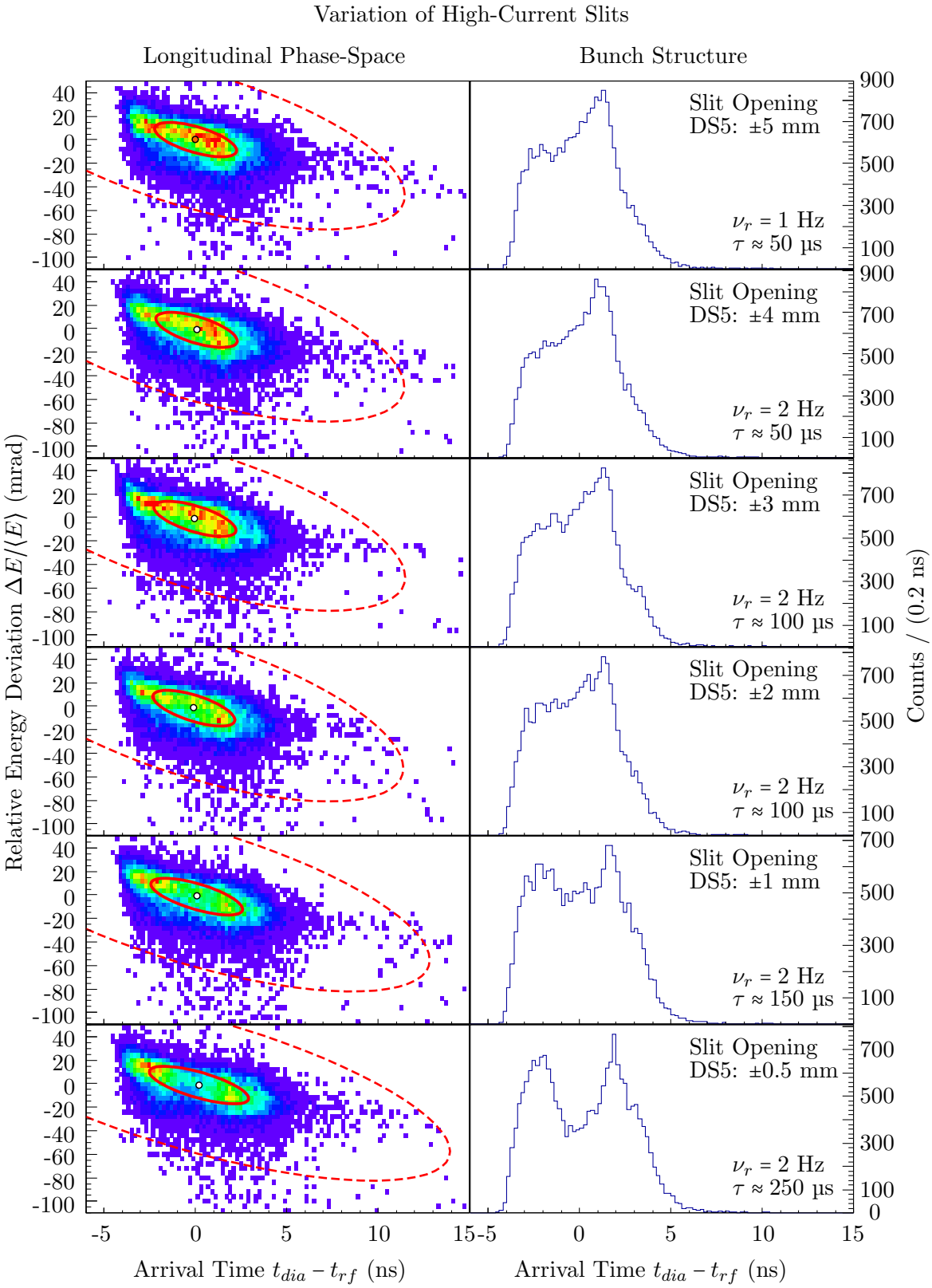

Fig. 5.5: Longitudinal phase-space recordings of different high-current slit (DS5) openings using the TOF setup. The stripper pressure has been 2000 mbar throughout the measurement. For the meanings of the ellipses see Sec. 5.2.1.

Tab. 5.3: Estimator values (MCD) of phase-space data shown in Fig. 5.5.

Slit DS5 (mm)	μ_b (ns)	μ_E (mrad)	σ_b (ns)	σ_E (mrad)	cov (mrad·ns)	ε_{rms} (mrad·ns)	α "Twiss"
±5	0.0	0.0	2.25	14.6	-21	25.41	0.82
±4	0.06	-0.8	2.22	15.0	-21	25.71	0.82
±3	-0.05	-0.8	2.25	15.0	-22	25.54	0.86
±2	-0.08	-1.3	2.24	15.2	-22	25.74	0.87
±1	0.06	-1.3	2.51	15.6	-27	28.48	0.95
±0.5	0.20	-0.9	2.71	16.0	-31	30.59	1.00
Δ_{mcd}	< 0.01	< 0.4	< 0.06	< 0.2	< 2	< 0.05	< 0.07

By closing the high-current slits US3DS5 from ±5 mm to ±0.5 mm the longitudinal energy spread gradually increases. At the same time the bunch structure does not significantly change within the range ±5 mm and ±2 mm. Further closing the slits results in a pronounced two-peak structure of the longitudinal phase projection and a significantly enlarged bunch length. Also, by closing the slits, the energy centre is shifted to lower energies which matches the later arrival times of the bunches. The magnitude of the covariance gradually increases from ≈ -21 mrad·ns to ≈ -31 mrad·ns, whereas the RMS emittance does not vary with a slit setting down to ±2 mm and increases about 20 % for smaller slit openings. The Twiss parameter α gradually increases from 0.8 to 1.0 towards smaller slit settings. An explanation for the emerging two peak structure may be related to the scattering off the high-current slits. A fraction of the beam particles interacts with the slit walls and, thus, arrives later.

Again, the energy width σ_E is significantly larger than expected by more than a factor of 1.6, while the correlation α is much lower than the expected value of ≈ 4.

5.2.4 High-Current Argon Data

Rounding off the presented TOF measurements, this section covers a high-current $^{40}Ar^{10+}$ measurement supporting an experiment of the GSI injector group. The longitudinal phase-space data has been requested in the course of the GSI work package of the "High Intensity Pulsed Proton Injector" (HIPPI, [62]) campaign. This measurement was performed in collaboration with the GSI injector division in particular Wolfgang Bayer. The physical motivation of HIPPI is not part of this work, but the recorded data serves as an example of the time-sliced phase-space analysis.

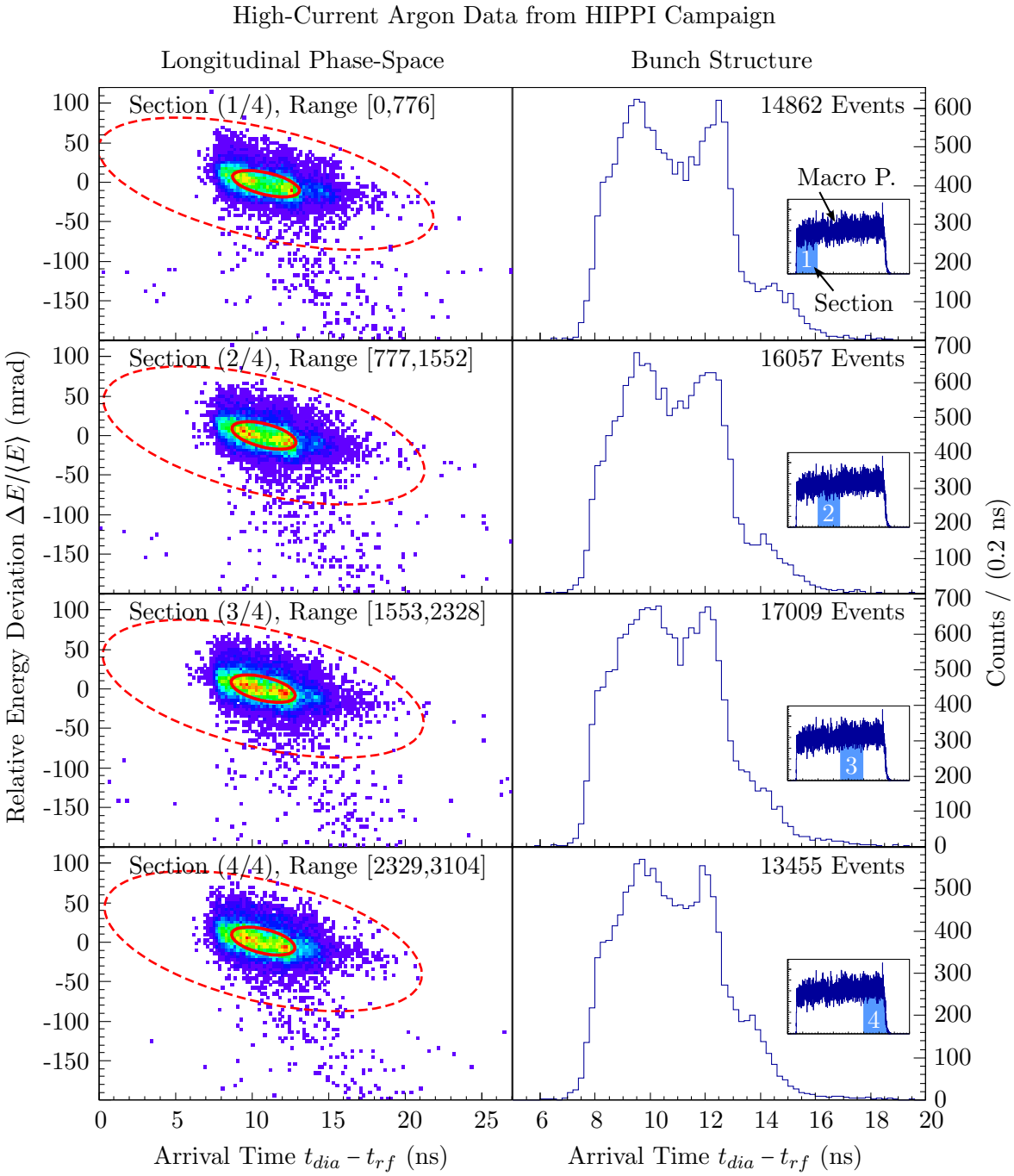

Fig. 5.6: High-current argon measurement for the HIPPI collaboration. A high amount of $\approx 6.0 \times 10^4$ events allows to evaluate the robust MCD estimator for different macro-pulse sections. The macro-pulse section taken into account is depicted in the event-density histogram, placed right of the bunch structures. For the meanings of the ellipses see Sec. 5.2.1. Stripper pressure has been 2000 mbar while slit settings for DS5 were set to ±1 mm.

The beam current was measured to be ≈ 6 mA at US2DT5, the transformer preceding the gas stripper, at a macro-pulse length of ≈ 80 μs. Particle attenuation has been accomplished using the high-current slits. With a comparably high statistics of ≈ 6×10^4 events it is possible to define cut regions, or "time slices", of the macro pulse as described in Sec. 4.4.2. This allows to directly investigate and compare the longitudinal phase-space distributions of different macro-pulse sections.

Phase-space distributions of bunches along the macro pulse are commonly expected to be the same. However, several aspects can relativise this assumption. For high currents, induced beam loading of all RF cavities has to be compensated by RF closed-loop controls. The effect of beam loading rises along the macro pulse and, thus, can affect the phase-space distributions in a characteristic way as any deviations from a perfect RF controlling at the RFQ, Superlense and IH-cavities accumulates. Furthermore, the chopper in front of the RFQ has an impact on the start and end of a macro pulse which is mainly characterised by the rise/fall time of the deflecting field. Even right from the start of the accelerator chain, pulsed ion-sources can exhibit time structures of the emittance and beam current. Hence, a measurement method to access sections of the macro pulse is useful.

The amount of events of the present measurement allows to divide the macro pulse into four macro-pulse section of equal length with ≈ 1.5×10^4 events each. Figure 5.6 shows the corresponding measured longitudinal distributions in the left column and the projected bunch structures in the right column. The sections are denoted by the number in the upper left corner together with the bunch range. A graphical representation of the section inside the macro pulse is given right of the bunch-structure histograms.

Comparing the phase-space distribution from the different sections only reveals minor deviations. The edge of the early arriving ions is stable for all four sections and the shape and location of the peaks differ only slightly. Some variation is present at the small hump of the late ions. The corresponding estimator values in Tab. 5.4 support the interpretation of a stable longitudinal phase-space distribution along the macro pulse.

Tab. 5.4: Estimator values (MCD) of the HIPPI phase-space data shown in Fig. 5.6.

Section (Macro-Pulse)	μ_b (ns)	μ_E (mrad)	σ_b (ns)	σ_E (mrad)	cov (mrad·ns)	ε_{rms} (mrad·ns)	α "Twiss"
(1/4)	10.89	-1.7	2.05	15.2	-17.4	25.8	0.67
(2/4)	10.81	-0.7	1.97	15.7	-16.6	26.1	0.64
(3/4)	10.72	0.4	1.98	15.8	-16.0	26.9	0.59
(4/4)	10.72	0.9	1.95	16.2	-16.0	27.3	0.58
Δ_{mcd}	< 0.01	< 0.3	< 0.04	< 0.2	< 0.9	< 0.2	< 0.04

5.3 Calorimetric Measurements with Mono-Crystalline Diamond

The preceding sections covered TOF measurements based on an MCP detector and a PC diamond detector. This section discusses the recorded data using only an MC diamond detector. As described in Sec. 3.3.2, the kinetic energy information is extracted by sampling the pulse shapes of the fully stopped ions at the MC diamond detector.

A low-current samarium beam was attenuated by defocusing quadrupole settings in front of the RFQ cavity. The macro-pulse repetition rate was 1 Hz. Right before entering the stripper section a beam current of about 10 µA was measured by current transformer US2DT5. The entrance current after stripping was 17 µA. Figure 5.7 shows the recorded $^{152}Sm^{20+}$ phase-space data. Calibration of the energy axis is done using a linear mapping of the pulse-integral information through the fix points of pulse-integral value zero and pulse-integral value corresponding to the centre phase-space. The latter one has been determined via the robust MCD estimator and marks the centre of the red solid ellipse. A kinetic energy according to the design value $\beta \approx 0.055$ was assigned to the phase-space centre. The measurement data contains 10^4 events which equals a measurement duration of about 3 hours with the current DAQ. Events inside the scaled first-shot ellipse (SFSE) are histogrammed to reflect the phase-space density qualitatively. All other dots, outside

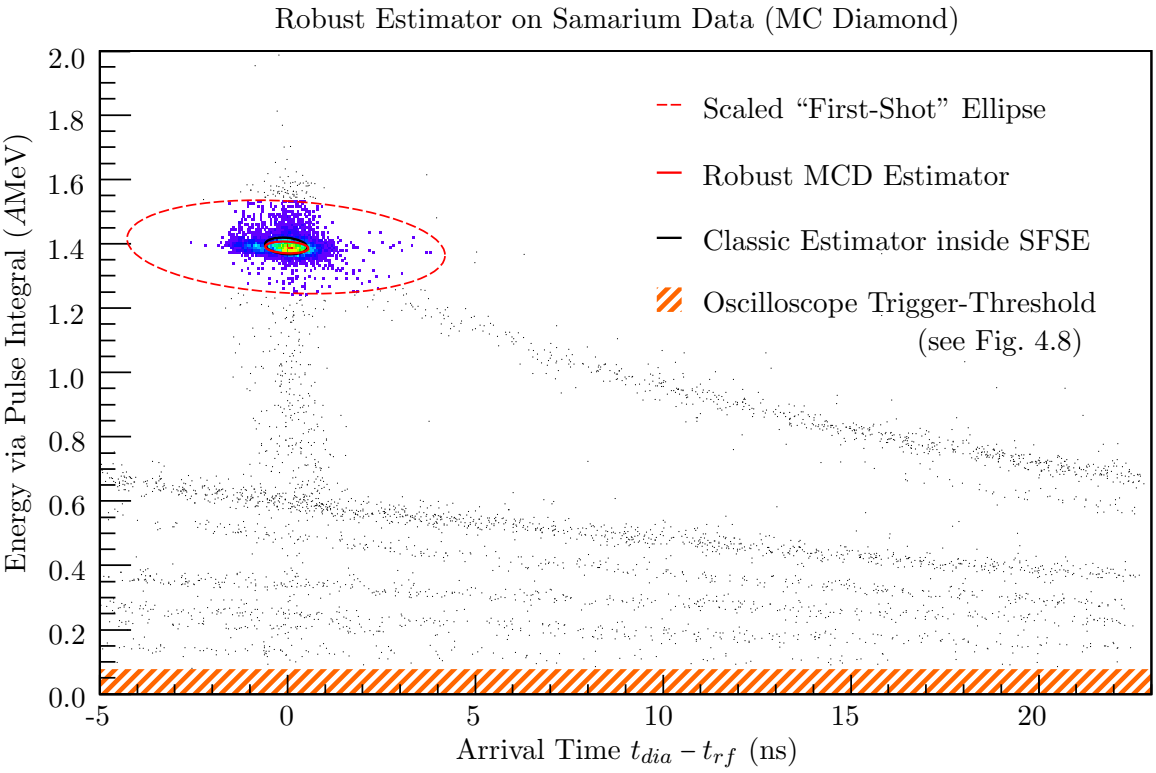

Fig. 5.7: Low current Samarium phase-space data recorded with the mono-crystalline diamond using the pulse-integral information and linear energy calibration. The ellipses are the scaled first-shot ellipse (red dashed), the robust estimator ellipse (red) and the classical estimator (black) applied to events inside scaled first-shot ellipse.

the SFSE, represent single events. At the bottom of the plot the detection threshold, due to the trigger threshold applied to the diamond pulses, is depicted by the hatched orange area. According to the linear calibration, the detection threshold for this measurement is effectively ≈ 75 *A*keV. The corresponding robust estimator data is given in Tab. 5.5. It covers the longitudinal phase-space spanned by the pulse-integration values, depicted

Tab. 5.5: Robust estimator values (MCD) of the Sm phase-space in Fig. 5.7.

$^{152}Sm^{20+}$ MC Diamond	σ_b (ns)	σ_E (mrad)	cov (mrad·ns)	ε_{rms} (mrad·ns)	α "Twiss"
Integration	0.57	13.5	-1.39	7.5	0.18
Pulse Height	0.52	30.2	-1.30	15.4	0.08
Δ_{mcd}	< 0.03	< 1.2	< 0.04	< 0.1	< 0.01

in Fig. 5.7, and the pulse height as described in the previous chapter. While the bunch lengths σ_b approximately agree, the energy widths σ_E differ significantly by more than a factor of two. An energy width of $\sigma_E \approx 1.4\,\%$ using the pulse-integral information is to be compared to $\sigma_E \approx 3\,\%$ using the pulse-height information. Although the energy resolution is significantly higher for the pulse integral, the absolute value is still larger than the expected energy width of $\sigma_E \approx 1\,\%$. The MC diamond in the given configuration does not provide for a higher energy resolution than the TOF setup. Similarly, the Twiss correlations α are very small compared to the expected value of $\alpha \approx 4$. It is noteworthy that those values are even significantly smaller than the measured α values in all TOF experiments. At TOF experiments the measured range of α has typically been $0.5 < \alpha_{tof} < 1$. However, the covariances measured using the pulse-integral and pulse-height information agree and, thus, the difference in the correlation α is dominated by the emittances. An explanation for this will be given in the next chapter, as well as why low Twiss correlation values α are a clear hint of a limiting resolution. In fact, as will be shown in the next chapter, the smaller correlation value α measured with the MC diamond approach in the current configuration, compared to typical TOF values, hints an even lower energy resolution than the TOF approach.

Pulse Properties. Having access to the pulse-integral and pulse-height information of all recorded events allows to visually correlate both properties. The top plot ❶ of Figure 5.8 shows the pulse-height information on the vertical axis versus the pulse-integral information extracted for each recorded event. Plot ❷ shows the longitudinal phase-space using the pulse integral and arrival-time information. Same-coloured dots in ❶ and ❷ refer to the same set of events.

It is evident from ❶ that the relation between pulse height and pulse integral is non-linear over the measured energy range. Towards larger kinetic energies of impinging ions, the pulse integral shows a higher sensitivity than the pulse height. This is also reflected by the higher energy resolution of the pulse integral.

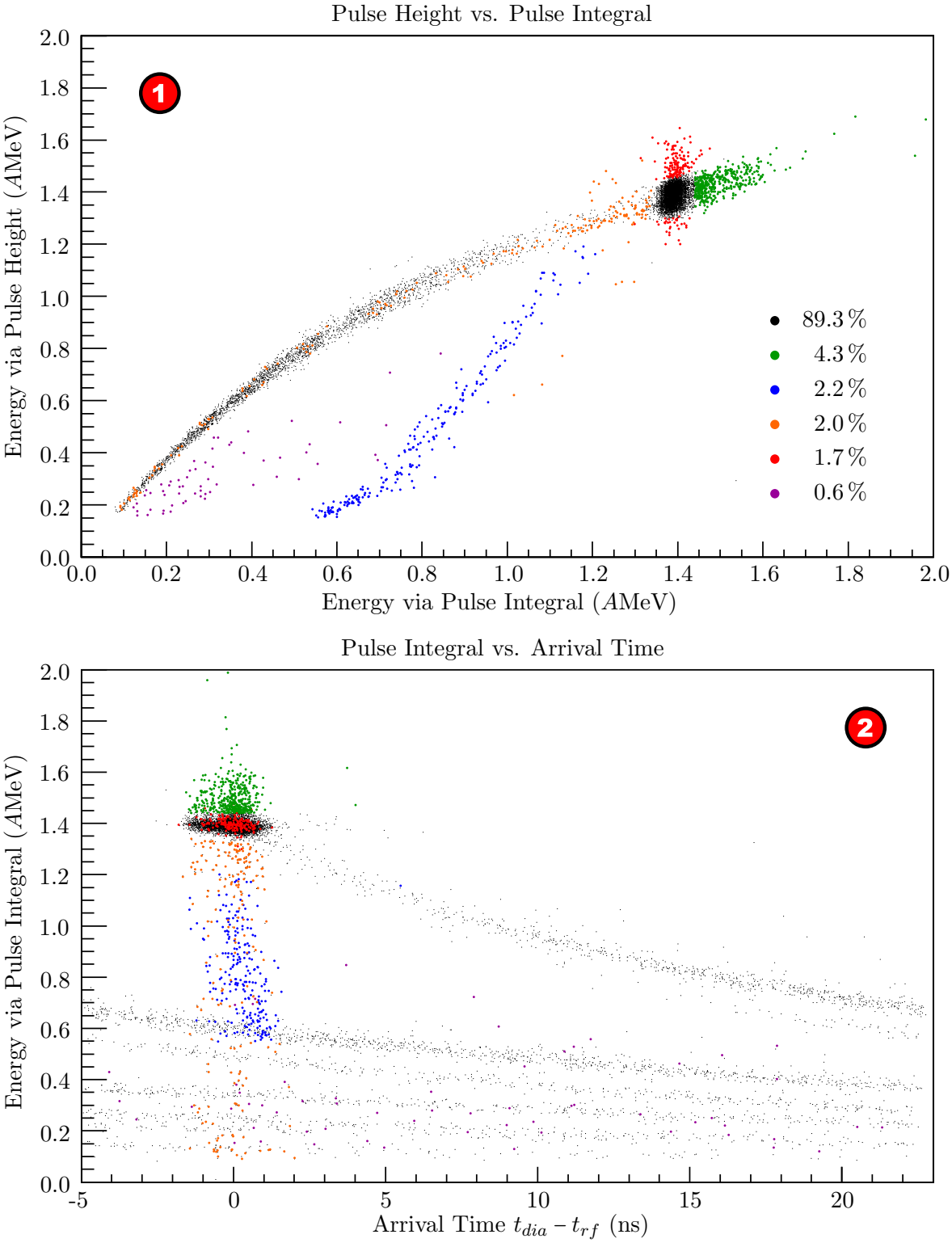

Fig. 5.8: Different representations of the recorded samarium data. Plot 1 shows the pulse height vs. the pulse integral, both in linear energy calibration. Plot 2 shows the kinetic energy via the pulse-integral information vs. the arrival time at the mono-crystalline diamond detector. Coloured events of both plots correspond to each other and are defined by certain cuts (see text).

Some events in ❶ show a deviating height-to-integral ratio from the main trend. To investigate the different classes of events, graphical cuts are introduced. This allows to relate certain sets of events between ❶ and ❷.

- The black-dotted events (89.3 %) do not show any peculiarities concerning the height-to-integral ratio. They constitute the core region of the phase-space and the long-range trails.
- The violet set of events (0.6 %) features a smaller height-to-integral ratio and is restricted to low kinetic energies. In the phase-space representation ❷, they are distributed over the full arrival-time range along the trails.
- The blue set of events (2.2 %) is contained in a distinct band in ❶. Contrary to the violet events, they form a vertical band in ❷ under the core region. This can only be explained as an effect by the diamond detector itself. Otherwise, the different energies would lead to a characteristic correlation between kinetic energy and arrival time.
- The orange set of events (2.0 %) is based on a graphical cut in ❷. It includes all events in the vertical bar under the core region which do not belong to the blue and violet sets of events and do not belong to the long-range trails. From ❶ it is evident that they follow the main trend of height-to-integral ratio as they lie on the strongly populated band of black dots. Nevertheless, the low integral values and, thus, the interpretation as ions of low kinetic energies must be an artefact of the diamond detector. The argumentation follows the one of the blue events. If the measured energy spectrum would be real, a clear correlation between the measured kinetic energy and the measured arrival time should be visible.
- The red events (1.7 %) comprise pulse shapes at the core region which feature greater or smaller pulse-heights than the main trend in ❶. They do not show any peculiarities in the phase-space representation ❷ as they are located in the core region.
- The green events (4.3 %) comprise pulse shapes with larger integrals than the core. This leads to an overestimation of the kinetic energy.

All listed effects are consistently reproduced in other measurements (see Appendix E). However, it is not understood if the cause of the local effects leading to different energies, in particular the green, blue and violet set of events can be generally attributed to charge-collection losses. The following section focuses on the bands which are not considered artefacts.

5.3.1 Interpretation of Measured Bands

Beside the core phase-space region of interest, the red-dashed ellipse in Fig. 5.7, events of lower energies form distinct bands. As will be seen, these bands are long-range trails extending over many RF periods and contain a large fraction of the total recorded events.

According to the previous section, a characteristic subset of events can be attributed to the diamond detector and discarded as artefacts. In particular, the vertical aligned events below the phase-space core do not represent physically meaningful events. The reason is as follows. The dipole magnet US3MK1, see Sec. 3.2.1, does not deflect ions of low energy to

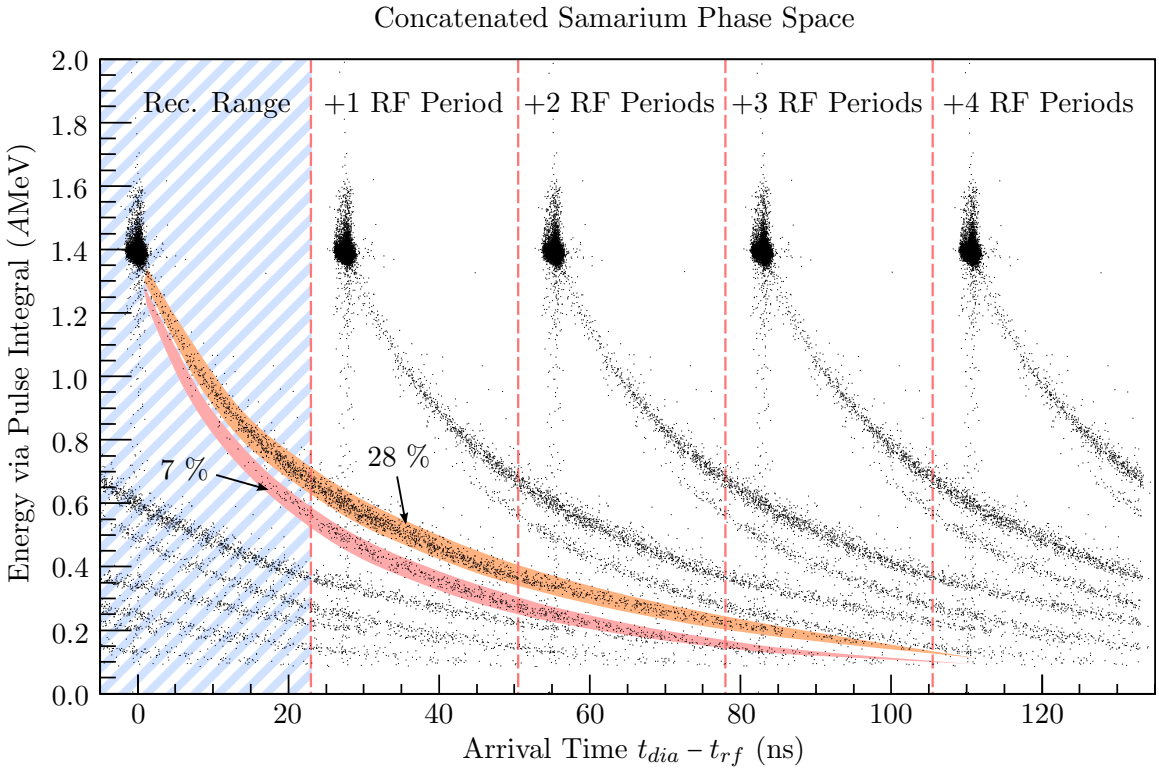

Fig. 5.9: Repeated samarium phase-space data by concatenating the measured events. Two trails are visible. They emerge from the core region and comprise, at least, a third of all registered events for this experimental configuration.

into the device acceptance. On the other hand, if the large range of low energies originates from some interaction within the dipole chicane, i. e. after the dispersive dipole section, a distinct correlation between energy and recorded arrival time at the diamond should be present. Such a correlation is present for the low-energetic trails in plot 2. As the arrival-time information is only known modulo the RF period $T_{rf} \approx 27.7$ ns, concatenating the same distribution, as done in Fig. 5.9, reveals a distinct long-range double-trail structure. The accumulated events in both trails, coloured in light red and orange, comprise about one third of the total registered events. Due to the detection threshold the actual number of events in the trails of this measurement is presumably even higher. The trails appear in the MC diamond measurements as well as in the TOF measurements. Dmitry Liakin first mentioned the bands during his tests of the TDC DAQ for the TOF setup, as an interesting "*longitudinal halo effect*" [79].

In the following it will be shown that the trails can be interpreted as the interaction of the bunch at certain locations inside the measurement setup. Furthermore, a quantitative estimation of the interaction vertices, the locations where the bunch interacts, will be presented.

5.3.2 Reconstruction of Interaction Vertices

The bands in Fig. 5.7, which are actually trails extending over many RF periods, have a characteristic correlation between kinetic energy and arrival time of the particles. As argued, these events can not be discarded as artefacts by the MC diamond detector and, thus, are considered valid events. Furthermore, the low kinetic energy of those particles, compared to the design values, would not allow them to reach into the acceptance of the measurement device due to the dispersive dipole section preceding the measurement setup. Hence, it is reasonable to assume that a fraction of particles interacts with components located *inside* the chicane after the first dipole magnet US3MK1. In this case, the characteristics of the measured trails origin from an interaction which, beyond a mean shift, generates a broad spectra of lower energies and, thus, leads to different arrival times at the diamond detector.

The arrival time of a particle depends on the momentum transfer at the interaction vertex and the separation of the vertex from the diamond detector. As long as the kinetic energy of the incident particle is properly reproduced by the measurement setup, and the previous assumption about the characteristics of the interaction holds true, an attempt to estimate the relative vertex location d_{vtx} can be made. In this case, the location of a potential interaction vertex d_{vtx}, with respect to the location of the diamond detector in use, can be estimated by fitting the trails to the classical energy-momentum relation

$$E_{kin}(t; t_0, \beta, d_{vtx}) = \frac{m_u}{2} \frac{d_{vtx}^2}{\left(t - t_0 + T_{\beta, d_{vtx}}\right)^2} = \frac{m_u}{2} \frac{1}{\left(\frac{t-t_0}{d_{vtx}} + \frac{1}{\beta c}\right)^2} \,. \tag{5.1}$$

This parameterisation accounts for the arbitrary arrival-time offset by the term t_0.[1] The data set in Fig. 5.7 is shifted horizontally to align the phase-space centre, the centre of the phase-space inside the red-dashed ellipse, at an arrival time $t_{dia} - t_{rf} = 0$. Hence, in this special case $t_0 = 0$. Furthermore, the term $T_{\beta, d_{vtx}} = d_{vtx}/(\beta c)$ implements the fit constraint

$$E_{kin}(t = t_0; t_0, \beta, d_{vtx}) \stackrel{!}{=} \langle E \rangle_{kin} = 1.4 \ A\text{MeV} \,. \tag{5.2}$$

An overview over the variables and parameters used in Eq. (5.1) is given in Tab. 5.6.

A precise estimate of the interaction vertex d_{vtx} via fit parameterisation Eq. (5.1) requires a trustworthy reconstruction of the kinetic energy without major nonlinearity. This is provided by the TOF measurement[2], but is not ensured for the calorimetric approach using the MC diamond and the DAQ chain. For this reason, the fit is first applied to the samarium TOF measurement recorded for the same beam setup immediately after the measurement using the MC diamond.

The corresponding TOF data containing 1.4×10^4 events is shown in Fig. 5.10.[3]

[1] The measured arrival time only carries the information up to a fixed but arbitrary offset.

[2] For this the energy is not reconstructed by a linearisation as explained in 4.1.5 but the classical energy momentum relationship. This is import for the fit.

[3] At the time of measurement, the MCP showed a significantly degraded signal quality of the rising edge and, thus, a degraded timing resolution beyond the typical contributions. A comparison of the estimator data of the TOF and MC diamond measurements is not meaningful. However, the additional jitter does not negatively affect the fit of trail. The MCP was replaced during the next shutdown.

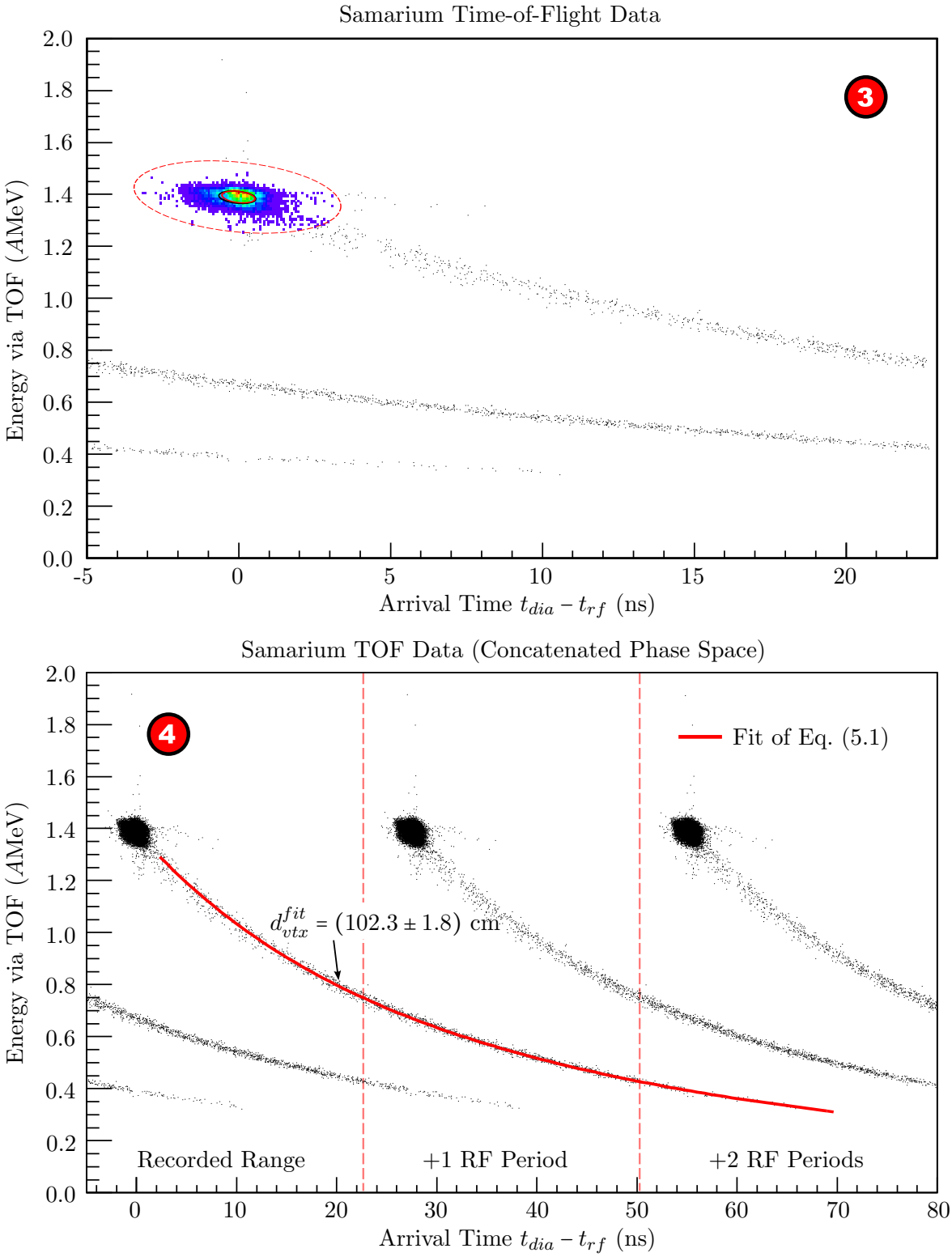

Fig. 5.10: Plot 3 shows the longitudinal Samarium phase space recorded with the TOF setup. The meaning of the ellipses corresponds to those in Fig. 5.7. Plot 4 concatenates three TOF recordings, which allows fitting of the trail with Eq. (5.1).

Tab. 5.6: Parameters and variables used in the trail fit Eq. (5.1).

$\boldsymbol{d_{vtx}}$	Distance of the interaction vertices w.r.t. diamond detector (PC or MC) **- Fit parameter -**
$\boldsymbol{m_u}$	Atomic mass unit
$\boldsymbol{\beta}$	Normalised design velocity (5.5 %)
t_0	Arrival time of phase-space centre (via robust MCD estimator)
$\boldsymbol{T_{\beta,d_{vtx}}}$	Time $\frac{d_{vtx}}{\beta c}$ it takes for a particle with design energy (1.4 AMeV) to travel from the interaction vertex to the diamond detector

Most noticeable is the presence of only one trail in the TOF measurement ❸ compared to the calorimetric measurement using the MC diamond detector which features two distinct trails, as can be seen in Fig. 5.9. This is also the case in the TOF data recorded by D. Liakin (Fig. 5 in [79]). A possible explanation for the different number of trails between TOF and MC diamond measurements will be given at the end of this section.

Plot ❹ shows the concatenated measured data spanning three RF periods. The red curve represents the fit of Eq. 5.1 which is applied to the events inside the trail only, i. e. excluding the data inside the core region. The very good agreement of the fit supports the initial hypothesis which connected a measured trail to an interaction of the bunch with a yet undetermined component preceding the diamond detectors.

For the quantitative estimate of d_{vtx} the uncertainties of t_0 and β (or $\langle E \rangle$) have been included. By reconstructing a set of altered phase-space distributions from the recorded detector timings and applying the fit of Eq. 5.1 to each distribution, the mean fit value of d_{vtx} is calculated. Furthermore, the uncertainty Δd_{vtx} is identified with the corresponding standard deviation based on the same set of fits. The set of distributions is generated by incorporating the uncertainties Δt_0 and $\Delta\beta$ as listed in Tab. 5.7. Each cell refers to a

Tab. 5.7: Parameter set (t_0', β') used in the determination of the mean value and uncertainty of the vertex location d_{vtx}.

$t_0 - \Delta t_0, \beta + \Delta\beta$	$t_0, \beta + \Delta\beta$	$t_0 + \Delta t_0, \beta + \Delta\beta$
$t_0 - \Delta t_0, \beta$	t_0, β	$t_0 + \Delta t_0, \beta$
$t_0 - \Delta t_0, \beta - \Delta\beta$	$t_0, \beta - \Delta\beta$	$t_0 + \Delta t_0, \beta - \Delta\beta$

different parameter set (t_0', β') which defines the reconstruction of an altered longitudinal phase-space distribution. In other words, this procedure aims to take into account the uncertainty of the location of the phase-space centre concerning the arrival time and kinetic energy. Considering the typical bunch lengths between 0.5 and 2 ns an uncertainty Δt_0 of 0.5 ns is reasonably safe. When it comes to the kinetic energy, an uncertainty of 3 % is assumed for $\Delta\langle E \rangle$ according to the energy spread. This relates to an uncertainty of

$\Delta\beta \approx 1.5\,\%$. Additionally, one has to account for the tantalum and aluminium[4] foils, which will be covered in Sec. 7. As will be seen, the foils contribute an average net energy loss of about 3 %.

Interpretation of the Fit. Applying the procedure outlined above, the vertex location relative to the PC diamond detector has been determined for the data in Fig. 5.9. As denoted in plot 4 the vertex location corresponding to the trail is $d_{vtx}^{fit} = (102.3 \pm 1.8)$ cm. A comparison of this value with the location of the components in Fig. B.1 points to the first collimator aperture located at a distance of (102.44 ± 0.05) cm upstream the PC diamond detector. This means that the trail originates from a significant fraction of the particles interacting with the aperture. At the given low kinetic energy of 1.4 *A*MeV the range in matter is very short. The ions are typically fully stopped within a few micrometers. This led to the wrong assumption that, in good approximation, the ions are perfectly shadowed by the aperture, thus, they either pass the aperture unaffected or they are fully stopped.

Fitting the Mono-Crystalline Diamond Trails. Based on the extracted vertex location from the TOF trail, a quantitative interpretation of the trails occurring in the MC diamond detector measurement will be given in the following. Contrary to the TOF measurement, where the reconstruction of the kinetic energy does not suffer from a potential non-linearity, it is not clear that either the pulse integral or pulse height delivers a linear measure of the kinetic energy in case of the MC diamond approach. At least, as seen from the data in plot 1, the pulse height versus pulse integral does not follow a linear relation.

Figure 5.11 shows the data cuts of both samarium trails corresponding to the coloured regions in Fig. 5.9. Both fits to the trails, using parameterisation Eq. 5.1, are plotted as red lines. Using the procedure outlined above, the determined distances of the interaction vertices are $d_{vtx}^{fit,T1} = (86 \pm 8)$ cm and $d_{vtx}^{fit,T2} = (66 \pm 4)$ cm. The MC diamond detector is located (629.0 ± 0.5) mm downstream the first collimator aperture. As described above, this aperture has been found to be the location of interaction leading to the trail in the TOF measurement. The second collimator aperture is located (150.0 ± 0.5) mm downstream the first aperture and (479.0 ± 0.5) mm upstream the MC diamond detector. In the first instance, the distance of the first collimator fits the calculated value $d_{vtx}^{fit,T2}$ within the given uncertainty but, in this case, there is no component along the beam axis which can be associated with the value of $d_{vtx}^{fit,T1}$. Since the MCP module is retracted from the beam axis during measurements with the MC diamond detector, the only components between the diamond detector and the high-current slit US3DS5[5] are the two collimator apertures.

Assuming a linear response of the pulse integral with respect to the kinetic energy of the registered ion, the fitted values cannot be explained. However, compared to the TOF data, the fit parameterisation does not match the shape of the trails equally well. For small arrival times, close to 0 ns, the fitted curve delivers larger values than most of the measured data and, similarly, decreases with a lower slope towards larger arrival times. While the fit parameterisation still shows a good agreement with the recorded events, this hints a

[4] In case of the calorimetric measurement, only the tantalum foil is present which dominates the mean energy loss in the TOF setup.

[5] The high-current slit is located 2 m upstream the MC diamond detector.

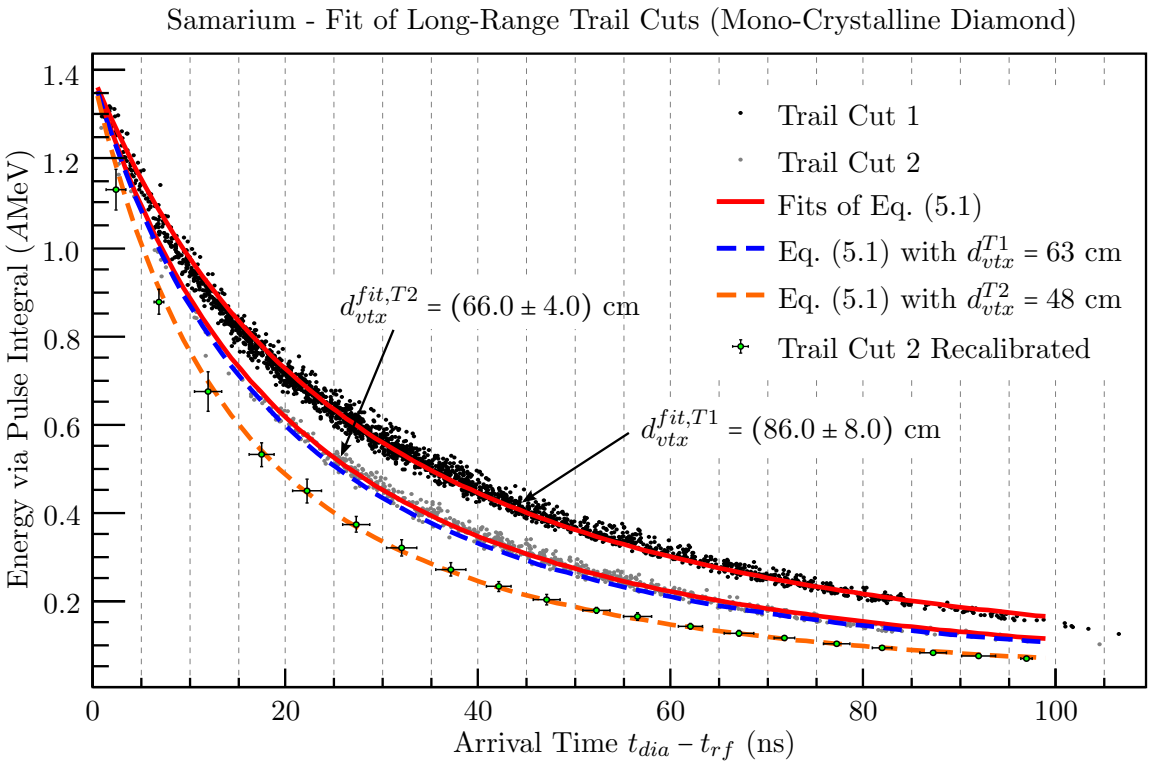

Fig. 5.11: Fit of trails visible in the samarium measurement. The black and grey events are inside the trail cuts highlighted in Fig. 5.9 and labeled "Trail Cut 1/2". The fit of Eq. (5.1) to each trail cut is given by the red lines. Additionally Eq. (5.1) is plotted for the collimator aperture locations d_{vtx}^{T1} = 64 cm and d_{vtx}^{T2} = 48 cm by the dashed lines. See text for data points labeled as "Trail Cut 2 Recalibrated".

possible non-linearity of the reconstructed kinetic energy with respect to the pulse-integral information.

In the following, the assumption that both trails originate from the collimator apertures is verified. The rightmost trail, at later arrival times, must then be associated with the vertex at a larger distance from the MC diamond detector. Hence, this trail is attributed to the first collimator aperture at a distance of about 63 cm. The expected functional relationship between kinetic energies and arrival times for this aperture is known by Eq. 5.1 and plotted as a blue dashed line in Fig. 5.11. This allows to set up a recalibration function which transfers the measured energies of the events in this trail to the expected one for the first collimator. The initial assumption requires that the very same recalibration function applied to the second trail must consequently agree with the theoretical trail function of the second collimator aperture plotted as a dashed orange line. This is accomplished by dividing the second trail, denoted as "Trail Cut 2", into bins of 5 ns with respect to the arrival time and calculating the average and RMS values. The latter ones are used as uncertainties given by the spread of the event distribution contained within the bin limits, marked as vertical dashed lines. Subsequently, the average values and uncertainties corresponding to the kinetic energy are rescaled according to the previously determined recalibration function,

denoted by "Trail Cut 2 Recalibrated".

A very good agreement of the recalibrated second trail with the theoretical trail function, given by the dashed orange line, strongly supports the hypothesis that the trails in the measurement are induced by the collimator apertures. Figure 5.12 shows the corresponding energy histograms of the trails, with the unprocessed energies on left plot and the recalibrated energies on the right plot. Energies below the detection threshold, given by the discrimination threshold of the diamond pulses and marked by the grey area, are not available. In either case, the broad energy distributions of the unprocessed and recalibrated data feature distinct maxima. A prominent smearing of the energy distributions around two different maxima is apparent which hints a stochastic process by multiple scattering.

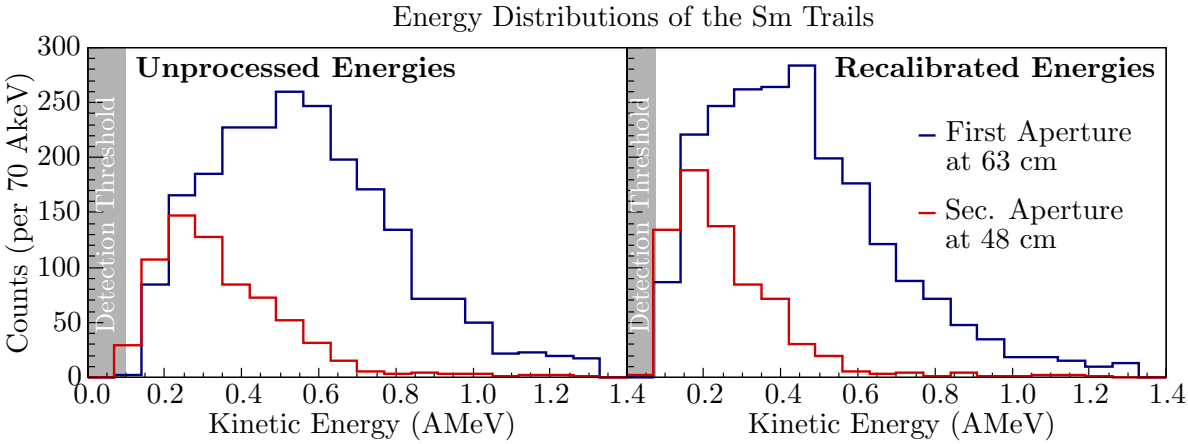

Fig. 5.12: Histogram of kinetic energies contained in the samarium trails. The left plot features the unprocessed energies, while the right plot shows recalibrated energies.

Gas clouds released by incident heavy-ion beams on metal targets, as used for imaging beam currents by Bieniosek et al. [80], can be ruled out as a dominant effect. The beam currents are significantly lower by orders of magnitudes in the setup at hand. Typical currents of several microamperes are then even further attenuated by the first collimator. Hence, the energy loss caused by a potential gas cloud should be smaller at the second aperture, closer to the diamond detector. On the contrary, as seen from the data in Fig. 5.12, this is not the case. The energy loss at the second aperture is significantly higher.

Nickel [81] studied slit scattering of proton microbeams. The author highlights the effect of surface roughness beyond transparency zones on energy and lateral displacement of scattered protons. Furthermore, he strengthens that the "*limited usefulness of experimental data from the literature indicates the need for dedicated slit scattering experiments*". While this may explain the origin of the trails discussed above, it didn't allow for a quantitative estimation of the effect. The underlying process of scattering at the collimator apertures for the given setup is still object to further investigation.

On a side note, the scattered ions at the aperture may have an impact on another measurement device relying on a high count of even smaller aperture holes of typically 0.1 mm diameter. The so-called pepperpot device targets the measurement of the 4-dimensional transverse phase-space distribution in a single shot. When a macro pulse hits the front

plate, a fraction of the pulse enters the regular grid of circular apertures and illuminate a small region on a scintillating screen. Depending on the transverse phase-space distribution the spot has a characteristic shape. The full ensemble of spots carries, in theory, the information of the transverse phase-space. However, the measured emittances are typically twice as large as expected [82–84]. While the focus is on improving the scintillation screen, the actual cause for this might be connected with scattering at the apertures, since it induces a lateral spread and alters the energy spectra of the incident ions.

Impact on the Longitudinal Phase-Space Distribution. Events inside the trails can be trivially trimmed as long as they are distinct from the core phase-space region at about 1.4 *A*MeV. However, the trails do reach into the core region, as can be seen in Fig. 5.8 for the calorimetric measurement and in Fig. 5.10 in case the TOF measurement. Unfortunately, the low statistics of the measurements does not allow for a sensible background treatment. On the other hand, judging by the energy distributions seen in Fig. 5.12 extrapolation to energies around 1.4 *A*MeV shows a significant decrease of trail events, in particular for the second aperture. Compared to the number of events inside the core region only a small fraction must be attributed to contributions from the trails.

Appendix E features the first measurement with the MC diamond detector setup using a low-current argon beam. Despite the low statistics, the two collimator apertures can be related to the trails in the same way as discussed above. In contrast to the samarium beam, a better linearity is provided. The experiment setup has been initially laid out for tests with an argon beam. Due to the higher energy deposited in the diamond detector in case of samarium, the amplifier is slightly driven into saturation for larger pulse heights. Therefore, it is not possible to evaluate the quality of the linearity associated with the pulse integral of the diamond detector, but only for the full DAQ chain consisting of the detector and the amplifier. The fit to the trail in the TOF measurement 4 was perfectly aligned to the trail distribution. The same fit parameterisation performed slightly worse on the calorimetric measurements in Fig. 5.11, as discussed above, and required a recalibration function using the theoretical values of the expected trail. However, the deviations of the fits in Fig. 5.11 are in agreement with an amplifier in slight saturation and, thus, supports the recalibration approach.

Number of Trails. In case of the TOF measurement only one prominent trail is visible while two trails appear in the calorimetric measurement. A possible explanation might be that scattered particles from the second aperture get stuck in the MCP PEEK module. In case of the calorimetric measurement, the MCP PEEK module is not exposed to the beam.

Final Remarks. All data consistently hinted a insufficient energy resolution. Furthermore, the correlation α is significantly smaller than expected by at least a factor of four. The next chapter introduces a Gaussian model space which allows to investigate the effect of the energy resolution on the covariance matrix and Twiss parameters.

Chapter 6

Influence of Finite Resolution

6.1 Introduction

All measured longitudinal phase-space distributions, using the experimental setup at hand, deviate from the expected energy spread σ_E and Twiss parameter α. According to the GSI injector division [77,78], the longitudinal phase-space parameters for the energy spread should be $\approx 1\,\%$ of the mean particle energy, whereas the Twiss parameter α should be ≈ 4 at the location of measurement as a rule of thumb. More precisely, the longitudinal RMS energy spread is expected to be below $1\,\%$ as can be seen from the expected high-current distribution of argon and uranium in Fig. 2.2 with $\sigma_E^{ar} = 0.80\,\%$ and $\sigma_E^{u} = 0.92\,\%$. Since an alternative longitudinal phase-space measurement is not available, these values are taken as reference. Significant deviations from the expected values can be safely considered unrealistic as they would not allow for a proper beam injection into the Alvarez structure.

All measurements in Chapter 5 show a larger energy spread σ_E and a significantly lower correlation α as expected, without exception. Typically, the energy spread is about $1.4\,\%$ to $1.6\,\%$ based on the robust estimator and even higher for the classical estimator. The robust estimate of the correlation α has been usually smaller than 0.7 and always smaller than 0.9. This suggests to investigate the effect of resolution on the measured phase-space distribution, the RMS emittance and the derived Twiss parameters. Table 6.1 gives an overview over the mentioned situation for high-current beams.

Tab. 6.1: Overview over expected (theoretical) characteristic values for high-current argon and uranium beams compared to the measured ones.

	Theoretical/Expected values	Measured values
Twiss α (correlation)	≈ 4	<1
Energy spread $\Delta E/\langle E\rangle$ ^{40}Ar	$0.92\,\%$ (92 mrad)	$1.40 - 1.60\,\%$
Energy spread $\Delta E/\langle E\rangle$ ^{238}U	$0.80\,\%$ (80 mrad)	

In this chapter this influence will be investigated qualitatively by approximating the phase-space distribution using a bivariate Gaussian model-space. The system response will also be of Gaussian type, which allows to derive a straightforward analytic approach.

6.2 Gaussian Model Space

A common approximation to describe the phase spaces in transverse and longitudinal degree of freedom in accelerator physics are Gaussian density distributions. One set of parameters to define those distributions is given by the variance-covariance matrix C, or the RMS emittance ε and the Twiss parameters $\{\alpha, \beta, \gamma\}$ which carry the same information and are explained in Sec. 2.3. As introduced in Eq. (2.24), this parameterisation can be connected to the bivariate Gaussian density distribution

$$G(x, y; \alpha, \beta, \gamma, \varepsilon) = \frac{1}{2\pi\varepsilon} \, \mathrm{e}^{-\frac{1}{2\varepsilon}\left(\gamma x^2 + 2\alpha x y + \beta y^2\right)} . \tag{6.1}$$

The distribution G serves as an approximation of the real phase-space distribution in the following sections. For simplicity, the degrees of freedom will be denoted generically as x and y. Variable x represents the phase or arrival time, whereas y represents the longitudinal energy or momentum degree of freedom.

6.3 Effect of Momentum Resolution

The TOF measurement features a detector separation of 80 cm. Together with the mean kinetic energy $\langle E \rangle \approx 1.4$ AMeV, the expected energy spread $\sigma_E \approx 1\,\%$ leads to an RMS spread of the TOF data of $\sigma_{tof} \approx 250$ ps, as will be discussed in Ch. 7. The RMS spread of the arrival time, i.e. the RMS bunch length, is typically larger than 1 ns. Hence, the measurement precision of the TOF timing needs to be significantly higher than the arrival timing. So far, this qualitative statement only considers the reproducibility of the projections on the x and y axes. At first, the investigation will be restricted to the one-dimensional case, where the influence of the TOF[1] resolution is take into account.

6.3.1 Transformed Emittance and Twiss Parameters

The actual measurement of the TOF is the sum of the exact value Y_G and uncertainty Y_g. These random variables are sampled in the measurement process. While Y_G is determined by the undisturbed longitudinal phase-space distribution of the beam $G(x, y; \alpha, \beta, \gamma, \varepsilon)$, Y_g comprises all uncertainties from discrimination jitter to actual dissipative contributions by the measurement setup. The underlying probability density function of Y_g is given by the system response g_y^{res}. As will be shown in the next chapter, many components contribute to

[1] This also applies to the direct calorimetric approach using the mono-crystalline diamond detector.

the system response. This suggests a normalised Gaussian system response function, with standard deviation $\sigma_{res,y}$ and mean μ

$$g_y^{res}(y;\sigma_{res,y},\mu) = \frac{1}{\sqrt{2\pi}\,\sigma_{res,y}}\,\mathrm{e}^{-\frac{(y-\mu)^2}{2\sigma_{res,y}^2}}\,. \tag{6.2}$$

The probability density of the compound random variable $Y_G + Y_g$, which represents the measurement process, is given by the convolution $\left(G * g_y^{res}\right)(x,y)$ of the corresponding probability distributions $G(x,y;\alpha,\beta,\gamma,\varepsilon)$ and $g_y^{res}(y;\sigma_{res,y},\mu=0)$,

$$\left(G * g_y^{res}\right)(x,y) = \int_{-\infty}^{+\infty}\mathrm{d}\kappa\; G(x,\kappa;\alpha,\beta,\gamma,\varepsilon)\; g(y-\kappa;\sigma_{res,y},\mu=0) = \\ \frac{1}{2\pi\varepsilon\sqrt{2\pi}\sigma_{res,y}}\int_{-\infty}^{+\infty}\mathrm{d}\kappa\;\mathrm{e}^{-\frac{1}{2\varepsilon}\left(\gamma x^2+2\alpha x\kappa+\beta\kappa^2\right)-\frac{(y-\kappa)^2}{2\sigma_{res,y}^2}}\,.$$

Taking the constant factor, with respect to the integration variable κ, out of the integral and rearranging the exponent in terms of κ and κ^2,

$$\left(G * g_y^{res}\right)(x,y) = \frac{1}{2\pi\varepsilon\sqrt{2\pi}\sigma_{res,y}}\,\mathrm{e}^{-\left(\frac{\gamma x^2}{2\varepsilon}+\frac{y^2}{2\sigma_{res,y}^2}\right)}\int_{-\infty}^{+\infty}\mathrm{d}\kappa\;\mathrm{e}^{-\left(\frac{\beta}{2\varepsilon}+\frac{1}{2\sigma_{res,y}^2}\right)\kappa^2+\left(\frac{y}{\sigma_{res,y}^2}-\frac{\alpha x}{\varepsilon}\right)\kappa}\,,$$

allows completion of the square of the exponent. The evaluation of the resulting integral is trivial using the well-known Gaussian integral

$$\int_{-\infty}^{+\infty}\mathrm{d}x\,\mathrm{e}^{-cx^2} = \sqrt{\frac{\pi}{c}}, \tag{6.3}$$

thus,

$$\left(G * g_y^{res}\right)(x,y) = \frac{1}{2\pi\varepsilon\sqrt{2\pi}\sigma_{res,y}}\,\mathrm{e}^{-\left(\frac{\gamma x^2}{2\varepsilon}+\frac{y^2}{2\sigma_{res,y}^2}\right)+\frac{1}{2}\frac{\left(\frac{y}{\sigma_{res,y}^2}-\frac{\alpha x}{\varepsilon}\right)^2}{\frac{\beta}{\varepsilon}+\frac{1}{\sigma_{res,y}^2}}} \\ \times\underbrace{\int_{-\infty}^{+\infty}\mathrm{d}\kappa\;\mathrm{e}^{-\frac{1}{2}\left(\frac{\beta}{\varepsilon}+\frac{1}{\sigma_{res,y}^2}\right)\left(\kappa-\frac{\left(\frac{y}{\sigma_{res,y}^2}-\frac{\alpha x}{\varepsilon}\right)}{\frac{\beta}{\varepsilon}+\frac{1}{\sigma_{res,y}^2}}\right)^2}}_{\sqrt{\frac{2\pi}{\frac{\beta}{\varepsilon}+\frac{1}{\sigma_{res,y}^2}}},\ \text{Eq. (6.3)}}\,.$$

Eventually, the phase space convoluted in y and denoted by $G'(x,y;\alpha',\beta',\gamma',\varepsilon')$ is represented by

$$\left(G * g_y^{res}\right)(x,y) = \frac{1}{2\pi\varepsilon\sigma_{res,y}\sqrt{\frac{\beta}{\varepsilon}+\frac{1}{\sigma_{res,y}^2}}}\,\mathrm{e}^{-\left(\frac{\gamma x^2}{2\varepsilon}+\frac{y^2}{2\,\sigma_{res,y}^2}\right)+\frac{1}{2}\frac{\left(\frac{y}{\sigma_{res,y}^2}-\frac{\alpha x}{\varepsilon}\right)^2}{\frac{\beta}{\varepsilon}+\frac{1}{\sigma_{res,y}^2}}}\,. \tag{6.4}$$

Hence, the bivariate Gaussian phase-space parameterisation is form-invariant under convolution with a Gaussian response function. After expansion of the exponent in Eq. (6.4), the transformed Twiss parameters can be extracted by equating the coefficients with respect to the definition of G' according to Eq. (6.1):

$$G'(x,y;\alpha',\beta',\gamma',\varepsilon') = \frac{1}{2\pi\varepsilon'}\,\mathrm{e}^{-\frac{1}{2\varepsilon'}\left(\gamma' x^2+2\,\alpha' x y+\beta' y^2\right)} \stackrel{!}{=} \left(G * g_y^{res}\right)(x,y)\,. \tag{6.5}$$

In the following, the transformed emittance and Twiss parameters are listed primed:

$$\varepsilon' = \varepsilon\sqrt{1+\sigma_{res,y}^2\frac{\beta}{\varepsilon}} \tag{6.6}$$

$$\alpha' = \frac{\alpha}{\sqrt{1+\sigma_{res,y}^2\frac{\beta}{\varepsilon}}} = \alpha\,\frac{\varepsilon}{\varepsilon'} \tag{6.7}$$

$$\beta' = \frac{\beta}{\sqrt{1+\sigma_{res,y}^2\frac{\beta}{\varepsilon}}} = \beta\,\frac{\varepsilon}{\varepsilon'} \tag{6.8}$$

$$\gamma' = \frac{\gamma+\frac{\sigma_{res,y}^2}{\varepsilon}}{\sqrt{1+\sigma_{res,y}^2\frac{\beta}{\varepsilon}}} = \left(\gamma+\frac{\sigma_{res,y}^2}{\varepsilon}\right)\frac{\varepsilon}{\varepsilon'} \tag{6.9}$$

The *Courant-Snyder invariant* is still valid:

$$\beta'\gamma' - \alpha'^2 = 1\,. \tag{6.10}$$

This is a strict requirement if $\{\alpha',\beta',\gamma'\}$ are Twiss parameters.

Furthermore, the product of Eq. (6.6) and Eq. (6.7) is an invariant under convolution with a Gaussian response function

$$\varepsilon\,\alpha \stackrel{!}{=} \varepsilon'\,\alpha'\,. \tag{6.11}$$

Together with the definition of the correlation α, see Eq. (2.21), it follows that the covariance σ_{xy} remains unaffected by the convolution

$$\sigma_{xy} \stackrel{!}{=} \sigma'_{xy}\,. \tag{6.12}$$

Alternative Approach. A more elegant way to calculate the transformed emittance and Twiss parameters Eqs. (6.6)-(6.9) is exploiting the fact that variances of independent com-

pound random variables $X + Y$ add. This means, within the presented model space, the standard deviation of the convoluted Gaussian is given by

$$\sigma'_y = \sqrt{\sigma_y^2 + \sigma_{res,y}^2}\,. \tag{6.13}$$

By definition, the RMS emittance and Twiss parameters are solely determined by the entries of the variance-covariance matrix Eq. (2.13). If the effect of the convolution on the covariance σ_{xy} is known, the transformed parameters can be written in terms of the new entries of the variance-covariance matrix C' after convolution. It turns out that the covariance of any two-dimensional function is invariant under convolutions of symmetric kernels and explains the equality in Eq. (6.11). The short proof is given in Appendix D.

6.3.2 Practical Implication on Experimental Data

To investigate the transformed Twiss parameters Eqs. (6.6)-(6.9), the longitudinal high-current argon phase-space distribution of Fig. (2.2) is taken as reference. In the first instance, the validity of the transformation is tested by comparing them to a sampled phase space (10^5 samples) which incorporates the argon reference distribution and the finite system response of the TOF measurement.

Figure 6.1 shows the sampled data in the top row, whereas the bottom row is the corresponding analytical phase-space density according to the transformed emittance and Twiss parameters. The leftmost column features the expected longitudinal phase-space distribution. The middle column shows the reference distribution and includes a finite system response g_y^{res} of two times the vertical waist[2] of the reference ellipse $2\cdot\sqrt{\beta/\varepsilon}$, which is about half the full projected width σ_y for the specific case of the reference distribution. Similarly, the right column considers a system response of 1.4 times the projection of the ellipse on the momentum axis. While the first case is an arbitrary intermediate choice, the second one transfers the expected emittance and Twiss parameters close to those of the measured data and will be discussed in detail in Sec. 6.5. All distributions feature the corresponding emittance ellipse and the prolonged big semi axis to emphasize its orientation. The dashed lines mark the orientation of the reference ellipse.

The distributions determined by the transformed emittance and Twiss parameters and the sampled ones agree. Hence, equations (6.6)-(6.9) describe the effect of the TOF resolution on the emittance and Twiss parameters in this model space. Furthermore, the effect of resolution is considerable. A width of the response function of two times the vertical ellipse waist $\sigma_y^{x=0}$, the middle column, is connected with a significant increase of the emittance ε by more than a factor of two with respect to the reference distribution. At the same time, the correlation α drops by the same factor. The effect on the Twiss parameters is even more evident in the right column. Although the covariance is invariant under the given transformation, the orientation of the ellipse, see Fig. 2.3, is not maintained and asymptotically approaches 0° towards lower resolution.

[2] See Fig. 2.3 for a visualisation of the vertical waist.

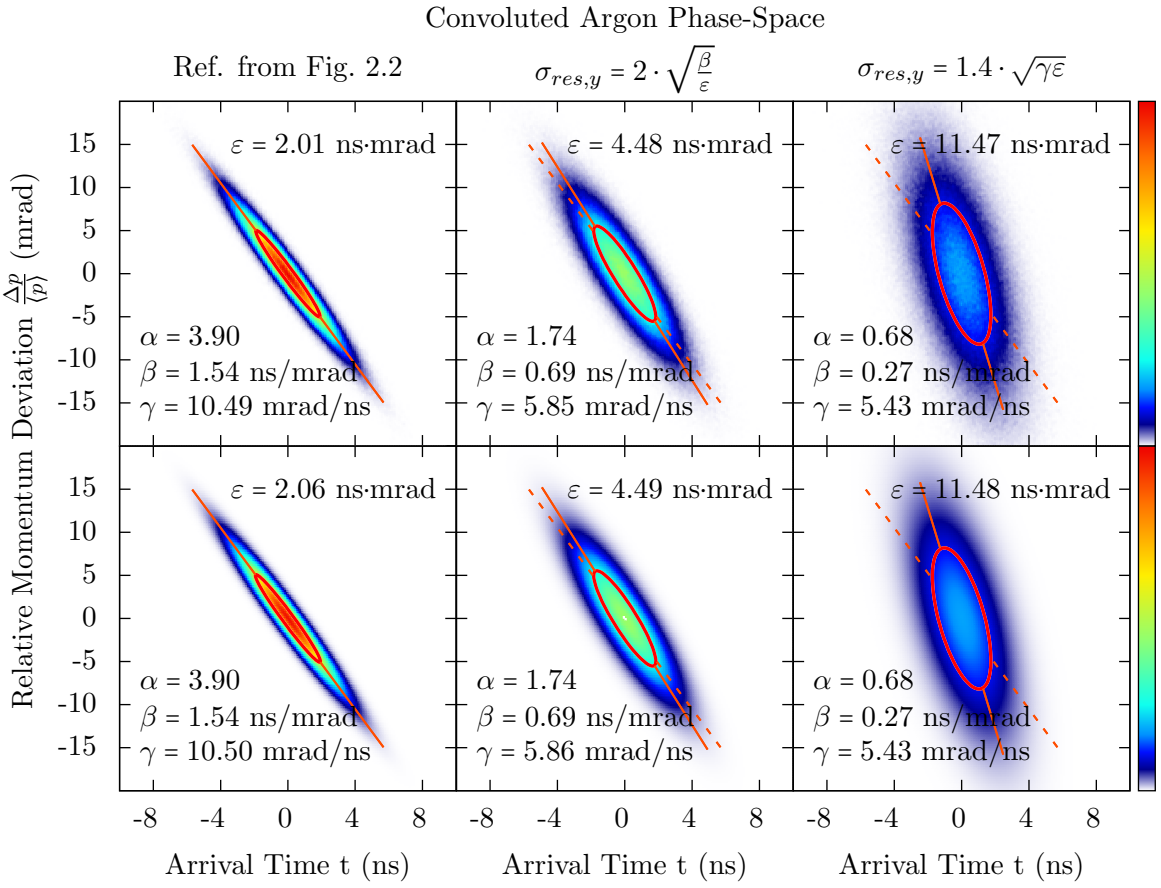

Fig. 6.1: Convolution of momentum with a Gaussian response functions of width $\sigma_{res,y}$. The top row data is the sampled theoretical distribution with the randomly sampled jitter from Eq. (6.2) added. The bottom row shows the corresponding analytical distribution Eq. (6.5) using the transformed Twiss parameters Eq. (6.6)-(6.9). The leftmost distributions corresponds to the expected longitudinal phase-space distribution of argon at high-currents, see Fig. 2.2, which has been provided by the GSI injector division [11].

6.3.3 Transformed Parameters vs. Resolution

The impact of TOF resolution is evident from the density plots in Fig. 6.1. It is interesting to investigate how the emittance and Twiss parameters change quantitatively with increasing width $\sigma_{res,y}$ of the response function g. Since the functional behaviour is dependent on the undisturbed phase-space distribution, mainly the vertical waist as introduced above, it is reasonable to use again the expected high-current argon distribution as reference.

In Fig. 6.2 and 6.3, the transformed values Eqs. (6.6)-(6.9) are plotted against the normalised system response $\sigma_{res,y}/\sigma_y^{x=0}$. In this work the normalised system response is defined as the width of the system response $\sigma_{res,y}$ in multiples of the vertical ellipse waist $\sigma_y^{x=0} = \sqrt{\varepsilon/\beta}$. For orientation purpose, all plots of the transformed parameters feature two vertical dashed lines which mark special widths $\sigma_{res,y}$ of the TOF response function g. They highlight

the abscissa values when the width of the response function is as large as the expected longitudinal beam energy width σ_y and $1.4\,\sigma_y$, with $\sigma_y = \sqrt{\gamma\varepsilon}$ (see Fig. 2.3). The red dot at $\sigma_{res,y} = 0$ should remind the reader of the real undisturbed value, i. e. when the response function is effectively a δ-distribution. All uncertainty of the system, i. e. timing uncertainties or dissipative effects, contribute to $\sigma_{res,y}$ and this aspect will be discussed in a later chapter.

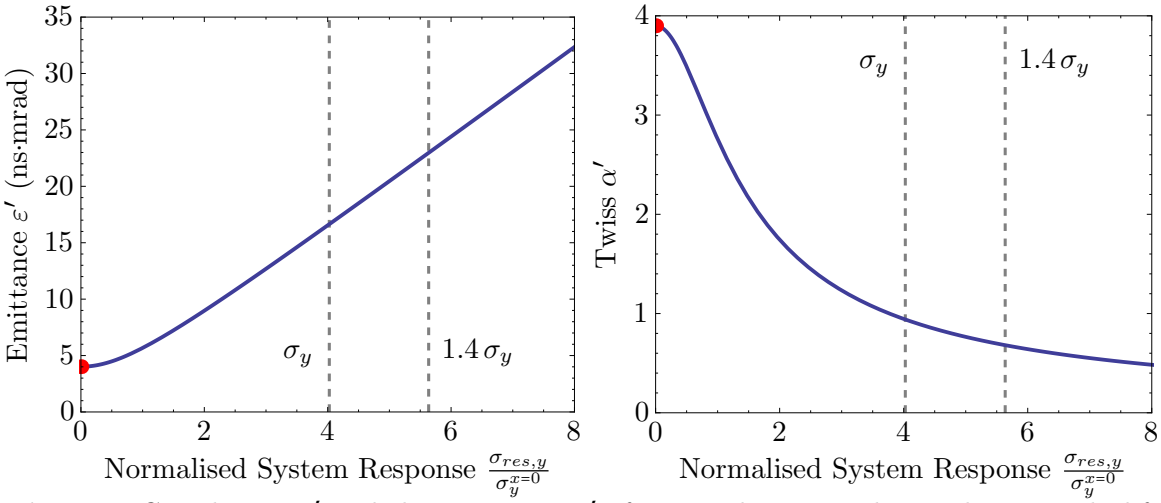

Fig. 6.2: Correlation α' and the emittance ε' after one-dimensional convolution with different widths of the TOF system response. See text for the abscissa scale.

RMS Emittance ε. The emittance ε' and correlation α' are shown in Fig. 6.2. As expected, the emittance increases as the TOF resolution decreases. The relationship between the width of the response function and the emittance ε' quickly levels towards an asymptotic slope of σ_x which is given by the bunch length. For a width $\sigma_{res,y} = \sigma_y$, the emittance is more than four times larger compared to the undisturbed phase space (red dot).

Twiss Paramter α. As the covariance σ_{xy} of an arbitrary distribution does not change under convolution with a symmetric kernel, the correlation α' scales in a reciprocal manner with ε'. The high sensitivity of α' with respect to width $\sigma_{res,y}$ of the response function is evident by the large gradient for small response widths. Already a response width equally to of the vertical $\sigma_y^{x=0}$, i. e. $\sigma_{tof} \approx 55$ ps for the given longitudinal phase-space, results in a drop of the measured value of α' by 30 %. This means that even with a theoretical TOF response $\sigma_{tof} \approx 55$ ps, this is connected with a large error. Once taking into a account a response width of same size as σ_y, i. e. the projected energy spread, α even drops by 75 %. In this case σ_{tof} is ≈ 225 ps. Finally, at a resolution $\sigma_{res,y} = 1.4\,\sigma_y$ ($\sigma_{tof} \approx 315$ ps), α drops by ≈ 83 %. Since this assumed response function reproduces the measured RMS emittance and Twiss parameters in very good agreement, see Sec. 6.5, one has to consider the effective response function of the system at about that regime.

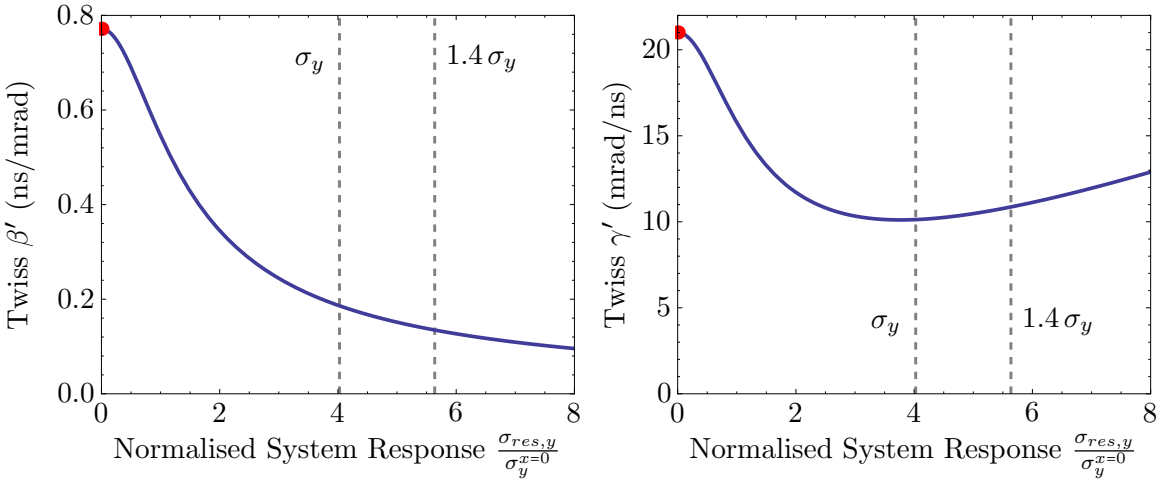

Fig. 6.3: Twiss parameter β' and γ' after one-dimensional convolution with different widths of the TOF system response function g. See text for the abscissa scale.

Twiss Parameter β. The remaining equations of the transformed Twiss parameters β' and γ' are plotted in Fig. 6.3. For the one-dimensional convolution, the behaviour of β' equals α' and, as σ_x remains unaffected, scales with ε'^{-1}.

Twiss Parameter γ. Contrary to the behaviour of β', γ' does not feature a monotonic trend for the reference distribution at hand. For small uncertainties, γ' decreases and starts to increase for response widths larger than σ_y. Rearranging Eq. (6.9) reveals a parabolic term which scales with α^2

$$\gamma' = \gamma\frac{\varepsilon'}{\varepsilon} - \sigma_{res,y}^2\frac{\alpha^2}{\varepsilon'}\,. \tag{6.14}$$

Hence, the dip is more distinct the larger the real, undisturbed value of α is.

6.3.4 Resolution Requirements

It is evident from Fig. 6.2 and Fig. 6.3 that the measurement of the emittance and Twiss parameters strongly depends on the TOF timing resolution. Even a small variation of the TOF resolution has a large effect on the measured values. One reason for this sensitivity can be extracted from Eq. (6.6), the transformation of the measured RMS emittance ε'. As described in Section 2.3 (see Fig. 2.3), the term ε/β relates to the vertical waist $\sigma_y^{x=0}$ of the emittance ellipse. Hence, Eq. (6.6) can be rewritten to yield

$$\varepsilon' = \varepsilon\sqrt{1 + \left(\frac{\sigma_{res,y}}{\sigma_y^{x=0}}\right)^2}\,. \tag{6.15}$$

This shows that the emittance can only be reproduced with a relatively low error of $\approx 10\,\%$ if $\sigma_{res,y} \lesssim \sigma_y^{x=0}/2$. Consequently, the measurement setup would require an effective timing

resolution of ≈ 28 ps for the given expected longitudinal phase-space distribution. Assuming a response width of $\sigma_{res,y} = \sigma_y^{x=0} (\approx 55\,\text{ps})$ would already result in an error of more than 40 %. The high sensitivity of the Twiss parameters on the timing resolution can be attributed to the high sensitivity on the RMS emittance.

It is important to note that the timing requirement to measure the projected energy spread is typically much lower compared to the Twiss parameters. As previously shown, the timing requirements of the emittance and Twiss parameters depend on the waist $\sigma_y^{x=0}$ of the undisturbed emittance ellipse. Hence, the ratio between ellipse waist and full projection provides the information about the timing requirement for the emittance and Twiss parameters compared to resolving the energy spread only. This is also motivates the abscissa scale in Fig. 6.2 to Fig. 6.3. Using the parameterisation given in Fig. 2.3 and exploiting the Courant-Snyder invariant leads to

$$\frac{\text{waist}_y}{\text{projection}_y} = \frac{\sigma_y^{x=0}}{\sigma_y} = \frac{\sqrt{\frac{\varepsilon}{\beta}}}{\sqrt{\varepsilon\gamma}} = \frac{1}{\sqrt{1+\alpha^2}}\,. \tag{6.16}$$

Hence, the Twiss parameter α is a measure for this required timing resolution. The larger α is, the higher the timing resolution has to be compared to the one required for the projection only. As a rule of thumb, for $\alpha > 2$, the ratio given in Eq. (6.16) is $\approx 1/\alpha$. Substitution of Eq. (6.16) into Eq. (6.15) yields

$$\varepsilon' = \varepsilon\sqrt{1 + (1+\alpha^2)\left(\frac{\sigma_{res,y}}{\sigma_y}\right)^2} \approx \varepsilon\sqrt{1 + \alpha^2\left(\frac{\sigma_{res,y}}{\sigma_y}\right)^2}\,. \tag{6.17}$$

Obviously, the goal of a measurement must be to guarantee $\varepsilon' \simeq \varepsilon$. This is only possible if the radical in Eq. (6.17) is close to one. As the non-constant term scales with α this task gets more difficult the larger α is. Taking the exemplary 10 %-error criteria for $\sigma_{res,y}$ leads to a rule for the TOF response-width:

$$\sigma_{res,y}^{10\,\%} \lesssim \frac{\sigma_y}{2\alpha} \tag{6.18}$$

For a given energy spread σ_y, the timing resolution has to be higher for larger values of α. The numbers at the beginning of this section are reproduced as required and yield $\sigma_{res,y} \lesssim 29$ ps for the given reference phase-space distribution.

6.4 Effect of Momentum and Phase Resolution

The previous section considered the influence of the TOF resolution only. In fact, the arrival timing determining the (relative) phase is also connected to an uncertainty. This contribution can also be described approximately as a Gaussian response function g_x^{res} analogous to g_y^{res}. Hence, for Gaussian error contributions in both longitudinal degrees of freedom, TOF and arrival timing, the corresponding transformation is provided by the two-dimensional convolution of the undisturbed phase space $G(x, y)$, Eq. (6.1), with the Gaussian distribution $(g_x^{res} \cdot g_y^{res})$

$$\left(G * (g_x^{res} \cdot g_y^{res})\right)(x,y) = \frac{1}{(2\pi)^2 \varepsilon\, \sigma_{res,x}\sigma_{res,y}} \iint_{-\infty}^{+\infty} \mathrm{d}\kappa\, \mathrm{d}\xi\, \mathrm{e}^{-\frac{1}{2\varepsilon}\left(\gamma\kappa^2 + 2\alpha\kappa\xi + \beta\xi^2\right) - \frac{(x-\kappa)^2}{2\sigma_{res,x}^2} - \frac{(y-\xi)^2}{2\sigma_{res,y}^2}} =$$

$$\frac{1}{2\pi\varepsilon''}\, \mathrm{e}^{-\frac{1}{2\varepsilon''}\left(\gamma'' x^2 + 2\alpha'' xy + \beta'' y^2\right)} = G''(x,y;\alpha'',\beta'',\gamma'',\varepsilon'')\,. \quad (6.19)$$

The integration of Eq. (6.19) and equating the coefficients with respect to $G(x,y)$ provides the Twiss parameters (double primed) after taking into account a limited resolution in both degrees of freedom. Non-primed Twiss parameters are associated with the undisturbed phase space.

$$\varepsilon'' = \varepsilon\sqrt{\left(1+\sigma_{res,x}^2\frac{\gamma}{\varepsilon}\right)\left(1+\sigma_{res,y}^2\frac{\beta}{\varepsilon}\right) - \left(\sigma_{res,x}\sigma_{res,y}\frac{\alpha}{\varepsilon}\right)^2} \quad (6.20)$$

$$\alpha'' = \frac{\alpha}{\sqrt{\left(1+\sigma_{res,x}^2\frac{\gamma}{\varepsilon}\right)\left(1+\sigma_{res,y}^2\frac{\beta}{\varepsilon}\right) - \left(\sigma_{res,x}\sigma_{res,y}\frac{\alpha}{\varepsilon}\right)^2}} = \alpha\,\frac{\varepsilon}{\varepsilon''} \quad (6.21)$$

$$\beta'' = \frac{\beta + \frac{\sigma_{res,x}^2}{\varepsilon}}{\sqrt{\left(1+\sigma_{res,x}^2\frac{\gamma}{\varepsilon}\right)\left(1+\sigma_{res,y}^2\frac{\beta}{\varepsilon}\right) - \left(\sigma_{res,x}\sigma_{res,y}\frac{\alpha}{\varepsilon}\right)^2}} = \left(\beta + \frac{\sigma_{res,x}^2}{\varepsilon}\right)\frac{\varepsilon}{\varepsilon''} \quad (6.22)$$

$$\gamma'' = \frac{\gamma + \frac{\sigma_{res,y}^2}{\varepsilon}}{\sqrt{\left(1+\sigma_{res,x}^2\frac{\gamma}{\varepsilon}\right)\left(1+\sigma_{res,y}^2\frac{\beta}{\varepsilon}\right) - \left(\sigma_{res,x}\sigma_{res,y}\frac{\alpha}{\varepsilon}\right)^2}} = \left(\gamma + \frac{\sigma_{res,y}^2}{\varepsilon}\right)\frac{\varepsilon}{\varepsilon''} \quad (6.23)$$

The calculation of $\beta''\gamma'' - \alpha''^2$ confirms that the Courant-Snyder invariant is still valid as required. Also the covariance σ_{xy} is still conserved as Eq. (6.23) shows. This must be the case as the convolution Eq. (6.19) can be applied in successive steps for each degree of freedom. For each step the proof given in Appendix D is valid. As required, in the limit $\sigma_{res,x} = 0$ the two-dimensional transformation are equal to Eq. (6.6)-(6.9).

Additionally to the vertical waist $\sigma_y^{x=0} = \sqrt{\beta/\varepsilon}$, the horizontal waist $\sigma_x^{y=0} = \sqrt{\gamma/\varepsilon}$ appears in the equations for symmetry reason. Hence, all argumentations for the required timing resolution, depending on the ellipse waist, can be applied in an analogous way for the horizontal degree of freedom.

6.4.1 Back-Transformation of Measured Values

If the widths $\sigma_{res,x}$ and $\sigma_{res,y}$ of the response functions are known, an attempt to approximate the real values for the RMS emittance and Twiss parameters is possible. The back-transformations of Eqs. (6.20)-(6.23) from the measured double-primed parameters to

the real parameters $\{\varepsilon'', \alpha'', \beta'', \gamma''\} \rightarrow \{\varepsilon, \alpha, \beta, \gamma\}$ are listed in the following:

$$\varepsilon = \varepsilon'' \sqrt{\left(1 - \sigma_{res,x}^2 \frac{\gamma''}{\varepsilon''}\right)\left(1 - \sigma_{res,y}^2 \frac{\beta''}{\varepsilon''}\right) - \left(\sigma_{res,x}\sigma_{res,y} \frac{\alpha''}{\varepsilon''}\right)^2} \tag{6.24}$$

$$\alpha = \frac{\alpha''}{\sqrt{\left(1 - \sigma_{res,x}^2 \frac{\gamma''}{\varepsilon''}\right)\left(1 - \sigma_{res,y}^2 \frac{\beta''}{\varepsilon''}\right) - \left(\sigma_{res,x}\sigma_{res,y} \frac{\alpha''}{\varepsilon''}\right)^2}} \tag{6.25}$$

$$\beta = \frac{\beta'' - \frac{\sigma_{res,x}^2}{\varepsilon''}}{\sqrt{\left(1 - \sigma_{res,x}^2 \frac{\gamma''}{\varepsilon''}\right)\left(1 - \sigma_{res,y}^2 \frac{\beta''}{\varepsilon''}\right) - \left(\sigma_{res,x}\sigma_{res,y} \frac{\alpha''}{\varepsilon''}\right)^2}} \tag{6.26}$$

$$\gamma = \frac{\gamma'' - \frac{\sigma_{res,y}^2}{\varepsilon''}}{\sqrt{\left(1 - \sigma_{res,x}^2 \frac{\gamma''}{\varepsilon''}\right)\left(1 - \sigma_{res,y}^2 \frac{\beta''}{\varepsilon''}\right) - \left(\sigma_{res,x}\sigma_{res,y} \frac{\alpha''}{\varepsilon''}\right)^2}} \tag{6.27}$$

Only considering the TOF resolution $\sigma_{res,y}$, the one-dimensional back-transformations can be derived from Eq. (6.6)-(6.9). This is identical to setting $\sigma_{res,x}$ to zero in Eq. (6.24)-(6.27).

$$\varepsilon = \varepsilon' \sqrt{1 - \sigma_{res,y}^2 \frac{\beta'}{\varepsilon'}} \tag{6.28}$$

$$\alpha = \frac{\alpha'}{\sqrt{1 - \sigma_{res,y}^2 \frac{\beta'}{\varepsilon'}}} \tag{6.29}$$

$$\beta = \frac{\beta'}{\sqrt{1 - \sigma_{res,y}^2 \frac{\beta'}{\varepsilon'}}} \tag{6.30}$$

$$\gamma = \frac{\gamma' - \frac{\sigma_{res,y}^2}{\varepsilon'}}{\sqrt{1 - \sigma_{res,y}^2 \frac{\beta'}{\varepsilon'}}} \tag{6.31}$$

6.5 Comparison to Real Data

The high-current argon measurement from Sec. 5.2.4 can be compared to the corresponding reference phase-space used in this chapter. The RMS emittances and Twiss parameters in Fig. 6.1 differ significantly between measurement and reference phase-space. As the bunch length σ_b is expected to be about 1.8 ns and $\alpha \approx 4$, Eq. (6.18) requires that $\sigma_{res,x}$ is smaller than ≈ 230 ps. This is certainly fulfilled for the arrival time precision as will be discussed in the next chapter. Hence, only the TOF resolution will be considered for this measurement.

Figure 6.4 shows the measured longitudinal data on the left and the transformed reference distribution on the right. The transformation is based on a TOF system-response of about 1.4 times the projected width σ_{tof} or, in terms of energy, 1.4 times the energy spread. This value has been determined by manually matching the transformed reference distribution to the measured one. Nevertheless, it is noteworthy how well the Twiss parameters and the emittance agree although the model is only based on bivariate Gaussian distributions. The measured data features a more complicated structure with a rather sharp edge for the

early arriving ions and a double peak at the centre. Other non-Gaussian contributions are the trails discussed in the previous chapter, i. e. scattered ions at the high-current slits and collimator apertures. For comparison, the reference ellipse is depicted in black.

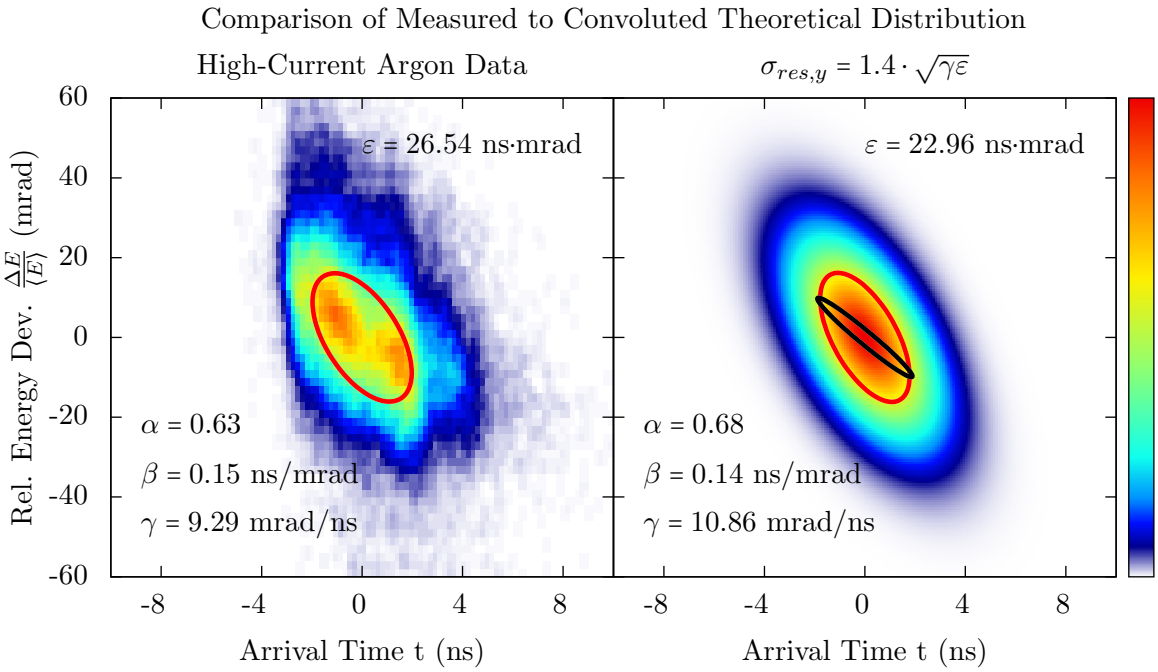

Fig. 6.4: The left longitudinal phase-space distribution shows the measured high-current argon data from the HIPPI campaign (see Sec. 5.2.4). For comparison, the right data shows the theoretical expected Gaussian distribution which has been convoluted in the energy degree of freedom to match the measured energy spread. The one-dimensional convolution has been accomplished using Eqs. (6.6)-(6.9).

According to the GSI injector division, the measured values, in particular the high energy spread and low correlation α, are very unlikely to be true. The measured distribution would not allow for high transmissions through the Alvarez structure, contrary to the actual situation during machine operation. Therefore, it is to assume that the resolution has indeed a major effect in on the measurement. This leads to extremely high timing requirements. Hence, systematic uncertainties of the TOF setup are investigated in the next chapter.

Chapter 7

Systematic Effects on Resolution

A reliable measurement setup requires reasonable access to sources of intrinsic uncertainties and systematic error contributions to get a quantified measure of the achievable resolution. While this holds true for all experimental setups and measurement instrumentation in general, it is most important if at least one component of the setup has a maximum resolution performance close to the minimum resolution required. This is not necessarily based on bad design decisions, but often represents a challenge due to available hardware.

To estimate the required resolution of the momentum/energy measurement via time-of-flight (TOF), it is helpful to take a closer look at the expected beam parameters in question. Longitudinal phase-space distributions downstream from the *High Current Injector* (HSI, see Fig. 2.10) right after the first stripper section (Fig. 3.3) are expected to have an RMS energy spread σ_E of about 1 % with respect to the mean particle energy $\langle E \rangle$ of about 1.4 AMeV [77]. Since the setup is based on timing measurements, the accuracy depends on the timing performance of detectors and readout electronics. A particle of mean energy $\langle E \rangle$ compared to a particle with energy of $\langle E \rangle + \sigma_E$ has an arrival time delay σ_t of (see Sec. 4.1.5)

$$\sigma_t = t_{\langle E \rangle} - t_{\langle E \rangle + \sigma_E} \approx \frac{\sigma_E}{\langle E \rangle} \cdot \frac{l_{tof}}{2c \langle \beta \rangle} \quad \text{with} \quad \frac{\sigma_E}{\langle E \rangle} \ll 1 \,. \tag{7.1}$$

Due to the limited space at the UNILAC site, the detector separation for the TOF measurement is about 800 mm which results in $\sigma_t \approx 240$ ps for $\sigma_E / \langle E \rangle = 0.01$. Figure 7.1 shows the relation of σ_t with respect to the drift length l_{tof} under the conditions stated above. Assuming a Gaussian energy distribution and a Gaussian function of the system response, an estimate of the impact of a resolution on the measurement can be made. In the following, the real width of the arrival time distribution is denoted by σ_t, whereas the width of the system response[1] function is denoted by σ_{res}. Consequently, the measured width σ_m is given by

$$\sigma_m^2 = \sigma_t^2 + \sigma_{res}^2 \,, \tag{7.2}$$

[1] The subscript *res* and its meaning is kept in the following. It should be strengthened that it relates to the system *response* and **not** to the *resolution*.

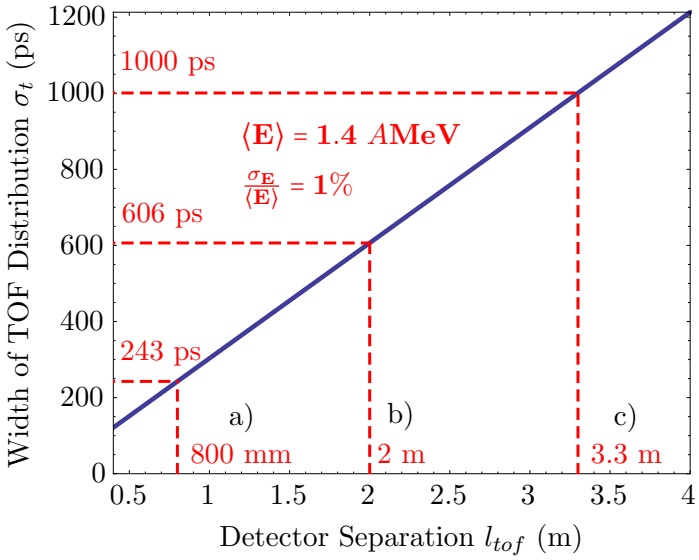

Fig. 7.1: The RMS difference in TOF σ_t between a particle of mean energy $\langle E\rangle$ = 1.4 AMeV and a particle with an energy of $\langle E\rangle + \sigma_E$ is plotted versus the drift length l_{tof}. A longitudinal energy distribution with an RMS energy spread of 1 % is assumed. The dashed lines mark **a)** the current TOF detector separation of 800 mm, **b)** a hypothetical drift length of 2 m with σ_t^{2m} and **c)** a drift length of about 3.3 m which would correspond to a much more relaxed $\sigma_t^{3.3m}$ of 1 ns.

using the fact that convoluting of Gaussian distributions effectively means to add their variances. A relative error f_{err} can be defined as

$$f_{err} = \frac{\Delta\sigma}{\sigma_t} = \frac{\sigma_m - \sigma_t}{\sigma_t} = \frac{\sqrt{\sigma_t^2 + \sigma_{res}^2} - \sigma_t}{\sigma_t} \,. \tag{7.3}$$

Generally, the allowed width of the system response σ_{res}, which corresponds to a certain relative error f_{err}, is given by

$$\frac{\sigma_{res}}{\sigma_t} = \sqrt{(f_{err}+1)^2 - 1} \tag{7.4}$$

and plotted in Fig. 7.2 as the fraction of σ_t. For the present experimental setup, a width of $\sigma_{res}^{1\,\%} \leq 34$ ps, representing the systems response, is required to reproduce the expected energy spread ΔE in a direct measurement within a relative resolution f_{err} of 1 %. On the other hand, aiming for an accuracy of 10 % would allow a system response of up to $\sigma_{res}^{10\,\%} \approx 110$ ps. This considers only the precision of how well the second momenta are represented by the measurement. Any details of the distribution of smaller scale than σ_{res} cannot be resolved.

The measurement setup is an intercepting device, which means by definition that major interaction between the particle distribution and the setup occurs. Since a significant amount

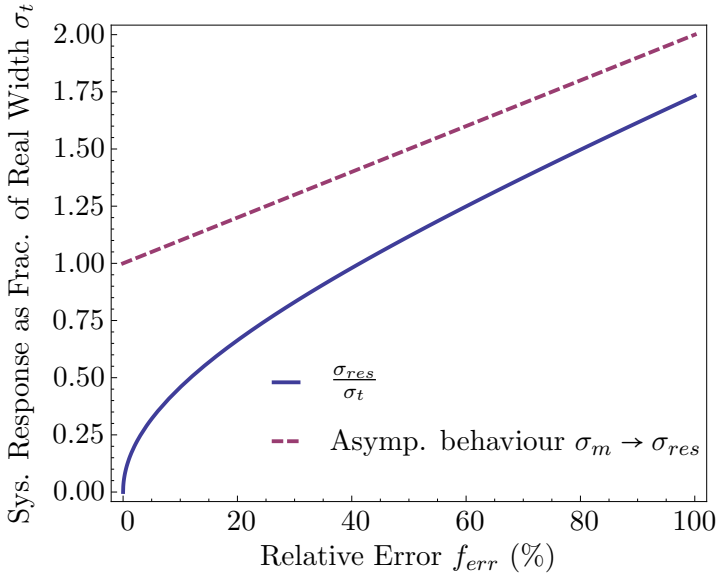

Fig. 7.2: The continuous line shows the maximum width allowed for the system response σ_{res} to provide a relative error f_{err}, generalised by the fraction with respect to the real width σ_t. For increasing f_{err} the actual energy distribution becomes irrelevant and the measurement only represents the response of the detector and readout electronics, such that $\sigma_m = \sigma_{res}$, given by the dashed asymptote.

of the particle-device interaction is contributed by the attenuation mechanism, dissipative effects are present prior to the actual measurement process between the two detectors. Hence, meeting the time resolution of the detector and readout electronics alone is not sufficient to provide a precise measurement. Moreover, all effects, i. e. interactions on the beam and, thus, parameters of interest must be small compared to typical values of beam parameters. This includes the accelerator setup necessary for the measurement procedure.

For the setup, two classes of error contributions can be coarsely differentiated which may lead to distortions of the original (unaffected) phase-space distribution:

- Effects on real physical phase-space distribution: $\{\Delta E_{diss,i}\}$
- Timing precision of electronic and detector components: $\{\Delta t_i\}$

The effective uncertainty is given by means of RMS timing uncertainties Δt_i, where possible, originating from different components of the measurement setup which in turn can be expressed as resulting uncertainties in energy observation ΔE_i in the classical limit

$$\Delta E_i \approx \frac{\mathrm{d}}{\mathrm{d}t} E(t)\bigg|_{t=t_{\langle E\rangle}} \cdot \Delta t_i = -2\,\frac{E(t_{\langle E\rangle})}{t_{\langle E\rangle}}\Delta t_i = -2\,\frac{\langle E\rangle}{t_{\langle E\rangle}}\Delta t_i\,. \tag{7.5}$$

Additionally, direct energy contributions of uncertainties $\Delta E_{diss,i}$ are imposed by dissipative elements, e. g. as given by the energy spread introduced by both foils. Consequently, the

net relative uncertainty of a given set of sufficient uncorrelated contributions[2] $\{\Delta E_{diss,i}\}$ and $\{\Delta t_i\}$ is calculated by

$$\frac{\Delta E}{\langle E\rangle} \approx \sqrt{\left(\frac{2}{t_{\langle E\rangle}}\right)^2 \sum_{\{\Delta t_i\}} (\Delta t_i)^2 + \frac{1}{\langle E\rangle^2} \sum_{\{\Delta E_{diss,i}\}} (\Delta E_{diss,i})^2}\,. \tag{7.6}$$

The direct measurement of the net resolution would require a well-known reference beam and sufficiently small longitudinal energy spread. A perfect reference would be a quasi-monochromatic beam with an energy spread of $\Delta E \ll 1\,\%\,\langle E\rangle$, which provides direct access to the response function and, thus, represents a measure of the net resolution.

In the following, components of the setup will be investigated in detail, focusing on a measure of uncertainty contribution. Finally, the total uncertainty will be compared to the measurement characteristics.

7.1 Tantalum Foil

Single-particle detection is accomplished by deflecting primary particles into the detector acceptance. This is done by Coulomb scattering at a thin tantalum foil of (210 ± 21) µg/cm^2, which corresponds to a thickness of (126 ± 13) nm, mounted behind a cylindrical aperture with a diameter of (2.0 ± 0.1) mm (see Fig. B.1). Subsequently, scattered particles are selected by a collimator under a small solid angle which provides an attenuation factor on the order of 10^8. For a detailed description, see Sec. 3.4.

This section covers several aspects concerning the impact of the tantalum foil on the measurement precision. It includes the discussion of energy straggling of heavy-ion projectiles in perfect foils and the more realistic assumption of variation of thickness. The section closes with a discussion of the possible impact of the transversal phase-space distribution on the total scattering angle and, thus, different momentum transfers to the target nucleus is covered.

7.1.1 Electronic Stopping and Straggling

In addition to the specific mean energy shift of the incident beam particles when passing through the tantalum foil, the statistical transfer of momentum to the electrons introduces a broadening of the energy distribution. Electronic stopping in matter and the resulting *mean* energy loss can be described by the well-known Bethe-Bloch formula [85]

$$-\frac{\mathrm{d}E}{\mathrm{d}x} = \frac{4\pi n z^2}{m_e c^2 \beta^2} \left(\frac{e^2}{4\pi\epsilon_0}\right)^2 \left[\ln\left(\frac{2\,m_e\,c^2\,\beta^2}{I\,(1-\beta^2)}\right) - \beta^2\right]. \tag{7.7}$$

[2] Slight but non-dominating correlated effects are for example the separation jitter due to the tilted aluminium foil inside the MCP module (Sec. 7.3.3) and the signal propagation time jitter on the diamond electrode (Sec. 7.4.2.2).

The specific parameters are the *projectile charge* z, the *electron number density* n of the target medium and the *mean ionisation potential* I. The mean ionisation potential I for a certain target can be approximated [53] by

$$I \approx (11 \pm 3)\, Z \text{ eV}, \tag{7.8}$$

where Z is the target atomic charge number.

The *mean* energy shift is not a critical issue for the determination of the phase space and will be covered in Sec. 7.7.1. Still, as a statistical process, fluctuations occur usually referenced as *(energy) straggling*, sometimes called *collisional straggling*, which is not described by the Bethe-Bloch equation. Such dissipative contributions affect the real phase and contribute a component $\Delta E_{diss,i}$ to Eq. (7.6). Quantitative estimations of collisional straggling can be received by Monte-Carlo simulation programs such as SRIM [54].

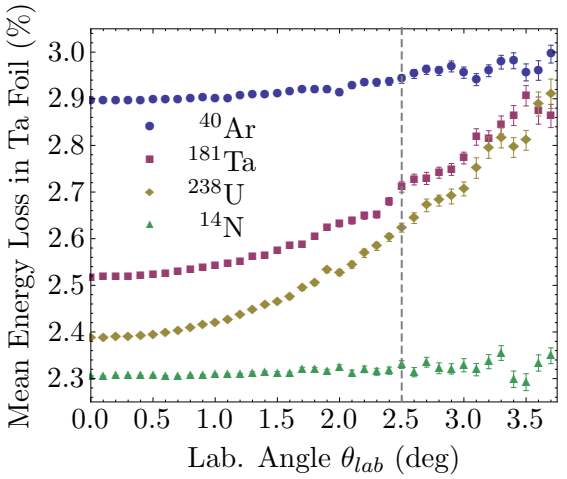

Fig. 7.3: SRIM: Total energy loss of $\langle E \rangle$=1.4 *A*MeV projectiles after transmission through the 126 nm Ta foil. The values are given in % with respect to the mean energy $\langle E \rangle$ as a function of the laboratory angle.

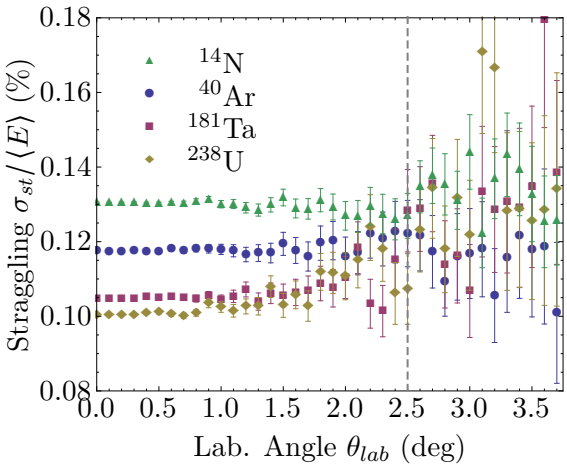

Fig. 7.4: SRIM: Energy broadening RMS after transmission through the 126 nm Ta foil. Values are given in % with respect to the mean energy $\langle E \rangle$=1.4 *A*MeV. The large error bars are connected to the low statistics, see text.

A SRIM calculation for nitrogen, argon, tantalum and uranium projectiles with 10^7 particles each has been carried out to estimate the dissipative straggling contribution. The projectiles were transmitted through a tantalum foil of 210 µg/cm^2 which corresponds approximately to a thickness of 126 nm or roughly about 1300 atomic layers. The incident angle of the projectiles was set to 1.25° to match the real configuration. Only those particles were taken into account which have been scattered into the given solid angle of $(8.0 \pm 0.5) \times 10^{-6}$ sr, sampled on scattering angles θ from 0° to 3.7° in the laboratory frame. A laboratory angle of θ = 2.5° represents the configuration of the measurement setup. Figure 7.3 shows the energy loss in % with respect to the mean energy $\langle E \rangle$ for different angles of particle emission. The dashed vertical line marks the measurement setup with an emission angle of $(2.50 \pm 0.01)°$. The stopping power $-\frac{\mathrm{d}E}{\mathrm{d}x}$, i. e. the energy loss per unit distance, for uranium is larger than that of argon and tantalum due to its higher charge z. Nevertheless, the overall energy loss

is smaller since the total energy of 333.2 MeV for uranium is much higher in comparison to that of argon with 56 MeV. As seen from the data, the relative mean energy loss is estimated in the range between 2.3 % and 3 %. Apart from the statistical error, represented by the error bars, the semi-empirical SRIM code, as of 2010, claims to provide an overall model based accuracy of about 5 % (1-sigma) concerning the calculation of the stopping power [86].

For an estimate of the straggling contribution, it is useful to extract the transmitted particle energy RMS value from the SRIM output. Figure 7.4 shows the RMS values of nitrogen, argon, tantalum and uranium projectiles with respect to the mean energy in % versus the emission angle θ. The configuration of the setup is, again, marked by the dashed vertical line. Since the particle data is evaluated by considering the geometry of the setup, and thus a very small solid angle, the statistical error increases significantly with $\theta > 1.5°$ For the statistic error contribution, the number of events N is considered via $\frac{\sigma_{st}}{\langle E \rangle}/\sqrt{2(N-1)}$, according to the statistical uncertainty of the classical estimator of the standard deviation ([65], p. 133). The spread between the four ion species used in the simulation are confined within a relative deviation of 30 %. If the obtained values are related to the *expected* RMS energy spread of 1 % $\langle E \rangle$, it seems legitimate to consider the straggling contribution of about 13 %. The histograms of uranium and argon for an angle of $\theta = 1°$ are shown in Fig. 7.5.

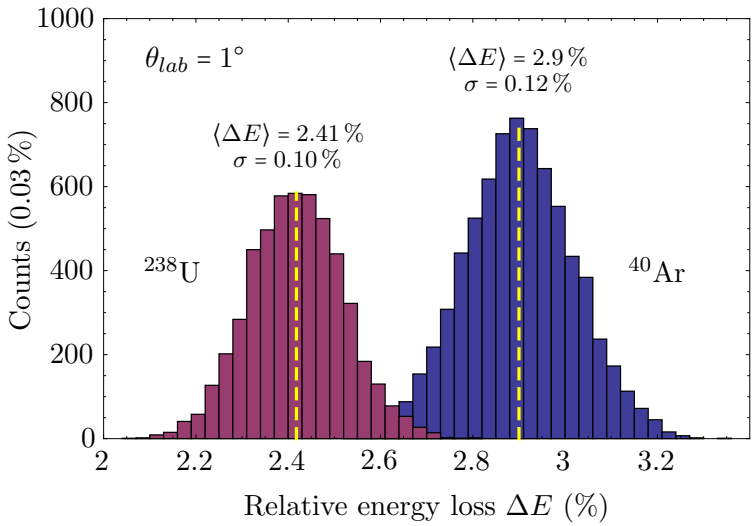

Fig. 7.5: Energy distribution of exemplary ^{40}Ar and ^{238}U ions after crossing of the tantalum foil at a net laboratory angle of $\theta = 1°$ and a solid angle of $\Delta\omega \approx 7.7 \times 10^{-6}$. The data sets have been calculated using SRIM with an input energy of 1.4 AMeV.

It should be noted that the simulation requires a very large number of primary particles since the fraction of particles scattered into θ and solid angle $\Delta\omega = 7.7 \times 10^{-6}$ sr is connected with a very small yield factor as shown in Fig. 3.15 and 3.17. As a result, significant fluctuations for the RMS value of the electronic stopping occur above $\approx 1.5°$ net emission angle where statistics is low. At a scattering angle of 2.5°, at the given solid angle $\Delta\omega$, only

about 150 particles are available of the initial 10^7 particles. Hence, in favour for the better statistics, the data of Fig. 7.5 shows the energy distributions for a scattering angle $\theta = 1°$.

7.1.2 Inhomogeneity in Thickness and Texture

The tantalum foil of (210±10) µg/cm^2 thickness installed in the collimator setup has been manufactured at the GSI target laboratory by a rolling process. This thickness is considered the lower limit which can be achieved by the process without disrupting the material. Rolled foils posses a much higher durability at beam radiation than those produced by evaporation onto a substrate. On the other hand, the homogeneity in thickness is lower in case of rolled foils. The determination of the variation in thickness or roughness of thin films proves to be difficult and is still an ongoing topic of research.

A variation in thickness implies a statistical variation in mean energy shift of the particles transmitted through the Ta foil on top of the collisional straggling contribution. When the mean energy loss $\langle \Delta E \rangle$ in a thin target of thickness $\langle x \rangle$ is small compared to the total energy $\langle E \rangle$, the energy loss is approximately given by Eq. (7.7) with

$$\langle \Delta E \rangle \approx \frac{\mathrm{d}E}{\mathrm{d}x} \langle x \rangle. \tag{7.9}$$

Albeit difficult to measure, the RMS variation in foil thickness σ_x^h leads to an energy spread contribution[3] due to the different distances the particles travel inside the foil material and can be approximated by

$$\sigma_E^h \approx \frac{\mathrm{d}E}{\mathrm{d}x} \sigma_x^h. \tag{7.10}$$

Since the expected RMS energy width of the beam is about 1 %, $\sigma_E^h / \langle E \rangle \ll 10^{-2}$ should be fulfilled to warrant a meaningful measurement of the longitudinal energy distribution.

Also the texture, i. e. the characteristics of the inhomogeneities, mainly the granularity of the pattern, plays an important role. Issues concerning the inhomogeneities have been raised for example in [87], where thin carbon foils were investigated for the characteristic electron capture using U^{91+} ions at 46 AMeV. The conclusion has been that for all tested manufacturers characteristic differences exist. Measured yields became significantly higher than predicted towards thinner foils and were attributed to their texture and inhomogeneity. This is supported by experiment runs with two foils stacked, which matched a single thicker foil of the same manufacture. The stacked setup provided significantly higher electron capture yields compared to the stacked configuration of two thinner foils.

An indirect method to access the inhomogeneities of the foil for Gaussian-like straggling profiles was suggested by Besenbacher et al. [88]. The authors assume the total straggling Ω to be described by the variances given by the *true* collisional straggling Ω_{ls} for a perfectly homogeneous material of constant width and a term Ω_h that depends on the texture and variation in thickness

$$\Omega^2 = \Omega_{ls}^2 + \Omega_h^2 \,. \tag{7.11}$$

[3] Superscript "h" denotes the contribution due to the inhomogeneity of the foil.

The contribution from the variation in thickness Eq. (7.10) varies to good approximation with the nuclear charge squared of the projectile accounted to the stopping power. Hence, a set of measurements with different projectile energies and ion species provides a way to isolate Ω_h^2. A similar method has been used in [89] where, amongst others, a rolled tantalum foil of 367 µg/cm^2 thickness was tested for homogeneity. According to this data, the inhomogeneity is large with a relative deviation in thickness of $\sigma_x^h / \langle x \rangle \approx 0.34$. This supports the tendency given in experimental data presented by Besenbacher et al. [88] and would cause a major effect on the energy resolution required for the present setup at hand. A relative mean energy loss $\langle \Delta E \rangle / \langle E \rangle \approx 3\,\%$ can be assumed, as given in Fig. 7.3. Together with Eq. (7.9) and (7.10)

$$\frac{\sigma_E^h}{\langle E \rangle} \approx \frac{\sigma_x^h}{\langle x \rangle} \frac{\langle \Delta E \rangle}{\langle E \rangle} \,, \tag{7.12}$$

the mean energy loss and relative deviation in thickness gives rise to a dissipative relative energy contribution $\sigma_E^h / \langle E \rangle \approx 1\,\%$.

Nevertheless, the impact of foil inhomogeneities on the performance of the setup presented in this work is an open question. The circular apertures of the collimator configuration close behind the tantalum foil are small with diameters of 0.5 mm (see Sec. 3.4) and are assumed to partly suppress the contributions of the thickness variation. While the same argumentation is also provided in [90] this effect is not considered negligible and still has to be studied in detail.

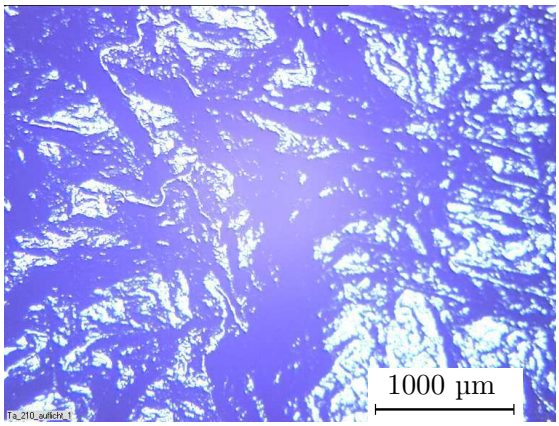

Fig. 7.6: Ta 210 µg/cm^2, rolled
Scale 1000 µm, reflected light.

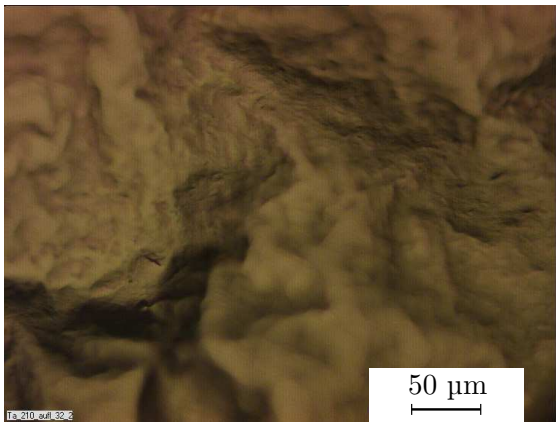

Fig. 7.7: Ta 210 µg/cm^2, rolled
Scale 50 µm, reflected light.

Figures 7.6-7.9 show a set of images (optical microscopy) of a *new* tantalum foil from the same delivery and the same rolling pass as the one currently installed. In Fig. 7.6 the tantalum foil is photographed using reflected light (scale 1000 µm). The surface features clear wrinkling which is unavoidable in the manufacturing process at the given thickness. Any stress on the material would lead to instant destruction. Thus, the material is fixed on the mount without tension. Obviously, the wrinkling structure is present on that scale and affects the energy spread by the *effective thickness* which scales approximately with $(\cos\theta_n)^{-1}$, where θ_n is the angle with respect to the normal of the foil at the impact location.

Figure 7.7 shows the same foil on a smaller scale (50 µm) also using reflected light. The different angles imposed by the wrinkles are obvious from the structural shadows. By using transmitted light it is possible to get a qualitative picture of the thickness variation. A typical area of the tantalum foil has been photographed accordingly and is shown in Fig. 7.8 at a scale of 1000 µm.

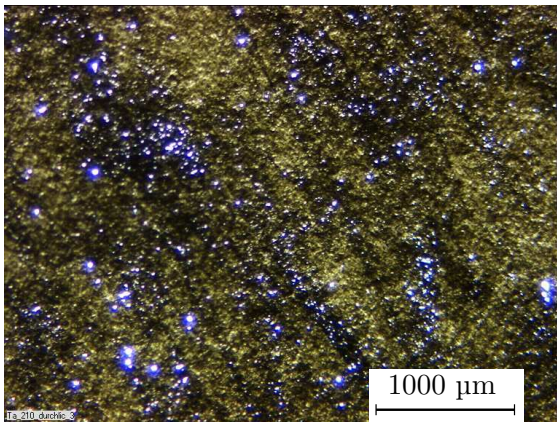

Fig. 7.8: Ta 210 µg/cm^2, rolled
Scale 1000 µm, transmitted light.

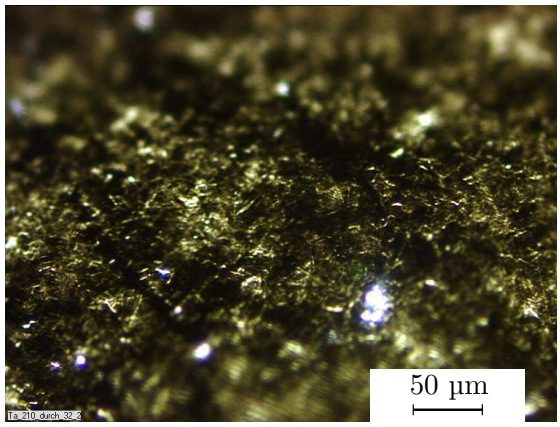

Fig. 7.9: Ta 210 µg/cm^2, rolled
Scale 50 µm, transmitted light.

An inherent texture and variation in homogeneity is evident. Even a significant amount of holes appear to be scattered over the surface in clusters where light is transmitted with a sharp high contrast. This leads to the assumption that these regions actually are real holes or at least singular areas covered by much less material than the average thickness suggests. Due to diffraction, holes are represented by their airy disc and are actually smaller than they appear on the photograph. Nevertheless, considering the circular collimator apertures of 0.5 mm it is to apprehend that the thickness of the foil varies within the location of the aperture. A higher magnification of the tantalum foil is shown in Fig. 7.9.

7.1.3 Dependence of Energy Transfer on Transverse Parameters

In Section 3.4.2, the momentum transfer from a projectile to the target nucleus depending on the net scattering angle θ has been determined using classical Coulomb Scattering. This assumes elastic scattering on the target nuclei only. A corresponding SRIM calculation, with the electronic stopping subtracted, indicates a good agreement within better than 5 %. Figures 3.16 and 3.18, respectively, show the net angle dependency of the momentum transfer to the target nucleus.

So far, the incoming bunch is approximately treated as a strictly parallel stream of particles, neglecting the transverse degree of freedom. More precisely, the net scattering angle θ' required for a certain particle to be scattered into the solid-angle acceptance ω of the collimator configuration depends on the transverse momentum as they contribute to a divergence angle $\{\vartheta_x, \vartheta_y\}$. On the other hand, the energy transfer to the target nuclei depends on the net scattering angle as given in Eq. (3.10). Figure 7.10 schematically depicts the dependence of the net scattering angle on the transverse momentum distribution, projected onto

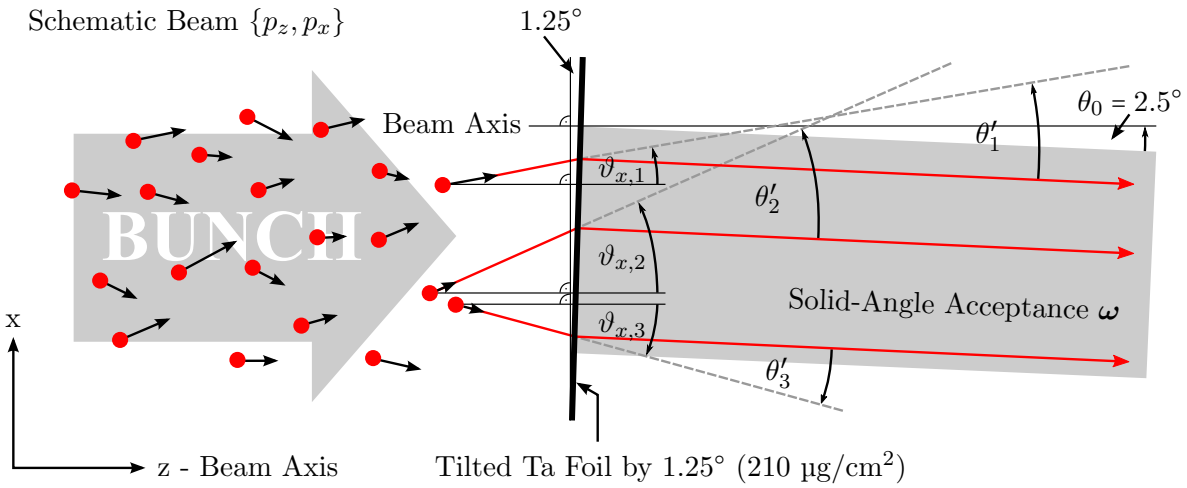

Fig. 7.10: Beam particles are schematically depicted by red dots with momentum vectors in the x-z plane only for simplicity. The resulting net scattering angle θ'_i, required for the particle to pass the collimator, depends on the transverse angle $\vartheta_{x,i}$. Consequently, an energy spread is imposed by the energy transfer to the target nucleus which depends on the net scattering angle θ'_i.

the x-z plane for simplicity. The particles arrive from the left and approach the tilted foil with different momenta marked by the arrows. Only particles scattered into the solid-angle acceptance, the grey area behind the foil, will be registered in the measurement setup. A beam suffers an additional longitudinal energy spread by the transverse momentum distribution and the geometrical constraint of the collimator acceptance. The different effective angles θ'_i required for particle i to scatter into the collimator acceptance are connected with a specific energy transfer to the target nucleus. If, for simplicity, the problem is restricted to the x-z plane at first, the resulting net angle is given by $\theta' = \theta_{2.5°} + \vartheta_x$, where the transverse divergence angle ϑ_x depends on the transverse and longitudinal momenta by $\vartheta_x = \mathrm{atan}(p_x/p_z)$ of the particles. Including the vertical degree of freedom y, the net angle θ' to fulfill the condition of matching the acceptance of the setup is a function of ϑ_x and ϑ_y, while the undisturbed angle is denoted by $\theta_0 (= 2.5°)$.

The net scattering angle $\theta'(\vartheta_x, \vartheta_y; \theta_0)$ can be derived from the unit vectors along the orientation of the solid-angle acceptance $\vec{e}_0$, given by θ_0, and the transverse degrees of freedom $\vec{e}_{x'}(\vartheta_x)$ and $\vec{e}_{x'}(\vartheta_x)$, respectively

$$\vec{e}_0 = \begin{pmatrix} -\sin\theta_0 \\ 0 \\ \cos\theta_0 \end{pmatrix}, \quad \vec{e}_{x'}(\vartheta_x) = \begin{pmatrix} \sin\vartheta_x \\ 0 \\ \cos\vartheta_x \end{pmatrix}, \quad \vec{e}_{y'}(\vartheta_y) = \begin{pmatrix} 0 \\ \sin\vartheta_y \\ \cos\vartheta_y \end{pmatrix}. \tag{7.13}$$

The net angle θ' is therefore given by the scalar product

$$\theta'(\vartheta_x, \vartheta_y; \theta_0) = \arccos\left(\frac{\vec{e}_0 \cdot (\vec{e}_{x'} + \vec{e}_{y'})}{|\vec{e}_0| \cdot |\vec{e}_{x'} + \vec{e}_{y'}|}\right) \tag{7.14}$$

and thus

$$\theta'(\vartheta_x, \vartheta_y; \theta_0) = \arccos\left(\frac{\cos\theta_0\,(\cos\vartheta_x + \cos\vartheta_y) - \sin\theta_0\,\sin\vartheta_x}{\sqrt{2\,(1+\cos\vartheta_x\,\cos\vartheta_y)}}\right). \tag{7.15}$$

To evaluate the contribution of the transverse angle distribution to the TOF uncertainty, the bunch is considered centred on the beam axis. Due to the small aperture of the collimator configuration, only a small region around $x \approx 0$ and $y \approx 0$ is selected by the setup. This allows the angle distribution $\rho_{\vartheta_x,\vartheta_y}(x, y, \vartheta_x, \vartheta_y)$ to be written as a product $\rho_{\vartheta_x}(\vartheta_x) \cdot \rho_{\vartheta_y}(\vartheta_y)$. The corresponding response function is given by

$$R(\Delta E; \theta_0, \omega) = \int_{-\infty}^{+\infty} \mathrm{d}\vartheta_x\, \rho_{\vartheta_x}(\vartheta_x) \int_{-\infty}^{+\infty} \mathrm{d}\vartheta_y\, \rho_{\vartheta_y}(\vartheta_y) \cdot P_{sc}\left(\theta'(\Delta E), \omega\right) \delta(\theta'(\Delta E) - \theta'(\vartheta_x, \vartheta_y; \theta_0))\,. \tag{7.16}$$

Integration is performed including both transverse angle distributions, ρ_{ϑ_x} and $\rho_{\vartheta y}$, thereby only taking into account net angles that contribute to a specific energy transfer ΔE. This selection is provided by the Dirac delta function and further weighted by the probability $P_{sc}\,(\theta'(\Delta E), \omega)$ of θ' to occur as given in Eq. (3.4). Alternatively, the effect can be calculated by a Monte-Carlo simulation. The angle distributions $\rho_{\vartheta_x}(x)$ and $\rho_{\vartheta_y}(y)$ are parameterised by Gaussian distributions, and a set of angles $\{\vartheta_x, \vartheta_y\}$ is sampled accordingly and weighted by the probability $P_{sc}\,(\theta'(\Delta E), \omega)$. Evaluating the standard deviation of the corresponding histogram allows to extract the system response.

High-current phase-space distributions of Ar^{10+} and U^{27+} are plotted in Fig. 2.2. These 6-dimensional phase-space distributions are considered realistic configurations at the TOF setup location by the GSI injector division [11]. They are used as boundary conditions for tracking simulations through the post-stripper section. It is therefore considered the best reference configuration for the transverse plane which is of importance in this case.

For completeness, it should be noted that the longitudinal phase-space configurations shown in Fig. 2.2 have been constructed by measurements of the longitudinal phase space using the TOF setup presented in this work. A detailed explanation of the procedure is given in [12]. The bunch length as well as the momentum spread has been adopted from the TOF measurement while the correlation α was empirically set to the expected values around $|\alpha| \approx 4$. Hence, the emittance is consequently calculated as

$$\varepsilon = \sqrt{\frac{\sigma_p \sigma_\phi}{\alpha^2 + 1}}\,. \tag{7.17}$$

A simulation has been carried out with the Ar^{10+} and U^{27+} phase-space distributions with the relevant data listed in Tab. 7.1. The relative error $\sigma_{tr}/\langle E\rangle$ is less than 2×10^{-5}. In relation to the expected energy width $\sigma_E^{1\%}$, listed as $\sigma_{tr}/\sigma_E^{1\%}$ in Tab. 7.1, this clearly shows that transverse momentum components have a negligible effect on the total resolution.

Tab. 7.1: Simulated effect of transverse momentum on energy resolution.

	$\sigma_{\vartheta x}$ (mrad)	$\sigma_{\vartheta y}$ (mrad)	$\langle \Delta E \rangle / \langle E \rangle$	$\sigma_{tr} / \langle E \rangle$	$\sigma_{tr} / \sigma_E^{1\%}$ (%)
$\mathbf{Ar}^{10+}$	0.55	0.60	4.2×10^{-4}	5.3×10^{-6}	5.3×10^{-2}
$\mathbf{U}^{27+}$	0.35	0.45	2.5×10^{-3}	2×10^{-5}	0.2

7.2 Energy Spread by Finite Solid Angle

The finite solid angle of the collimator setup imposes an energy spread σ_E^θ as the transferred energy depends on the net scattering angle θ. The variation of Eq. (3.10) with respect to the net scattering angle θ in the laboratory frame is given by

$$\sigma_E^\theta = \frac{\mathrm{d}E}{\mathrm{d}\Theta} \frac{\mathrm{d}\Theta}{\mathrm{d}\theta} \sigma_\theta \tag{7.18}$$

with

$$\frac{\mathrm{d}E}{\mathrm{d}\Theta} = -8\, E_0 \sin\Theta \frac{A_{red}}{A_p + A_t} \tag{7.19}$$

and the reciprocal derivative of Eq. (3.7)

$$\frac{\mathrm{d}\Theta}{\mathrm{d}\theta} = \left(\frac{\mathrm{d}\theta}{\mathrm{d}\Theta}\right)^{-1} = \frac{1 + \left(\frac{A_p}{A_t}\right)^2 + 2\,\frac{A_p}{A_t}\cos\Theta}{\frac{A_p}{A_t}\cos\Theta + 1}. \tag{7.20}$$

Hence, the imposed energy spread is given by the knowledge of σ_θ. Assuming, in good approximation, a homogeneous probability density within the very small solid angle ω, allows the variance of the net scattering angle σ_θ^2 to be extracted

$$\sigma_\theta^2 = \left\langle \Delta\theta^2 \right\rangle = \frac{2}{\pi r_{ap}^2 d_{sep}^2} \int_{-r_{ap}}^{r_{ap}} \mathrm{d}r\, r^2 \sqrt{r_{ap}^2 - r^2} = \frac{r_{ap}^2}{4 d_{sep}^2} \approx \frac{\omega}{4\pi}\,. \tag{7.21}$$

Another simplification has been made by neglecting the azimuthal component, which is suppressed by more than one order of magnitude. An estimate of the uncertainty can now be deduced using Eqs. (7.18) - (7.20). For the given configuration a value $\sigma_\theta = 8.3 \times 10^{-4}$ rad has been calculated. Figure 7.11 shows the energy spread according to Eq. (7.18) for different projectiles using the calculated value of σ_θ. From the dashed, vertical line (at $\theta = 2.5°$) a maximum contribution to the energy spread of 0.017 % in case of uranium shows a minor effect and can be safely neglected compared to other contributions to the energy spread.

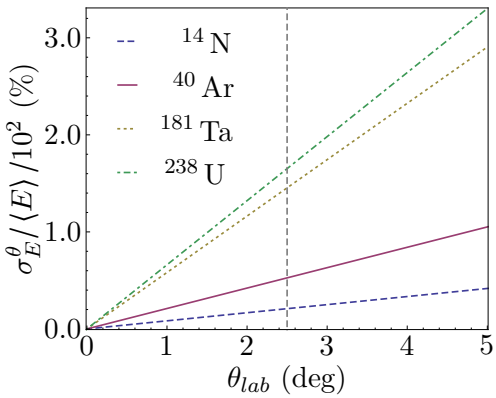

Fig. 7.11: Maximum energy spread imposed by the finite solid angle ω of the collimator.

7.3 Aluminium Foil

The TOF measurement relies on two timing signals at a well-defined separation. Since the first timing signal has to be created by a minimum interaction of the particle under consideration, to prevent a major negative impact on the TOF, a thin aluminium foil of about (10 ± 1) µg/cm^2 is mounted in front of the MCP, tilted by an angle of $(42.5 \pm 0.5)°$. When a heavy-ion projectile passes the foil, electrons are liberated and accelerated towards the MCP front at a voltage of 2 kV. An avalanche of electrons is generated inside the MCP stack with an applied voltage applied of 1.9 kV. Eventually, the avalanches of electrons leaving the MCP are collected at an anode and the pulse is extracted via a Bias tee. For details see Sec. 3.3.1.

7.3.1 Electronic Stopping and Straggling

In contrast to the tantalum foil used in the particle-attenuation setup, the aluminium foil has been manufactured in an evaporating process at the GSI target laboratory. Table 7.2 lists values calculated with the ATIMA programme [91] for typical projectiles at $\langle E \rangle = 1.4$ AMeV. Due to the very thin foil, the mean energy as well as the collisional straggling contribution is much lower compared to the tantalum foil. Using the ATIMA code, the largest contribution has been 0.033 % with respect to the mean energy $\langle E \rangle$. This is very small compared to the expected energy width of 1 % but the value is based on the assumption of a perfectly homogeneous foil.

7.3.2 Inhomogeneity in Thickness and Texture

As mentioned before, the aluminium foil has been manufactured by evaporating the material onto a substrate. While this provides a more homogeneous thickness than the rolling process and allows thinner foils, the material is not as resistive. Moreover, the surface structure of the solvable substrate manifests as the negative relief on the foil material. On the other side, this is a structure of absolute scale and thus becomes more relevant the thinner the foils are.

Tab. 7.2: ATIMA calculation for straggling contribution (at ideal thickness) for the MCP aluminium foil of about 370 Å at an incident angle of $(42.5 \pm 0.5)°$.

	$\langle \Delta E \rangle / \langle E \rangle$ (%)	σ_{st} (AMeV)	$\sigma_{st} / \langle E \rangle$ (%)
N	0.35	4.6×10^{-4}	3.3×10^{-2}
Ar	0.46	3.1×10^{-4}	2.2×10^{-2}
Ta	0.38	1.5×10^{-3}	1.1×10^{-2}
U	0.34	1.3×10^{-3}	9.2×10^{-3}

For a qualitative measure of the surface characteristics, optical microscopy was used as in the case of the rolled tantalum foil (see Sec. 7.1.2). Figures 7.12-7.13 show two photographs of an aluminium 10 µg/cm^2 foil at different magnification. The foil stems from the same delivery as the foil currently installed in the TOF measurement setup. Only photographs using reflected light were possible due to the low contrast in case of transmitted light. In Fig. 7.12, at the scale of 1000 µm, the imprint of the substrate is visible. Nevertheless, apart from the scratch-like structure, regions of an even surface are present on a scale of about a quarter millimeter. Holes are scarcely featured although a big clustered disruption can be seen at the lower border next to the scale. Figure 7.13 shows the foil using reflected light at a scale of 50 µm and reveals a granular structure with a small grain size of about 3-5 µm. Other regions which correspond to the scratch-like shapes on the lower magnification appear embossed but with a very even and smooth surface area. It appears that the surface can be characterised by mainly two thickness levels, the emboss and the granular level. This is different from the rolled tantalum foil, which features a rather continuous thickness distribution (see Fig. 7.8).

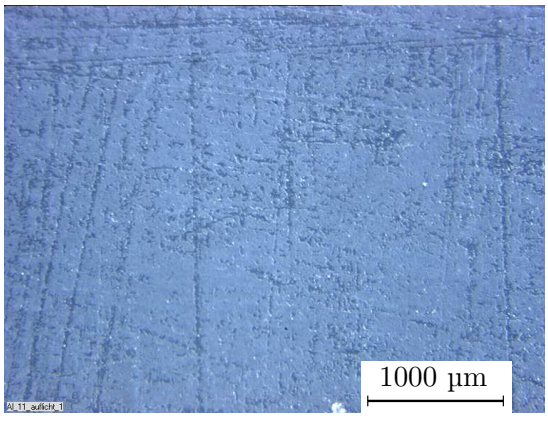

Fig. 7.12: Al 10 µg/cm^2, evaporated Scale 1000 µm, reflected light.

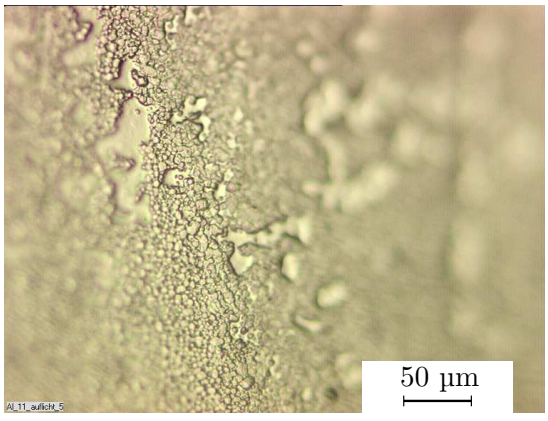

Fig. 7.13: Al 10 µg/cm^2, evaporated Scale 50 µm, reflected light.

Although quantitative data concerning the thickness variation is not available, some upper limits on the uncertainty can be derived from the thickness variation of the tantalum foil and the given mean energy loss at the aluminium foil for projectiles of energy $\langle E \rangle = 1.4$ AMeV. It is known that evaporated foils are less prone to thickness variation than rolled foils. Taking the variation in thickness given in [89] for the rolled tantalum foil, the evaporated aluminium foil can be assumed to be of higher homogeneity, thus, $\sigma_x / \langle x \rangle < 0.34$. According to Eq. (7.10) this would contribute an uncertainty $\sigma_{al}^h < 0.15\,\%$ with respect to $\langle E \rangle$.

7.3.3 Tilted Foil Geometry

As explained in Sec. 3.3.1, the aluminium foil is tilted at a certain angle with respect to the plane orthogonal to the beam axis z. This is a strict requirement as the MCP front must be installed centric parallel with respect to the foil and assure a homogeneous, symmetric electric field. Additionally, the ion must transit the foil only and bypass the MCP at the same time. Thus, the angle also depends on the geometry of the MCP module (Sec. 3.3.1). A tilt angle of $\varphi = 42.5°$ represents a minimum for the current distance between the foil and the MCP front. The finite solid angle of the beam together with the tilted foil geometry introduces a geometric jitter $\Delta l_{tof}(x)$ in total drift space which is schematically depicted in Fig. 7.14. In the following, the particles are considered to follow parallel trajectories which

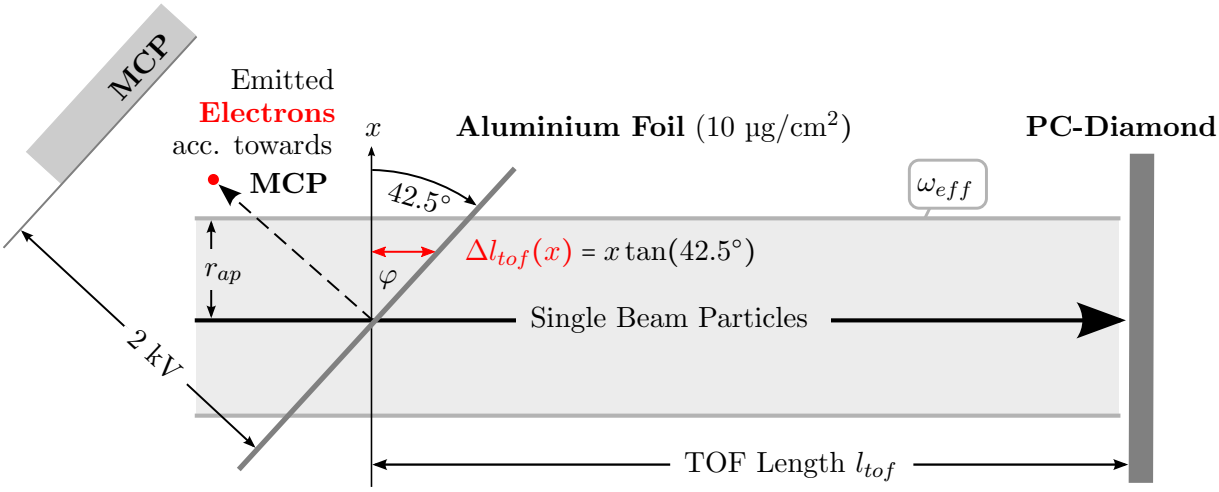

Fig. 7.14: The MCP module is shown including the aluminium foil. All ions are uniformly distributed within the range of the *effective aperture* given by the radius r_{ap}. Due to the inevitable tilted placement of the foil, the TOF length depends on the lateral offset from the centre.

significantly simplifies the evaluation of uncertainty without major tampering, since lateral contribution are suppressed by at least one order of magnitude. Furthermore, the diamond electrode is assumed to be illuminated uniformly.

The first moment $\langle \Delta l \rangle$ vanishes which reduces the uncertainty estimation of the rms drift jitter to the evaluation of

$$\sigma_{\Delta l} = \sqrt{\langle \Delta l^2 \rangle}\,. \tag{7.22}$$

As can be seen from Fig. 7.14, the dependence of Δl on x is given by

$$\Delta l(x) = x \tan\varphi \,. \tag{7.23}$$

Depending on either the solid angle ω given by the collimator configuration or the distance of the diamond detector electrode, the illuminated area on the aluminium foil is different. The maximum effective solid angle is given by the size of the diamond detector electrode and its distance to the tantalum foil. This is taken into account by limiting the integration within the projected circular boundary that matches the *effective aperture* r_{ap}

$$\langle \Delta l^2 \rangle_\varphi = \frac{1}{\pi r_{ap}^2} \int_{-r_{ap}}^{r_{ap}} \mathrm{d}x\, x^2 \tan^2\varphi \int_{-\sqrt{r_{ap}^2 - x^2}}^{\sqrt{r_{ap}^2 - x^2}} \mathrm{d}y = \frac{\tan^2\varphi}{4} r_{ap}^2 \,. \tag{7.24}$$

The aperture can be treated as an effective value depending on the solid angle spanned by the circular area of the diamond, given by means of r_{dia} and its separation to the primary (Ta) foil squared. In the following, l_{mcp} is the separation of the MCP to the primary foil, l_{dia} marks the separation of the diamond detector to the primary foil and $l_{tof} = l_{dia} - l_{mcp}$ is the drift distance relevant for the TOF. The technical drawing Fig. B.1 provides an overview. Starting with the *effective solid angle* ω_{eff} given by the separation l_{dia} of the poly-crystalline detector

$$\omega_{eff} = \frac{A_{dia}}{l_{dia}^2} = \frac{\pi r_{dia}^2}{(l_{mcp} + l_{tof})^2} \,, \tag{7.25}$$

the effective aperture r_{ap} is given accordingly by

$$r_{ap} = \sqrt{\frac{A_{dia}}{\pi}} \frac{l_{mcp}}{l_{mcp} + l_{tof}} = \frac{r_{dia}}{1 + \frac{l_{tof}}{l_{mcp}}} \,. \tag{7.26}$$

Together with Eq. (7.24), the jitter in detector separation writes as

$$\sigma_{\Delta l} = \sqrt{\langle \Delta L^2 \rangle}_\varphi = \frac{\tan\varphi}{2} \frac{r_{dia}}{1 + \frac{l_{tof}}{l_{mcp}}} \tag{7.27}$$

and is trivially transformed into the corresponding time jitter by taking the mean velocity $\langle\beta\rangle\, c$ of the particles into account

$$\sigma_t = \frac{\sigma_{\Delta l}}{\langle\beta\rangle\, c} \,. \tag{7.28}$$

For the current configuration of the setup and the typical velocity of $\beta = 0.055$ this results in an absolute RMS time jitter of about 25 ps.

7.3.4 Secondary Electron Emission Spectra

The first generated timing signal in the TOF setup is realised as an indirect measurement by the secondary electrons liberated from the aluminium foil. Backwards emitted electrons are accelerated through 2 kV as depicted in Fig. 7.15, after which they have a velocity

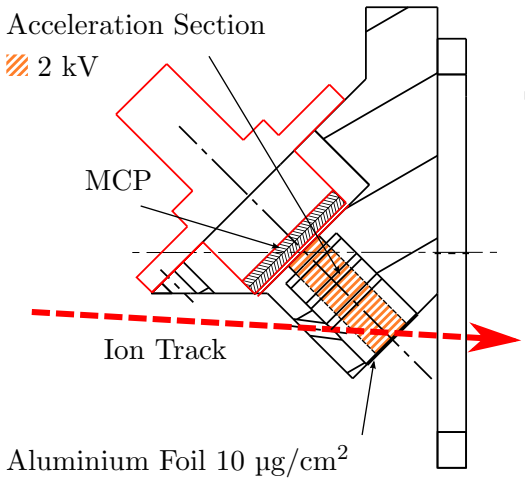

Fig. 7.15: Cut through the PEEK mounting of the MCP, the aluminium foil and the MCP module.

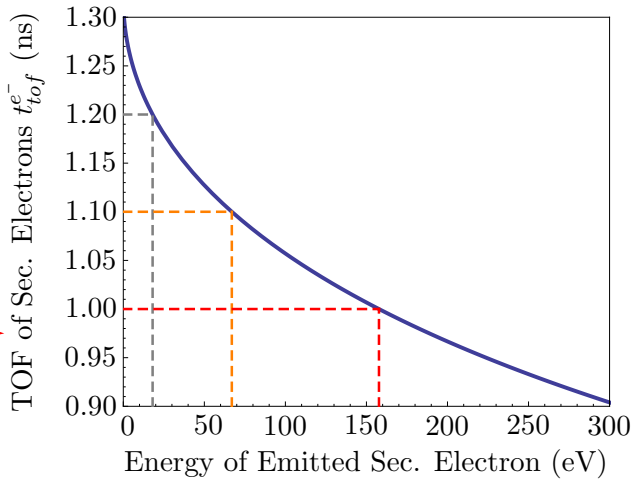

Fig. 7.16: TOF (Al-foil→MCP) of secondary electrons vs. kinetic energy (projection on MCP axis) at emission.

of about 9 % of the speed of light. This considers a low initial kinetic energy at emission from the aluminium foil with an order of magnitude of a few electronvolts. To provide a homogeneous electric field, three guide rings have been included and are connected to an appropriate voltage divider circuit.

Ideally, the TOF of the secondary electrons between the aluminium foil and the MCP is constant. The TOF $t^{e^-}_{tof}$ of the electrons depends on the separation d between the aluminium foil and the MCP, the voltage U applied and the initial velocity component $v_0^\perp$ along the symmetry axis, thus, in the classical limit

$$t^{e^-}_{tof} = \sqrt{\frac{2d}{\xi} + \left(\frac{v_0^\perp}{\xi}\right)^2} - \frac{v_0^\perp}{\xi} \qquad \text{with} \qquad \xi = \frac{U}{m_{el} \cdot d}\,. \tag{7.29}$$

Figure 7.16 shows the TOF $t^{e^-}_{tof}$ vs. the initial kinetic energy of the electrons for the configuration of the setup with $d = (17.5 \pm 0.1)$ mm and $U = (2.00 \pm 0.05)$ kV and under the assumption that the energy of the electrons are attributed to $v_0^\perp$ alone. The difference in TOF between an electron with initially 0 eV kinetic energy and 18 eV is about 100 ps, while an electron of 68 eV and 0 eV will have a difference in TOF of about 200 ps. Therefore, it cannot be precluded that the electron spectra does affect the accuracy of the first timing signal. On the other hand, multiple electrons will be liberated per ion passage of the aluminium foil. The Sternglass formula [92] allows to estimate the amount of liberated secondary electrons with several electron volts of kinetic energy. According to Sternglass, the electron yield for the given configuration is about 150 electrons in case of argon and about 600 electrons in case of uranium. Hence, for narrow energy spectra one could conclude that a large number of liberated electrons per ion would result in a more or less identical distribution on each passage of an ion. In other words, the ensemble of electrons from a single ion event would already be a good representation of the energy distribution itself and the response of the MCP could be expected to consist of very similar pulse shapes.

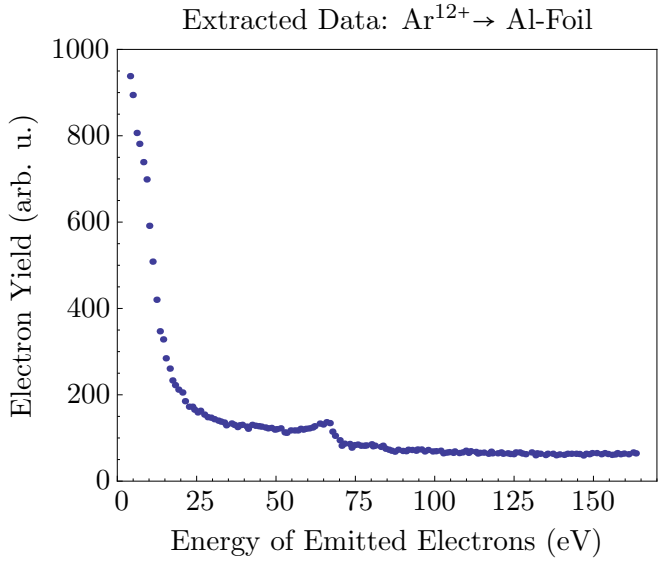

Fig. 7.17: Energies of backward scattered secondary electrons as measured in [93] for Ar^{12+} ions at 1.1 *A*MeV. Although no angles are resolved, the total solid angle of the detector has been only 1 sr, which is small enough to consider all electrons being within the acceptance of the MPC/foil setup. The original data provides no information about statistical and systematic errors.

Nevertheless, the actual spectra of the secondary electrons are unknown. Experimental data up to 163 eV of the electron spectra can be extracted from [93] for the argon case and are shown in Fig. 7.17. The configuration of the experimental setup which has been used is very similar to the situation present in the TOF setup at hand. Although no angle information is included, one can safely assume all electrons to be inside the acceptance of the foil-MCP detector setup because Koyama et al. specify the solid-angle acceptance of their setup to be 1 sr which is equal to a polar angle of 32.8°. From this data, a high-energy tail is apparent and cannot be considered a narrow distribution. Since the MCP is sensitive to single electrons, at typical gains of $10^6 - 10^7$, those electrons reaching the MCP front first are most relevant to the leading edge of the pulse. A large high-energy tail can negatively influence the timing accuracy as the highest energy occurring in each ion event could fluctuate on a large scale. Even with several hundreds of electrons per ion, these fluctuations may be prominent. Taking the energy spectra of Fig. 7.17 as reference, the most likely energies to occur are those of low energy below 20 eV. At the same time those are the least relevant for leading edge of the pulse. It may even be, that the fluctuations connected to the electron with the highest energy is responsible for the random distortions of the leading edge which will be discussed in Sec. 7.4.1.1.

A simple Monte Carlo simulation has been performed to test the time jitter imposed by the TOF of the fastest electron per sample only. A set of 150 electrons have been randomly sampled from the distribution shown in Fig. 7.17. The TOF for the electron of highest

energy was histogrammed for 10^5 cycles. The effect is only very minor with a FWHM of 2-3 ps. It is even smaller when sampling 600 electrons each time. This contribution is neglectable.

7.4 Detectors

7.4.1 Microchannel Plate

Time measurements with the TDC requires NIM pulses as input. Those logical pulses are delivered using the *double-threshold discriminators* described in Sec. 4.1.1. Typically, the MCP pulses at the 50 Ω anode readout deliver a pulse-height distribution from ≈ 150 mV to 1.2 V.

7.4.1.1 Pulse-Shapes and Discrimination

As it turned out, evaluation of precise timings is falsified by distorted pulse shapes at the falling edge, as can be seen in Fig. 7.18. The left trace shows a "normal" pulse shape, while the right picture shows the leading-edge distortions of frequent occurrence. To estimate the resulting timing jitter, the recorded pulse has been complemented by dashed lines to reconstruct the expected leading edge. Based on this method, typical pulse shapes are shown with a timing jitter of ≈ 150 ps and ≈ 400 ps. Pile-ups caused by multiple ions as the reason for the bump can be eliminated. The multiple-hit occurrence can be deduced from the bunch separation distribution Eq. (3.15) which has been experimentally verified.

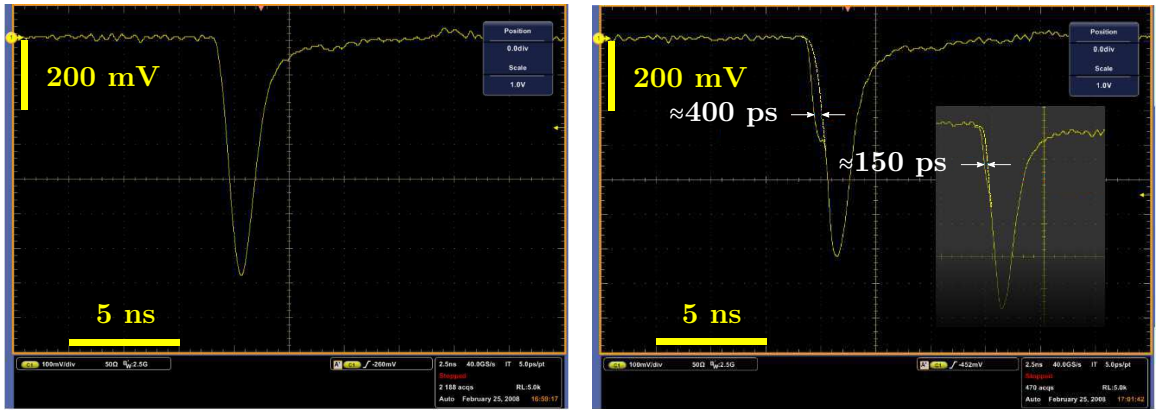

Fig. 7.18: Left: Normal MCP pulse shapes with a well defined rising edge with a rise-time of about 850 ps. **Right:** Distorted MCP pulse shapes which randomly feature an additional bump on the falling edge with different time offsets. The dashed yellow curve has been added manually representing the expected shape that allows the estimation of the corresponding error contribution.

Consultation of the manufacturer confirmed that the mechanical and electrical installation is in compliance with the companies' guidelines. Ion feedback is equally unlikely the cause

of the distortions, given the low pressure of 1×10^{-6} to 1×10^{-7} mbar and the Chevron configuration, in particular with the frequent occurrence. Since the MCP is sensitive to single electrons, this effect might be correlated with the electron emission spectra at the aluminium foil. Isolated fast electrons may reach the MCP earlier by several 100 picoseconds as depicted in Fig. 7.16. As a safe estimate of the RMS timing contribution 150 ps seems legitimate.

7.4.2 Poly-Crystalline Diamond Detector

7.4.2.1 Pulse Shapes and Discrimination

The diamond detector does not suffer from significant distortions of the leading edge. Based on the characteristics of the double-threshold discriminator and the amplifier stage, an RMS uncertainty of 50 ps is considered.

7.4.2.2 Signal Propagation on Diamond Electrode

Particles scattered into the solid-angle acceptance of the collimator are detected directly at a diamond detector on an circular electrode area with a radius of 4 mm. Signals are collected at the connector as depicted schematically in Fig. 7.19. Depending on the location of impact, the distance to the connector differs. A uniform illumination of the electrode

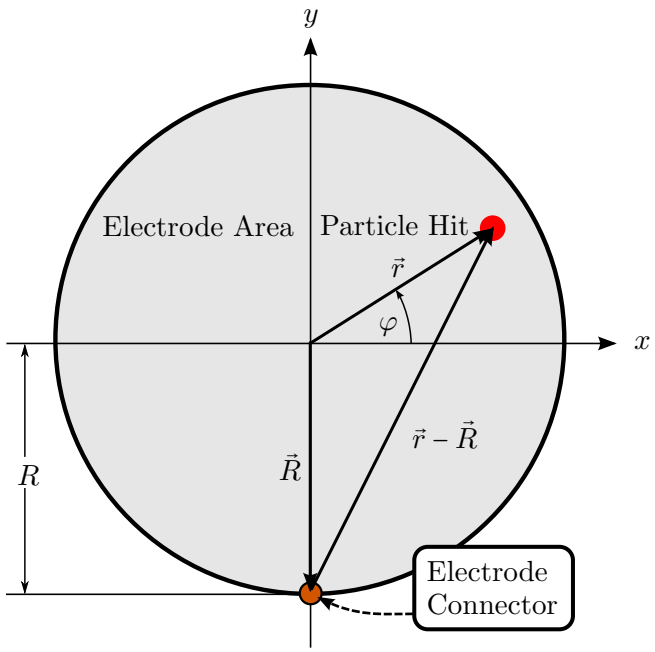

Fig. 7.19: Depending on the point of impact, a different propagation time to the electrode connector has to be considered. This results in an uncertainty concerning the timing precision.

area can be assumed since the scattering statistics does not change significantly inside the very small solid angle. According to Fig. 7.19, a given impact location can be parameterised by

$$\vec{r}(r,\varphi) = r(\cos\varphi\,\vec{e}_x + \sin\varphi\,\vec{e}_y) \qquad \text{and} \qquad \vec{R} = -R\,\vec{e}_y\,. \tag{7.30}$$

Therefore, the square of the distance from location of impact to the electrode connector writes as

$$\left|\vec{r}(r,\varphi) - \vec{R}\right|^2 = r^2\cos^2\varphi + (r\,\sin\varphi + R)^2\,. \tag{7.31}$$

Consequently, the mean signal transport distance on the detector is evaluated by the following integral

$$\langle|\vec{r} - \vec{R}|\rangle = \frac{\int_0^R r^2\mathrm{d}r\int_0^{2\pi}\mathrm{d}\varphi\sqrt{\cos^2\varphi + \left(\sin\varphi + \frac{R}{r}\right)^2}}{\int_0^R r\mathrm{d}r\int_0^{2\pi}\mathrm{d}\varphi}\,. \tag{7.32}$$

As the integral is of elliptical type, no analytical solution exists. A numerical calculation for electrode radius $R = 4$ mm delivers a mean distance $\langle|\vec{r} - \vec{R}|\rangle \approx 4.5$ mm. The RMS value $\sigma_{|\vec{r}-\vec{R}|}$ of 3.3 mm has been also evaluated numerically by

$$\sigma_{|\vec{r}-\vec{R}|} = \frac{\int_0^R r\mathrm{d}r\int_0^{2\pi}\mathrm{d}\varphi\left(\langle|\vec{r} - \vec{R}|\rangle - r\sqrt{\cos^2\varphi + \left(\sin\varphi + \frac{R}{r}\right)^2}\right)^2}{\int_0^R r\mathrm{d}r\int_0^{2\pi}\mathrm{d}\varphi}\,. \tag{7.33}$$

Even in a very optimistic scenario where signals propagate with speed of light this contributes an RMS time jitter of 11 ps.

7.5 Influence of Accelerator Settings

7.5.1 Coupling of Transverse and Longitudinal Phase Space

The measurement is installed inside a dipole chicane used for charge state selection (see Fig. 3.3). As the dispersion after the first dipole magnet (US3MK1) is fully uncompensated, it is important to investigate the effects related to the coupling of the transverse and longitudinal phase-space planes. In standard operation of the beam line, the beam is further deflected by two dipole kicker magnets which accomplish partial compensation of the net dispersion before the bunch is prepared to be injected into the first Alvarez cavity. While the transverse and longitudinal phase-space planes along the prestripper section are considered to be decoupled in good approximation, this is not necessarily the case within the dispersive dipole section. If the transverse and longitudinal phase-space planes are uncorrelated, the corresponding six dimensional density ρ can be written as a direct product of the transverse and longitudinal densities

$$\rho(x, p_x; y, p_y; \phi, p_z) = \rho_t(x, p_x; y, p_y)\cdot\rho_l(\phi, p_z)\,. \tag{7.34}$$

In this case, measurement of the longitudinal phase space would be independent of the location (x, y).

The present setup relies on a narrow aperture at the entrance. Hence, the measurement only reflects the longitudinal phase space connected to a certain transverse offset (x, y) if the transverse and longitudinal planes are strongly correlated. The duration required for a measurement does not allow for a sampling at several offsets x. Data is therefore taken at the centre of the transverse distribution only. Moreover, the count rate drops fast for a larger offset from the beam centre.

Schematically, the coupling of the horizontal degree of freedom is depicted in Fig. 7.20. On the left figure, the dispersion leads to a horizontal beam spread depending on the initial longitudinal momentum distribution and the strength of the dipole field. This means for a narrow aperture that the spatial point-to-point mapping from a transverse position before entering the dipole and the location of the aperture is connected with a small longitudinal momentum range (neglecting the transverse momenta for simplicity). On the right figure, different initial transverse offsets are guided to the aperture with the matching momenta.

To estimate the influence of the dispersive section, a DYNAMION [22] tracking simulation has been used for the typical case of an Ar^{1+} beam of 10 mA entering the gas stripper. The particles were tracked [94] through the gas stripper and the consecutive dipole section to the location of the setup. The simulation was restricted to the charge-state equilibrium 1+ → 10+ at 1.4 AMeV. Due to the symmetry of the charge-state spectrum, a current of 100 mA can be assumed. Figure 7.21 shows the longitudinal phase ϕ and relative momentum deviation $\Delta p/p$ versus the transverse horizontal offset x, at which the top row corresponds to the start configuration before entering the gas stripper. The middle row represents the beam at the measurement setup tracked without taking space-charge effects into account, i. e. the beam has been treated as an ensemble of non-interacting particles. The bottom row considers realistic values of the space-charge. For completeness the associated longitudinal

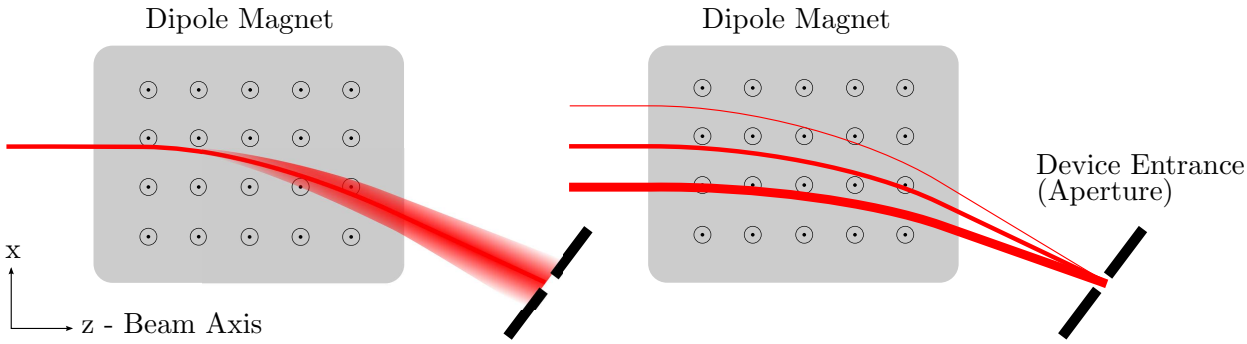

Fig. 7.20: Schematic effect of transverse and longitudinal coupling along a dispersive dipole section (neglecting the interaction of the particles and transverse momenta). Particle trajectories are depicted by red lines. Considering the narrow aperture, two systematic contributions can be distinguished. On the **left** figure, a beam section of small transverse extension enters the dipole. The longitudinal momentum spectra give rise to different radii of the particle trajectories. Thus, the aperture selects a certain range of energies from the incoming particle stream. The **right** figure shows particle sections with different transverse offsets. The magnitude of the longitudinal momenta is schematically denoted by the thickness of the trajectories.

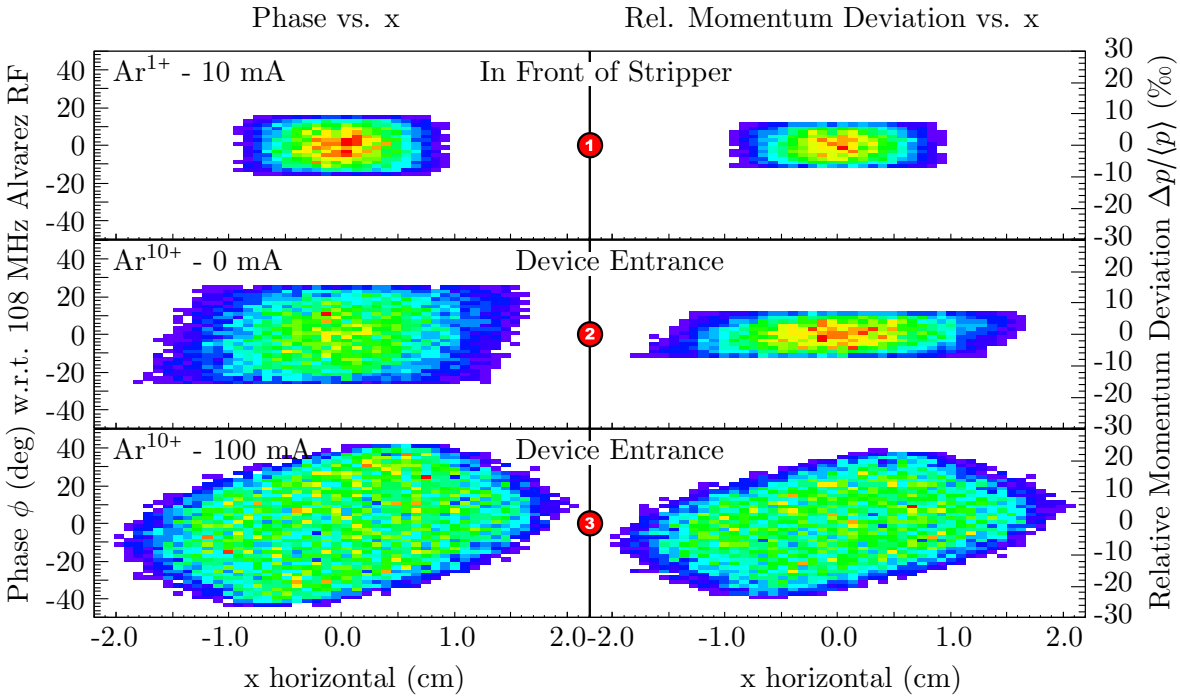

Fig. 7.21: Subspaces (ϕ vs. x and $\frac{\Delta p}{p}$ vs. x) of DYNAMION tracking data calculated by S. Yaramishev [94]. To investigate the effect of the transverse and longitudinal coupling at the dispersive dipole section, a start distribution of Ar^{1+} (10 mA), (top row 1) has been tracked through the gas stripper to the measurement setup. After stripping (1+ → 10+) the distribution has been further tracked without considering particle interaction (middle row 2) and considering full space-charge (bottom row 3).

phase spaces are given in Fig. 7.22.

From the tracked phase spaces it is apparent that under low space-charge influence the phase space undergoes shear mapping in the $(\phi \otimes x)$ and $(\frac{\Delta p}{p} \otimes x)$ plane. Hence, an uncorrelated phase space at the entrance of the gas stripper remains largely uncorrelated at the measurement setup. A realistic picture requires the consideration of the strong interparticle effects, mainly due to space-charge. Then, as can be seen from the bottom row subspaces of Fig. 7.21, a prominent correlation is present. Nevertheless, a range of ±0.5 cm from the centre obviously provides about the same particle distribution, but at a strongly correlated mean value. This can be seen from Fig. 7.23 where cuts at equidistant locations $x \pm 0.25$ cm have been evaluated for their mean value and sample standard deviation. While the coupling of the transverse and longitudinal phase-space planes may lead to a strong correlation of the mean values for the realistic space-charge simulation, the sample means vary by a smaller margin within $[-1.25\ \text{cm}, 1.25\ \text{cm}]$ of less than 5 % for a fraction of the total particles of about 60 %. Nevertheless, neglecting any dissipative effects as well as timing limitations, a measurement at the transverse centre may underestimate the total bunch length and momentum distribution. This is obvious since the mean values vary about 10° (0.8 ns) concerning the phase and about 0.8 % for the relative momentum distribution. Thus, the total projection is affected.

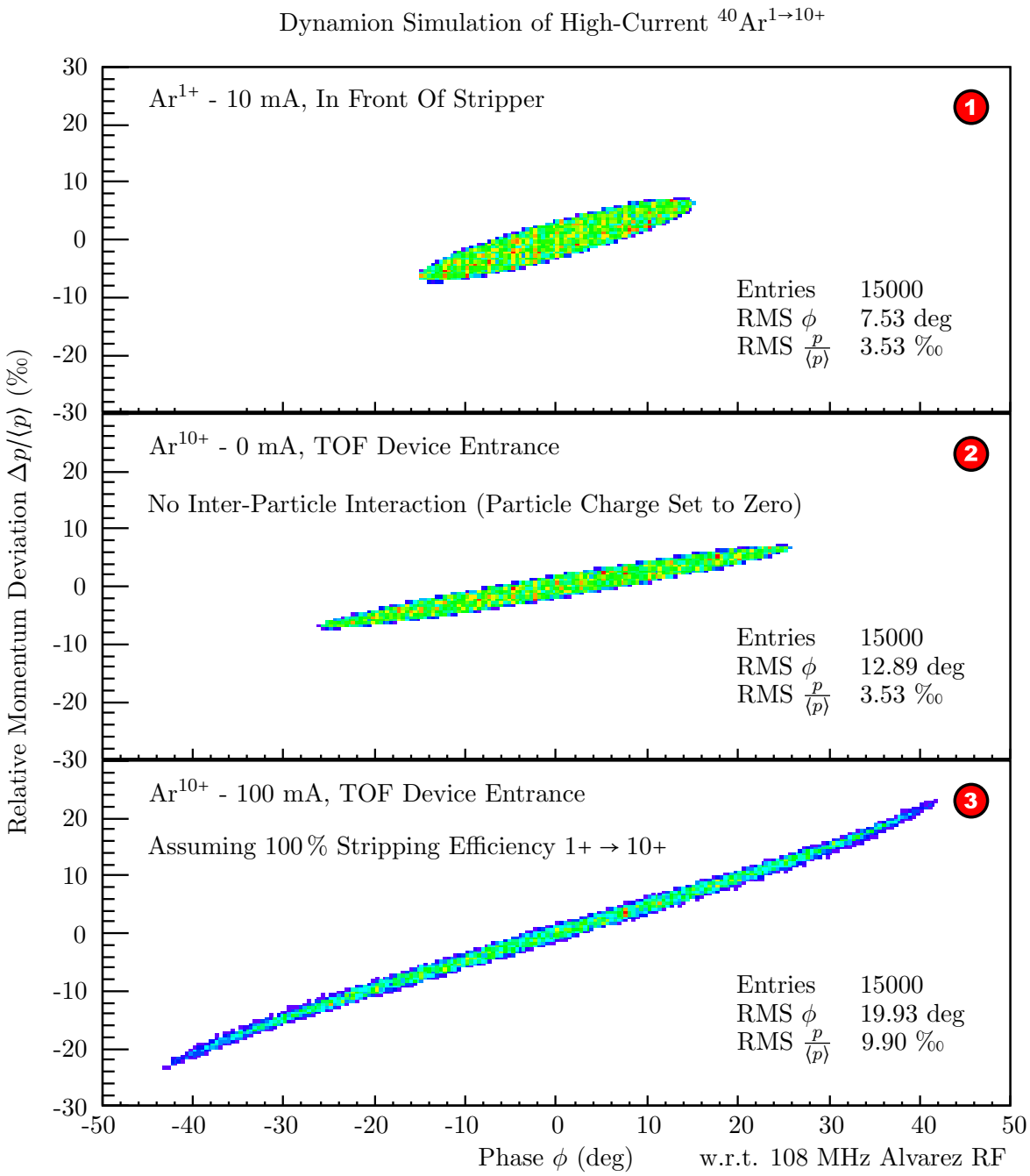

Fig. 7.22: Figure 1 shows the longitudinal phase space which is used as *start distribution* in a DYNAMION calculation [94] to estimate the influence of the dispersive dipole section (US3MK1) and space-charge. The start distribution is located right in front of the UNILAC gas stripper. For simplicity, a homogeneous test distribution with a sharp elliptic bound is assumed to be a sufficiently good representation for the 10 mA Ar^{1+} beam. The particle distribution is tracked to the TOF device entrance using two different assumptions. Figure 2 shows the tracked longitudinal phase space at the height of the device when particle interaction is not considered. Figure 3 shows the complementary tracking with the particle interaction included at a stripping efficiency of 100 %.

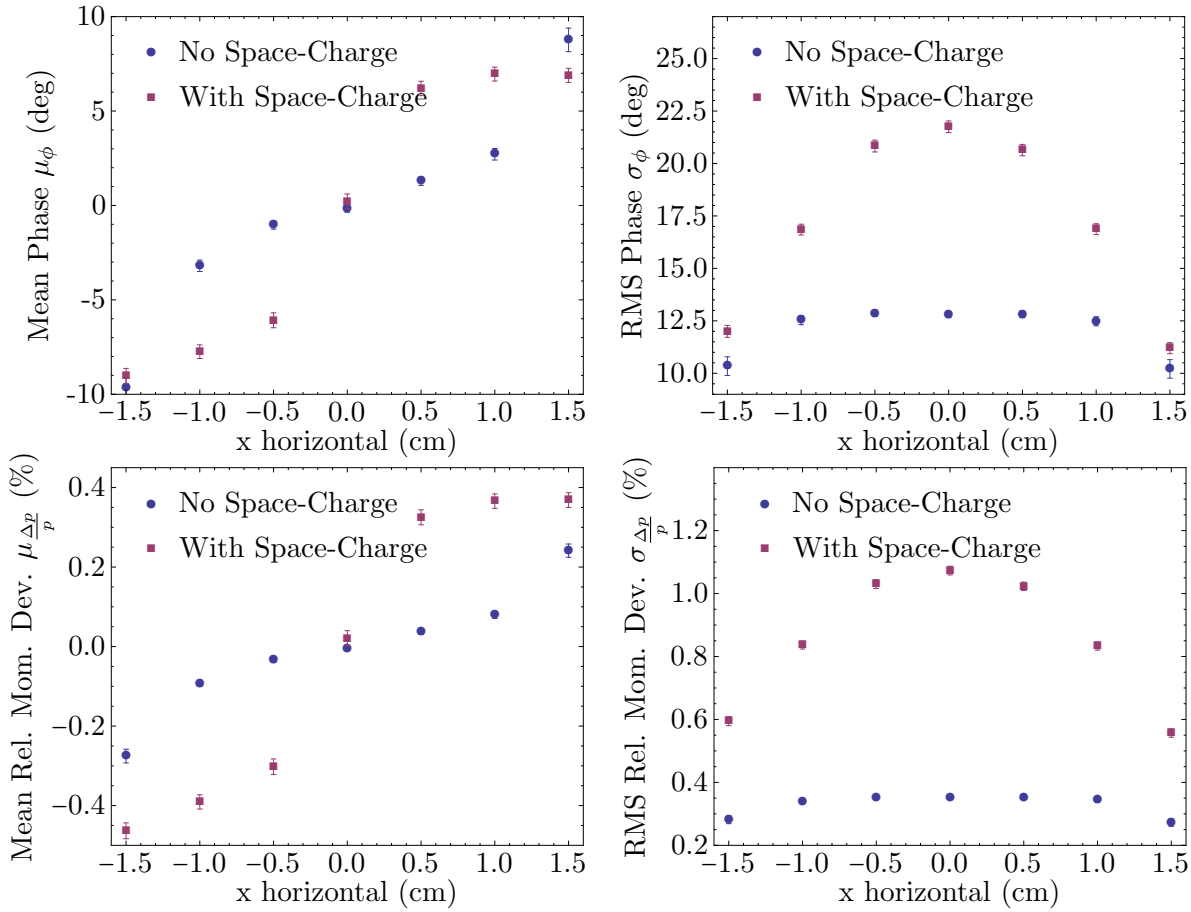

Fig. 7.23: Mean and standard variation for different cuts (horizontal location ±0.25 cm) at horizontal degree of freedom x based on the data shown in Fig. 7.21 (device entrance).

On the other hand, these effects are less significant compared to the sample simulation during a measurement for two reasons: At first, the stripping efficiency for the equilibrium charge state is far below the 100 % taken as an extreme case. Therefore, the blow-up effects due to the lower charge density after a short distance inside the dipole are lower. Furthermore, the measurement requires the primary beam current to be attenuated to several microamperes before hitting the Ta-foil (see Sec. 5.1.1). Usually this is accomplished by appropriate settings of the high-current slits (DS4/5), and therefore more than 1 m drift is taken into account with only minor space-charge effects. Hence, the actual properties of coupling between the transverse and longitudinal phase space lie in between the non-interacting and space-charge case shown in Fig. 7.23. The required extensive simulations, e.g. with the code DYNAMION, are beyond the scope of this work.

7.6 DAQ Electronics

Testing of the TOF DAQ electronics has been performed with a Berkeley DB-2 random pulse generator. It serves as an idealistic monochromatic source by splitting the signals and

feeding them instead of the diamond and MCP signals. While this approach would help to reveal severe systematic limitations of the electronics and the TDC, it does not reflect the real pulse shape situation as described in Sec. 7.4.1.1 and 7.4.2.1. Figure 7.24 shows the recorded histogram with a standard deviation of ≈ 0.934 channels, which corresponds to ≈ 22.8 ps. The RF RMS deviation turns out to be about the same value as determined from

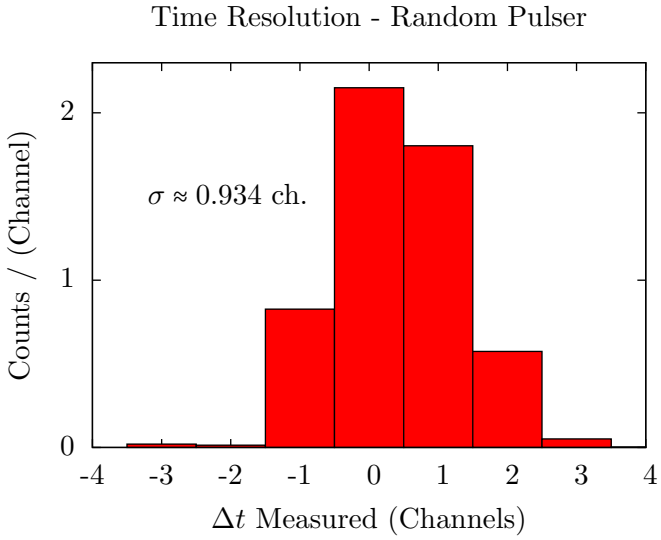

Fig. 7.24: The signal from a random pulser is split and feeds the DAQ chain of the diamond and MCP detector simultaneously as an idealised monochromatic source. The full NIM chain is explained in Sec. 4.1.2 and the TDC has an LSB of 25 ps.

the linear fit (see Fig. 4.6). This suggests that the resolution of the DAQ electronics, in this idealistic approach with deterministic pulse shapes from the random-pulse generator, is dominated by the TDC and not by the NIM chain. Inami [95] determined a RMS timing 7-9 ps for a similar NIM/CAMAC configurations fed by a random pulser, which supports a RMS timing resolution of better than 10 ps for the NIM chain. For simplicity, the total measured jitter is assigned to the TDC input channels. Since two of them are involved to measure the timing separation the input jitter for a single input is smaller by a factor of $1/\sqrt{2}$. Hence, the RMS jitter per TDC input is ≈ 17 ps.

7.7 Linear Approximation at Phase-Space Reconstruction

An absolute determination of the TOF requires both detectors to be synchronised, i. e. the knowledge of the relative offset of both timing signals. Not only relative cable delays are involved in the total time delay but also delays of relevant scale inside the detectors itself as the TOF of the emitted secondary electrons at the foil mounted in front of the MCP module. A synchronisation has not been accomplished in the present setup which focuses on relative evaluation of momentum and energy with respect to their mean values.

As described in Sec. 4.1.5 the phase-space mapping of the relative momentum and energy deviation follows a linear approximation in TOF for particle i,

$$\frac{\Delta p_i}{\langle p \rangle} \approx -\frac{\Delta t_i}{t_{\langle p \rangle}} \tag{7.35}$$

$$\frac{\Delta E_i}{\langle E \rangle} \approx -2\frac{\Delta t_i}{t_{\langle E \rangle}} \tag{7.36}$$

with $\Delta p_i = p_i - \langle p \rangle$, $\Delta E_i = E_i - \langle E \rangle$ and $\Delta t_i = t_i - t_{\langle p \rangle}$ or $\Delta t_i = t_i - t_{\langle E \rangle}$, respectively. In the following $t_{\langle p \rangle}$ denotes the TOF of the mean particle velocity (which is not necessarily the synchronous particle) along the detector separation l_{tof} with

$$t_{\langle p \rangle} = \frac{l_{tof}}{\langle \beta \rangle c}, \tag{7.37}$$

so that

$$p(t = t_{\langle p \rangle}) = \langle p \rangle \ . \tag{7.38}$$

In the same way, $t_{\langle E \rangle}$ denotes the TOF of the mean kinetic energy particle with

$$E(t = t_{\langle E \rangle} \approx t_{\langle p \rangle}) = \langle E \rangle \ . \tag{7.39}$$

Both, momentum and kinetic energy are considered in non-relativistic limit since the setup is located at a section that is traversed by a reference particle at about $\langle \beta \rangle \approx 5.5\,\%$. Thus, with the atomic mass unit m_u and TOF t_i between the MCP and diamond detectors at separation l_{tof}, the equations for the momentum p_i and kinetic energy E_i per nucleon of particle i are given by

$$p_i = p(t_i) = m_u\, l_{tof} \frac{1}{t_i} \tag{7.40}$$

and

$$E_i = E(t_i) = \frac{m_u\, l_{tof}^2}{2} \frac{1}{t_i^2} \, . \tag{7.41}$$

As the kinetic energy E_i in Eq. (7.41) is not a linear function in p_i, the TOF of the mean momentum particle and the particle mean energy is not identical in the general case, i. e. $t_{\langle p \rangle} \neq t_{\langle E \rangle}$. In other words, a particle of mean momentum is not necessarily a particle of mean energy. Evaluating the average of momentum and energy with the corresponding TOF distribution $\{t_i\}$ using Eq. (7.38) and (7.39) allows comparison of $t_{\langle p \rangle}$ and $t_{\langle E \rangle}$.

$$\langle p \rangle = m_u\, l_{tof} \left\langle \frac{1}{t} \right\rangle \stackrel{!}{=} m_u\, l_{tof} \frac{1}{t_{\langle p \rangle}} \qquad \Rightarrow \quad t_{\langle p \rangle} = \left\langle \frac{1}{t} \right\rangle^{-1} \tag{7.42}$$

$$\langle E \rangle = \frac{m_u\, l_{tof}^2}{2} \left\langle \frac{1}{t^2} \right\rangle \stackrel{!}{=} \frac{m_u\, l_{tof}^2}{2} \frac{1}{t_{\langle E \rangle}^2} \qquad \Rightarrow \quad t_{\langle E \rangle} = \sqrt{\left\langle \frac{1}{t^2} \right\rangle^{-1}} \tag{7.43}$$

Although not identical, treating $t_{\langle p\rangle} \approx t_{\langle E\rangle}$ is feasible if the standard deviation of the momentum distribution σ_p is sufficiently smaller than $\langle p\rangle$, i. e. $\sigma_{\frac{p}{\langle p\rangle}} \ll 1$. This can be seen by expressing the standard deviation of $\{\frac{p_i}{\langle p\rangle}\}$ by means of $\{t_i\}$ using Eq. (7.40) and (7.41)

$$\sigma_{\frac{p}{\langle p\rangle}} = \frac{\sqrt{\left\langle\frac{1}{t^2}\right\rangle - \left\langle\frac{1}{t}\right\rangle^2}}{\left\langle\frac{1}{t}\right\rangle} = \frac{\sqrt{\frac{1}{t^2_{\langle E\rangle}} - \frac{1}{t^2_{\langle p\rangle}}}}{t_{\langle p\rangle}} = \sqrt{\left(\frac{t_{\langle p\rangle}}{t_{\langle E\rangle}}\right)^2 - 1}, \tag{7.44}$$

which shows that $t_{\langle p\rangle}$ and $t_{\langle E\rangle}$ differ by a factor of $\sqrt{\sigma^2_{\frac{p}{\langle p\rangle}} + 1}$. Therefore, with the typical relative momentum spread $\sigma_{p/\langle p\rangle}$ of less than 1 %, $t_{\langle p\rangle}$ and $t_{\langle E\rangle}$ are used synonymously for this setup, as $\sqrt{(0.01)^2 + 1} \approx 1.00005$. Furthermore, with Δt_i denoting the time deviation of an arbitrary particle i with respect to $t_{\langle p\rangle}$ or $t_{\langle E\rangle}$, respectively,

$$\Delta t_i = t_i - t_{\langle p\rangle} \approx t_i - t_{\langle E\rangle}\,, \tag{7.45}$$

the absolute longitudinal momentum deviation per nucleon writes as

$$\begin{aligned}\Delta p_i = p(t_i) - \langle p\rangle &= m_u\, l_{tof}\left\{\frac{1}{t_{\langle p\rangle} + \Delta t_i} - \frac{1}{t_{\langle p\rangle}}\right\} = \\ &= -m_u\, l_{tof}\frac{\Delta t_i}{t_{\langle p\rangle}(t_{\langle p\rangle} + \Delta t_i)} = -\underbrace{m_u\, l_{tof}\frac{1}{t_{\langle p\rangle}}}_{m_u v_{\langle p\rangle} \overset{!}{=} \langle p\rangle}\frac{\frac{\Delta t_i}{t_{\langle p\rangle}}}{1 + \frac{\Delta t_i}{t_{\langle p\rangle}}}\,,\end{aligned} \tag{7.46}$$

which finally delivers the exact relative momentum deviation in the classical limit

$$\left.\frac{\Delta p_i}{\langle p\rangle}\right|_{ex} = -\frac{\frac{\Delta t_i}{t_{\langle p\rangle}}}{1 + \frac{\Delta t_i}{t_{\langle p\rangle}}}\,. \tag{7.47}$$

In the same manner the absolute longitudinal energy deviation per nucleon is given by

$$\begin{aligned}\Delta E_i = E(t_i) - \langle E\rangle &= \frac{m_u\, l^2_{tof}}{2}\left\{\frac{1}{\left(t_{\langle E\rangle} + \Delta t_i\right)^2} - \frac{1}{t^2_{\langle E\rangle}}\right\} = \\ &= \frac{m_u\, l^2_{tof}}{2}\frac{t^2_{\langle E\rangle} - (t_{\langle E\rangle} + \Delta t_i)^2}{\left(t_{\langle E\rangle}(t_{\langle E\rangle} + \Delta t_i)\right)^2} = -\underbrace{\frac{m_u\, l^2_{tof}}{2}\frac{1}{t^2_{\langle E\rangle}}}_{\frac{m_u v^2_{\langle E\rangle}}{2} \overset{!}{=} \langle E\rangle}\frac{2\,\frac{\Delta t_i}{t_{\langle E\rangle}} + \left(\frac{\Delta t_i}{t_{\langle E\rangle}}\right)^2}{\left(1 + \frac{\Delta t_i}{t_{\langle E\rangle}}\right)^2}\,.\end{aligned} \tag{7.48}$$

This allows to calculate the exact relative kinetic energy deviation in the classical limit.

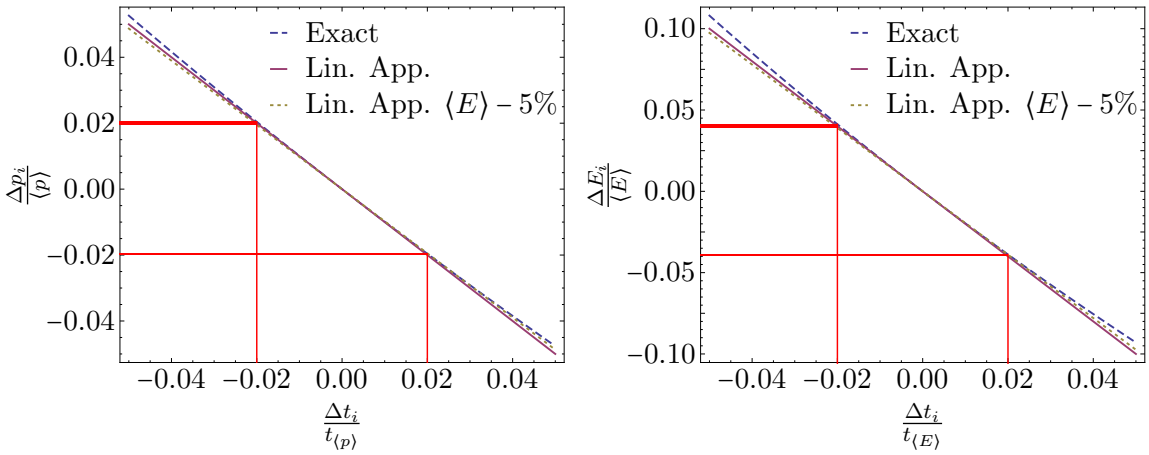

Fig. 7.25: *Relative momentum deviation* $\Delta p_i/\langle p\rangle$ and *relative energy deviation* $\Delta E_i/\langle E\rangle$ in linear approximation (solid lines) and classical exact representation (dashed lines) in terms of the *relative time deviation* $\Delta t_i/t_{\langle p\rangle}$ and $\Delta t_i/t_{\langle E\rangle}$, respectively. Additionally, the linear approximations are plotted with a different evaluation point $t_{\langle E\rangle}$ of the Taylor series (see Sec. 4.1.5), shifted to a lower kinetic energy by 5 %. The effect of a mismatched evaluation point is discussed in Sec. 7.7.1. To visualise the minor impact from the exact classical description, the width of the red lines corresponds to the deviation of $\Delta p_i/\langle p\rangle$ and $\Delta E_i/\langle E\rangle$, respectively, at a deviation from the mean energy ±4 standard deviations of the expected energy distribution.

Rearranging Eq. (7.48) delivers

$$\left.\frac{\Delta E_i}{\langle E\rangle}\right|_{ex} = -\frac{2\,\frac{\Delta t_i}{t_{\langle E\rangle}} + \left(\frac{\Delta t_i}{t_{\langle E\rangle}}\right)^2}{\left(1+\frac{\Delta t_i}{t_{\langle E\rangle}}\right)^2}\,. \tag{7.49}$$

Comparison of the exact relative deviations of momentum Eq. (7.47) and kinetic energy Eq. (7.49) to their linear approximations Eq. (7.35) and (7.36) as a function of $\frac{\Delta t_i}{t_{\langle p\rangle}}$ are visualised in Fig. 7.25. The deviations from the exact values have a trivial asymmetric characteristic, being smaller than the classical exact values for faster particles, while slower particles overestimate the relative momentum and energy deviation. For a particle with an exemplary difference in TOF of $\Delta t_i = \pm 1$ ns with respect to a particle of mean velocity (red guide lines), corresponding to $\frac{\Delta t}{t_{\langle p\rangle}} \approx 2\,\%$, the linear approximation is still very close to the exact values as listed in Tab. 7.3. As this represents four times the expected standard deviation of the kinetic energy to either side, this correction can be neglected.

7.7.1 Deviations from the Expected Mean Energy

Timing signals recorded at the MCP and diamond detector exhibit a constant offset, turning it into a relative measurement (see Sec. 4.1.5). Due to the nonlinearity in Δt_i of the exact

Eqs. (7.47) and (7.49) for the relative momentum and energy deviation, those are not form-invariant under translations with a constant offset c_{off} in time

$$\Delta t_i \quad \longrightarrow \quad \Delta t_i + c_{off}, \tag{7.50}$$

except for a constant shift, which is irrelevant using central moments, and hence do not conserve the shape of the phase space:

$$\left.\frac{\Delta p_i}{\langle p\rangle}\right|_{ex} = -\frac{\frac{\Delta t_i}{t_{\langle p\rangle}}}{1+\frac{\Delta t_i}{t_{\langle p\rangle}}} \quad \longrightarrow \quad -\frac{\frac{\Delta t_i + c_{off}}{t_{\langle p\rangle}}}{1+\frac{\Delta t_i + c_{off}}{t_{\langle p\rangle}}} \neq \left.\frac{\Delta p_i}{\langle p\rangle}\right|_{ex} + const\,, \tag{7.51}$$

$$\left.\frac{\Delta E_i}{\langle E\rangle}\right|_{ex} = -\frac{2\,\frac{\Delta t_i}{t_{\langle E\rangle}} + \left(\frac{\Delta t_i}{t_{\langle E\rangle}}\right)^2}{\left(1+\frac{\Delta t_i}{t_{\langle E\rangle}}\right)^2} \quad \longrightarrow \quad -\frac{2\,\frac{\Delta t_i + c_{off}}{t_{\langle E\rangle}} + \left(\frac{\Delta t_i + c_{off}}{t_{\langle E\rangle}}\right)^2}{\left(1+\frac{\Delta t_i + c_{off}}{t_{\langle E\rangle}}\right)^2} \neq \left.\frac{\Delta E_i}{\langle E\rangle}\right|_{ex} + const\,. \tag{7.52}$$

Consequently, the determination of the Twiss parameters (Sec. 2.4) is not independent from c_{off}, when using the exact equations. On the other hand, the fact that by the linear approximations the Twiss parameters are intrinsically invariant under translations with respect to Δt_i can be exploited. Fortunately, as seen in Fig. 7.25 and the corresponding values in Tab. 7.3, the error through the linear approximation is negligible compared to other experimental uncertainties.

Tab. 7.3: Exemplary values of the exact relative momentum $\Delta p_i/\langle p\rangle|_{ex}$ Eq. (7.47) and relative kinetic energy $\Delta E_i/\langle E\rangle|_{ex}$ Eq. (7.49) and their linear approximation Eq. (7.35) and (7.36) for a particle that is separated four standard deviations of the expected relative momentum and energy deviation ($\Delta t_i/t_{\langle p\rangle} \approx \pm 0.02$). The third column additionally considers the effect of a mean energy shift $\Delta\langle E\rangle$ due to the gas stripper and foils of 5 % and thus for an evaluation point being slightly off.

	Exact	**Lin. approx.**	**Lin. approx., $\langle E\rangle$ – 5 %**
$\frac{\Delta p_i}{\langle p\rangle}\times 10^2$	2.04, −1.96	2.00, −2.00	1.95, −1.95
$\frac{\Delta E_i}{\langle E\rangle}\times 10^2$	4.12, −3.88	4.00, −4.00	3.89, −3.89

Nevertheless, the validity of this procedure obviously depends on the evaluation point of the series expansion, which is the TOF of a mean-momentum particle $t_{\langle p\rangle}$ or a mean-energy particle $t_{\langle E\rangle}$ in case of the relative momentum deviation or relative energy deviation. The design energy of the accelerator at the stripper section is about 1.4 MeV per nucleon. The influence of an exemplary mean energy loss to account for a shifted evaluation point using the linear approximation is investigated in the following. A range of 5 % of mean energy loss on passage of the gas stripper is reasonable. This includes dissipative effects at the tantalum and aluminum foils and the jitter in output energy for different ion species given by the nature of the IH structures.

According to Eq. (7.36), a mean energy shift $\Delta\langle E\rangle$ of 5 % with respect to the design energy can be mapped to the timing data by

$$\frac{\Delta t_{\langle p\rangle}}{t_{\langle p\rangle}} \approx \frac{\Delta t_{\langle E\rangle}}{t_{\langle E\rangle}} \approx -\frac{\Delta\langle E\rangle}{2\langle E\rangle}\,. \tag{7.53}$$

This allows modification of Eq. (7.35) and (7.36) to comprise a shift in mean TOF $\Delta t_{\langle p\rangle}$ using the following approximation since $\frac{\Delta t_{\langle p\rangle}}{t_{\langle p\rangle}} \ll 1$:

$$\frac{\Delta t_i}{\left(t_{\langle p\rangle} + \Delta t_{\langle p\rangle}\right)} = \frac{\Delta t_i}{t_{\langle p\rangle}\left(1 + \frac{\Delta t_{\langle p\rangle}}{t_{\langle p\rangle}}\right)} \overset{\frac{\Delta t_{\langle p\rangle}}{t_{\langle p\rangle}} \ll 1}{\approx} \frac{\Delta t_i}{t_{\langle p\rangle}}\left(1 - \frac{\Delta t_{\langle p\rangle}}{t_{\langle p\rangle}}\right) \approx \frac{\Delta t_i}{t_{\langle p\rangle}}\left(1 - \frac{\Delta\langle E\rangle}{2\langle E\rangle}\right). \tag{7.54}$$

Fig. 7.25 includes the corresponding approximations with a mean energy shift of 5 %. Within a *four sigma range* (both, positive and negative), with respect to the expected standard deviation of the kinetic energy, there are no significant deviations from the classical exact formulae, and thus these discrepancies are also negligible.

7.8 Summary to TOF Uncertainties

The uncertainties which have been accounted for in this chapter are of different quality and significance when it comes to the effect on the measurement of the longitudinal phase space. Most timing uncertainties and dissipative effects can be attributed to uncertainties in the Gaussian sense. The overall effect of Gaussian contributions on an two-dimensional Gaussian model space has been investigated and discussed in detail in Chapter 6. Effects that cannot be treated as Gaussian contributions occurred during the variation of the gas pressure at the stripper section, the variation of the position of the high current slits (DS4/5) and the interaction of particles with the collimator configuration responsible for particle number attenuation of an intense beam where, e.g., space-charge effects on the longitudinal phase space are supposed to be studied. All uncertainties taken into account are listed in Tab. 7.4.

The tantalum foil at the entrance of the collimator configuration, which serves as a thin target to provide Coulomb scattering, is inherently connected to the particle number attenuation and is an essential concept of the measurement setup. From the consideration of uncertainties, a major impact on the capabilities of the method is apparent. While the contribution from the collisional straggling, i. e. by assuming a perfect and homogeneous foil thickness, is already about 10 – 15 % of the expected energy width, the texture of the rolled foils represents an even larger impact. Other authors, such as Bitao et al. [89], claim a significant contribution of the texture to the effective straggling. Their measurements with a rolled tantalum foil of 367 µg/cm^2, compared to 210 µg/cm^2 installed in the present setup, hinted an effective thickness variation of about 34 %. Optical microscopy of the tantalum foil supports the experimental results by revealing prominent inhomogeneities on a small scale that does not allow to consider the foil sufficiently homogeneous within the aperture dimensions. The mean energy loss together with an assumed thickness variation

of 34 % alone contributes about 1 % of energy spread which is the expected energy spread of the bunch. Thus, it represents a very strong limitation on the capabilities of the setup. Evaporated foils, on the other hand, are expected to feature a more homogeneous thickness of about 10 % but are known to be not as resistant to the particle beam and, thus, are not feasible for particle number attenuation.

Compared to the straggling contribution of the first foil, the thin aluminium foil of ≈ 37 nm mounted in front of the MCP is negligible. The collisional straggling is about four times smaller than the corresponding contribution from the tantalum foil. More importantly, the evaporated aluminium foil is expected to be more homogeneous compared to the rolled tantalum foil. Nevertheless, even assuming a comparable inhomogeneity to the tantalum foil, the effective straggling is about six times smaller due to the lower mean energy loss. Hence, the tantalum foil clearly dominates the limiting overall dissipative contribution originating from straggling.

Another effect connected to the aluminium foil is the unavoidable geometric alignment which comes with an uncertainty of the detector separation. This contribution scales inversely with the separation and is about 25 ps for the setup at hand.

No quantitative value of timing jitter can be provided for the spectra of the liberated secondary electrons. Although more than 100 electrons per ion will be emitted it is not clear if this results in a sufficiently low jitter timing characteristic. In fact, since the TOF between the aluminium foil and the MCP front is very sensitive to the initial energy of the electrons, at the same time the MCP is sensitive to single electrons. Fluctuations of the fastest electrons may contribute a major jitter in the generation of the logic time signal. In particular, distortions of the leading edge of the MCP pulse shape may be connected to them.

The time resolution connected with the discrimination of the particle detector signals was estimated by the plain pulse shapes recorded with a fast oscilloscope. Additionally, using the logic signal from the discriminator as external trigger in persistence mode, provides rough information about the timing jitter. While the poly-crystalline diamond material shows a pulse-height distribution with a dynamic range within about a factor of 2, the leading edge does not feature any significant distortions. Together with the design properties of the double threshold discriminator, a time jitter of 50 ps is considered a realistic value. Due to the extension of the electrode and the finite propagation of the signal, an additional (but minor) time jitter of about 10 ps is taken into account. The MCP pulse shapes have a higher dynamic range of pulse height than the poly-crystalline diamond detector and do feature shoulders of fluctuating duration (see Fig. 7.18) which makes an estimate of the effect problematic. Nevertheless, taking into account a time jitter of 150 ps appears to be an appropriate choice without overestimating the effect.

It is important to distinguish absolute timing effects, such as the trigger accuracy, from dissipative effects. While all absolute timing contributions will get less significant with a (theoretical) larger separation of the detectors, the later ones affect the phase space itself and thus represent an asymptotic limitation to the measurement capability that cannot be overcome by extending the separation of the detectors. Figure 7.26 shows the systematic relative error according to Eq. (7.6) with respect to the detector separation. It incorporates all systematic contributions described in this chapter and listed in Tab. 7.4 which can be

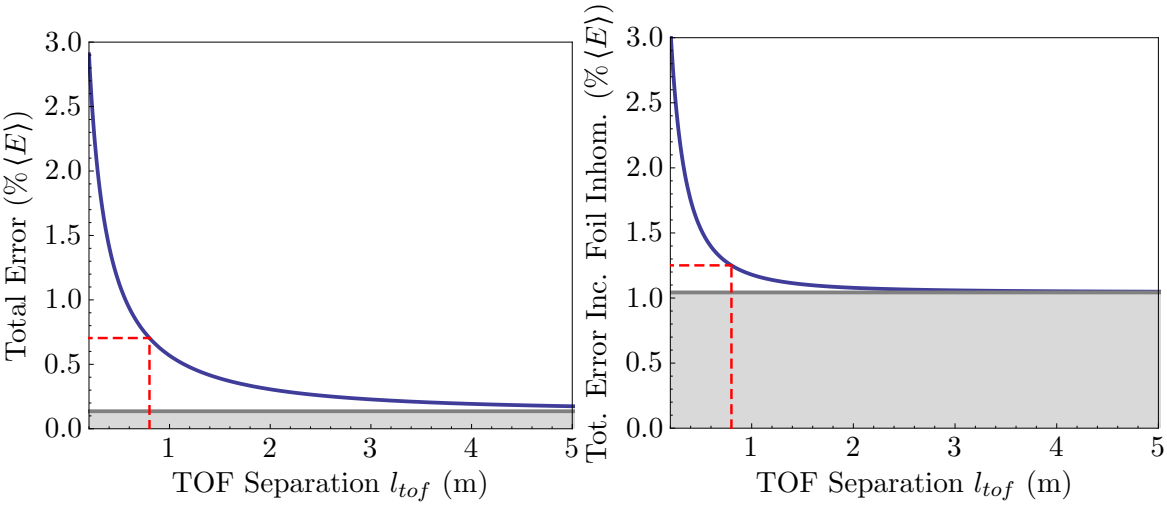

Fig. 7.26: Both plots show the effective relative error contribution $\sigma_E^{tot}/\langle E\rangle$ versus the detector separation l_{tof} used in the TOF section. The left plot includes the error components listed in Tab. 7.4 omitting the major impact of the foil inhomogeneities which are included in the right plot. Absolute timing uncertainties can be damped by an extended TOF separation l_{tof}, which is clearly seen by the shown characteristic. Nevertheless, the grey areas at the bottom mark the asymptotic error contribution introduced by all quantified effects on the phase space itself and cannot be overcome by a larger detector separation. In both plots the red dashed line denotes the current detector separation of about 801 mm and the corresponding relative error σ_E^{tot}. Not including the foil inhomogeneities results in an estimate of the total error of $\sigma_E^{tot}/\langle E\rangle$=0.7 % whereas by taking the foil structure into account the error is $\sigma_E^{tot}/\langle E\rangle$=1.25 %.

treated in the Gaussian sense. This excludes the influences of the gas stripper, the high current slits and the collimator. The reference to the detector separation of the measurement is provided by the red dashed line. As mentioned before, for larger separations of the detectors the relative error asymptotically approaches the dissipative offset represented by the grey area. The left figure does not include the contribution of the foil inhomogeneities in order to visualise the major impact on the total resolution of the measurement setup, which is evident from the right figure. Referring to the expected energy width of 1 %, a direct measurement of the total phase space is not possible. Even if an extended separation of the detectors was possible, the dissipative effects alone would be on the order of the expected energy spread itself. Since both, the true energy spread of the bunch as well as the limited resolution, are of about the same order of magnitude it is obvious that a certain sensitivity to the energy distribution is available, but a reliable direct measurement is not possible.

Tab. 7.4: Systematic contributions ordered according to the beam direction. Absolute time contributions σ_t are given at the current TOF separation of about 801 mm, in case the value depends on the detector separation.

	$\frac{\sigma_E}{\langle E \rangle}$ (%)	σ_t (ps)	Section #
Gas pressure at stripper section	n/a	n/a	5.2.2
Coupling of transverse and longitudinal phase space	n/a	n/a	7.5.1
High current slits (US3DS4/5)	n/a	n/a	5.2.3
Ta foil (part. atten.) - Collisional straggling	0.13		7.1.1
Ta foil (part. atten.) - Texture/variation of thickness	≈ 1.0		7.1.2
Ta foil (part. atten.) - Transversal momentum contrib.	0.001		7.1.3
Ta foil (part. atten.) - Finite solid angle	0.015		7.2
Interaction with collimator apertures	n/a	n/a	5.3.2
Al foil (sec. e^-) - Collisional straggling	0.033		7.3.1
Al foil (sec. e^-) - Texture/variation of thickness	≈ 0.17		7.3.2
Al foil (sec. e^-) - Energy spectra/TOF $e^- \rightarrow$ MCP		3	7.3.4
Al foil (sec. e^-) - Tilt/variation of TOF length		25	7.3.3
MCP pulse shape distortion/discrimination		150	7.4.1.1
Poly-crystalline diamond detector - discrimination		50	7.4.2.1
Poly-crystalline diamond detector - propagation time		10	7.4.2.2
TDC input jitter per channel incl. NIM setup		17	7.6
Linear Approximation: phase space reconstruction	n/c	n/c	7.7.1

n/a - qualitative analysis/quantitative analysis not available

n/c - not considered/not an error in the Gaussian sense

(see referred section)

Chapter 8

Conclusion

The goal for this work was a feasibility study of longitudinal phase-space measurements at the GSI linear accelerator UNILAC. The starting point has been the existing time-of-flight setup installed inside the UNILAC charge-separation chicane.

Originally, this experimental setup aimed at bunch-length measurements only. The device was used during the commissioning of the then new high-current injector in 1999 [6]. A major upgrade of the setup in 2000 included an MCP module, which additionally allowed to extract the time-of-flight of individual ions beyond the arrival time at the poly-crystalline diamond detector. This allows, in principle, to reconstruct the longitudinal phase-space distribution. The necessary optimisations of the existing high-current injector to match the FAIR requirements revived the interest in longitudinal phase-space distribution measurements.

However, measurements by Forck et al. [7] hinted a larger energy width by about a factor of two compared to the expected theoretical values. An energy width of that value is considered too large, such a beam would not be transported. The measurements in Chapter 5 clearly support a limiting energy resolution insufficient for the determination of the phase space. Typical measured longitudinal energy spreads were significantly larger than 1 %, whereas the expected theoretical values are $\lesssim 1\,\%$. For instance, the measured energy spreads for high-current Ar beams ranged between 1.5 % to 1.6 %, whereas the expected theoretical value is $\approx 0.9\,\%$

Intentionally disturbing the longitudinal phase-space distribution by varying the RF phase of the IH2 cavities within a range of 20° revealed a sensitivity on the longitudinal phase space which can be mainly attributed to the time arrival. While the mean energies can be resolved properly, the measured energy widths stay about the same within the uncertainty. This is unexpected, given the high sensitivity of the KONUS beam-dynamics on the RF phase. All energy projections are consistently close to Gaussian distributions, also hinting at a limiting energy resolution.

A thorough analysis of contributions to the uncertainties of the unavoidable beam attenuation has been presented, including the influence of the gas jet and the high-current slits. Variation of the gas-jet pressure showed a small but measurable effect due to the enhanced energy straggling contribution of higher pressures. After the drift between stripper and

measurement setup, this resulted in the expected correlation of energy widths and bunch lengths, as well as mean energy shifts and arrival times. During this measurement, an unexpected long-ranged, low-energy trail emerged for lower pressures. While the underlying effect is not understood, the prominent trail can be unambiguously attributed to scattering at the high-current slit located 1.5 m upstream the Ta scattering foil. Dedicated measurements were performed to study the effect of the high-current slit configurations and revealed a clear effect on the measured parameters for slit openings smaller than 1 mm. The measured energy spreads and bunch lengths increased, while the bunch structure showed a depletion zone at the centre by developing two distinct peaks. Hence, only larger slit openings larger than 1 mm, better 2 mm, should be used for a trustful experimental determination.

An alternative measurement approach has been introduced by using a mono-crystalline diamond detector with calorimetric properties which does not rely on TOF. The measurement is based on sampling the detector pulse and RF signal. Event information such as pulse integral and arrival time are determined by offline post-processing of the raw data. However, the diamond detector does not provide stable pulse shapes. While the amplitude dropped by $\approx 5\,\%$ during the irradiation with only $\approx 10^5$ fully stopped argon ions, the integral value of the same set of events dropped by $\approx 2\,\%$. The gain loss was accounted for by fitting the trend and subsequent rescaling. It is important to note that this gain loss alone is larger than the expected energy spread. Therefore, a correction is mandatory. Measured energy spreads, based on the pulse integral, were also larger than the expected values. The use of a mono-crystalline diamond did not improve the quality of the measured data compared to the TOF data. Background contamination originating from the diamond detector itself further complicated the analysis.

Prominent trails could be exactly identified as scattering off the collimator apertures. In case of the samarium measurement, more than 35 % of the recorded events are located in the long-ranged trails. Those contributions from scattering are unexpected and may be problematic as they also populate the phase-space core region and, thus, have influence on the covariance matrix. Moreover, a good understanding of this contribution may be of great importance to other measurement methods which are based on small apertures directly exposed to the beam at similar energies. In particular, the so-called Pepperpot device, which aims for single-shot transverse emittance determination, is known to have discrepancies between the predicted and measured transverse emittances. Measured emittances are a factor of two larger than expected [82–84].

To have a consistent and reproducible method of analysing heavily contaminated data, the robust MCD estimator [70] for covariance matrices was used throughout this work. This avoids manual, biased trimming of outliers.

All measurements consistently feature energy spreads larger than expected by theoretical considerations and plausibility arguments. Together with the Gaussian energy distribution this is a strong hint on a limiting energy resolution. Additionally, the characteristic Twiss parameter α (correlation) is consistently too small. Expected values for Twiss parameter α range around 4 while measured values are smaller than 1, typically around 0.7. A Gaussian model-space delivered the dependency of the Twiss parameters on the experimental resolution. The dependencies clearly show that the real Twiss parameters are not accessible directly. An effective timing resolution of 35 ps, by means of the system response, would

already falsify the measured value of α by 10 %. Transformation and back-transformation equations have been derived for the emittance and Twiss parameters between the real and disturbed phase-space distribution for given experimental resolutions. This allows to estimate the real parameters if the experimental resolution is known. A very good agreement for the high-current HIPPI measurement is reached for an empirical Gaussian system response with standard deviation of 1.4 times the theoretical energy width. Hence, the system response alone is already larger than the actual width of the energy distribution.

Systematic error contributions of the individual components have been studied in detail. Originally, the idea has been that the collisional straggling inside the foils is the dominating contribution. It turned out that the impact of the homogeneity of the foils is even more crucial and dominates all other contributions.

While the experimental setup is not yet able to measure the full longitudinal phase-space distribution, it is capable of providing valuable information about the bunch structure, as long as the high-current slit opening is larger than 1 mm. Several campaigns have been successfully supported with bunch-structure measurements [62, 96, 97].

Outlook The largest impact on the device performance is the inhomogeneity of the foils. However, even if this problem can be solved, the requirements for a direct measurement of the longitudinal phase-space are extremely high as can be seen from Eq. (6.18). The main reason for this is the high α value. Simply prolonging the TOF separation does not help to overcome the various dissipative contributions connected with the attenuation mechanism.

The device will be still useful for bunch structure and bunch length measurements and has been requested by the injector group for a measurement campaign in 2014. Alternative measurement devices for the longitudinal phase-space distributions are not available. For this, using the MC diamond detector instead of the TOF setup would significantly improve on the complicated handling but requires a completely new DAQ to sample all registered ions in a macro pulse.

Furthermore, the measurement device can be used to study the effects of the scattering at the collimator apertures. This is potentially an overlooked issue in other diagnostic devices, for instance the Pepperpot device.

Since the FAIR design parameters for the injector are currently re-evaluated, no statement about the necessity of the device for the optimisation process can be made.

Chapter A

Schematic Aperture and Technical Drawing of High-Current Slit

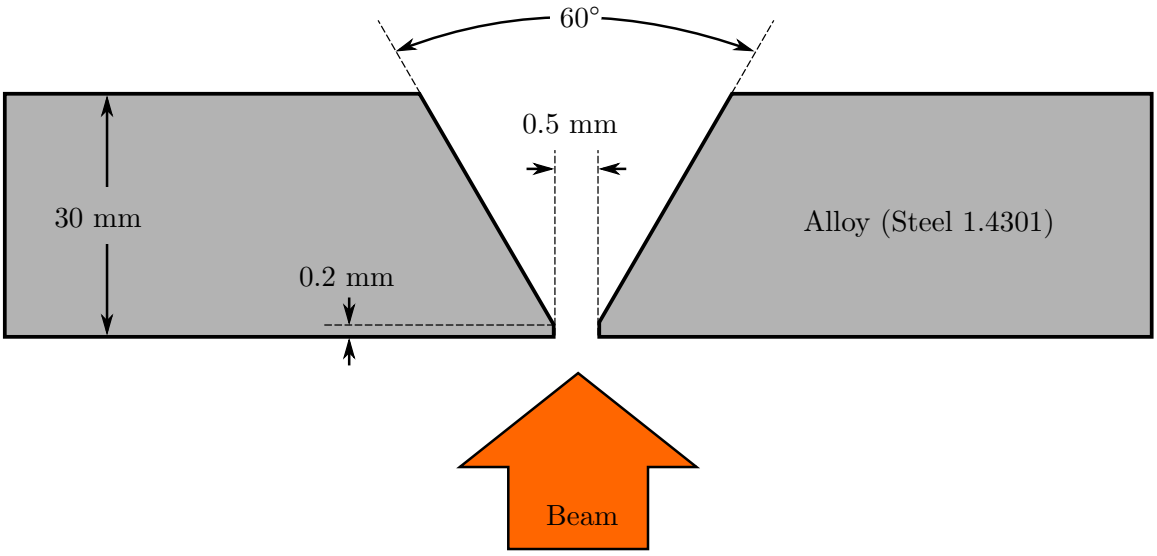

Fig. A.1: Schematic cut along one of the two identical apertures. The plate is made of steel alloy: Fe 73 %, Cr 18 %, Ni 9 %.

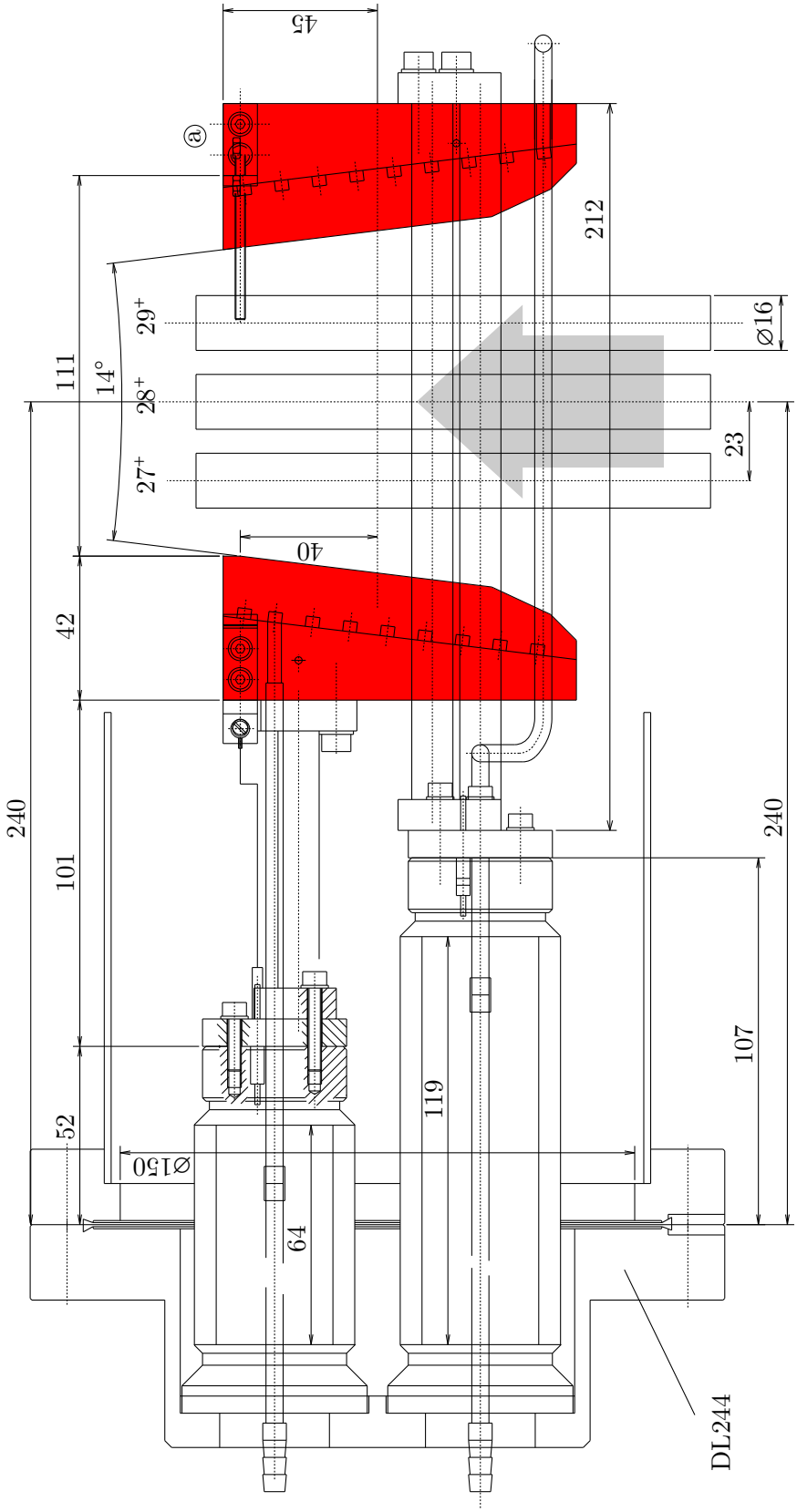

Fig. A.2: High-current slits (cooled) used for charge separation and late attenuation of the beam during high-current measurements of the longitudinal phase space [36]. All units in mm. Uncertainties for fixed cuts and boreholes ±0.1 mm, relative alignments ±0.5 mm.

Chapter B

Technical Drawing of Measurement Setup

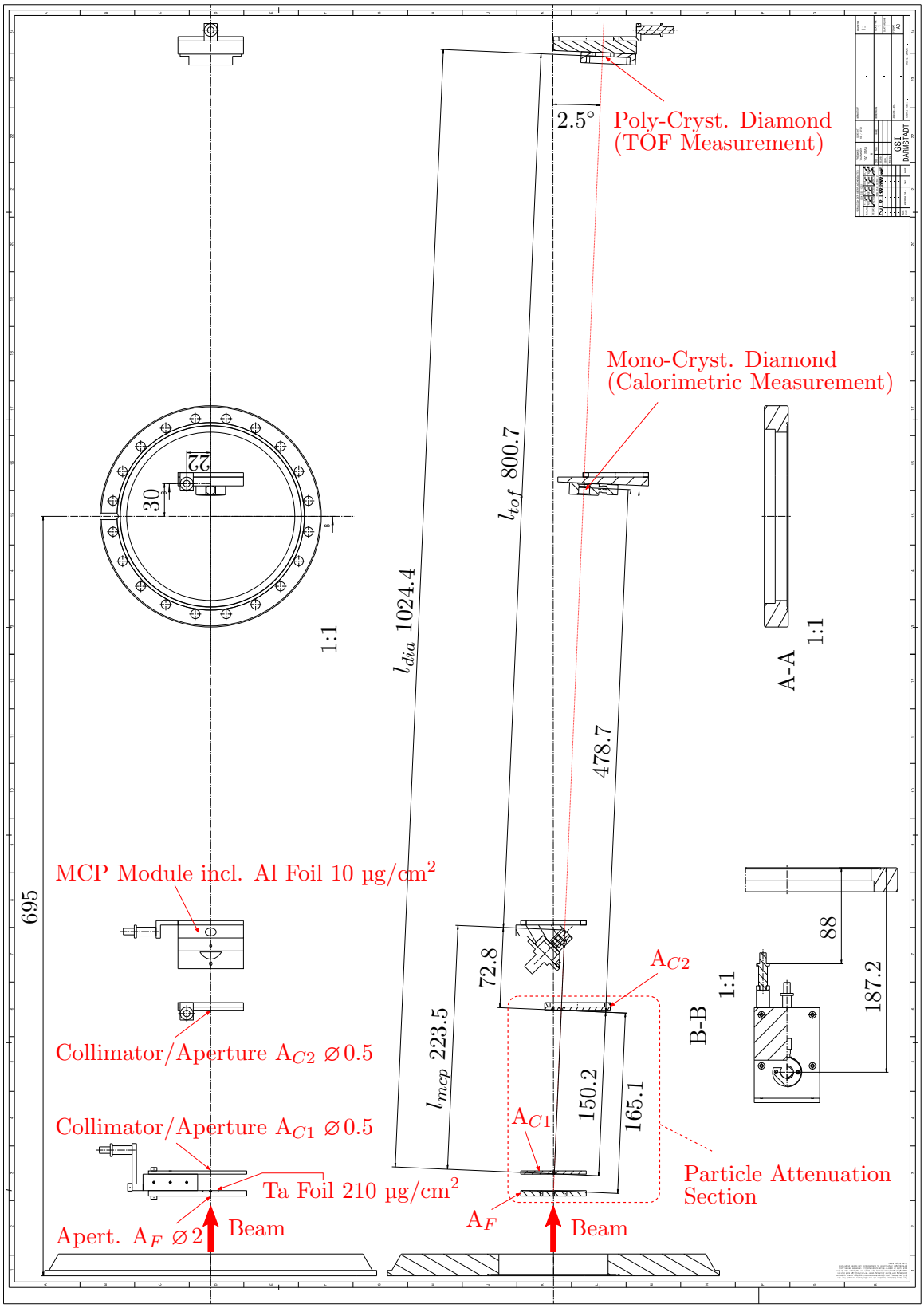

Fig. B.1: Technical drawing of the diagnostics chamber. All units in mm.
Left: Side view. **Right:** Top view. Uncertainties for fixed cuts and boreholes ±0.1 mm, relative alignments ±0.5 mm.

Chapter C

CST Simulation of MCP Module

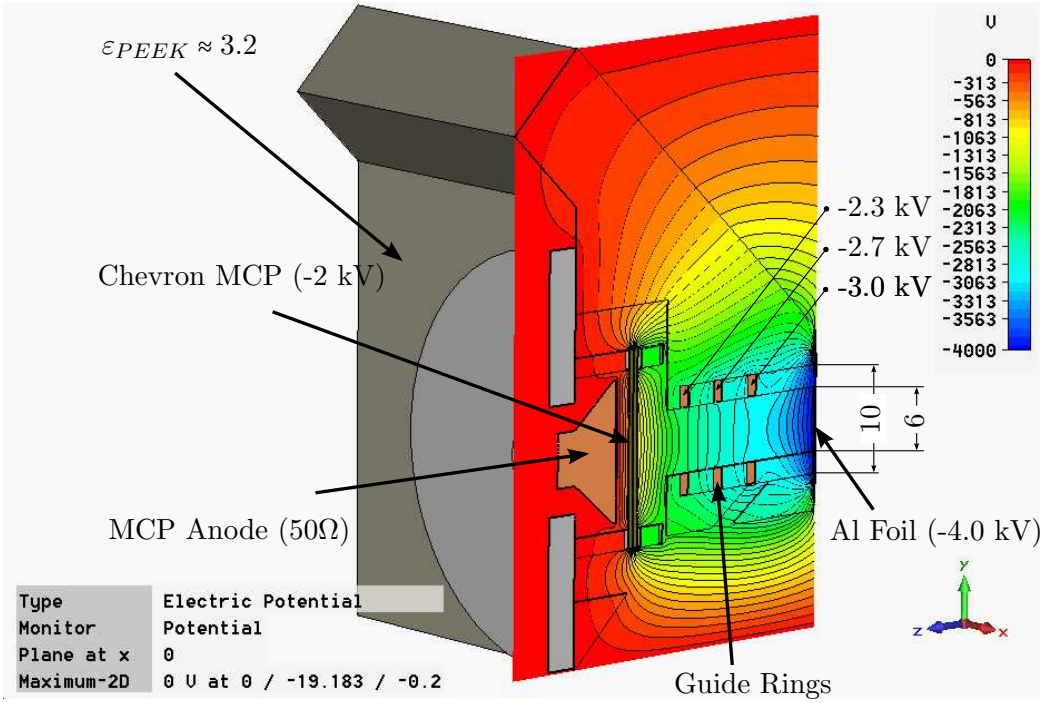

Fig. C.1: CST Microwave Studio simulation of equipotential lines inside the MCP detector module by P. Kowina [43]. Simulation includes the PEEK mounting, MCP Hamamatsu F4655-13 module (Sec. 3.3.1), the guide rings and Al foil.

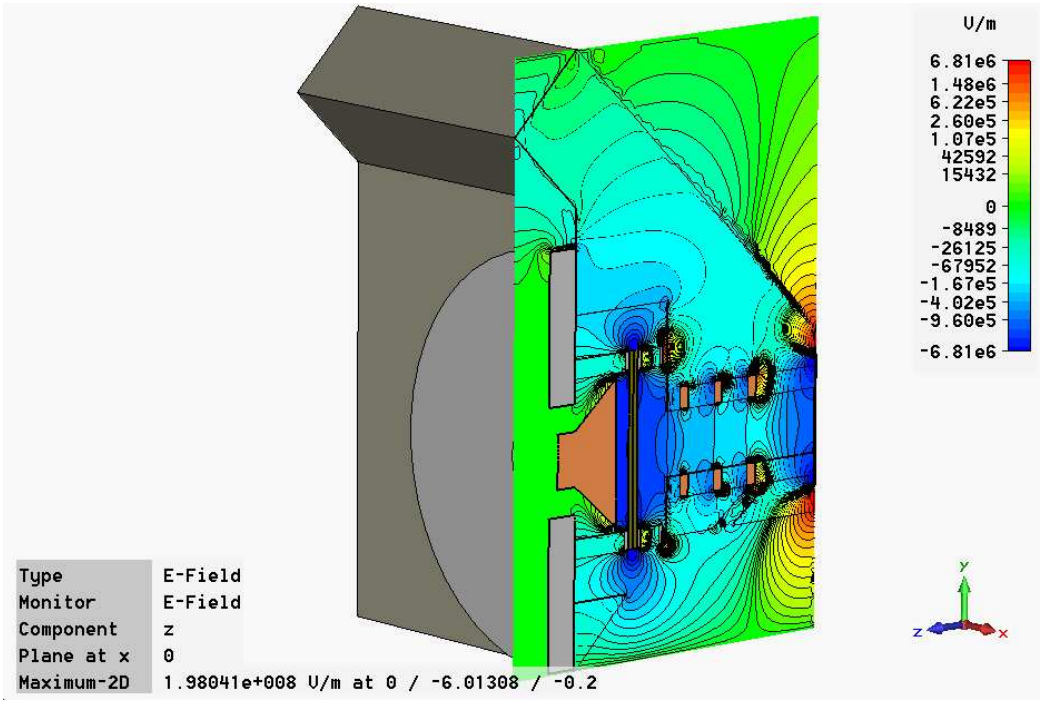

Fig. C.2: Simulation by P. Kowina [43] of the E-field z-component, parallel to the guide-ring axis. This is the ideal path of the secondary electrons towards the MCP front.

Chapter D

Invariance of Convoluted Covariances with Symmetric Kernels

In Chapter 6 the straightforward convolution of the real phase-space distribution $\rho(x, y)$ with a Gaussian response function $g(y)$ showed that the covariance σ_{xy} is conserved (see Eq. (6.11)). More generally, it can be proven hat the covariance of any arbitrary distribution $\rho(x, y)$ is conserved under convolution with a normalised, symmetric kernel, i. e. $k(-y) = k(y)$ and $\int_{-\infty}^{+\infty} \mathrm{d}y\, k(y) = 1$. The calculation is carried out in y-direction to match Sec. 6.3.

The formal convolution of distribution $\rho(x, y)$ with kernel $k(y)$ writes

$$\rho'(x, y) = (\rho * k)(x, y) = \int_{-\infty}^{+\infty} \mathrm{d}\kappa\, \rho(x, \kappa)\, k(y - \kappa)\,, \tag{D.1}$$

whereas the covariance of $\rho'(x, y)$ is determined via

$$\sigma'_{xy} = \int_{-\infty}^{+\infty} \mathrm{d}x \int_{-\infty}^{+\infty} \mathrm{d}y\, \rho'(x, y)\, (x - \langle x \rangle)\, (y - \langle y \rangle)\,. \tag{D.2}$$

Applying Eq. (D.1)

$$\sigma'_{xy} = \int_{-\infty}^{+\infty} \mathrm{d}x \int_{-\infty}^{+\infty} \mathrm{d}y \int_{-\infty}^{+\infty} \mathrm{d}\kappa\, k(y - \kappa)\, \rho(x, \kappa)\, (x - \langle x \rangle)\, (y - \langle y \rangle) \tag{D.3}$$

and rearranging the integral gives.

$$\sigma'_{xy} = \int_{-\infty}^{+\infty} \mathrm{d}x\, (x - \langle x \rangle) \int_{-\infty}^{+\infty} \mathrm{d}\kappa\, \rho(x, \kappa) \int_{-\infty}^{+\infty} \mathrm{d}y\, k(y - \kappa)\, (y - \langle y \rangle)\,. \tag{D.4}$$

After substitution of $y - \kappa \to y'$, one summand of the integral vanishes due to the uneven integrand and symmetric integration limits

$$\sigma'_{xy} = \int_{-\infty}^{+\infty} \mathrm{d}x \, (x - \langle x \rangle) \int_{-\infty}^{+\infty} \mathrm{d}\kappa \, \rho(x, \kappa) \int_{-\infty}^{+\infty} \mathrm{d}y' \underbrace{k(y') \, (y' + \kappa - \langle y \rangle)}_{\substack{\text{uneven in } y', \\ \text{integral vanishes}}} . \tag{D.5}$$

The residual part of the y' integral delivers $(\kappa - \langle y \rangle)$ as $k(y)$ is normalised. Finally, back-substitution of $\kappa \to y$ delivers the equality of σ'_{xy} and σ_{xy}

$$\sigma'_{xy} = \int_{-\infty}^{+\infty} \mathrm{d}x \, (x - \langle x \rangle) \int_{-\infty}^{+\infty} \mathrm{d}\kappa \, \rho(x, \kappa) \, (\kappa - \langle y \rangle) \overset{\substack{subst. \\ \kappa \to y}}{=} \int_{-\infty}^{+\infty} \mathrm{d}x \int_{-\infty}^{+\infty} \mathrm{d}y \, \rho(x, y) \, (x - \langle x \rangle) \, (y - \langle y \rangle) = \sigma_{xy} . \tag{D.6}$$

Chapter E

Argon Data with Mono-Crystalline Diamond

Calorimetric $^{40}Ar^{10+}$ low-current measurement using the MC diamond detector. Before entering the stripping section a current of ≈ 10 µA was measured at current transformer US2DT5. This delivered an entrance current of ≈ 10 µA after stripping for charge state 10+. The following procedure is identical as outlined in Sec. 5.3.

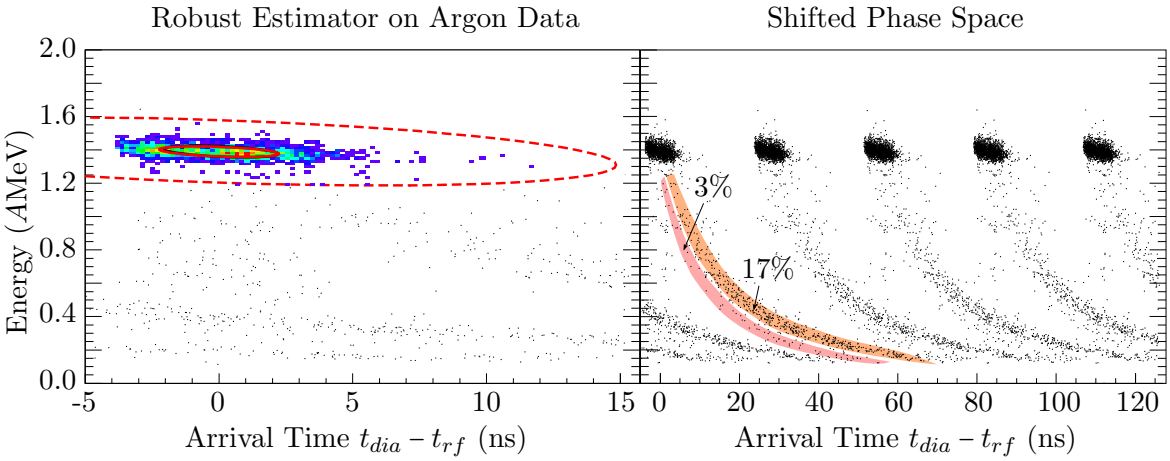

Fig. E.1: Argon measurement using the mono-crystalline diamond detector and the repeated phase space to visualise the trails.

Tab. E.1: Robust estimator values (MCD) of the Ar phase-space in Fig. E.1.

$^{40}Ar^{10+}$ MC Diamond	σ_b (ns)	σ_E (mrad)	cov (mrad·ns)	ε_{rms} (mrad·ns)	α
Integration	2.26	21.2	-20.2	43.5	0.46
Pulse Height	2.22	36.3	-12.7	79.6	0.16
Δ_{mcd}	< 0.03	< 0.2	< 0.5	< 0.2	< 0.01

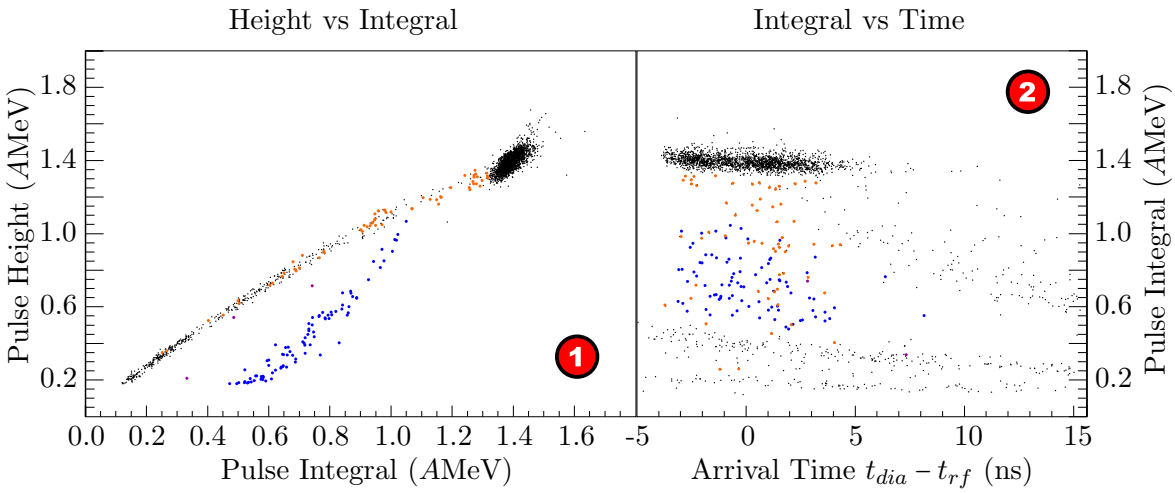

Fig. E.2: Different representation of the recorded argon data. Plot 1 shows the pulse height vs. the pulse integral, both in linear energy calibration. Plot 2 shows the kinetic energy via the pulse-integral information vs. the arrival time at the mono-crystalline diamond detector. Coloured events of both plots correspond to each other.

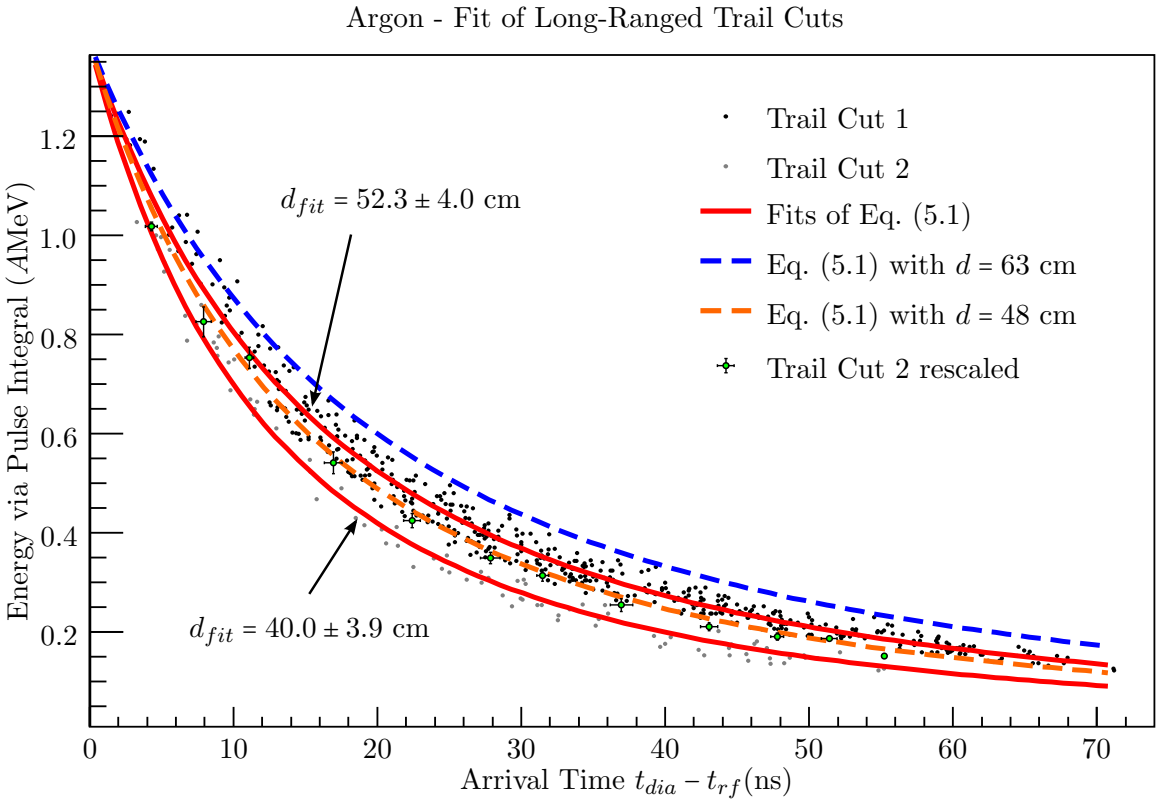

Fig. E.3: Determination of interaction vertices via fit of trails with Eq. (5.1). For a detailed description see Fig. 5.11 and Sec. 5.3.

Bibliography

[1] P. Forck. Joint University Accelerator School - Lecture Notes on Beam Instrumentation and Diagnostics. `http://indico.cern.ch/getFile.py/access?contribId=172&resId=22&materialId=slides&confId=162969`, Retrieved December 16, 2013.

[2] Overview of the accelerator facility at GSI (webpage). `http://www.gsi.de/en/research/accelerator_facility.htm`, Retrieved December 16, 2013.

[3] G. Riehl, J. Pozimski, W. Barth, and H. Klein. A Multifunctional Profile and Emittance Measurement System. In *Proceedings of the "European Particle Accelerator Conference"*, page 756, Nice, France, 1990.

[4] A. Reiter, C. Kleffner, and B. Schlitt. Improved Signal Treatment for Capacitive Linac Pickups. In *Proceedings of the "DIPAC"*, page (in print), Hamburg, Germany, 2011.

[5] S. Richter, W. Barth, L. Dahl, J. Glatz, L. Groening, and S. Yaramyshev. High current beam transport to sis18. In *Proceedings of "22nd International Linear Accelerator Conference"*, page 45, Lübeck, Germany, 2004.

[6] P. Forck, F. Heymach, U. Meyer, P. Moritz, and P. Strehl. Aspects of Bunch Shape Measurements for Slow, Intense Ion Beams. In *Proceedings of the "DIPAC"*, page 186, Chester, UK, 1999.

[7] P. Forck, F. Heymach, T. Hoffmann, A. Peters, and P. Strehl. Measurements of the six Dimensional Phase Space at the New GSI High Current Linac. In *Proceedings of the "International Linac Conference"*, page 166, Monterey, California, 2000.

[8] R. Hollinger, M. Galonska, B. Gutermuth, F. Heymach, H. Krichbaum, K.-D. Leible, K. Ochs, P. Schäffer, P. Spädkte, M. Stork, A. Wesp, and R. Mayr. Status of high current ion source operation at the GSI accelerator facility. *Rev. Sci. Intrum.*, 79:523, 2008.

[9] T. Hoffmann, W. Barth, P. Forck, A. Peters, P. Strehl, and D. A. Liakin. Emittance Measurements of High Current Heavy Ion Beams Using a Single Shot System. In *Proceedings of the "Beam Instrumentation Workshop"*, page 432, Cambridge, Massachusetts, 2000.

[10] F. Becker. *Zerstörungsfreie Profilmessung intensiver Schwerionenstrahlen.* Doctoral Dissertation D17, Technische Universität Darmstadt, 2010.

[11] L. Groening. High current Argon (10+) and Uranium (27+) start distributions at TOF device location used for tracking simulation runs through the post-stripper section. priv. comm., 2010.

[12] L. Groening et al. Benchmarking with UNILAC Experiment. `http://indico.cern.ch/contributionDisplay.py?contribId=23&confId=39839`, Retrieved July 1, 2013. Presentation at "HIPPI 2008 Annual Meeting".

[13] P. M. Lapostolle. Possible Emittance Increase through Filamentation Due to Space Charge in Continuous Beams. *IEEE Trans. Nucl. Sci. NS-18*, 3:1101, 1971.

[14] Stanley Humphries Jr. *Charged Particle Beams*. John Wiley & Sons, New York, 1986.

[15] J. D. Lawson, P. M. Lapostolle, and R. L. Gluckstern. Emittance, Entropy and Information. *Particle Accelerators*, 5:61, 1973.

[16] R. Wideröe. Über ein neues Prinzip zur Herstellung hoher Spannungen. *Archiv für Elektrotechnik*, 21:387, 1928.

[17] W. Barth, P. Forck, J. Glatz, W. Gutowski, G. Hutter, J. Klabunde, R. Schwedhelm, P. Strehl, W. Vinzenz, D. Wilms, and U. Ratzinger. Commissioning of IH-RFQ and IH-DTL for the GSI High Current Linac. In *Proceedings of the "International Linac Conference"*, page 1033, Monterey, California, 2000.

[18] L. W. Alvarez. The design of a proton accelerator. *Phys. Rev.*, 70:799, 1946.

[19] U. Ratzinger. H-type LINAC Structures. In *Proceedings of the "CERN Accelerator School for Radio Frequency Engineering", CAS*, page 351, Seeheim, Germany, 2000.

[20] R. Tiede, U. Ratzinger, H. Podlech, C. Zhang, and G. Clemente. KONUS Beam Dynamics Designs using H-Mode Cavities. In *Proceedings of "Hadron Beam"*, page 223, Nashville, Tennessee, USA, 2008.

[21] R. Tiede. *Simulationswerkzeuge für die Berechnung hochintensiver Ionenbeschleuniger*. Doctoral Dissertation, Johann Wolfgang Goethe Universität, Frankfurt am Main, 2009.

[22] S. Yaramyshev, W. Barth, L. Groening, A. Kolomiets, and T. Tretyakova. Development of the versatile multi-particle code DYNAMION. *NIM, Nuclear Instruments and Methods in Physics Research A*, 558:90, 2006.

[23] J. H. Billen and H. Takeda. PARMILA Manual. *Los Alamos National Laboratory report*, page 90, 1998 (Rev. 2004).

[24] Edwin M. McMillan. The Relation between Phase Stability and First-Order Focusing in Linear Accelerators. *Phys. Rev.*, 80:493, 1950.

[25] T. P. Wangler. *RF Linear Accelerators*. John Wiley and Sons, New York, 1998.

[26] S. Hofmann. Approaching the superheavy elements. *Nuc. Phys. News*, 6:26, 1996.

[27] J. Dilling, D. Ackermann, J. Bernhard, F.P. Hessberger, S. Hofmann, W. Hornung, H.-J. Kluge, E. Lamour, M. Maier, R. Mann, G. Marx, R.B. Moore, G. Münzenberg, W. Quint, D. Rodriguez, M. Schädel, J. Schönfelder, G. Sikler, C. Toader, L. Vermeeren, C. Weber, G. Bollen, O. Engels, D. Habs, P. Thirolf, H. Backe, A. Dretzke, W. Lauth, W. Ludolphs, M. Sewtz, and the SHIPTRAP Collaboration. The SHIPTRAP project: A capture and storage facility at GSI for heavy radionuclides from SHIP. *Hyperfine Interactions*, 127:491, 2000.

[28] C.E. Düllmann. Physical separators for the heaviest elements. *NIM, Nuclear Instruments and Methods in Physics Research B - Beam Interactions with Material & Atoms*, 266:4123, 2008.

[29] U. Ratzinger. The New High Current Ion Accelerator at GSI and Perspectives for LINAC Design Based on H-Mode Cavities. In *Proceedings of the "EPAC"*, page 98, Vienna, Austria, 2000.

[30] W. Barth and P. Forck. The New Gas Stripper and Charge State Separator of the GSI High Current Injector. In *Proceedings of the "International Linac Conference"*, page 235, Monterey, California, 2000.

[31] W. Barth, W. Bayer, L. Dahl, L. Groening, S. Richter, and S. Yaramyshev. Upgrade program of the high current heavy ion UNILAC as an injector for FAIR. *NIM, Nuclear Instruments and Methods in Physics Research Section A*, 557:211, 2007.

[32] W. Barth, L. Dahl, L. Groening, S. Richter, and S. Yaramyshev. Application of Beam Diagnostics for Intense Heavy Ion Beams at the GSI UNILAC. In *Proceedings of the "DIPAC"*, page 161, Mainz, Germany, 2003.

[33] U. Raich. The Longitudinal Emittance Measurement Line at CERN's Proton Linac. In *Proceedings of "Workshop on Transverse and Longitudinal Emittance Measurement in Hadron-(Pre-)Accelerators"*, page 107, Bad Kreuznach, Germany, 2008.

[34] D. Liakin. GSI Generic VME Timing Board. priv. comm., 2007.

[35] E. Berdermann, M. Pomorski, W. de Boer, M. Ciobanu, S. Dunst, C. Grah, M. Kiš, W. Koenig, W. Lange, W. Lohmann, R. Lovrinčić, P. Moritz, J. Morse, S. Mueller, A. Pucci, M. Schreck, S. Rahman, and M. Träger. Diamond detectors for hadron physics research. *Diamond & Related Materials*, 19:258, 2010.

[36] O. Zurkan. Konstruktive und thermische Auslegung eines Hochstrom-Schlitzsystems. Diploma thesis, Fachhochschule Heidelberg, 1996.

[37] J.-C. Denard. Beam Current Monitors. In *Proceedings of "CERN Accelerator School: Course on Beam Diagnostics", CAS*, page 141, Dourdan, France, 2008.

[38] J. W. Wiza. Microchannel plate detectors. *Nucl. Inst. Meth.*, 162:587, 1979.

[39] Krasimir Milchev Kosev. *A High-Resolution Time-of-Flight Spectrometer for Fission Fragments and Ion Beams.* Doctoral Dissertation, Technische Universität Dresden (Institut für Kern und Teilchenphysik), 2007.

[40] P. Forck, A. Bank, T. Giacomini, and A. Peters. Profile Monitors Based on Residual Gas Interaction. In *Proceedings of the "DIPAC"*, page 223, Lyon, France, 2005.

[41] Hamamatsu Photonics K.K. Specification sheet of the MCP compound module F4655-13 used in the Time-of-Flight setup. `http://www.hamamatsu.com/resources/pdf/etd/F4655-13_TMCP1021E05.pdf`.

[42] Hamamatsu Photonics K.K. MCP Selection & MCP Assembly Guide. `http://www.hamamatsu.com/resources/pdf/etd/MCPassy_TMCP0001E10.pdf`, Retrieved July 1, 2013.

[43] P. Kowina. Simulation of the electric field distribution via CST Microwave Studio®. priv. comm., 2009.

[44] E. Berdermann, K. Blasche, P. Moritz, and B. Voss. The use of CVD-diamond for heavy-ion detection. *Diamond & Related Materials*, 10:1770, 2001.

[45] A. Brambilla, D. Tromson, P. Bergonzo, C. Mer, and F. Foulon. Thin CVD Diamond Detectors with High Charge Collection Efficiency. *IEEE Transactions on Nuclear Science*, 49:277, 2002.

[46] E. Berdermann, K. Blasche, P. Moritz, H. Stelzer, and F. Zeytouni. Diamond detectors for heavy ion measurements. In *Proceedings of the "XXXVI International Winter Meeting on Nuclear Physics"*, page 589, Bormio, Italy, 1998.

[47] J. Isberg, J. Hammersberg, E. Johansson, T. Wikström, D. J. Twitchen, A. J. Whitehead, S. E. Coe, and G. A. Scarsbrook. High Carrier Mobility in Single-Crystal Plasma-Deposited Diamond. *Science*, 297:1670, 2002.

[48] A. Galbiati, S. Lynn, K. Oliver, F. Schirru, T. Nowak, B. Marczewska, J.A. Dueas, R. Berjillos, I. Martel, and L. Lavergne. Performance of Monocrystalline Diamond Radiation Detectors Fabricated Using TiW, Cr/Au and a Novel Ohmic DLC/Pt/Au Electrical Contact. *IEEE Transactions on Nuclear Science*, 56:1863, 2009.

[49] M. Pomorski, E. Berdermann, M. Ciobanu, A. Martemyianov, P. Moritz, M. Rebisz, and B. Marczewska. Characterisation of single crystal CVD diamond particle detectors for hadron physics experiments. *Phys. Stat. Sol. (a)*, 202:2199, 2005.

[50] M. Pomorski, E. Berdermann, W. de Boer, A. Furgeri, C. Sander, J. Morse, and for the NoRHDia Collaboration. Charge transport properties of single crystal CVD-diamond particle detectors. *Diamond and Related Materials*, 16:1066, 2007.

[51] P. Strehl. *Beam Instrumentation and Diagnostics*. Springer-Verlag, Berlin, Heidelberg, 2006.

[52] P. Sigmund. *Particle Penetration and Radiation Effects*. Springer-Verlag Berlin Heidelberg New York, 2008.

[53] R. D. Evans. *The Atomic Nucleus*. McGraw-Hill Book Co., New York, 1955.

[54] J. F. Ziegler, J. P. Biersack, and M. D. Ziegler. *SRIM - The Stopping and Range of Ions in Matter*. SRIM Co., 2008.

[55] G. F. Knoll. *Radiation Detection and Measurement (3rd Ed.)*. John Wiley & Sons, Inc., 2000.

[56] W. R. Leo. *Techniques for Nuclear and Particle Physics Experiments, 2nd Ed.* Springer-Verlag, Berlin, Heidelberg, 1994.

[57] A. R. Folov, T. V. Oslopova, and Yu. N. Pestov. Double threshold discriminator for timing measurements. *Nucl. Inst. Meth.*, 356(5):447, 1994.

[58] C. Neyer. A Discriminator Chip for Time of Flight Measurements in ALICE. In *Proceedings of the "3rd Workshop on Electronics for LHC Experiments"*, page 238, London, UK, 1997.

[59] U. Krause and P. Kainberger. UNILAC-event-timing documentation (german) "PZU - Unilac-Pulsezentrale", 6 December 2007. `http://bel.gsi.de/mk/hfu/gm_hfu.pdf`, Retrieved July 1, 2013.

[60] CAEN S.p.A. Homepage of the manufacturer of the VME TDC module V1290N. Manuals and specifications are available online. `http://www.caen.it`.

[61] Struck Innovative Systeme GmbH. Homepage of the manufacturer of the USB 2.0 to VME interface SIS3150. Manuals and specifications are available online. `http://www.struck.de`, Retrieved July 1, 2013.

[62] HIPPI "High Intensity Pulsed Proton Injectors" collaboration part of the CARE framework: JRA3 in the CARE proposal. `http://care.lal.in2p3.fr/Joint/JRA3/HIPPI-modif-26-09-03.doc`, Retrieved July 1, 2013.

[63] Tektronix Inc. Homepage of the manufacturer of the oscilloscope DPO 7254. Manuals and specifications are available online. `http://www.tek.com`, Retrieved July 1, 2013.

[64] ROOT - A Data Analysis Framework. `http://root.cern.ch`, Retrieved July 1, 2013.

[65] E. Lohrmann V. Blobel. *Statistische und numerische Methoden der Datenanalyse*. B. G. Teubner, Stuttgart, 1998.

[66] P. Filzmoser, S. Serneels, and R. Maronna. Robust multivariate methods in chemometrics. *Comprehensive Chemometrics*, page 681, 2009.

[67] M. P. Stockli, R. F. Welton, and R. Keller. Self-consistent, unbiased root-mean-square emittance analysis. *Rev. Sci. Intrum.*, 75:1646, 2004.

[68] P. J. Rousseeuw. Multivariate Estimation with High Breakdown Point. *Mathematical Statistics and Applications*, B:283, 1985.

[69] P. Allison R. Keller, J. D. Sherman. Use of a Minimum-Ellipse Criterion in the Study of Ion-Beam Extraction Systems. *IEEE Transactions on Nuclear Science*, NS-32:2579, 1985.

[70] P. J. Rousseeuw and K. v. Driessen. A fast algorithm for the minimum covariance determinant estimator. *Technometrics*, 41(3):212, 1999.

[71] TRobustEstimator - ROOT implementation of the FAST-MCD concept proposed by P. J. Rousseeuw et al. `http://root.cern.ch/root/html/TRobustEstimator.html`, Retrieved July 1, 2013.

[72] R, The R Project for Statistical Computing'. `http://www.r-project.org/`, Retrieved July 1, 2013.

[73] V. Todorov. robustbase - R package which includes an implementation of FAST-MCD (covMcd). `http://cran.r-project.org/web/packages/robustbase/index.html`, Retrieved July 1, 2013.

[74] Peter Rousseeuw and Katrien van Driessen. Maintained FASTMCD code - rffastmcd.f (rev. 137, 27. Oct. 2007). `http://r-forge.r-project.org/scm/viewvc.php/pkg/src/rffastmcd.f?view=log&root=robustbase&pathrev=137`, Retrieved July 1, 2013.

[75] D. Eddelbuettel and R. Francois. Rcpp/RInside, Easier embedding of R in C++ application. `http://dirk.eddelbuettel.com/code/rinside.html`, Retrieved July 1, 2013.

[76] G. Pison, S. Van Aelst G., and Willems. Small sample corrections for lts and mcd. *Metrika, International Journal for Theoretical and Applied Statistics*, 55:111, 2002.

[77] L. Groening and W. Barth. Expected energy width at GSI stripper section. priv. comm., 2007.

[78] L. Groening. Low correlation α during longitudinal phase space measurement. priv. comm., 2008.

[79] D. Liakin, P. Forck, and T. Hoffmann. An Emittance Evaluation Toolbox. In *Proceedings of the "EPAC"*, page 1191, Genoa, Italy, 2008.

[80] F. M. Bieniosek, S. Eylon, P. K. Roy, and S. S. Yu. Optical faraday cup for heavy ion beams. In *Proceedings of the "Particle Accelerator Conference"*, page 1805, Knoxville, Tennessee, USA, 2005.

[81] J. Nickel. Slit scattering in a microbeam set-up. *NIM, Nuclear Instruments and Methods in Physics Research B - Beam Interactions with Material & Atoms*, 225:402, 2004.

[82] L. Groening and W. Barth. Measurements and Simulations on the Beam Brilliance in the Universal Linear Accelerator at GSI. In *Proceedings of the "International Linac Conference"*, page 344, Gyeongju, Korea, 2002.

[83] J. Pfister, O. Kester, L. Dahl, T. Hoffmann, P. Forck, and U. Ratzinger. Single-Shot Emittance Measurements at HLI and HITRAP. In *GSI Scientific Report 2007*, page 292, Darmstadt, Germany, 2008.

[84] A. Peters and M. Ripert. Pepper Pot Emittance Measurements for Low Energies at GSI and HIT. In *Proceedings of "Workshop on Transverse and Longitudinal Emittance Measurement in Hadron-(Pre-)Accelerators"*, page 86, Bad Kreuznach, Germany, 2008.

[85] H. A. Bethe. Zur Theorie des Durchgangs schneller Korpuskularstrahlen durch Materie. *Ann. Phys.*, 5:325, 1930.

[86] J. F. Ziegler, J. P. Biersack, and M. D. Ziegle. SRIM - The Stopping and Range of Ions in Matter. *NIM, Nuclear Instruments and Methods in Physics Research B - Beam Interactions with Material & Atoms*, 11:325, 2010.

[87] H. Bräuning, A. Bräuning-Demian, G. Bednarz, F. Bosch, X. Cai, C. Cohen, D. Dauvergne, A. Gumberidze, R. Kirsch, C. Kozhuharov, D. Liesen, P. H. Mokler, J.-P. Rozet, Z. Stachura, Th. Stölker, M. Terasawa, S. Toleikis, and A. Warczak. Multiple electron capture from thin C-foils into 46 MeV/u U^{91+}. *NIM, Nuclear Instruments and Methods in Physics Research Section B*, 205:826, 2003.

[88] F. Besenbacher, J. U. Andersen, and E. Bonderup. Straggling in Energy Loss of Energetic Hydrogen and Helium Ions. *Nuclear Instruments and Methods*, 168:1, 1980.

[89] Hu Bitao, Li Yuhong, Cheng Ximen, Liu Zhengmin, and Liu Zhaoyuan. Energy-loss straggling of low energetic ^{16}O ion in Co, Ni and Lu. *Journal of Radioanalytical and Nuclear Chemistry*, 262:489, 2004.

[90] N. Nankov, E. Grosse, A. Hartmann, A. R. Junghans, K. Kosev, K. D. Schilling, M. Sobiella, and A. Wagner. A High-Resolution Time-of-Flight Spectrometer with Tracking Capabilities for Fission Fragments and Beams of Exotic Nuclei. In *GSI Scientific Report 2005*, page 266, Darmstadt, Germany, 2006.

[91] H. Geissel, C. Scheidenberger, P. Malzacher, and J. Kunzendorf. ATIMA - ATomic Interaction with MAtter. `http://www-linux.gsi.de/~weick/atima/`, Retrieved July 1, 2013.

[92] E. J. Sternglass. Theory of Secondary Electron Emission by High-Speed Ions. *Phys. Rev.*, 108:1, 1957.

[93] A. Koyama, O. Benka, Y. Sasa, and M. Uda. Energy spectra of secondary electrons from Al induced by heavy-ion impact. *Phys. Rev. B*, 34:8150, 1986.

[94] S. Yaramyshev. DYNAMION tracking simulations through gas stripper and dispersive dipole section for estimation of transverse and longitudinal coupling. priv. comm., 2011.

[95] K. Inami. Time-of-Flight Measurement with MCP-PMT. In *Proceedings of the "SNIC Symposium"*, Stanford, California, 2006. PSN 044.

[96] L. Groening, I. Hofmann, W. Barth, W. Bayer, G. Clemente, L. Dahl, P. Forck, P. Gerhard, M. S. Kaiser, M. Maier, S. Mickat, T. Milosic, S. Yaramyshev, and D. Uriot. Experimental Evidence of Space Charge Driven Emittance Coupling in High Intensity Linear Accelerators. *Phys. Rev. Lett.*, 103:224801, 2009.

[97] L. Groening, W. Barth, W. Bayer, G. Clemente, L. Dahl, P. Forck, P. Gerhard, I. Hofmann, M. S. Kaiser, M. Maier, S. Mickat, T. Milosic, D. Jeon, and D. Uriot. Experimental Evidence of the 90° Stop Band in the GSI UNILAC. *Phys. Rev. Lett.*, 102:234801, 2009.

Danksagung

Ich möchte mich an dieser Stelle in besonderem Maße bei meinem Doktorvater Prof. Dr. Joachim Enders bedanken. Dr. Peter Forck danke ich für die Betreuung innerhalb der Strahldiagnosegruppe, Dr. Marcus Schwickert für die Unterstützung meiner Arbeit. Herrn Prof. Dr. Dr. h.c./RUS Dieter H.H. Hoffmann danke ich dafür, als Korreferent zur Verfügung zu stehen.

Ich danke den vielen hilfsbereiten Kollegen, die mir sehr ans Herz gewachsen sind und der gesamten Strahldiagnosegruppe für die herzliche Aufnahme. Insbesondere gilt das für meine ehemaligen Bürokollegen Carsten Müller und Dr. Andreas Reiter und meinem neuen Bürogefährten Rainer Haseitl.

Ich danke für die Unterstützung der Injektorengruppe, insbesondere Dr. Lars Groening und Dr. Winfried Barth.

Frau Dr. Bettina Lommel und ihren Kollegen aus dem Targetlabor danke ich für die freundliche Hilfe bei der Untersuchung der Folien.

Weiterer Dank geht an Dr. Piotr Kowina für die CST-Simulation des MCP-Moduls sowie Dr. Stepan Yaramishev für die DYNAMION-Simulationen.

Ein Dank an die Betriebsgruppe darf nicht fehlen. Jener geht ebenso an Hansi Rödl, der keinen Knopf im Hauptkontrollraum scheute und mir immer in Fragen Beschleuniger zur Seite stand.

Wie wichtig ist beste Gesellschaft während des Studiums. In Euch hatte ich sie gefunden: Dr. Robert Cussons, Thomas Reichert, Dr. Ilka Petermann, Benjamin Hellwig, Dominik Bogerts, Dr. Alexander Schmidt, Dr. Felix Schmitt und Dr. Markus Hild - danke für eine wunderbare Zeit!

Ich danke allen Weggefährten und Freunden, die das Leben so bunt und lebenswert machen.

Nicht zuletzt geht mein tiefster Dank an meine Familie, die mich immer unterstützt hat. Ich werde Euch das nicht vergessen.

Erklärung

Hiermit erkläre ich an Eides statt, dass ich die vorliegende Dissertation selbständig verfasst, keine anderen als die angegebenen Hilfsmittel verwendet und bisher noch keinen Promotionsversuch unternommen habe.

Ort, Datum	Unterschrift